



**University of
Nottingham**

UK | CHINA | MALAYSIA

Novel magnetic micro-structured porous materials for biomedical applications

Jesús Molinar Díaz, B.Eng.

A thesis submitted to the University of Nottingham for the
degree of Doctor of Philosophy

December 2022

Abstract

Novel, porous and dense, ceramic (Fe_3O_4 & $\text{Ca}_2\text{Fe}_2\text{O}_5$) and glass-ceramic (phosphate-based glass matrix with magnetic domains) magnetic microspheres have been manufactured for the first time *via* a rapid, single-stage, flame spheroidisation process. Morphological, structural, and compositional investigations provide evidence into the microsphere formation mechanisms, as a function of Fe_3O_4 precursor particle size, precursor-to-porogen mass ratio, and gas flow settings. Optimised conditions for the flame spheroidisation processing of these ceramic and glass-ceramic, porous and dense magnetic microspheres are identified. The magnetic properties of the materials provided for controlled induction heating to a constant level (40 – 45 °C), making these microspheres highly appropriate for localised magnetic hyperthermia applications. Complementary, cytocompatibility investigations confirmed the suitability of porous microspheres for biomedical applications. It is suggested that the flame-spheroidised materials developed opens up new opportunities for the rapid manufacture of innovative synergistic biomaterials, towards magnetic hyperthermia applications.

Acknowledgements

With gratitude, I acknowledge God for bestowing upon me the determination, wisdom and vitality required to accomplish my PhD. Most prominently, I am grateful for the opportunity to use my skills and knowledge to make a meaningful impact on the lives of those affected by cancer.

Profoundly grateful for the outstanding guidance, unwavering support, and exceptional mentorship of my supervisors, Dr Ifty Ahmed and Professor Paul Brown. Eternally thankful for the time, commitment, patience and dedication invested tirelessly in my professional development.

My sincere thanks to the CONACyT and the Faculty of Engineering, University of Nottingham for funding my PhD. Special thanks to colleagues in the Advanced Materials Research Group for fruitful research collaborations. The technical support of the Nanoscale and Microscale Research Centre (nmRC) and Wolfson technical teams is also sincerely appreciated.

My heartfelt gratitude to Sara Wang for her invaluable love, support and compassionate care throughout my PhD journey. Additionally, deep appreciation for my friends in Nottingham, whom I consider to be my family away from home.

My warmest gratitude to my beloved parents, Verónica Rosario and Jesús, for their unconditional and precious love, support, and guidance in every stage of my life. This PhD thesis is dedicated to them with the utmost appreciation for their unwavering dedication to my success.

Journal publications

- **Jesús Molinar-Díaz**, John L. Woodliffe, Elisabeth Steer, Nicola A. Morley, Paul D. Brown, and Ifty Ahmed; “Optimisation of the flame spheroidisation process for the rapid manufacture of Fe₃O₄-based porous and dense microspheres”; *Molecules*, 2023, 28(6), 2523. DOI: 10.3390/molecules28062523
- **Jesús Molinar Díaz**, John L. Woodliffe, Benjamin Milborne, Lauren Murrell, Towhidul Islam, Elisabeth Steer, Nicola Weston, Nicola A. Morley, Paul D. Brown, and Ifty Ahmed; “Ferromagnetic cytocompatible glass-ceramic porous microspheres for magnetic hyperthermia applications”; *Advanced Materials Interfaces*, 2023, DOI: 10.1002/admi.202202089
- **Jesús Molinar Díaz**, Sabrin Abdus Samad, Elisabeth Steer, Nigel Neate, Hannah Constantin, Md Towhidul Islam, Paul D Brown and Ifty Ahmed; “Flame spheroidisation of dense and porous Ca₂Fe₂O₅ microspheres”; *Materials Advances*, 2020, 1, 3539-3544. DOI: 10.1039/d0ma00564a

Abbreviation and acronyms

a.f.u.	Arbitrary fluorescence units
a.u.	Arbitrary units
ABO₃	Perovskite prototype structure
AC	Alternating current
AMF	Alternating magnetic field
BSE	Backscattered electrons
CAGR	Compound annual growth rate
CFO	Calcium iron oxide
Dc	Critical single-domain sizes
DMEM	Dulbecco's Modified Eagle Medium
DNA	Deoxyribonucleic acid
EDS or EDX	Energy dispersive x-ray spectroscopy
EPR	Enhanced permeability and retention
ESCA	Electron spectroscopy for chemical analysis
ESEM	Environmental scanning electron microscope
FDA	Food and Drug Administration
FM	Ferromagnetism
HT+CT	Hyperthermia and chemotherapy
HT+RT	Hyperthermia and radiotherapy
HT-SQUID	High-temperature superconducting quantum interference device magnetometry
HT-XRD	High-temperature X-ray diffractometry
IMS	Industrial methylated spirit
ISP	Irregular shaped particles
MLA	Mineral Liberation Analyser
MRI	Magnetic resonance imaging
MS	Microspheres
NHS	National Health Service
NIR	Near infrared irradiation
PVA	Polyvinyl alcohol

SAED	Selected area electron diffraction
SD	Standard deviation
SE	Secondary electrons
SEM	Scanning electron microscopy
SI	International System of Units
SPM	Superparamagnetism
SQUID	Superconducting quantum interference device magnetometry
Std.	Standard
T1	Longitudinal relaxation time
T2	Transverse relaxation time
TCP	Tissue culture plastic
TEM	Transmission electron microscopy
TER	Thermal enhancement ratio
TGA	Thermogravimetric analysis
UPAC	Union of Pure and Applied Chemistry
XPS	X-ray photoelectron spectroscopy
XRD	X- ray diffractometry

Table of symbols

λ	X-ray wavelength
\sim	Approximately
$<$	Less than
$>$	Greater than
\leq	Less or equal to
\geq	Greater or equal to
$^{\circ}\text{C}$	Degree Celsius
$^{\circ}\text{C}/\text{min}$	Degree Celsius per minute
μ	Magnetic moment
μm	Micrometre
A/m	Amper per metre
$\text{A}_2\text{B}_2\text{O}_5$	Brownmillerite type structure
Am^2/kg	Ampere metre square per kilogram
B	Magnetic induction
B_{hf}	Hyperfine magnetic splitting
d	Lattice spacing
emu	Electromagnetic unit
emu/g	Electromagnetic unit per gram
eV	Electron volts
g	Grams
H	Magnetic field
H_c	Coercive field
I	Current
I_b	Bias current
J/T	Joules per Tesla
kA/m	Kiloampere per metre
keV	Kiloelectron volts
kHz	Kilohertz
kV	Kilovolt
L	Liquid

<i>M</i>	Magnetisation
MHz	Megahertz
mm	Millimetre
mm²	Millimetre square
Mr	Remanent magnetisation
Ms	Magnetic saturation
n	Number
nm	Nanometre
Oe	Oersted
rpm	Revolutions per minute
s	Seconds
T	Tesla
V	Voltage
V	Volume
W	Power
wt%	Weight percentage
δ	Centre shift
θ	Diffraction angle
μ₀	Permeability of free space,
Φ₀	Field (flux) quantum
χ	Magnetic susceptibility

Table of contents

1.0 Introduction.....	18
1.1 Overview.....	18
1.2 Aim and objectives.....	22
1.2.1 Aim.....	22
1.2.2 Objectives.....	22
1.3 Thesis outline.....	23
2.0 Literature review.....	25
2.1 Introduction.....	25
2.2 Magnetic biomedicine.....	25
2.2.1 Introduction.....	25
2.2.2 Global healthcare market: Magnetic micro- and nanoparticles...26	
2.2.3 Commercial iron oxide-based medicines.....26	
2.2.3.1 Iron-oxide diagnostic agents.....26	
2.2.3.2 Iron-oxide therapeutic agents.....28	
2.2.4 Magnetic particles – Clinical trials.....29	
2.2.5 Magnetic micro- and nanoparticles delivery routes.....32	
2.3 Magnetic hyperthermia.....	35
2.3.1 Introduction.....	35
2.3.2 Magnetic hyperthermia overview.....	36

2.3.3 Intracellular and extracellular magnetic hyperthermia.....	37
2.3.4 Cancer cell death mechanism <i>via</i> hyperthermia.....	38
2.3.5 Hyperthermia combined with radiotherapy.....	39
2.3.6 Hyperthermia combined with chemotherapy.....	41
2.3.7 Magnetic hyperthermia combined with MRI.....	42
2.3.8 Clinical magnetic hyperthermia.....	44
2.4 Magnetic biomaterials.....	45
2.4.1 Introduction.....	45
2.4.2 Iron oxides.....	45
2.4.2.1 Magnetite.....	46
2.4.2.2 Maghemite.....	47
2.4.3 Calcium ferrites.....	49
2.4.4 Magnetic glass-ceramics.....	52
2.5 Basics of magnetism and magnetic materials.....	54
2.5.1 Introduction.....	54
2.5.2 Classification of magnetic materials.....	54
2.5.3 Multi- and single- domain particles.....	59
2.5.4 Heating mechanisms for magnetic hyperthermia.....	60
2.6 Manufacture of magnetic porous microspheres	62
2.6.1 Introduction.....	62
2.6.2 Porous biomaterials preparation methods.....	62

2.7 Concluding remarks.....	66
3.0 Materials and methodology.....	67
3.1 Introduction.....	67
3.2 Materials.....	67
3.3 Glass formulation.....	67
3.4 Preparation of microspheres <i>via</i> flame spheroidisation.....	68
3.4.1 Dense microspheres.....	68
3.4.2 Porous microspheres.....	70
3.4.2.1 Fe ₃ O ₄ -based porous microspheres.....	70
3.4.2.2 P40-Fe ₃ O ₄ porous microspheres.....	72
3.5 Microsphere characterisation.....	72
3.5.1 Scanning electron microscopy (SEM).....	72
3.5.2 Energy-dispersive X-ray spectroscopy (EDS).....	76
3.5.3 Mineral liberation analysis (MLA)	77
3.5.4 X-ray diffractometry (XRD).....	78
3.5.5 Superconducting quantum interference device magnetometry (SQUID).....	79
3.5.6 High frequency induction.....	81
3.5.7 Complementary techniques.....	83
3.5.7.1 Mössbauer spectroscopy.....	83
3.5.7.2 Thermogravimetric analysis (TGA).....	83

3.5.7.3 Selected area electron diffraction (SAED) <i>via</i>	
Transmission electron microscopy (TEM)	83
3.5.7.4 X-ray photoelectron spectroscopy (XPS).....	84
3.6 Cytocompatibility investigations.....	84
3.6.1 Cell culturing.....	84
3.6.2 Cell metabolic activity and statistical analysis	85
3.7 Summary.....	86
4.0 Flame spheroidisation of magnetic microspheres using Fe₃O₄ (≤ 45 µm)	
precursors.....	87
4.1 Introduction.....	87
4.2 Fe ₃ O ₄ precursor powder.....	88
4.2.1 Structural transformation as a function of temperature.....	88
4.2.2 Magnetisation as a function of temperature.....	89
4.3 Dense Fe ₃ O ₄ microspheres	92
4.3.1 Fe ₃ O ₄ microsphere topography (<i>unsieved</i>).....	92
4.3.2 Structural characterisation (<i>unsieved microspheres</i>).....	93
4.3.3 Magnetic characterisation (<i>unsieved microspheres</i>).....	96
4.3.4 Compositional analysis (<i>sieved and sectioned microspheres</i>)...98	
4.3.4.1 Mineral liberation analysis.....	98
4.3.4.2 Energy-dispersive X-ray analysis.....	100
4.4 Fe ₃ O ₄ porous microspheres.....	102

4.4.1 Effect of mass ratio.....	102
4.4.1.1 Microsphere topography (<i>unsieved</i>)	103
4.4.1.2 Structural characterisation (<i>unsieved microspheres</i>)..	104
4.4.1.3 Magnetic characterisation (<i>sieved</i>).....	106
4.4.1.4 Compositional analysis (<i>sieved and sectioned</i>).....	107
4.4.1.4.1 Mineral liberation analysis.....	107
4.4.1.4.2 Energy dispersive X-ray analyses.....	114
4.4.2 Effect of gas flow setting.....	118
4.4.2.1 Microsphere topography (<i>unsieved microspheres</i>).....	119
4.4.2.2 Compositional analysis (<i>sieved and sectioned</i>).....	120
4.5 Discussion.....	125
4.5.1 Introduction.....	125
4.5.2 Formation mechanism of dense microspheres	126
4.5.3 Formation mechanism of porous microspheres.....	127
4.5.4 Magnetic properties of Fe ₃ O ₄ dense microspheres.....	129
4.5.5 Fe ₃ O ₄ porous microspheres (<i>1:1 mass ratio</i>).....	130
4.5.6 Ca-rich porous microspheres (<i>1:3 mass ratio</i>).....	131
4.5.7 Fe-rich porous microspheres (<i>3:1 mass ratio</i>).....	132
4.5.8 Sample preparation and effect of particle size.....	133
4.6 Summary.....	133

5.0 Development of compositionally uniform ferromagnetic microspheres

using ($\leq 5 \mu\text{m}$) Fe_3O_4 precursors.....136

5.1 Introduction.....	136
5.2 Effect of mass ratio.....	137
5.2.1 Microsphere topography (<i>unsieved</i>)	138
5.2.2 Structural characterisation (<i>unsieved microspheres</i>).....	140
5.2.3 Magnetic characterisation (<i>sieved microspheres</i>).....	142
5.2.4 Chemical analysis (<i>sieved and sectioned microspheres</i>).....	143
5.2.4.1 Mineral liberation analysis.....	143
5.2.4.2 Energy dispersive X-ray (EDS) analyses.....	149
5.3 Effect of gas flow setting.....	152
5.3.1 Microsphere morphologies (<i>unsieved</i>)	153
5.3.2 Microsphere compositions (<i>sieved and sectioned</i>).....	155
5.4 Compositionally uniform, $\text{Ca}_2\text{Fe}_2\text{O}_5$ magnetic microspheres.....	160
5.4.1 $\text{Fe}_3\text{O}_4:\text{CaCO}_3$ (1:1 mass ratio) precursor powder.....	160
5.4.1.1 Thermal analysis.....	160
5.4.1.2 Structural transformations as a function of temperature.....	161
5.4.1.3 Magnetic properties as a function of temperature.....	163
5.4.2 Structural characterisation of $\text{Ca}_2\text{Fe}_2\text{O}_5$ microspheres.....	165
5.4.2.1 X-ray diffraction (<i>unsieved microspheres</i>).....	165

5.4.2.2 Selected area electron diffraction (SAED) (<i>sieved microspheres</i>).....	166
5.4.3 Ca ₂ Fe ₂ O ₅ microsphere topography (<i>unsieved</i>).....	168
5.4.4 Surface chemical analysis of Ca ₂ Fe ₂ O ₅ microspheres (<i>sieved</i>).....	170
5.4.5 Magnetic characterisation of Ca ₂ Fe ₂ O ₅ microspheres (<i>sieved</i>).....	171
5.4.6 Induction heating of Ca ₂ Fe ₂ O ₅ microspheres.....	173
5.5 Discussion.....	175
5.5.1 Introduction.....	175
5.5.2 Effect of precursor size.....	175
5.5.3 Effect of particle size distribution.....	177
5.5.4 Effect of mass ratio.....	177
5.5.5 Effect of gas flow setting.....	179
5.5.6 Compositionally uniform, Ca ₂ Fe ₂ O ₅ microsphere	180
5.5.6.1 Formation mechanism.....	180
5.5.6.2 High-temperature investigations.....	183
5.5.6.3 Magnetic properties.....	185
5.5.6.4 Induction heating investigations.....	186
5.5.6.5 Biomedical applications.....	187
5.6 Summary.....	187

6.0 Development of ferromagnetic porous and dense glass-ceramic microspheres for biomedical applications.....	189
6.1 Introduction.....	189
6.2 P40-Fe ₃ O ₄ dense microspheres (<i>no porogen</i>)	190
6.2.1 Microsphere topography (<i>unsieved</i>)	191
6.2.2 Structural characterisation (<i>unsieved</i>)	192
6.2.3 Magnetic characterisation via SQUID magnetometry (<i>unsieved</i>).....	193
6.2.4 Compositional analyses (<i>sieved and sectioned</i>).....	195
6.2.4.1 Mineral liberation analysis.....	195
6.2.4.2. Energy dispersive X-ray	202
6.3 P40-Fe ₃ O ₄ highly porous microspheres.....	206
6.3.1 Microsphere topography (<i>sieved microspheres</i>).....	207
6.3.2 Structural characterisation (<i>sieved microspheres</i>).....	211
6.3.3 Magnetic properties of P40-Fe ₃ O ₄ porous microspheres (<i>sieved</i>).....	212
6.3.4 Compositional analyses (<i>sieved and sectioned</i>).....	213
6.3.4.1 Mineral liberation analysis.....	213
6.3.4.2. Energy dispersive X-ray spectroscopy.....	216
6.3.5 Induction heating.....	219
6.3.6 Cytocompatibility.....	221

6.4 Discussion.....	224
6.4.1 Introduction.....	224
6.4.2 P40-Fe ₃ O ₄ dense microspheres.....	225
6.4.2.1 Formation mechanisms of core-shell microspheres....	225
6.4.2.2 Parameter optimisation for P40-Fe ₃ O ₄ core-shell microspheres.....	226
6.4.2.3 Applications and manufacturing routes of core-shell structures.....	227
6.4.2.4 Effect of mass ratio.....	228
6.4.3 Highly porous P40-Fe ₃ O ₄ microspheres.....	231
6.4.3.1 Formation mechanism.....	231
6.4.3.2 Induction heating and ferromagnetic properties.....	233
6.4.3.3 Cytocompatibility.....	236
6.4.3.4 Role of iron oxide in influencing degradation.....	236
6.4.3.5 Routes of delivery.....	238
6.5 Summary.....	240
7.0 Conclusions and future work.....	242
7.1 Conclusions.....	242
7.2 Contributions.....	245
7.3 Future work.....	245
References.....	247

1.0 Introduction

1.1 Overview

Cancer therapy and treatment is one of the most challenging problems for modern medicine [1]. The main cancer treatments of chemotherapy, radiotherapy and surgery, often used in combination, have demonstrated effectiveness in the eradication of primary tumours in the clinical setting [2]. However, the benefits of these strategies are usually accompanied by adverse side effects: *e.g.* (i) conventional chemotherapy is not tumour-selective, equally damaging both healthy and cancerous cells [3, 4]; (ii) radiotherapy delivered to tumours is dose-limited due to toxicity effects on surrounding tissue, resulting in decreased effectiveness [5, 6]; and (iii) cancer can reappear post-surgical removal of tumours, arising from residual malignant cells and cancer stem cells [2]. Also, significant amounts of healthy tissue may be lost as a consequence of tumour removal *via* surgery. The success of a cancer treatment may be measured by its ability to eliminate malignant cells whilst minimising damage to healthy tissue and maintaining functionality. Also, the regeneration of healthy tissue depends on the survival of stem cells post-treatment. Accordingly, complementary clinical strategies are required to eradicate the resistance of malignant cells whilst maintaining patient well-being and quality of life.

Hyperthermia, a method of inducing cancer cell death by the application of heat, uses non-ionising radiation or convective methods to increase temperature (to ~ 40 - 45°C) in targeted regions of the body, while magnetic hyperthermia uses heat generated by localised ferromagnetic particles exposed to an alternating magnetic field [7-9]. Magnetic hyperthermia has been investigated in combination with

radiotherapy and chemotherapy as a strategy for drug-delivery [10]. The main benefit of magnetic hyperthermia relates to its ability to treat site-specific cancer whilst avoiding hazardous systemic effects [11]. Furthermore, magnetic hyperthermia is minimally invasive (*i.e.* delivered intratumorally or intravenously by injection), with mild side effects compared to radiotherapy or chemotherapy [10], and shows synergistic effects with many cancer treatments, *e.g.*, brachytherapy [12], drug-delivery [13], immunotherapy [14] and gene therapy [15].

From magnetic biomaterials available, Fe_3O_4 based superparamagnetic nanoparticles have been the most extensively investigated for localised magnetic hyperthermia applications due to their superparamagnetic expression, non-toxicity [16, 17], and because iron oxide metabolism is readily achieved by heme oxygenase-1 gene which generates haemoglobin and promotes iron cell homeostasis [18]. Superparamagnetism is a form of magnetism that appears in single-domain ferromagnetic or ferrimagnetic nanoparticles. In single-domain nanoparticles magnetisation randomly flips direction under the effect of temperature [19]. Indeed, the use of superparamagnetic iron oxide nanoparticles to deliver heat to various tumour types has been reported, including prostate [20] and glioblastoma [21]. Moreover, aminosilane coated ferrofluid, combined with a clinical alternating magnetic field system, has been used clinically to target glioblastoma tumours [10]. Related ferrites, such as NiFe_2O_4 [22], MnFe_2O_4 [23], CoFe_2O_4 [24] and $\text{Li}_x\text{Fe}_{3-x}\text{O}_4$ [25] have also been investigated, to improve magnetic strength and thermal stability. However, the inherent toxicity of Ni, Mn, Co and Li limits their application [18]. In addition, magnetic bone cements [26], glass-ceramic thermoseeds [27] and Fe-based nanoparticles [28] have also been developed for bone cancer therapy *via* magnetic hyperthermia. Nevertheless, despite multiple ongoing trials, magnetic hyperthermia

has still not achieved regular use in clinical practice, mainly due to its inability to *effectively* heat cancerous cells [29]. It is recognised that the action of a single nanoparticle is insufficient for local hyperthermia [30], with agglomeration of a large number of superparamagnetic nanoparticles needed to generate sufficient heat to damage tumour cells [31, 32]. However, agglomeration can affect the superparamagnetic expression of such nanoparticles, compromising heat performance [31, 33].

An alternative approach is to introduce non-magnetic Ca^{2+} into the ferrite crystalline structure, to generate significant improvements in terms of biocompatibility whilst maintaining magnetic expression and heating control [34, 35]. Non-toxic calcium ferrites have been shown to metabolise safely within the body [36, 37], making them appropriate for a range of biomedical applications, including magnetic hyperthermia. Biomedical investigations using calcium ferrites have been reported in relation to drug-delivery systems [34, 35, 38, 39] and cytocompatibility [34, 36, 38, 40]. Approaches combining metal cations and calcium ferrites for therapeutic applications have also been explored [35, 37, 41-44]. Further, it is suggested a dispersion of *micrometre-scale*, ferro- or ferrimagnetic material, in a suitable matrix, could be used instead of a large number of superparamagnetic nanoparticles [45]. Moreover, a micro-system combining bone-tissue regeneration, cancer thermotherapy and biomechanical support, such as the conjugation of an iron oxide ferromagnetic phase (e.g., magnetite) with a bioactive glass matrix, could provide a promising approach for cancer treatments mediated *via* magnetic hyperthermia, for example, targeting bone oncology [46]. Nevertheless, the present challenge is to develop these materials into practical morphologies for enhanced biomedical investigations.

Microspheres have been widely investigated for a variety of healthcare applications. Porous microspheres, in particular, offer functional advantages, including the incorporation of payloads (drugs, cells, biologics, *etc.*) on external surfaces and within their pores [47, 48], along with cell attachment and proliferation over the enhanced surface area available [47]. However, biomedical applications of microspheres are dependent strongly on the type of material employed. For the case of polymer-based microspheres, applications have included targeted drug-delivery, tissue engineering and regenerative medicine [49, 50]. Whilst ceramic and glass-based microspheres are more commonly associated with tissue regeneration applications, *e.g.*, bone repair [51, 52], orthopaedics [53], dental [54] and cancer therapeutics (radiotherapy) [55], along with magnetic hyperthermia. Moreover, developing magnetic glass ceramics into *porous* morphologies could expedite complementary clinical strategies for tumour treatment and facilitate repeated magnetic hyperthermia treatment to help safeguard against tumour regrowth. Porous microspheres possess large surface areas and can be manufactured with large external and internal (usually interconnected) pores, to enable delivery of drugs, cells or other biologics [48, 56, 57]. There are various strategies for the production of porous bioactive glasses and/or ceramics, including the incorporation of a removable space holder (*via* sintering) [58], sol-gel [59], gel-cast forming [60], polymer foam replication [61], solid-free form (3D printing) [62] and more recently flame spheroidisation [53]. The single-stage, flame-process is a rapid, cost-effective and highly promising technique for large-scale production of porous glass microspheres [47]. Flame spheroidisation may also be used for the manufacture of magnetic, porous and dense, ceramic [63, 64] and glass-ceramic microspheres [65].

In this context, this project focuses on the development of novel, magnetic, porous and dense ceramic and glass-ceramic microspheres *via* the rapid, single-stage flame spheroidisation process as candidates for magnetic hyperthermia applications. Magnetic biomaterials studied includes iron oxides, calcium ferrites and phosphate-based magnetic glasses. Further, the optimisation of precursor-to-porogen mass ratio and O₂/C₂H₂ gas flow conditions for the flame spheroidisation of porous and dense, magnetic microspheres, with highly controlled microsphere sizes and morphologies was also investigated. Complementary magnetisation, induction heating and cell viability assay investigations have also been undertaken to validate the potential of microsphere products for magnetic hyperthermia applications.

1.2 Aim and objectives

1.2.1 Aim

To develop multidomain microspheres with controlled levels of macroporosity for magnetic mediated hyperthermia applications.

1.2.2 Objectives

- To develop highly porous and dense magnetic microspheres *via* a rapid, single-stage, flame spheroidisation process.
- To investigate the parameters associated with the flame spheroidisation process (precursor-to-porogen mass ratio, gas flow ratio and particle size) for the production of magnetic microspheres with high levels of homogeneity and/or porosity.
- To characterise magnetic microsphere product morphology, structure, composition and magnetic properties.

- To study the effects of temperature on precursor powder combinations, prior- and post-flame spheroidisation *via* thermal, structural and magnetic characterisation.
- To investigate the suitability of optimised products for magnetic hyperthermia applications through induction heating experiments and cell viability assays.

1.3 Thesis outline

The thesis comprises seven chapters:

Chapter 1: outlines introduction, aims and objectives.

Chapter 2: reviews the literature related to magnetic biomedicine, magnetic hyperthermia, and magnetic biomaterials (iron oxides, calcium ferrites, and magnetic glass-ceramics). In addition, the basics of magnetism are introduced, including magnetic micro- and nanoparticle heat generation mechanisms. Literature on manufacturing routes for porous biomaterials is also presented.

Chapter 3: introduces the experimental methods used throughout this thesis.

Chapter 4: explains the formation mechanisms of porous and dense magnetic microspheres formed using large (<45 μm) Fe_3O_4 precursor powders during rapid flame spheroidisation. This chapter also discusses the effects of CaCO_3 porogen incorporation with precursor powders, to generate porous microspheres.

Chapter 5: considers the effects of precursor particle size, magnetite precursor to porogen mass ratio, and gas flow setting. Further, this chapter presents a process-map for the manufacture of magnetic microspheres using small (<5 μm) Fe_3O_4 precursors.

Chapter 6: describes the preparation of both dense and porous magnetic microspheres incorporating a phosphate-based glass. A comparative analysis of three different phosphate-based glass - magnetite mass ratios on morphological, structural, compositional and magnetic properties is presented. Moreover, highly porous glass-ceramic microspheres were manufactured. Finally, induction heating and viability assay investigations for porous magnetic microspheres are described.

Chapter 7: presents a general discussion of the main findings presented in the results chapters, in the context of established literature, and summarises the contributions of this thesis, in addition to an outline of possible strategies for future work.

2.0 Literature review

2.1 Introduction

This literature review begins with an overview of magnetic biomedicine, leading on to a consideration of magnetic hyperthermia applications of magnetic particles and magnetic biomaterials. The basics of magnetism are then reviewed. Procedures for the manufacture of porous microspheres are then presented.

2.2 Magnetic biomedicine

2.2.1 Introduction

This project is concerned with the potential of magnetic (bio)materials at the microscale. Over the past few years biomedical research and clinical studies have focused on magnetic particles at the nanoscale, with very limited attention to micron-sized particles. It is well-known that magnetic nanoparticles once exposed to a magnetic field display superparamagnetic expression that results in magnetic saturation and delivery of heat [66]. Additionally, due to their nanometric scale, their mobility within the bloodstream could be manipulated *via* an external magnetic field [67]. Hence, magnetic nanoparticles are attractive for biomedical applications, such as targeted drug delivery, magnetic resonance imaging (MRI) applications & magnetic mediated hyperthermia [18, 68-74]. Regardless of the potential of magnetic nanoparticles, magnetic microspheres also present remarkable advantages for a range of biomedical applications. In this context, this section overviews magnetite nano- and microsphere market growth, commercial iron oxide-based medicines and

associated clinical trials. Delivery routes for magnetic micro- and nanoparticles are discussed later in the present section.

2.2.2 Global healthcare market: Magnetic micro- and nanoparticles

According to Deloitte, by the year 2025, medicine will undergo a paradigm shift, with clinicians basing their diagnoses and treatment decisions on predictive, preventative, personalised and participatory (4P) medicine. This will result from technological and scientific advancements in: digital therapeutics, genomics, epigenetics, artificial intelligence and nanotechnology [75]. Further, Deloitte predicts that by 2040, worldwide healthcare expenditure (~\$8.3 trillion) will be aimed at prevention, and early detection and treatment methods for disease [76]. According to Grand View Research, Inc., the global magnetic beads market size (including both magnetic micro- and nanoparticles) was valued at ~ \$2.79 billion in the year 2021 and predicted to grow at a compound annual growth rate (CAGR) of 11.6% from 2022 to 2030 [77]. It is noted that market expansion has been driven by the healthcare sector, with increasing investments in research to develop more cost-effective therapies with fewer side-effects, *e.g.*, drug-delivery systems and drug carriers; and *in vitro* diagnostic applications such as cell-separation techniques.

2.2.3 Commercial iron oxide-based medicines

2.2.3.1 Iron-oxide diagnostic agents

Iron-oxide particles have demonstrated preclinical and clinical potential as MRI contrast agents. At present, many iron oxide-based diagnostic agents have been developed for the market (Table 2.1), from which only one remains available for MRI (Ferucarbotran) and one for non-MRI clinical applications (Sienna+), a dextran-coated superparamagnetic iron oxide nanoparticle product, injected intravenously into the

Table 2.1 Commercial iron oxide particles developed for clinical diagnoses

Name/Brand	IOP type	Core size/D _H (nm)	Detection system	Application	Commercial status	Reference
Ferucarbotran (Cliavist™, Resovist®)	SPION	~10/60–80	MRI	L, S, MRA, CTL	Available	[71, 73, 78]
Ferumoxytol (Feraheme®, Rienso®)	USPION	6.7/20–30	MRI	L, LN, MRA, M, I, CTL, BT, BL, S	Discontinued for MRI / Available for anemia treatment	[71, 73, 78, 79]
Magtrace (Sienna+)	SPION	-/~60	Sienna+	LN, BRC	Available in Europe	[71, 80]
Ferucarbotran C (SHU 555C, Supravist)	USPION	3–5/20–25	MRI	MRA, CTL, M	Discontinued	[73]
Feruglose (Clariscan®)	USPION	5–7/11–15	MRI	L, LN, P, MRA	Discontinued	[71, 73, 78]
Ferumoxtran-10 (Sinerem®, Combidex®)	USPION	4–6/20–50	MRI	L, LN, S, MRA, M, CTL, BT	Discontinued	[73, 78]
Ferristene (Abdoscan)	MIOP	-/~3500	MRI	GI	Discontinued (2000)	[71, 73]
Ferumoxide (Feridex®, Endorem®)	SPION	4.5–5.6/50–100	MRI	L, S, BM, CTL, BT	Discontinued (2008)	[71, 73, 78, 79, 81]
Ferumoxsil (Lumirem®, GastroMARK®)	MIOP	-/300	MRI	GI, MRA	Discontinued (2012)	[71, 73, 78, 79]
VSOP C184	USPION	4–5	MRI	L, MRA, CTL, M	Stopped development	[73, 78]

Abbreviations: iron oxide particle (IOP), micron-sized iron oxide particle (MIOP), superparamagnetic iron oxide nanoparticle (SPION), ultrasmall superparamagnetic iron oxide nanoparticle (USPION), hydrodynamic diameter (D_H), magnetic resonance imaging (MRI), gastrointestinal (GI), liver (L), spleen (S), magnetic resonance angiography (MRA), bone marrow (BM), lymph node (LN), macrophage (M), cell tracking and labeling (CTL), perfusion (P), brain tumor (BT), inflammation (I), sarcoma (S), brain lesions (BL) and breast cancer (BRC).

tissue of patients with suspected breast cancer, for sentinel lymph node biopsy imaging. This diagnostic agent is detected with an independent SentiMag® magnetometer, rather than MRI [71].

However, regardless the clinical success of those products for MRI, the majority of iron-oxide based products have been discontinued commercially. One of the main concerns that have limited healthcare providers to incorporate iron-oxide based products into regular practice is related to toxicity concerns issued by the Food and Drug Administration (FDA) [73]. For example, ferumoxytol administration studies revealed small, but quantifiable, risks of serious adverse reaction effects (0-1%) and anaphylaxis (0.02-0.2%) [81-84]. Nowadays, Ferumoxytol is approved specifically for use only in adults with iron deficiency anaemia, in patients with chronic kidney disease [85]. Moreover, radiologists are not as familiar with dark contrast imaging generated by iron oxides in transverse relaxation time (T2). Thus, misinterpretation of dark contrast enhancement may result in erroneous diagnosis [86]. Another issue relates to the reluctance of pharmaceutical companies to manufacture iron-oxide contrast agents [87]. The demand for iron-oxide contrast agents is low because their diagnostic utility is usually questioned when compared to conventional contrast agents. Regardless of the discontinuation of some iron-oxides for MRI applications, researchers have continue working to develop a new generation of contrast agents with no notable toxicity and higher blood circulation times [73].

2.2.3.2 Iron-oxide therapeutic agents

For therapeutic applications there are two iron oxide-based agents available (Table 2.2). NanoTherm® is an agent, commercialized in Europe, for the magnetic fluid hyperthermia treatment of brain tumours. Once the particles are injected into the tumour, they are heated to a temperature of ~44.6°C, generating heat within the

tumour whilst avoiding damage to surrounding healthy tissue. Conversely, Feraheme® (Ferumoxytol) is a treatment for iron deficiency anaemia in adult patients with chronic kidney disease, as approved by the FDA in the United States [71, 79], as previously stated.

Table 2.2 Commercial iron oxide particles for clinical treatment.

Name/Brand	IOP type	Core size / D _H (nm)	Application	Commercial status	Reference
Ferumoxytol (Feraheme®, Rienso®)	USPION	6.7 / 20–30	IDA	Available	[71, 78, 88]
NanoTherm®	USPION	- / 15	MHT for BT	Available	[10, 71, 88]
Magnablate I	N/A	N/A	MHT for PC	Clinical trials completed	[71, 89]
Abbreviations: ultrasmall superparamagnetic iron oxide nanoparticle (USPION), hydrodynamic diameter (D _H), iron deficiency anemia (IDA), brain tumor (BT), magnetic hyperthermia (MHT), prostate cancer (PC)					

Indeed, the use of iron oxides is becoming more important in medical imaging and the treatment of cancer and other diseases. In particular, magnetic hyperthermia treatment represents a promising approach for cancer therapeutics, with a small number of products now on the market or in clinical trials (Table 2.2).

2.2.4 Magnetic particles – Clinical trials

The clinical trials indexed on clinicaltrials.gov (U.S. National Library of medicine, 2022), identified against the term ‘iron oxide’, totals 208 studies, focused mainly on diagnostic applications *via* MRI. An overview of the status of these clinical trials is presented in Table 2.3.

Table 2.3 Overview of ‘iron oxide’ related clinical trials (*clinicaltrials.gov, 2022*) [90].

Clinical phase								
Phase 0 / <i>early phase 1</i>		Phase 1	Phase 2	Phase 3	Phase 4	Not defined		
8		27	36	44	37	47		
Status								
Not yet recruiting	Recruiting	Enrolling by invitation	Active, not recruiting	Suspended	Terminated	Completed	Withdraw	Unknown
6	26	2	4	2	18	112	14	23
Main conditions								
<i>Anemia / such as iron-deficiency, hypochromic</i>		Kidney diseases	Renal insufficiency	Neoplasm	Heart disease	Gastrointestinal diseases	Carcinoma	
100		38	36	19	16	14	11	
Type of cancer								
Breast	Pancreatic	Liver	Prostate	Leukemia	Lung	Osteosarcoma	Kidney	Colon and rectal
12	2	4	5	3	1	1	1	1
Iron oxide-based brand								
Ferumoxytol	Ferucarbotran	Feruglose	Ferumoxtran-10	Magtrace	NanoTherm	Magnablate		
107	45	31	31	9	1	1		
Clinical trials per country								
United States	United Kingdom		Rest of Europe		Mexico		Rest of the world	
76	23		49		4		56	

The number of clinical trials, either ongoing or completed, demonstrates the increasing use of iron oxide-based medicines in modern healthcare. For example, *Sienna+* (commercially available for breast cancer) has also been utilised for sentinel lymph node visualisation for rectal cancer investigations at Oxford University Hospitals NHS Trust. NanoTherm[®] (commercially available for brain tumour magnetic hyperthermia) is currently on the recruiting stage for prostate cancer treatment in the U.S. Ferumoxytol has been tested as contrast agent in a Phase 4 pancreatic cancer study; whilst ferumoxytol and ferumoxtran-10 have been involved in clinical trials for drug-delivery applications. Further, Magneblate-I was studied for magnetic hyperthermia of prostate cancer patients at University College London Hospitals. Additionally, several clinical trials are being directed towards medical imageology, *via* MRI. Hence, magnetic particles have been shown to be biocompatible with strong potential for real-world applications. They offer advantages over non-magnetic biomaterials, *e.g.* external magnetic field controllability; theranostic potential; and dual therapeutic approaches (*e.g.* drug delivery and hyperthermia) within the same system. However, further research efforts are needed to improve the efficiency of magnetic biomaterials in clinical trials *e.g.*, by testing novel magnetic material formulations. Calcium ferrites, for example, have shown attractive magnetic properties suitable for healthcare applications (detailed in 2.4.3). Moreover, due to the presence of calcium within their structure, they have potential to enhance biocompatibility. Nonetheless, nowadays there are no clinical trials using calcium ferrites. Furthermore, glass-ceramics are a type of biomaterials that have reached clinical trials for dental applications. However, no magnetic glass-ceramics are reported. In this context, novel magnetic biomaterials could be designed into practical morphologies (*e.g.*,

microspheres) with size control, highly suitable for delivery in a range of routes, depending on the target tissue/tumour.

2.2.5 Magnetic micro- and nanoparticles delivery routes

Drugs can be administered through different routes depending on the target tissue, physicochemical properties of the drug, or duration of the treatment [91, 92]. In particular, the administration route depends on the target tissue, drug pharmacokinetics, and drug permeability. Figure 2.1 illustrates the different routes of drug delivery.

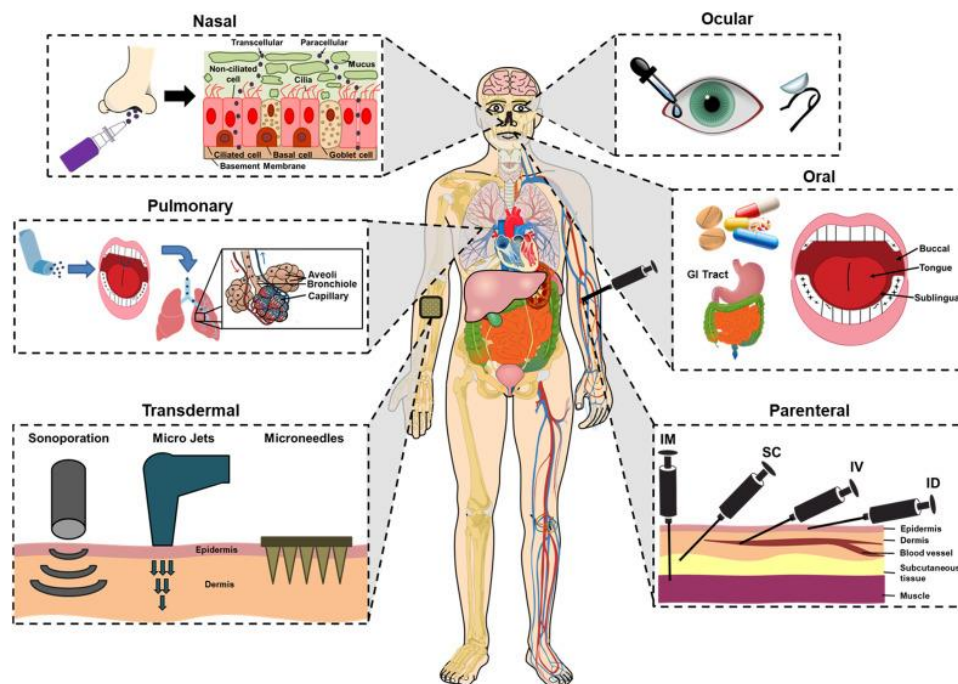


Figure 2.1. Schematic of drug delivery routes [93]

For biomedical applications, size is a key feature that determines the half-life of drug clearance in tissue, for specific target applications. Depending on size, particles can be used to target specific cell channels, or be engulfed for drug delivery inside tumour cells. Moreover, they can be delivered through the bloodstream, or *via* the

respiratory tract as an aerosol formulation [50]. Table 2.4 presents an overview of particle sizes and their delivery targets according to size.

Table 2.4 Drug delivery routes & targets of micro- and nanoparticles

Tissue	Delivery route	Delivery target	Particle size $\mu\text{m} / \text{nm}$	Reference
Bone	Intra-tumoral / Implant	Bone tissue / Tumour site	60 – 200	[51, 94]
Blood	Intra-arterial	Capillaries	~ 8	[95]
		Hepatic arteries	< 3 (mm)	
	Intra-venous	Blood stream	<i>10 - 100</i>	[96]
		Tumour site	<i>50 -100</i>	
Prostate	Intra-tumoral / Implant	Tumour site	60-200	[97, 98]
	Intra-venous	Tumour site	<i>15-20</i>	
Gastrointestinal	Intra-cavity e.g., Oral	Gastrointestinal tract	3-5	[99, 100]
Brain	Intra-tumoral	Tumour site	<i>15-20</i>	[21]
Lung	Intra-cavity e.g., inhalable aerosol or drops	Tracheo-bronchio	> 10	[101-103]
		Alveolar region	< 100 & 1- 5	
		Bronchioles	<i>500 – 1</i>	
		Alveoli	<i>< 250</i>	
		Endothelium fenestrate	<i>< 60 - 80</i>	
Kidney	Intra-venous	Glomerulus	< 5 - 6	[103, 104]
		Filtration diagram	< 4 - 6	
		Perisinusoidal space	< 50	
Liver	Intra-arterial (catheter)	Hepatic vasculature	20-30	[103, 105]
	Intra-venous	Billiary excretion	< 6	
		Sinusoidal sieve	< 200	
Eye	Drops Contact lens	Ocular	1	[106]
		Respiratory tract	< 3	
		Capillaries	2 - 13	
Skin	Transdermal	Stratum corneum surface, furrows, and openings of hair follicles	<i>300</i>	[107]

Indeed, magnetic microparticles can be delivered to tumours *via* intra-tumoral, intra-arterial and intra-cavity administration, whereas magnetic nanoparticles are usually delivered intra-venously [10].

- ***Intra-tumoral:*** Microparticles injected into a variety of tissue tend to remain where they are delivered [108]. Hence, they are suitable for direct delivery to a site of interest. For magnetic hyperthermia, magnetic particles may be subjected to a reheating process, to eliminate newly born malignant cells in order to prevent tumour reappearance [109]. Hence, the ability to remain in tissue is crucial.
- ***Intra-arterial:*** Magnetic microparticles have been used as MRI contrast agents for arterial-infused chemoembolization [95, 110, 111]. The size of microparticles aggregates must fall into the range limits of specific blood vessels, for hepatic arteries no larger than ~ 3 mm, and ~ 8 μm for the case of capillaries (Table 2.4) [95].
- ***Intra-venous:*** Magnetic nanoparticles, 10 - 100 nm, are optimal for long circulation times *in vivo* by intravenous injection [68, 69, 112]. Nanoparticles smaller than 10 nm are rapidly removed by renal clearance, *i.e.* kidney filtration. In contrast, particles larger than 200 nm are sequestered by phagocytic cells in the spleen, or by macrophage cells in blood, *i.e.* splenic and liver filtration [70, 113-116]. Broadly, nanoparticles have the virtue of smaller size, which enables them to cross biological barriers, whilst microparticles rarely cross such barriers. However, nanoparticles are too small to produce embolic phenomena. Microparticles can be used to embolise vessels of similar diameter. Hence, blood flow can be intentionally blocked for diverse medical approaches, *e.g.*, chemoembolization of hepatocellular carcinomas [108].

- ***Intra-cavity:*** As summarised in Table 2.4 for inhalable particle delivery, microparticles $\geq 10 \mu\text{m}$ will deposit in the upper respiratory tract; and microparticles, $1 - 3 \mu\text{m}$, will reach the lower respiratory tract, including alveoli [108]. Indeed, magnetic microparticles have been reported for targeted pulmonary delivery via aerosol delivery [117, 118]. It is noted that large porous microspheres can be tailored to reach the lower airways [119]. Further, large magnetic nanoparticles ($\sim 300\text{--}400 \text{ nm}$) have shown relevance as magnetic hyperthermia agents for lung cancer [120]. Small nanoparticles ($< 60 \text{ nm}$) will be inhaled and exhaled [121]. For oral particle delivery, magnetic particles $3.5 \mu\text{m}$ and 300 nm have been used as contrast agents for MRI applications (Ferristene and Ferumoxsil, respectively, Table 2.1). However, oral administration is challenging because most of the magnetic particles will be excreted [122].

It is noted that magnetic particles can be delivered by a range of routes, depending on size. For biomedical applications, a combination of particle size and spherical shape are strongly desired to promote easy flow [123]. In particular, magnetic biomaterials offer further, high potential for a wide variety of applications.

2.3 Magnetic hyperthermia

2.3.1 Introduction

Magnetic biomaterials have application in many different areas of medicine, including molecular and cell biology, cardiology, neurosurgery, oncology and radiology [124]. In this section, emphasis is made on magnetic hyperthermia for cancer treatment. Synergistic approaches of magnetic hyperthermia with radiotherapy, chemotherapy

(i.e., targeted drug delivery) and MRI are also outlined. The state of the art of clinical magnetic hyperthermia is briefly described.

2.3.2 Magnetic hyperthermia overview

Hyperthermia, a method to induce cancer cell death by raising the temperature of cancerous regions of the body to 40 - 45 °C, has been widely studied for cancer treatment [10, 109, 125]. There are three types of hyperthermia treatment: (1) **whole body**, e.g., immersion in hot water bath and radiant heat applied by UV; (2) **regional**, e.g., patient's blood is removed, heated and returned into patient's blood stream, typically with anticancer therapeutics; and (3) **local**, whereby heat is generated in relatively small tumours located within accessible body cavities, such as the oesophagus or the rectum [109, 125]. In this context, magnetic hyperthermia uses heat generated by localised ferromagnetic particles exposed to an alternating magnetic field (Figure 2.2) [7-9].

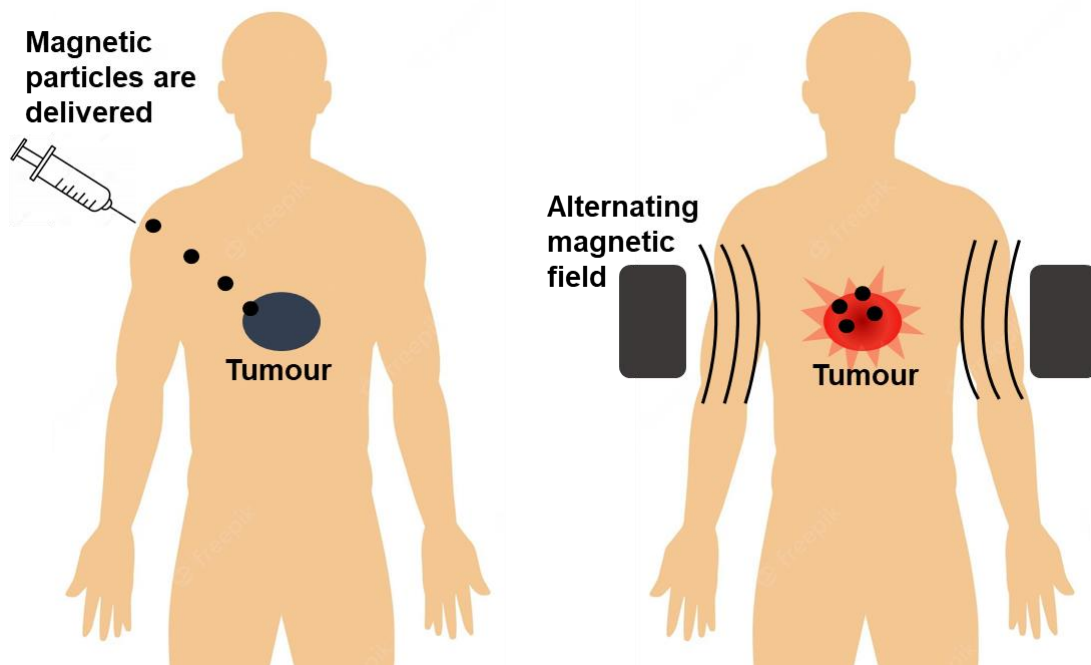


Figure 2.2 Schematic of magnetic hyperthermia.

Typically, high frequencies in the range of 0.4 – 3000 MHz (*i.e.*, microwave hyperthermia [126, 127]) are applied in clinical hyperthermia [109, 128-131], in order to enhance cancer cell death. However, recent investigations aimed to achieve magnetic hyperthermia at lower frequency levels, in order to avoid direct electrical stimulation of nerves and muscles, which is avoided if frequencies used are higher than few hundred kHz, *e.g.*, 135 – 400 kHz [132-134]. These low frequency levels can be achieved through electromagnetic methods, *e.g.*, induction heating system [129].

2.3.3 Intracellular and extracellular magnetic hyperthermia

The raise of temperature in the range of 40 – 45 °C, referred as hyperthermia, induces cell death by apoptosis. **Apoptosis** is a regulated cell death process that plays a fundamental role in the balance between cell survival and death signalling essential to prevent disease. Unregulated apoptosis promotes abnormal cellular proliferation and genetic defects downstream, leading to tumorigenesis [135]. In this context, hyperthermia promotes cellular alterations, such as protein unfolding and aggregations; disruption of the cytoskeleton, fragmentation of the Golgi system and endoplasmic reticulum; a reduction in the number of mitochondria & liposomes; along with nuclear and cell membrane damages [136, 137]. Moreover, magnetic particles can also induce cell death by **necrosis** which occurs when the cancer cells cannot survive to major external damage (*e.g.*, extracellular magnetic hyperthermia [138] or thermoablation in temperatures above 45°C [139]).

Beola, *et al* [140], investigated intra- and extracellular magnetic hyperthermia in 3D cell culture models. The cell death mechanism activated by magnetic particles located inside the cells was through apoptosis, whereas magnetic particles heterogeneously distributed outside and inside the cells triggered cell death *via* necrosis. In this context, it is noted that magnetic microparticles (*e.g.*, magnetic

microspheres) delivered in the cancerous tissue induce cell death by necrosis and apoptosis (Figure 2.3a), whereas magnetic nanoparticles, having the virtue of their smaller size can cross biological barriers (cellular internalisation) to induce cell death *via* apoptosis (Figure 2.3b). The mechanisms of cancer cell death *via* hyperthermia are now briefly explained.

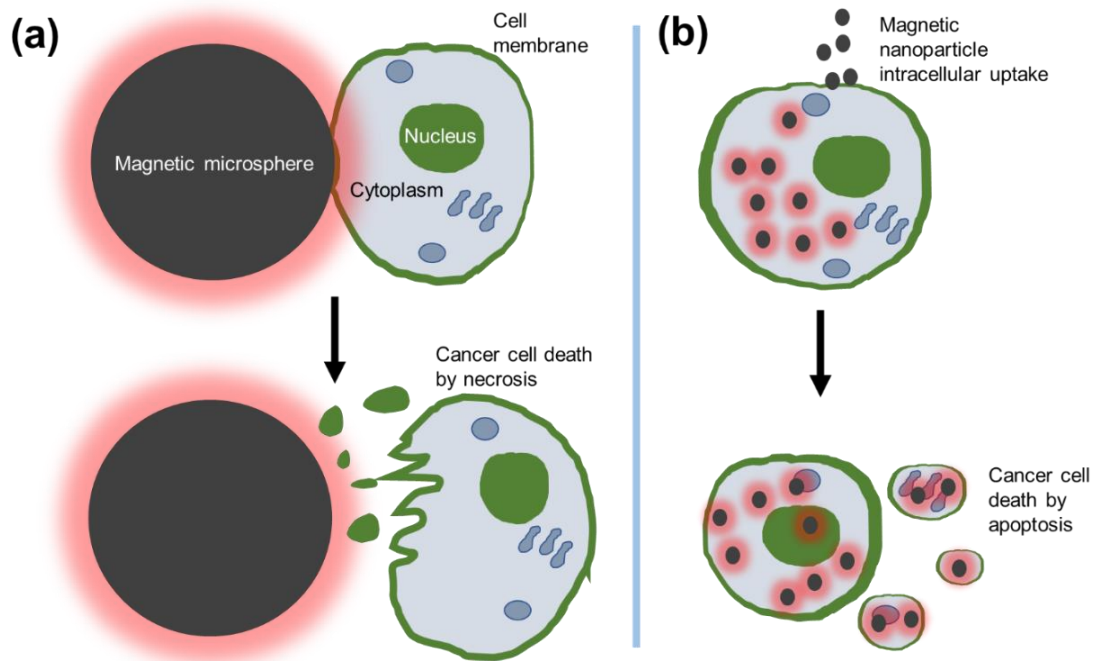


Figure 2.3. Schematic representation of **(a)** extracellular and **(b)** intracellular magnetic hyperthermia

2.3.4 Cancer cell death mechanism *via* hyperthermia

The poor vasculature of solid tumours results from a combination of low pH and hypoxia, distinct from healthy tissue under normal conditions [109, 125, 141]. These conditions make malignant cells more sensitive to heat [125], and hyperthermia can trigger cell death through a number of different mechanisms [7, 109]. For example, **(i)** individual proteins have well-defined temperature thresholds for denaturation [10, 109,

142]. At temperatures in the range of 40 – 45°C, only a small fraction become denatured. However, with time, some of these proteins can co-aggregate with native proteins and the level of aggregation increases significantly [109]. Notably, the combination of heat-induced denaturation and subsequent co-aggregation can affect several pathways downstream, *e.g.*, the inactivation of protein synthesis, cell cycle progression and DNA repair [10, 109, 143]. Another mechanism responsible for cell death is **(ii)** heat-induced alterations to plasma and sub-cellular organelle membranes. Whilst sufficient heat application can result in cell death, surviving cells may develop thermotolerance due to activation of heat shock proteins, proteolytic enzymes, RNA- and DNA-modifying proteins, *etc* [109, 125, 144]. Hence, hyperthermia has rarely been considered as a single modality for cancer therapeutics, primarily due to the development of thermotolerance (which would make subsequent hyperthermia treatments less effective) and poor specificity, *i.e.* equally affecting non-malignant and malignant cells.

To overcome these challenges, there has been a tendency to investigate hyperthermia in combination with other therapeutic approaches, *e.g.*, hyperthermia and radiotherapy (HT+RT) or hyperthermia with chemotherapy (HT+CT) [109, 139, 145].

2.3.5 Hyperthermia combined with radiotherapy

In order to improve their individual efficacies, the synergic modalities of HT+RT and HT+CT have been investigated. One way to evaluate the effectiveness of radiotherapy or chemotherapy is through the thermal enhancement ratio (TER), which is the ratio between the radiation or drug dose needed to achieve a specific endpoint, and the radiation or drug dose combined with hyperthermia to achieve the same endpoint [109, 145, 146]. Both clinical and preclinical studies demonstrate that TER is highest when

hyperthermia is delivered in synergy with radiotherapy [109, 125]. In conventional radiotherapy, the radiation dose required to eradicate all malignant-cell populations usually cannot be applied because it may trigger long-term secondary effects, e.g., tissue-fibrosis or secondary malignancies [145]. However, hyperthermia is a powerful radiosensitiser, meaning that lower radiation doses can achieve the same local tumour therapeutic effect, whilst reducing secondary side effects on normal tissue [109, 145]. An example of this is brachytherapy, a type of internal radiotherapy that requires surgical intervention to deliver radioactive sources (brachytherapy seeds) to specific cancer sites [55, 147]. This localised method is used usually as a complementary therapy to conventional surgery, chemotherapy and external, conventional radiotherapy. However, an issue with permanent brachytherapy seeds is that they would eventually require surgical removal [55]. However, in real-world applications, these combined approaches remain challenging, mainly because of the complication of avoiding cytotoxic effects of HT+RT / HT+CT on surrounding healthy tissue.

Nevertheless, one promising approach to overcome this barrier is **magnetic hyperthermia**. For example, magnetic hyperthermia represents an alternative direction for brachytherapy, through enhancement of the locally injected dose of magnetic particles combined with simultaneous hyperthermia stimulation [10, 109]. An important advantage in this case is that the radionuclides do not have to be released, thus removing the control of release requirement [124]. Furthermore, this approach represents an exciting area of research, e.g., with the potential to combine brachytherapy with magnetic particles.

2.3.6 Hyperthermia combined with chemotherapy

It is well known that chemotherapeutic methods are relatively non-specific. Consequently, drugs are “wasted” when residing in areas where they are not needed, often leading to secondary, unwanted side effects. Magnetic particles have been extensively studied to transport drugs to target tissue, whilst drug release control would be extremely advantageous once the carrier reached the target (e.g., cancerous tumour). Drug release can then be triggered *via* several different mechanisms, including pH changes in the microenvironment, mechanical forces, near infrared irradiation (NIR), chemical reduction or magnetic hyperthermia [148]. In particular, magnetic hyperthermia can improve synergistically the application of certain chemotherapeutic agents, such as cisplatin, cyclophosphamide and bleomycin [149-151]. As stated previously, tumours are associated with acid environments and hypoxia, conditions which sensitise cancer cells to higher temperatures [109]. In a clinical setting, heat can facilitate perfusion within a tumour, leading to improved delivery of chemotherapeutic agents and the elevation of oxygen concentrations [109, 125].

Magnetic nanoparticles are considered advantageous for targeted drug-delivery for many reasons, such as their superparamagnetic properties, remote control capability, and cellular internalisation, *i.e.*, endocytosis. In order to enhance magnetic nanoparticles hydrophilic and biocompatibility properties, magnetic nanoparticles are surface functionalised with a hydrocarbon layer and loaded with drugs for targeted delivery [152-154]. However, low drug loading capacity is associated with systems where drugs are attached to the particle surface, with the drugs being lost easily when they interact with the biological environment. In response, the use of polymers coating to protect magnetic carrier nanoparticles are promising for minimising wastage of

drugs whilst in bloodstream transit [155]. Regardless of the opportunity to coat magnetic nanocarriers with polymers, it has been reported that immobilising magnetic particles at tumour sites is likely to be more effective for treatment efficiency, since they are unlikely to be removed by blood flow due to enhanced permeability and retention (EPR) effects in tumour vasculature [156]. **Porous magnetic microspheres** exhibit ideal storage features, to protect drugs travelling through the biological environment, thereby avoiding unnecessary waste of drugs during their time in the body. Further, their strong magnetism means that microspheres can be manipulated by an alternating magnetic field (AMF) within the vascular system and retained within the capillaries of the target tissue. Indeed, drug-loaded porous magnetic microspheres could be injected directly into the tumour for controlled delivery.

2.3.7 Magnetic hyperthermia combined with MRI

The MRI technique presents outstanding sensitivity to detect the magnetic moments of iron oxide particle protons [124, 157]. This effect is detailed as follows. A steady magnetic field ($\sim 1\text{T}$) is applied to a material, stimulating proton parallel alignment to the field. The net magnetic moment processes around the direction of this field. Subsequently, a transverse radio frequency magnetic field (perpendicular to the steady field) is applied to measure the resultant signal produced by the alignment. Once the second field is removed, the magnetic moments relax back to their initial equilibrium state, and this relaxation occurs *via* two distinct processes, *i.e.*, T1 (longitudinal relaxation) and T2 (transverse relaxation). In this context, if a region is decorated with magnetic particles, the relaxation time is reduced; contrary to untagged regions where relaxation times are faster. Consequently, contrast is produced between tagged and untagged regions [124, 158].

Interestingly, the magnetic gradient coils, used for slice selection and image encoding in MRI systems, can also be employed to apply 3D steering forces on magnetised particles [159]. This can potentially improve the targeting of magnetic microspheres in tissue, with MRI integration providing for direct imaging of **magnetic hyperthermia** treatment efficacy. Investigations on combined magnetic hyperthermia / MRI approaches have been reported. Sánchez-Cabezas, *et al* [160] evaluated iron oxide superparamagnetic nanoparticles T1/T2 relaxation times and demonstrated relevance for dual magnetic hyperthermia and MRI approaches. Shingte, *et al* [161] studied the effect of iron oxide nanoparticle shape on hyperthermic and MRI contrast performance. Salimi, *et al* [72] developed dendrimer-coated iron-oxide nanoparticles for breast cancer theragnostic using combined hyperthermia and MRI applications.

Notably, most research attention has been given to superparamagnetic nanoparticles (instead of micron-scale particles) as contrast agents for MRI [79, 162, 163]. However, recent investigations have shown that micron-sized particles represent an attractive alternative for medical diagnosis *via* MRI. For example, Mathieu and Martel [159] have demonstrated that novel MRI systems, using $10.9 \pm 1.6 \mu\text{m}$ microparticles, can address the limitations of magnetic targeting approaches. Alternative approaches build on the manufacture of large microsphere platforms, integrated with magnetic clusters composed of agglomerated superparamagnetic nanoparticles. For example, Li *et al* [95] reported on the preparation of superparamagnetic nanoparticles with therapeutics embedded in a polymer matrix (to produce microparticles in the range $230 \pm 35 \mu\text{m}$), as an MRI particle injection system with application in human liver chemoembolization. Further, to address some of the limitations of iron-based MRI cell tracking, Melo *et al* [164] explored an alternative imageology modality termed magnetic particle imaging (MPI). Magnetic microspheres

(0.9 – 1.63 μm) were used with multiple iron crystals (5 – 10 nm) distributed throughout a polymer matrix for cancer cell imaging in mouse brain. Similarly, Li *et al* [165] fabricated polyvinyl alcohol (PVA) microspheres (262 – 958 μm) encapsulating magnetic nanoparticles for contrast imageology, mediated by iron oxide nanoparticles, whilst the PVA matrices functioned as embolization agents.

Indeed, most clinical trials exploring iron oxide have focused on MRI applications, highlighting the potential and importance of these materials as contrast agents in medical imageology. However, further research and clinical trials of magnetic microparticles are needed, in particular for magnetic hyperthermia combined with MRI.

2.3.8 Clinical magnetic hyperthermia

Nowadays, the main company promoting iron-oxide based products for clinical hyperthermia applications is MagForce AG, based in Berlin. The company pioneered NanoTherm[®], an aminosaline coated ferrofluid, along with a clinical AMF system, NanoActivator[®], and associated simulation software, NanoPlan[®] [10, 109]. Phase 1 and 2 clinical trials using intratumorally delivered superparamagnetic nanoparticles with simultaneous AMF MagForce[®] have been reported for patients with glioblastoma and prostate cancers [10]. However, despite the development of the NanoTherm[®] system, multiple ongoing clinical trials, and a large scientific literature on the topic, magnetic hyperthermia is still not a regular clinical practice, mainly due to its inability to effectively heat cancerous cells [29]. It is recognised that the action of a single nanoparticle is insufficient for local hyperthermia [30], with agglomeration of a large number of superparamagnetic nanoparticles needed to generate sufficient heat to kill tumour cells [32, 166]. However, agglomeration can affect the superparamagnetic expression of such nanoparticles, compromising heat performance [31, 33]. In the present work, it is proposed a dispersion of micrometre-scale, ferro- or ferrimagnetic

material, in a suitable matrix, could be used instead of a large number of superparamagnetic nanoparticles [45].

2.4 Magnetic biomaterials

2.4.1 Introduction

This section overviews iron-based particles, such as iron oxides, calcium ferrites and magnetic glass-ceramics, most strongly concerned with the present project.

2.4.2 Iron oxides

Compared with other biomaterials, iron oxides exhibit superior magnetic and biochemical properties, *e.g.*, superparamagnetism (*nanoscale particles*), ferro- or ferrimagnetism (*micro-metric particles*), non-toxicity, biodegradability and biocompatibility. In particular, iron oxide metabolism is readily achieved by heme oxygenase-1 gene which generates haemoglobin and promote iron cell homeostasis [18]. Such characteristics provide for effective application across a number of medical fields [70, 113, 116, 167]. The different oxidation states of iron oxide include: iron (II) oxide (FeO), iron (III) oxide (Fe₂O₃) and iron (II, III) oxide (Fe₃O₄). Iron (III) oxide (Fe₂O₃) exhibits a number of different crystalline polymorphs: α-Fe₂O₃, β-Fe₂O₃, γ-Fe₂O₃ and ε-Fe₂O₃, as shown in Fe-O binary phase diagram (Figure 2.4). The most biocompatible iron oxides are maghemite (γ-Fe₂O₃) and magnetite (Fe₃O₄). Of these two, magnetite (Fe₃O₄) is the most commonly used form for biomedical applications [16, 17].

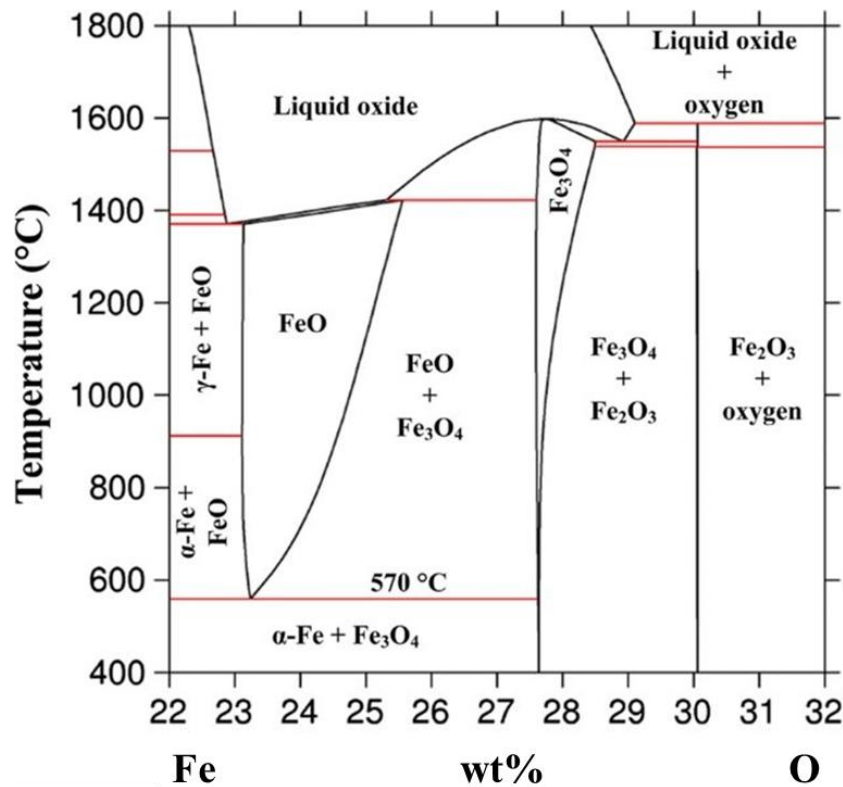


Figure 2.4 Fe-O binary phase diagram [168]

2.4.2.1 Magnetite

Magnetite (Fe₃O₄) is a cubic ferrite that exhibits *ferrimagnetic* behaviour. Cubic ferrites are represented as MFe₂O₄, where M is a metal. In the case of Fe₃O₄, Fe ions exist in both the 2+ and 3+ valence states. The two types of Fe ions have different magnetic moments; and a net magnetic moment can arise because, for the solid as a whole, the spin moments are not completely cancelled, *i.e.* magnetisation arises from parallel alignment of Fe²⁺ ion moments, whilst the spin moments of Fe³⁺ ions cancel one another [124, 169, 170]. Fe₃O₄ adopts an inverse spinel structure [171] (Figure 2.5a) which “is based on an fcc arrangement of O²⁻ in which Fe³⁺ occupy ½ of the tetrahedral interstices, and a 50:50 mix of Fe³⁺ and Fe²⁺ cations occupy 1/8 of the octahedral interstices” [172] (Figures 2.5b,c). Magnetite has a Curie temperature of 580°C and a melting point of 1597°C.

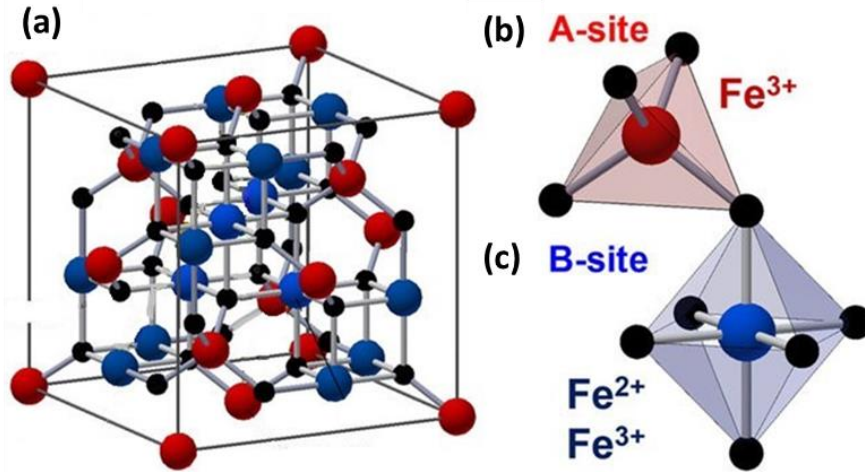
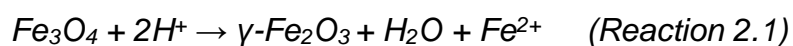


Figure 2.5 (a) The inverse spinel structure of Fe_3O_4 (b) tetrahedral and (c) octahedral sites. Reproduced from [173]

2.4.2.2 Maghemite

The magnetite phase readily oxidises into maghemite ($\gamma\text{-Fe}_2\text{O}_3$) by weathering or low-temperature oxidation with partial conversion of all Fe^{2+} (ferrous ions) into Fe^{3+} (ferric ions) (Reaction 2.1) [174]:



The oxidation process of magnetite generates cation vacancies in the maghemite inverse spinel structure (Figure 2.6) upon removal of Fe^{2+} , to compensate for the positive charges [174, 175]. It is noted that $\gamma\text{-Fe}_2O_3$, a ferric oxide, exhibits similar properties to magnetite (Table 2.5) including an inverse spinel structure and ferrimagnetic expression at room temperature [176]. Hence, it is challenging to distinguish between $\gamma\text{-Fe}_2O_3$ and Fe_3O_4 solely on the basis of their crystallographic arrangement and magnetic properties [177].

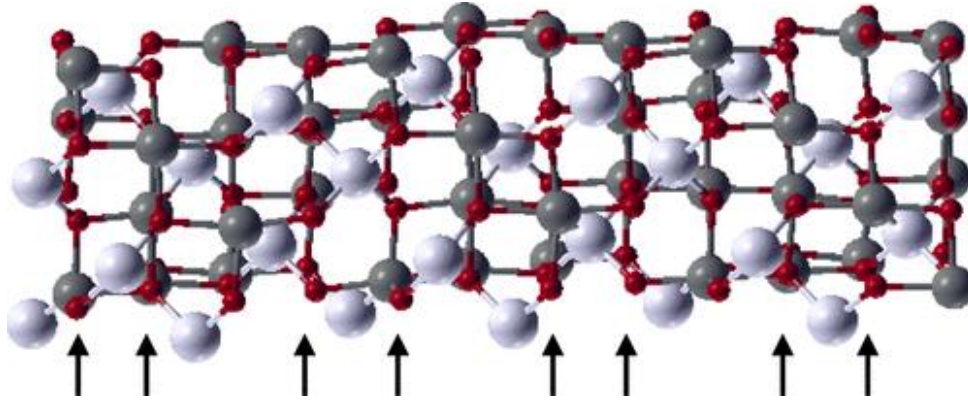


Figure 2.6 Maghemite ($\gamma\text{-Fe}_2\text{O}_3$) inverse spinel structure. Light and dark grey spheres represent tetrahedral and octahedral Fe^{3+} ions, respectively. Oxygen atoms are represented as red spheres. Black arrows highlight the octahedral Fe-O planes where the iron vacancies are located [178].

Table 2.5 Summary of magnetite and maghemite properties.

Properties	Magnetite	Maghemite	Ref
Structural geometries	Face-centred cubic inverse spinel	Cubic inverse spinel with octahedral sites vacancies	[179-183]
Cubic unit cell	0.839 nm	0.834 nm	
	32 O^{2-} ions, 8 Fe^{2+} & 8 Fe^{3+} ions on octahedral sites, and 8 Fe^{3+} ions on tetrahedral sites	32 O^{2-} ions, $21^{1/3}$ Fe^{3+} ions and $2^{1/3}$ vacancies.	
Fe oxidation state	Contains Fe^{2+} and Fe^{3+}	Contains only Fe^{3+}	
Magnetic	Ferrimagnetic at room temperature with small magnetic anisotropy		
Magnetic saturation (bulk) (Am^2/kg)	92	76	
Curie temp. ($^\circ\text{C}$)	585	655	
Melting temp. ($^\circ\text{C}$)	1597	-	
Band gap (eV)	0.1	2.0	

2.4.3 Calcium ferrites

Related ferrites, such as NiFe_2O_4 [22], MnFe_2O_4 [23], CoFe_2O_4 [24] and $\text{Li}_x\text{Fe}_{3-x}\text{O}_4$ [25] have also been investigated, to improve magnetic strength and thermal stability. However, the inherent toxicity of Ni, Mn, Co and Li has limited their application [18]. An alternative approach is to introduce non-magnetic Ca^{2+} into the ferrite crystalline structure, to generate significant improvements in terms of biocompatibility whilst maintaining magnetic expression and heating control [34, 35]. Indeed, non-toxic calcium ferrites metabolise safely within the body [36, 37], making them appropriate for a range of biomedical applications, including magnetic hyperthermia. As summarised in Table 2.6, biomedical investigations using calcium ferrites have been reported in relation to drug-delivery systems [34, 35, 38, 39] and cytocompatibility [34, 36, 38, 40]. Approaches combining metal cations and calcium ferrites for therapeutics (e.g., magnetic hyperthermia) have also been investigated [35, 37, 41-44].

Calcium ferrites are divided into two crystal phases: brownmillerite ferrite-type ($\text{Ca}_2\text{Fe}_2\text{O}_5$, dicalcium ferrite, ***srebrodolskite***) and CaFe_2O_4 [184]. The $\text{Ca}_2\text{Fe}_2\text{O}_5$ structure derives from the perovskite prototype structure (ABO_3) [185] and presents ordered oxygen vacancies with alternating layers of corner-sharing FeO_6 octahedra and FeO_4 tetrahedra (Figure 2.7) [186]. This structure provides for the allocation of various metal cations of diverse valences and has the singular capacity to support several types of defects. Regarding the functional properties of $\text{Ca}_2\text{Fe}_2\text{O}_5$, it has a narrow bandgap, ~ 1.8 to 2.2 eV, and exhibits low electrical conductivity at room temperature, because the majority valence state of the iron in $\text{Ca}_2\text{Fe}_2\text{O}_5$ is Fe^{3+} , i.e., there is a lower concentration of electron (Fe^{2+}) or hole (Fe^{4+}) carriers. Furthermore, $\text{Ca}_2\text{Fe}_2\text{O}_5$ exhibits two types of magnetic moment, coming from FeO_4 and FeO_6 displaying antiferromagnetic and weak ferromagnetic behaviour, respectively,

because Fe^{3+} spins are roughly directed along the y -axis, leading to a G-type antiferromagnetic order [185, 187]. $\text{Ca}_2\text{Fe}_2\text{O}_5$ has a melting point at $\sim 1350^\circ\text{C}$. As relevant for the present investigation, the binary phase diagram for Ca-Fe-O is shown in Figure 2.8 [188].

Table 2.6 Overview of biomedical investigations using calcium ferrites.

Calcium ferrite / size	Description	Reference
$\text{CaFe}_2\text{O}_4 / 5.2 \pm 1.2 \text{ nm}$	Calcium ferrites covered by magnetoliposomes for drug delivery in breast cancer	[34]
$\text{Ca}_x\text{Mg}_{1-x}\text{Fe}_2\text{O}_4$ ($x = 0.25, 0.50, 0.75$) / $< 10 \text{ nm}$	Magnetoliposomes containing calcium ferrites for drug release and magnetic hyperthermia	[35]
$\text{CaFe}_2\text{O}_4 / 5-10 \text{ nm}$	Biocompatibility investigations	[36]
$\text{Ca}_{1-x}\text{Zn}_x\text{Fe}_2\text{O}_4 / 0.97 \text{ to } 1.38 \mu\text{m}$	Magnetic investigations on calcium ferrite with Zn incorporated for magnetic hyperthermia	[37]
$\text{CaFe}_2\text{O}_4 / 30-60 \text{ nm}$	Biocompatibility and antibacterial activity investigations	[38]
$\text{CaFe}_2\text{O}_4 @ \text{PVA}$ / -	Drug delivery system and cytotoxicity evaluation	[39]
$\text{CaFe}_2\text{O}_4 / 3-6 \text{ nm}$	Magnetic characterisation and biocompatibility studies	[40]
$\text{Mg}_{1-x}\text{Ca}_x\text{Fe}_2\text{O}_4$ ($x = 0.0-0.9$) / $10 \pm 2.86 \text{ nm}$	Thermoseeds for magnetic hyperthermia applications	[41]
$\text{NiFe}_2\text{O}_4 / 106 \pm 43 \text{ nm}$	Development of nickel ferrite embedded calcium phosphate nanoparticles for magnetic hyperthermia and cytocompatibility studies	[42]
$\text{Zn}_{(1-x)}\text{Ca}_x\text{Fe}_2\text{O}_4 / 12-14 \text{ nm}$	Developed calcium ferrites showed relevance for magnetic hyperthermia	[43]
$\text{Mg}_x\text{Ca}_x\text{Fe}_2\text{O}_4$ ($x=0.2-0.8$) / 10-14 nm	Cytocompatibility investigations of calcium ferrites for magnetic hyperthermia applications	[44]

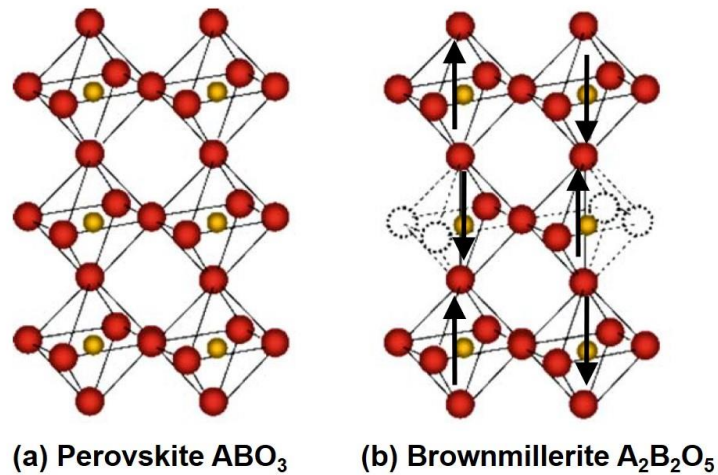


Figure 2.7. (a) Perovskite ABO_3 ($A = Ca$, $B = Fe$ for $CaFeO_3$) and (b) brownmillerite $A_2B_2O_5$ ($A = Ca$, $B = Fe$ for $Ca_2Fe_2O_5$) crystal geometries (Figure adapted from [186]). Brownmillerite shows spin ordering with respect to the G-type antiferromagnet (black arrows) and oxygen vacancies. B cations are shown as yellow spheres, and oxygen atoms are red spheres.

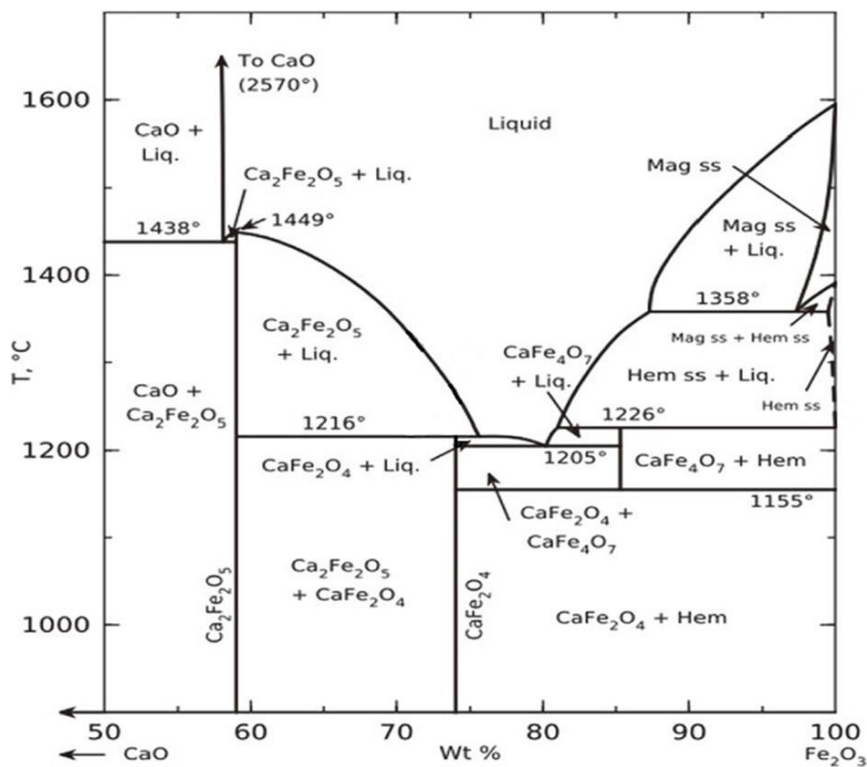


Figure 2.8 Equilibrium phase diagram of the Fe_2O_3 - CaO system [188].

Despite the potential of calcium ferrites for healthcare applications, information is still limited, thus further efforts are required to validate calcium ferrites as candidates for clinical trials. Notably, there is no literature reporting on micro-sized calcium ferrites for biomedical approaches. Hence, the present challenge is to develop calcium ferrites into practical morphologies for clinical investigations.

2.4.4 Magnetic glass-ceramics

Bioactive glasses are not only of interest to promote the regeneration of soft (*e.g.*, skin, nerve, ligament) and hard tissue (*i.e.*, bone) [189-191], but can also be designed to stimulate growth of new blood vessels (*i.e.*, angiogenic properties) [192]. Accordingly, glass-ceramics are considered to offer great potential in biomedical applications, including tissue engineering and regenerative medicine. Further, osteoconductivity, osteoinductivity, and antibacterial properties are characteristic of many bioactive glass phases [109].

Regardless their angiogenic, osteoconductive, osteoinductive and antibacterial properties, bioactive glasses lack of the magnetic features of ferro- and ferrimagnetic materials. **Magnetic-glass-ceramics** are considered to offer great potential in the healthcare sector, for hyperthermia and tissue engineering & regeneration applications [109]. In the context of bone cancer, some treatments for primary tumours (*e.g.*, osteosarcomas) involve chemotherapy, radiotherapy, and surgery with limb-sparing or limb amputation [193]. The drawback with this treatment is the surgical resection of osteosarcoma with wide margins (including normal tissue) [194]. Moreover, malignant cells may leave the primary tumour and form undetectable micro-metastases at distant areas which ultimately could promote tumour reappearance [195]. On this basis, bioactive glasses are not only of interest to promote the regeneration of soft and hard tissue, but also are angiogenic (able to stimulate the

growth of new blood vessels). Thus, a combination of ferro- or ferrimagnetic materials (e.g., magnetite) embedded in a bioactive glass system represents a promising alternative for cancer treatments, particularly mediated *via* magnetic hyperthermia.

A modern magnetic hyperthermia strategy consists of implanting a bioactive matrix conjugated with a magnetic phase to work as an internal heat source [196]. To achieve this goal, there is need for a balance between magnetic properties and bioactivity, for safe application and performance of hyperthermia. Further, this approach would facilitate repeated hyperthermia treatment to help safeguard against tumour regrowth. Accordingly, magnetic bone cements [26], glass-ceramic thermoseeds [27] and Fe-based nanoparticles [28] have been developed for bone cancer therapy *via* magnetic hyperthermia.

In this context, a micro-system combining bone-tissue regeneration, cancer thermotherapy and biomechanical support, such as the conjugation of an iron oxide ferromagnetic phase (e.g., magnetite) with a bioactive glass matrix, could provide a promising approach for cancer treatments mediated *via* magnetic hyperthermia, e.g., targeting bone oncology [46]. It is proposed, as bioactive matrix, the use of phosphate glass, a type of bioglass in which P_2O_5 performs as network former oxide. These glasses contain PO_4 tetrahedron structural units, which are asymmetric by nature [197]. The tetrahedra in each polymorph are linked to three other tetrahedra *via* bridging (P–O–P) oxygens [198] (Figure 2.9).

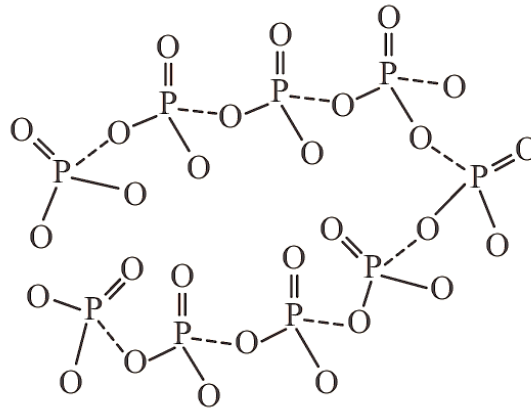


Figure 2.9 Phosphate glass structure [199].

Phosphate glasses modified with oxides such as CuO [200], ZnO [201], TiO₂ [202] or Fe₂O₃ [203] have been explored for biomedical applications.

2.5 Basics of magnetism and magnetic materials

2.5.1 Introduction

This section overviews magnetic materials classifications. Emphasis is made on the effect of particle size (multi- and single-domain particles), with reference to the magnetic materials mostly studied in this Thesis. The mechanisms associated with magnetic particle heat generation are also described.

2.5.2 Classification of magnetic materials

Materials can be classified according to their magnetic response, *i.e.* as diamagnetic, paramagnetic or ferromagnetic (ferrimagnetism, superparamagnetism and antiferromagnetism fall into this category) [204, 205]. Figure 2.10 presents the magnetic dipole arrangement for each type of magnetism and Table 2.7 provides a summarise of each type of magnetism.

Table 2.7. Summary of types of magnetism

Type of magnetism	Description	Reference
Ferromagnetism	A type of magnetic order with a parallel alignment of intrinsic magnetic dipole moments or spin of electrons in a crystal. Ferromagnetic phases with spontaneous magnetisation even in the absence of an external magnetic field are achieved below a critical point, <i>i.e.</i> , Curie temperature (T_c).	[124, 206, 207]
Ferrimagnetism	A typical magnetic expression for cubic spinel ferrites and certain ceramics. This type of magnetism is observed in systems where two different types of ions are present <i>e.g.</i> , Fe^{2+} & Fe^{3+} for the case of magnetite. These two species produce different sublattices, A and B, influencing each other through a negative exchange interaction, resulting in an antiparallel alignment of magnetic dipoles. Similar to ferromagnetism, the susceptibility of this type of material is large.	[208, 209]
Paramagnetism	Materials are weakly attracted to a magnetic field. In the absence of a magnetic field, magnetic dipoles are randomly ordered. When a magnetic field is applied, each atom dipole aligns with the field.	[210, 211]
Superparamagnetism	Appears in ferro- and ferrimagnetic nanomaterials. In the absence of magnetic field, their magnetisation is zero. Once a magnetic field is applied, the nanoparticles are magnetised, similar to paramagnets. Nonetheless, their magnetic susceptibility is considerably larger than that of paramagnets.	[19, 212]
Antiferromagnetism	For this type of magnetism, the material magnetic moments are spontaneously ordered. Nonetheless, the net magnetic moment that is zero or small when considering the sum of magnetic moments involved. The classic example for this type of magnetism is chromium.	[213]
Diamagnetism	This is the weakest kind of magnetic response. In the absence of a magnetic field, magnetic dipoles are not present. Conversely, once an external magnetic field is applied, a magnetic dipole is produced with opposite direction of the magnetic field, <i>i.e.</i> , the magnetic field is repelled.	[19, 214]

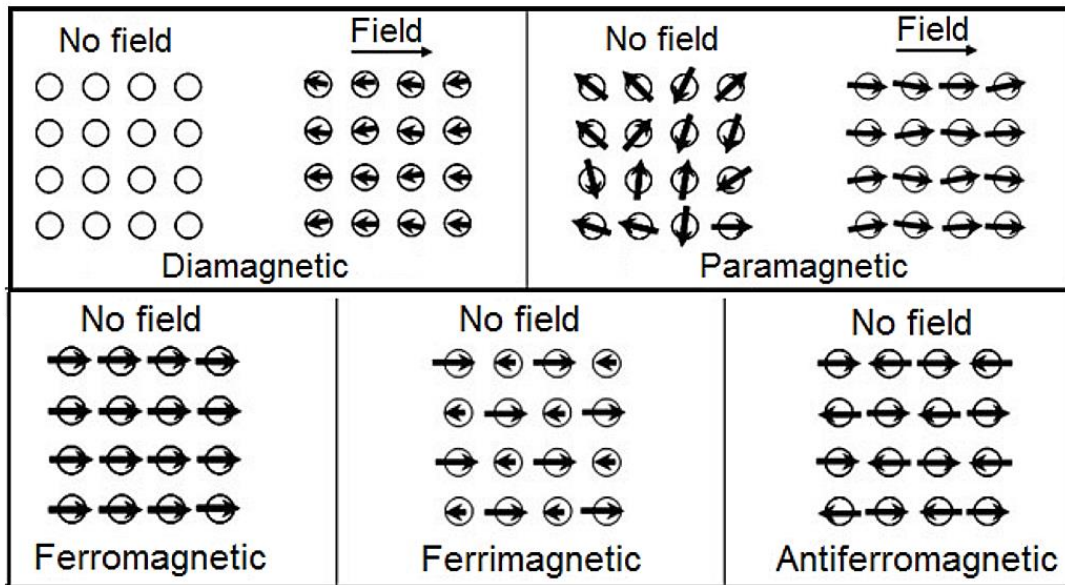


Figure 2.10. *Magnetic dipoles of magnetic materials in the absence and presence of an external magnetic field.*

Once a magnetic material experiences a magnetic field of strength H , the individual atomic moments contribute to the general magnetic induction B in the material:

$$B = \mu_0 (H + M) \quad (\text{Equation 2.1})$$

“where μ_0 is the permeability of free space, and magnetisation, $M = \mu/V$, is the magnetic moment per unit volume” (μ , magnetic moment; V , volume). In general, every material could be catalogued as a magnetic material since they all respond to magnetic fields in a certain manner. However, they are most often classified according to their volumetric magnetic susceptibility, χ , which expresses the relationship between magnetisation, M , induced in the material and magnetic field, H [215]:

$$M = \chi H \quad (\text{Equation 2.2})$$

In the SI unit system, χ is dimensionless, whilst M and H are expressed in A/m. For paramagnets, susceptibility values are typically in the range 10^{-6} to 10^{-1} , while susceptibility values for diamagnetic materials are in the range of -10^{-6} to -10^{-3} . The negative χ value of diamagnetic materials indicates that magnetisation, M , and magnetic field, H , are in opposite directions for these materials. Conversely, ferromagnets, ferrimagnets and antiferromagnets exhibit ordered magnetic states [215]. Figure 2.11 illustrates a comparison between ferromagnetic / ferrimagnetic, superparamagnetic, paramagnetic and diamagnetic materials where typical magnetisation vs magnetic field (M - H) hysteresis loop is presented. Additionally, Figure 2.12 shows the periodic table, indicating magnetic expression of the elements in the solid state.

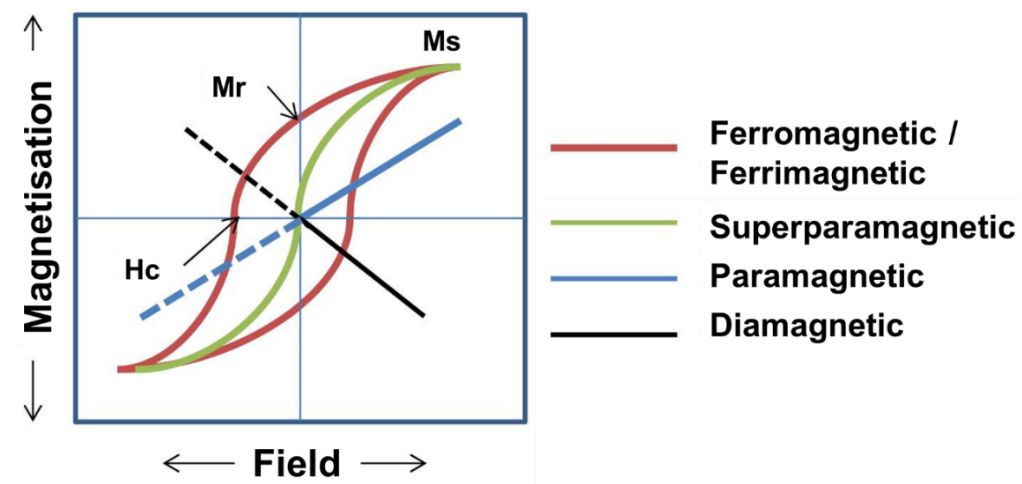


Figure 2.11. Typical magnetization vs field (M - H) comparison of ferromagnetic, ferrimagnetic, superparamagnetic, paramagnetic and diamagnetic materials. Figure adapted from [214]. H_c : coercive field; M_r : remanent magnetisation; M_s : magnetic saturation.

1 IA												13 IIIA						14 IVA		15 VA		16 VIA		17 VIIA		18 VIIIA	
1 H 1.0079	2 He 4.0026											5 B 10.81	6 C 12.011	7 N 14.007	8 O 15.999	9 F 18.998	10 Ne 20.179										
3 Li 6.941	4 Be 9.012											13 Al 26.982	14 Si 28.086	15 P 30.974	16 S 32.06	17 Cl 35.453	18 Ar 39.948										
11 Na 22.990	12 Mg 24.305	3 III B	4 IV B	5 V B	6 VI B	7 VII B	8 ←	9 VIII B	10 →	11 IB	12 IIB	13 Al 26.982	14 Si 28.086	15 P 30.974	16 S 32.06	17 Cl 35.453	18 Ar 39.948										
19 K 39.098	20 Ca 40.08	21 Sc 44.956	22 Ti 47.90	23 V 50.941	24 Cr 51.996	25 Mn 54.938	26 Fe 55.847	27 Co 58.933	28 Ni 58.70	29 Cu 63.546	30 Zn 65.38	31 Ga 69.72	32 Ge 72.59	33 As 74.922	34 Se 78.96	35 Br 79.904	36 Kr 83.80										
37 Rb 85.468	38 Sr 87.62	39 Y 88.906	40 Zr 91.22	41 Nb 92.906	42 Mo 95.94	43 Tc [97.91]	44 Ru 101.07	45 Rh 102.905	46 Pd 106.4	47 Ag 107.868	48 Cd 112.41	49 In 114.82	50 Sn 118.69	51 Sb 121.75	52 Te 127.60	53 I 126.904	54 Xe 131.30										
55 Cs 132.905	56 Ba 137.33	57-71 Lanthanides	72 Hf 178.49	73 Ta 180.948	74 W 183.85	75 Re 186.21	76 Os 190.2	77 Ir 192.22	78 Pt 195.05	79 Au 196.966	80 Hg 200.59	81 Tl 204.37	82 Pb 207.2	83 Bi 208.98	84 Po [208.98]	85 At [209.99]	86 Rn [222.02]										
87 Fr [223.02]	88 Ra [226.03]	89-103 Actinides	104 Rf [265.12]	105 Db [268.13]	106 Sg [271.13]	107 Bh [270]	108 Hs [277.15]	109 Mt [276.15]	110 Ds [281.16]	111 Rg [280.16]	112 Cn [285.17]	113 Nh [284.18]	114 Fl [289.19]	115 Mc [288.19]	116 Lv [293]	117 Ts [294]	118 Og [294]										
		57 La 138.905	58 Ce 140.12	59 Pr 140.907	60 Nd 144.24	61 Pm [145]	62 Sm 150.4	63 Eu 151.96	64 Gd 157.25	65 Tb 158.925	66 Dy 162.50	67 Ho 164.930	68 Er 167.26	69 Tm 168.934	70 Yb 173.04	71 Lu 174.967											
		89 Ac [277.03]	90 Th 232.038	91 Pa 231.036	92 U 238.029	93 Np [237.05]	94 Pu [244.06]	95 Am [243.06]	96 Cm [247.07]	97 Bk [247.07]	98 Cf [251.08]	99 Es [252.08]	100 Fm [257.10]	101 Md [258.10]	102 No [259.10]	103 Lr [262.11]											

Figure 2.12. Table of elements and their magnetic properties.

Ferromagnetism occurs in body centred cubic materials, e.g. iron, cobalt, nickel (Figure 2.12) and alloys composed of these elements. Compared to diamagnetic and paramagnetic materials, they present higher susceptibility values and durable magnetic moments, even when the magnetic field has been removed (*i.e.*, spontaneous magnetisation). This phenomenon occurs because of atomic spin moments and associated interactions provoke a joint alignment of magnetic moments. Consequently, large regions of ferromagnetic crystals exhibit aligned atomic spins [124]. Once all magnetic dipoles are aligned with the applied magnetic field, then a maximum value of magnetisation is established, termed magnetic saturation (M_s) (Figure 2.11) [114, 124, 215]. As soon as the magnetic field becomes weaker, spin alignment ceases resulting in a decrease in material magnetization. For the case of ferromagnetic materials, when the magnetization value becomes zero, *i.e.* when the magnetic field has been removed, the material still presents a residual magnetic

moment, *i.e.*, remanent magnetisation (M_r). To bring the material magnetisation back to zero, a magnetic field in the negative direction needs to be applied, and the magnitude of this field is termed the coercive field (H_c) [109, 114, 215]. Conversely, superparamagnets exhibit no hysteresis for their magnetization curves, and an overlap of magnetization curves at different temperatures [215].

2.5.3 Multi- and single- domain particles

A domain is essentially an association of spins whose magnetic moments follow the same direction and act in a coordinated way when exposed to a magnetic field. In bulk materials, domains are divided by domain walls with specific width and energy related to their formation and existence [216]. The characteristic movement of domain walls is the basis of magnetisation reversal, whilst acting as a principal source of energy dissipation. Figure 2.13 shows the relationship between coercivity in particle systems and particle size. Large particles (above 1 μm) are multi-domain particles within which domain walls form energy-favourably. The magnetisation of multi-domain particles is associated with the nucleation and movement of these walls. When particle size decreases to approach a critical size (diameter, D_c), the formation of domain walls becomes energetically disadvantageous. There are no domain walls in such “single-domain particles” and magnetisation occurs through coherent spin rotation. As the particles become smaller than D_c , thermal fluctuations occur in the particle spins and they are termed superparamagnetic [215]. Table 2.8 summarises D_c values for different spherical magnetic materials.

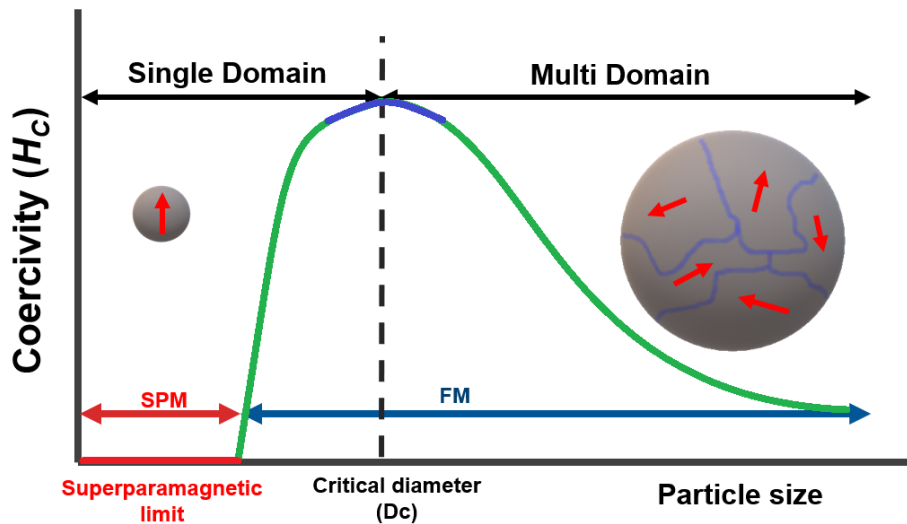


Figure 2.13. Relationship between coercivity and particle sizes. Particles with size close to D_c exhibit large coercivities. SPM: Superparamagnetism; FM: Ferromagnetism. Image adapted from [215].

Table 2.8 Critical single-domain sizes (D_c) for spherical magnetic particles [215].

Material	D_c (nm)
Co	70
Fe	14
Ni	55
Fe_3O_4	128
γ - Fe_2O_3	166

Ferromagnetic and ferrimagnetic materials at the micro-scale (e.g., magnetite or calcium ferrite microspheres) contain magnetic domains [217] whereas ultra-small, single-domain nanoparticles display superparamagnetism.

2.5.4 Heating mechanisms for magnetic hyperthermia

For multi-domain, ferro- and ferrimagnetic materials, heating is produced *via hysteresis losses* [10, 109]. Multi-domains in large particles exhibit a definite magnetisation direction. When exposed to a magnetic field, sub-domains with magnetisation direction along the magnetic field axis grow, whilst others shrink, *i.e.* a

domain wall displacement phenomenon. In this context, hysteresis loss is the energy entrapped in the magnetic materials in the form of remanent magnetisation, which is then released as heat whilst demagnetisation occurs [218]. In contrast, heat within single-domain superparamagnetic particles is produced by **Néel and Brownian relaxations** [219]. When an external alternating magnetic field is applied, magnetic moments rotate (Néel mode), and nanoparticles themselves rotate (Brownian relaxation), and then relax back to the original magnetic field orientation. The rotation of magnetic moments and the friction produced from particle oscillations leads to a phase delay between the applied magnetic field and the direction of the magnetic moments. Consequently, heat is produced [109]. Figure 2.14 illustrates heat generation mechanisms for multi- and single-domain magnetic particles.

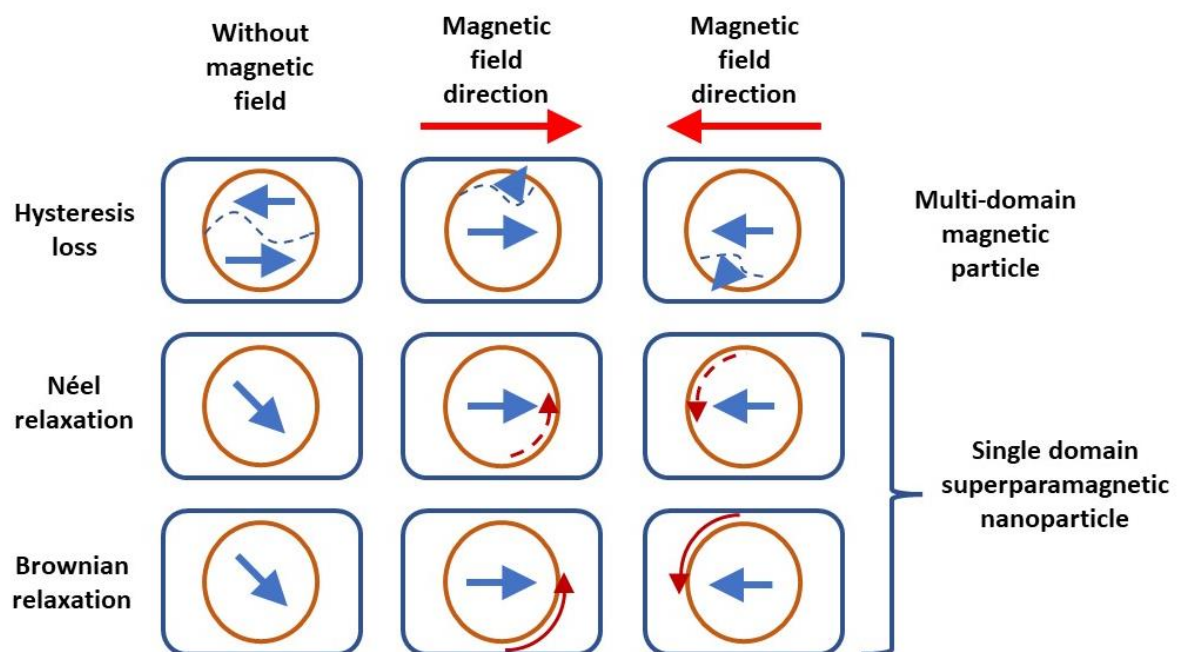


Figure 2.14. Heat generation mechanisms in magnetic particles, in response to an alternating magnetic field. Orange circles represent magnetic particles; short straight arrows represent magnetic field direction; curved arrows represent movement (solid) or change in magnetic moment direction (dashed); whilst irregular dashed lines represent domain boundaries in multi-domain particles. Image adapted from [10].

2.6 Manufacture of magnetic porous microspheres

2.6.1 Introduction

Magnetic particles have great potential in the biomedical field. Hence, it is necessary to develop these materials into practical morphologies for clinical strategies. For healthcare applications, spherical morphologies provide physical advantages over non-spherical, *i.e.*, irregular shaped particles (ISP), with uniform size and shape facilitating transport and/or delivery to the target tissue, combined with functionalised surfaces allowing for the attachment of therapeutic coatings with increased rates of degradation and ion release. Porous microspheres with large surface areas can be manufactured, with external and internal pores (usually interconnected), to enhance cell attachment, proliferation and ion release [56]. In addition, porous microspheres enable payloads (for drugs, cells, biologics, *etc*) to be incorporated onto the surfaces or within the pores [47, 48]. The International Union of Pure and Applied Chemistry (UPAC) classifies porous materials according to their pore sizes [48]: microporous (≤ 2 nm), mesoporous (2 – 50 nm), macroporous (50 – 200 nm) and gigaporous (≥ 200 nm).

2.6.2 Porous biomaterials preparation methods

The manufacture of porous structures is dependent strongly on the type of material employed. In this section, attention is placed on **glass and/or ceramic** material processing methods. Table 2.9 summarises advantages and disadvantages of porous biomaterial processing methods. Approaches such as polymer foam replication, sol-gel, gel-cast foaming or solid free-form (3D printing) are typically employed. It is noted that most of the methods used for the manufacture of ceramic and/or glass-based porous biomaterials (with the exception of the flame spheroidisation process) involves a final consolidation step: *i.e.*, high temperature sintering. For the case of bioglasses,

this is a crucial issue because devitrification of the material whilst sintering (*i.e.*, sinter-crystallisation) may lead to a decrease in the bioactive properties of the glasses [220, 221]. Also, sintering at too low temperatures can produce materials with poor mechanical properties. Moreover, these methods generally involve numerous processing steps which can be time-prolonged and laborious [53].

Table 2.9 Summary of glass and/or ceramic porous biomaterials preparation methods.

Preparation method	Advantages	Limitations	Ref
Sol-gel foaming	Scaffolds with high surface area; final porous structure can be designed by tailoring process parameters, <i>e.g.</i> , glass composition, type of surfactant, catalyst, and temperature; interconnected porosity	High brittleness; involves numerous processing steps which can be time-prolonged and laborious	[59, 222, 223]
Gel-cast foaming	The strength-to-porosity ratio is higher compared to that of the porous ceramics prepared by other processes	Complex process and laborious (multiple steps: premixing, casting, drying, and sintering). Risk of shrinkage during drying, and disappearance of bubbles	[60, 224]
Polymer foam replication	Porosity levels ~ 90 vol. % in trabecular structures, which are similar to that of cancellous bone (>100 μm).	Post thermal dissolution of space holders or sacrificial polymer templates, not only can result in contamination of the porous products, but also affect their mechanical and physical properties	[53, 61, 225]
Thermally induced phase separation	Simple method; high levels of porosity (97 vol. %) can be obtained by tuning process parameters	Possibility of residual solvent; small scale production; time-prolonged	[222, 226]
Freeze drying	High compressive strength compared to other methods; environmentally friendly; pore size range control; low sintering shrinkage	To obtain suitable pore diameters for bone tissue engineering using only water is not possible, hence, additional solvent is required, <i>e.g.</i> , 1,4-dioxane, or camphene	[224, 227]
Additive manufacturing <i>e.g.</i>, 3D printing	Complex internal features of macroporous structures can be easily tailored using computer-aided design (CAD)	Multiple steps are required such as data-acquisition, design/modelling, ink preparation, printing and post-process treatments such as drying or sintering; high cost	[62, 228-230]
Flame spheroidisation	Rapid, single-stage process; high levels of interconnected porosity; potential for large scale-production of porous and dense microspheres; low cost	High-energy required; number of processing variables (gas flow ratio, precursor-to-porogen mass ratio, <i>etc.</i>); relatively new for ceramic porous materials with limited literature available.	[53, 63, 231]

For the case of magnetic materials, mesoporous particles have been developed. Ruiz-Hernandez, *et al* [232] synthesised magnetic mesoporous silica microparticles with incorporated hematite nanoparticles using the evaporation induced self-assembly method, assisted by an aerosol technique. Drug loading and release *in vitro* studies of developed microparticles provided evidence of the suitability of these materials for magnetic drug delivery applications. Gao, *et al* [233] reported on poly(ionic liquid) – silica - iron oxide composite mesoporous microparticles, developed through sol-gel method and self-assembly by magnetic solid-phase extraction. Li, *et al* [234] manufactured ammonium bromide Fe_3O_4 -based core-shell magnetic mesoporous microspheres *via* sol-gel method. Moreover, a strategy that consists of agglomerating magnetic nanoparticles and coating them with cetyltrimethyl ammonium bromide, to develop core-shell structures, has been proposed by Liu [235]. Similarly, Gao *et al* [236] prepared polymer porous particles hosting drug and Fe_3O_4 nanoparticles *via* an electrospinning technique. Notably, some of these investigations used irregular-shaped particles, instead of microspheres. Moreover, multiple steps were needed, making the processes prolonged.

Alternatively, the single-stage, flame spheroidisation process is a unique, fast, cost-effective [47] and promising technique for the large-scale manufacture and production for porous ceramic and/or glass, magnetic microspheres with high levels of interconnected porosity. The flame spheroidisation process has been used for the production of highly porous glass microspheres [53, 57, 231, 237-241], and more recently for ceramics [63]. However, the need for parameter optimisation is recognised, for the controllable flame spheroidisation of glass-ceramic and ceramic, porous microspheres.

2.7 Concluding remarks

Magnetic hysteresis, present in multidomain materials, is a significant feature for localised magnetic hyperthermia applications. In this context, the present project contributes towards the development of novel microstructure therapeutics, employing multidomain microspheres to maximise the effectiveness of potential treatments whilst minimising side-effects. The development of multidomain microspheres (both, dense and porous) *via* a rapid flame-spheroidisation process, with particular attention to parameter-space for this process (Fe_3O_4 precursor size, magnetite-to-porogen mass ratio, and oxygen-acetylene gas flow setting), aims to impart control over composition (Fe_3O_4 , $\text{Ca}_2\text{Fe}_2\text{O}_5$, P40- Fe_3O_4), size and shape, (dense microspheres $\sim 20 - 100 \mu\text{m}$; porous microspheres $\sim 100 - 200 \mu\text{m}$), porosity levels (~ 1 to $60 \mu\text{m}$) and coercive field strengths ($\sim 0.5 - 10 \text{ kA/m}$) of the products. The opportunity to design these microspheres with inner and external porosity would also bring the possibility to enclosure and deliver chemotherapeutic agents, making them potential candidates for local magnetic hyperthermia ($40 - 45^\circ\text{C}$), MRI, and drug-delivery in a single micro-system. The magnetic hyperthermia / drug delivery combination can also improve synergistically the application of certain drugs. Additionally, the heating of multidomain microspheres *via* an induction heating system with low frequency level ($135 - 400 \text{ kHz}$) fits within the clinically accepted range for magnetic hyperthermia [132-134]. Furthermore, it is considered that combinations of iron oxides with bioactive glasses would allow microspheres to remain in place within tumour tissue, for repeated magnetic hyperthermia sessions in a clinical environment, towards the treatment of *e.g.*, bone or prostate cancer.

3.0 Materials and methodology

3.1 Introduction

This Chapter outlines the materials and methodology used for the flame spheroidisation of both dense and porous magnetic microspheres. The preparation steps followed for the flame spheroidisation of microsphere products, and the associated cell seeding process, are described in detail. Descriptions of each relevant characterisation technique are briefly outlined.

3.2 Materials

The starting feedstock comprised as-supplied powders of **small** iron(II,III) oxide (Fe_3O_4 ; $\leq 5 \mu\text{m}$, 95%; Merck, UK), **large** iron(II, III) oxide (Fe_3O_4 ; $\leq 45\mu\text{m}$, 98.1%; Inoxia, UK); calcium carbonate porogen (CaCO_3 , 98%; Fisher Scientific UK Ltd); and chemical precursors used for glass production, *i.e.*, calcium hydrogen phosphate (CaHPO_4), magnesium hydrogen phosphate trihydrate ($\text{MgHPO}_4 \cdot 3\text{H}_2\text{O}$), sodium dihydrogen phosphate (NaH_2PO_4) and phosphorous pentoxide (P_2O_5) (all Merck, UK).

3.3 Glass formulation

The quaternary phosphate-based glass 40- P_2O_5 -16CaO-24MgO-20Na₂O (in mol%), denoted P40, was produced using the melt-quench technique. 21.8 g of CaHPO_4 , 41.8 g of $\text{MgHPO}_4 \cdot 3\text{H}_2\text{O}$, 24 g of NaH_2PO_4 and 56.8 g of P_2O_5 were placed into a platinum rhodium alloy crucible (Birmingham Metal Company, U.K.) mixed using a stainless-steel spatula, and dried at 350°C for 30 minutes in a furnace. The mixture was then melted at 1150°C for 90 minutes, poured onto a steel plate and left to cool to room

temperature [237]. The glass was then ground to a fine microparticle powder using a milling machine (Retsch PM100 Planetary Ball Mill) for 5 minutes and sieved (stainless steel frame; 203 x 50 mm²; ≥ 63 μm and ≥ 125 μm mesh; VWR International) to collect particles in the size range of 63 – 125 μm.

3.4 Preparation of microspheres *via* flame spheroidisation

3.4.1 Dense microspheres

Dense microspheres were produced *via* the flame spheroidisation process (Figure 3.1a) [63]. The particles were flame-spheroidised by feeding into the funnel placed on top of the spray gun. The first collection tray, placed below the spray gun, was used to collect unprocessed / unreacted powders, whilst trays 2 and 3 collected microspheres post flame-ejection. The products were stored in glass vials for detailed characterisation. The flame spheroidisation system (Figure 3.1b,c) consisted of a thermal spray gun (MK74, Metallization Ltd, UK) coupled to oxygen and acetylene gas cylinders, their gas flow settings measured *via* flowmeters; a stainless-steel funnel; three rectangular collection trays; and a spray booth. Importantly, gas flow ratios influence the flame length, which subsequently influences particle residence time, as the flame length can increase or decrease in size depending on the ratios used. Figures 3.1d-f show flame length measurements, as a function of gas flow settings 2:2 (Figure 3.1d), 2.5:2.5 (Figure 3.1e), and 3:3 (Figure 3.1f). Notably, flame length decreases (from ~ 37 to 31 cm) with increasing gas flow setting (from 2:2 to 3:3).

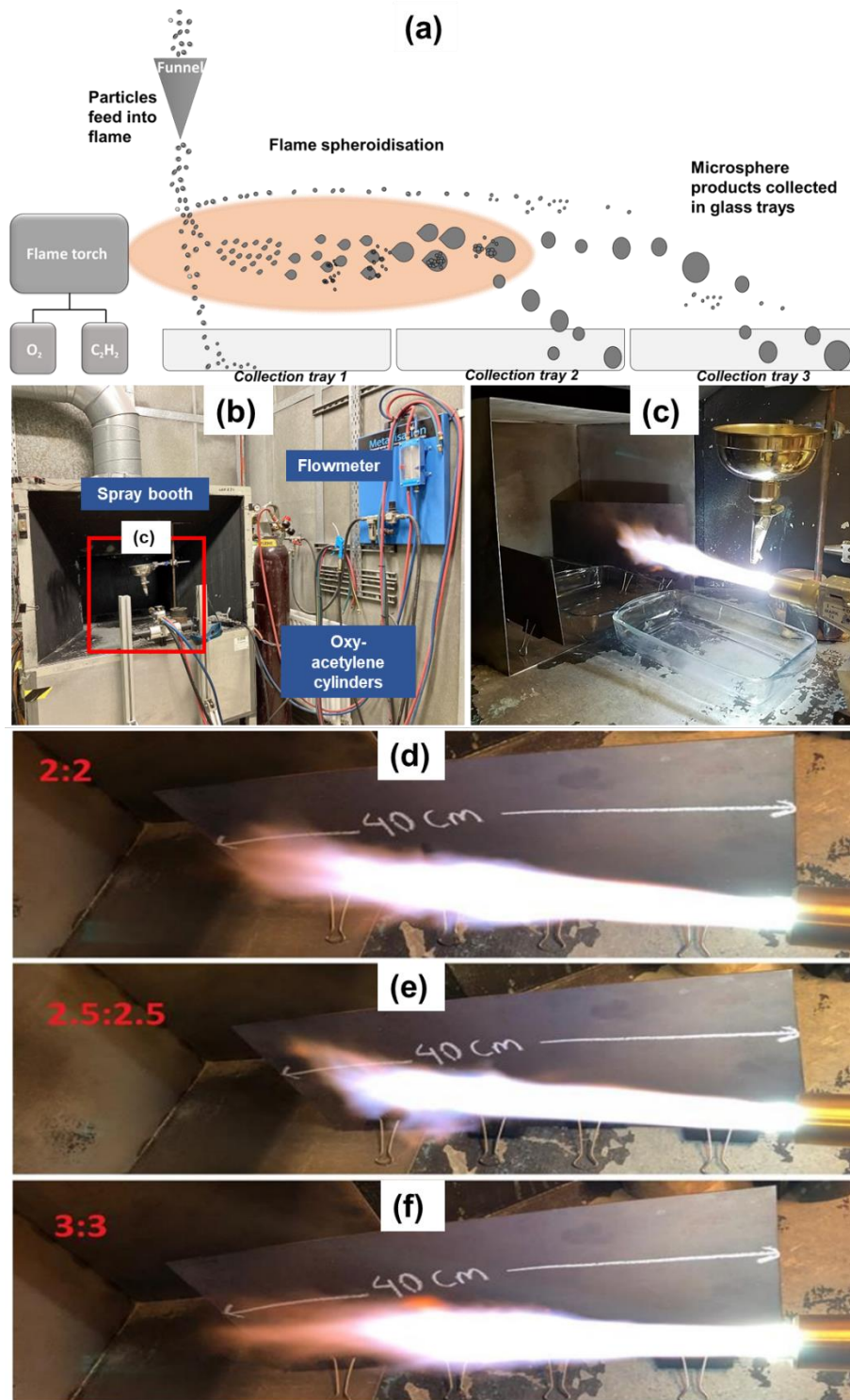


Figure 3.1. Flame spheroidisation process. (a) Schematic depiction of the flame spheroidisation process; (b) system set-up showing spray booth, flowmeter and oxygen and acetylene cylinders; (c) spray gun, funnel and spray booth (boxed in region (b)); and flame lengths for (d) 2:2, (e) 2.5:2.5 and (f) 3:3 gas flow settings. ((d-f) images acquired by Md Towhidul Islam [242])

As summarised in Table 3.1, dense flame-spheroidised materials processed in this work utilised large and small Fe₃O₄ feedstock powders (*Chapters 4 and 5*, respectively), along with vortex mixer prepared glass-ceramic powders (P40:Fe₃O₄, mass ratios of 1:1, 4:1 and 16:1) (*Chapter 6*).

Table 3.1 Parameters for the manufacture of **dense** microspheres *via* flame spheroidisation

Fe ₃ O ₄ size / μm	P40 size / μm	Mass ratio P40:Fe ₃ O ₄	Preparation	Oxy-acetylene gas flow ratio / arb. units
≤ 45 (large)	-	-	-	2.5:2.5
	63 – 125	1:1	vortex mixer	
		4:1		
≤ 5 (small)	-	-	-	

3.4.2 Porous microspheres

3.4.2.1 Fe₃O₄-based porous microspheres

Large (≤ 45 μm, 5g) and small (≤ 5 μm, 5g) iron oxide powders were mixed with porogen (calcium carbonate, **CaCO₃**, ≤ 5 μm) (mass ratios of 3:1, 1:1 and 1:3) using a mortar and pestle, combined with droplets of 2% aqueous solution poly vinyl alcohol (PVA; Merck, UK) to act as binder, and dried at 37 °C for 24 h. The prepared powders were flame-spheroidised using O₂/C₂H₂ (gas flow settings of 2:2, 2.5:2.5 or 3:3). A gas flowmeter (Platon, Roxspur, UK) coupled to the gas cylinders was used to adjust & monitor the gas flow setting. The microsphere products exiting the flame were collected, again using glass trays positioned a short distance away from the thermal spray gun and stored in glass vials for characterisation. The parameters used to

evaluate the effects of Fe_3O_4 precursor to CaCO_3 porogen mass ratio (3:1, 1:1 or 1:3) and oxy-acetylene gas flow setting on the microsphere products are summarised in Tables 3.2 and 3.3, respectively. The range of porogen concentrations (3:1, 1:1 & 1:3) were chosen to investigate the precursor-to-porogen mass ratio effect on the generation of porous microspheres; to study microsphere products compositional uniformity; and to compare the actual flame-spheroidised structures in relation to their anticipated equilibrium phases. Importantly, the selection of the $\text{CaO-Fe}_2\text{O}_3$ binary phase equilibrium diagram relates to the chemical reaction pathways involved in the formation of calcium ferrites, *i.e.*, Fe_3O_4 oxidation to produce Fe_2O_3 , and CaCO_3 decomposition to produce CaO and CO_2 .

Table 3.2 Parameters to evaluate the effects of **Fe_3O_4 : CaCO_3 mass ratio**.

Fe_3O_4 size / μm	CaCO_3 size / μm	Mass ratio Fe_3O_4 : CaCO_3	Preparation	Oxy-acetylene gas flow ratio / arb. unit
≤ 45	≤ 5	3:1	Mixed with PVA	2.5:2.5
		1:1		
		1:3		
≤ 5	≤ 5	3:1	Mixed with PVA	2.5:2.5
		1:1		
		1:3		

Table 3.3 Parameters to evaluate the effects of **gas flow setting**.

Fe_3O_4 size / μm	CaCO_3 size / μm	Mass ratio Fe_3O_4 : CaCO_3	Preparation	Oxygen-Acetylene gas flow setting / arb. unit
≤ 45	≤ 5	1:1	Mixed with PVA	2:2
				2.5:2.5
				3:3
≤ 5	≤ 5	1:1	Mixed with PVA	2:2
				2.5:2.5
				3:3

3.4.2.2 P40-Fe₃O₄ porous microspheres

For the case of glass-ceramic microsphere manufacture, 3 g of Fe₃O₄ ($\leq 45 \mu\text{m}$) and 3 g of P40 (63 – 125 μm) (1:1 mass ratio) were combined using a vortex mixer. The P40-Fe₃O₄ powders were then mixed with 18 g of CaCO₃ (as porogen, $\leq 63 \mu\text{m}$) (1:3 mass ratio). The prepared powders were then processed into porous microspheres *via* the flame spheroidisation process (O₂/C₂H₂: 3:3 gas flow ratio) [63]. The microsphere products were washed using acetic acid (5 molar) for 2 minutes and deionised water for 1 minute, and then dried at 37°C for 24 h. The resultant microspheres were then sieved to a size range 125 – 212 μm (stainless steel frame; 203 x 50 mm²; $\geq 125 \mu\text{m}$ and $\geq 212 \mu\text{m}$ mesh; VWR International) and stored in glass vials for characterisation.

3.5 Microsphere characterisation

3.5.1 Scanning electron microscopy (SEM)

The SEM characterisation technique is used primarily to image surface topography [243]. Figure 3.2 illustrates a typical SEM configuration. An electron gun emits a beam of monochromatic electrons (with energy ranging from 0.2 to 40 keV). The electron beam is focused by a condenser system to a spot of 0.4 to 5 mm in diameter. The first condenser lens forms the beam and limits current, whilst a condenser aperture eliminates unwanted high-angle electrons. A second condenser lens is used for fine control of the beam. The electron beam travels down the electron-optic column, under high vacuum, and bombards the sample. Scan coils allow the electron probe to be rastered over the sample surface. A high vacuum environment is employed to minimise scattering of the electron beam before reaching the sample [244].

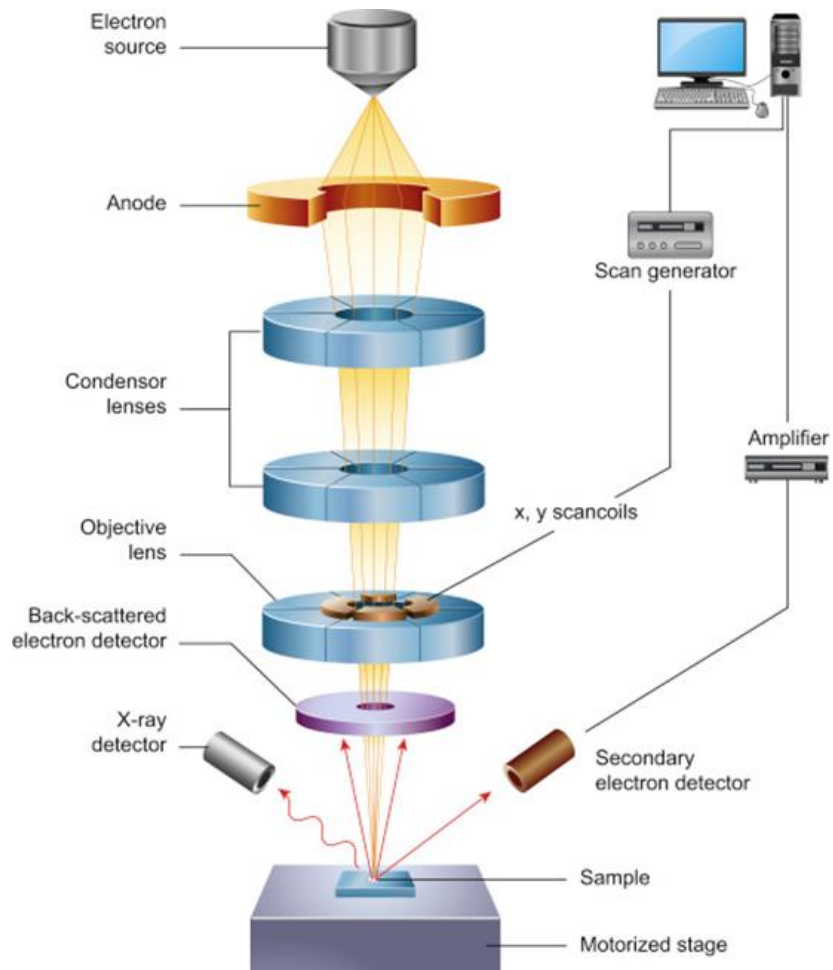


Figure 3.2 Schematic arrangement of a typical SEM [245].

Once incident electrons are decelerated in the sample, electron-sample interactions lead to the generation of a variety of signals (e.g., secondary electrons (SE), backscattered electrons (BSE) and characteristic X-rays), as illustrated in Figure 3.3.

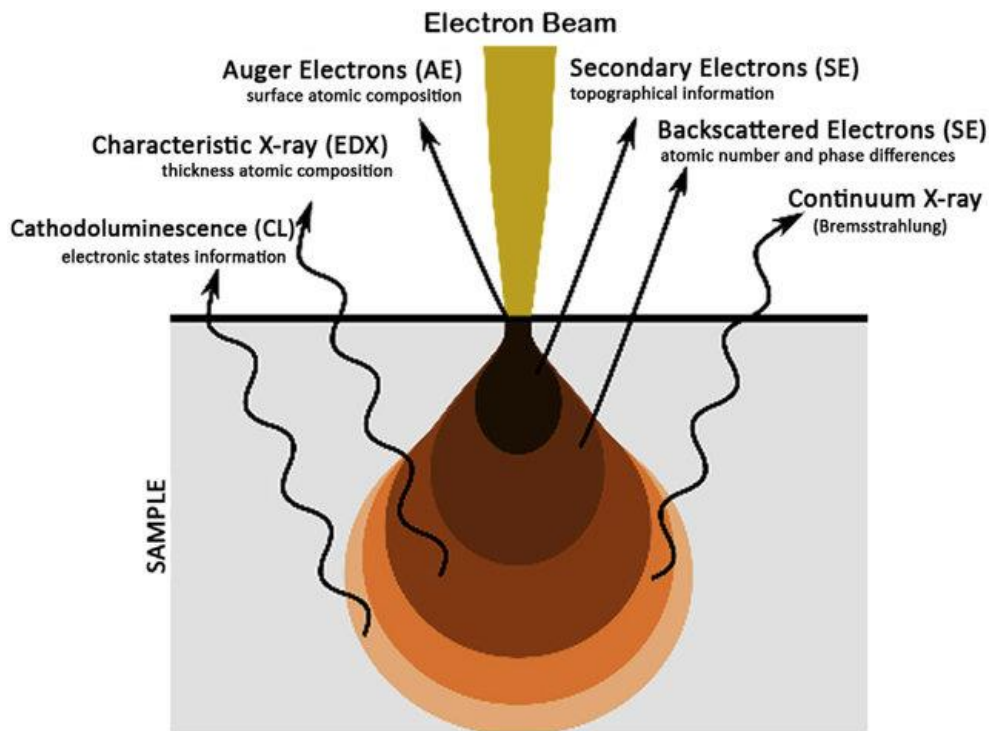


Figure 3.3 Electron beam-sample interactions [246].

Secondary electrons are those electrons emitted from an atom with kinetic energies below 50 eV as a consequence of inelastic collisions between the primary beam and weakly bound electrons (for ionically or covalently bonded materials), or conduction band electrons (for metals). Since secondary electrons have low energy, only those generated from a region within a few nanometres of the material surface are detected. Hence, secondary electrons are used mainly for imaging in SEM, as they exhibit high levels of spatial resolution and topographic sensitivity [247].

Conversely, backscattered electrons (high energy electrons) are generated as a result of elastic scattering between primary electrons and atom nuclei. The higher the atomic number of an element, the stronger the interaction leading to a higher number of electrons being backscattered. Hence, as an electron beam passes from a low atomic number area to a high atomic number area, the brightness of the image will increase, *i.e.*, there is contrast caused by elemental differences, providing locally

averaged compositional information on the sample. Topographical information is also obtained; however, the larger volume associated with BSE signal emission results in a lower level of spatial resolution, as compared to SE imaging [248].

Characteristic X-rays are generated when an inner shell electron is displaced by inelastic scattering of a highly energetic primary electron, and is replaced by an outer shell electron to re-establish charge balance in its orbitals. The ionized atom returns to its ground state by emitting an X-ray photon, with energy dependent on atomic number, and hence provides for chemical information [247].

Topographic imaging of flame-spheroidised products was performed using an FEI XL30 SEM. Micrographs were acquired for Fe₃O₄-based microsphere products (5kV; spot size 2.5; 13.3 mm working distance, secondary electron (SE) imaging mode), and P40-Fe₃O₄ microsphere products (10 kV; spot size 5; 25.3 mm working distance; secondary electron (SE) imaging mode). Differences in the imaging conditions adopted was due to differences in material electrical properties. Prior to SEM characterisation, microsphere specimens were mounted onto double-sided conductive carbon tabs, stuck to aluminium stubs, and (for the case of P40-Fe₃O₄ samples) coated with ~10 nm of platinum (Agar Scientific, Sputter Coater), whilst Fe₃O₄-based microspheres were imaged uncoated. Measurements of microsphere size distributions and surface pores diameters were performed using ImageJ 1.51h software (National Institutes of Health, USA).

Fixed MG-63 cells (*Section 3.6*) decorating P40-Fe₃O₄ porous microspheres (*Chapter 6*) were imaged using an environmental scanning electron microscope (ESEM; FEI Quanta 650 ESEM; 10 kV; spot size 5; 6.7 mm working distance; 4.76 torr; 2.0°C; humidity 89.5%).

3.5.2 Energy-dispersive X-ray spectroscopy (EDS)

Energy dispersive x-ray spectroscopy (EDS or EDX) is a chemical microanalysis technique used in conjunction with SEM. The detection of X-rays emitted from a sample during electron beam bombardment [249] reveals the elemental composition of the analysed volume. As outlined above, once a sample is bombarded by the SEM's high-energy electron beam, photoelectrons are ejected from the core shells of the atoms. The resulting electron vacancies are filled by electrons from a higher state, and characteristic X-rays are emitted, according to the energy difference between two electron states. The X-ray energy is characteristic of the element from which it was emitted, thus, each element can be identified uniquely. EDS detectors separate characteristic X-rays from each element into an energy spectrum, allowing the abundance of specific elements to be determined [250].

In the present study, energy dispersive X-ray (EDX; BRUKER software, FEI Quanta 600; 20 kV; 12.9 mm working distance) analysis investigations were performed to appraise elemental distributions across ***sectioned microspheres***. For EDS quantification, Bruker software assumed oxides were utilised, with compositional measurements averaged across different point locations.

For sectioned sample preparation, a test sieve (stainless steel frame; 203 x 50 mm; 32 μm mesh; VWR International) was used to filter out particles sized below 32 μm . Sieved microspheres products were embedded in cold epoxy resin and sectioned by sequential mechanical grinding (400, 800 and 1200 SiC papers) and polishing (6 and 1 μm diamond paste). The polished samples were then cleaned using deionised water and industrial methylated spirit (IMS) and dried before carbon coating (Edwards coating System E306A).

3.5.3 Mineral liberation analysis (MLA)

Mineral Liberation Analyser (MLA) combines large specimen automated SEM, with multiple EDS detectors, with state-of-the-art automated quantitative mineralogy software. MLA was developed to automate the identification of minerals in polished sections of drill core, particulate or lump materials, and to quantify a wide range of mineral characteristics *e.g.*, mineral abundance, grain size and liberation; using unique combinations of high-resolution (0.1 – 0.2 μm), BSE image analysis and advanced X-ray identification techniques to target the analytical requirements [251]. Image analysis functions related to MLA include particle de-agglomeration and phase segmentation; whilst for X-ray analysis three techniques are used: *i.e.* **(i) point X-ray**: spectrum acquisition for each grey level identified within a segmented particle, **(ii) area X-ray**: phase detection through the resulting mixed spectra; and **(iii) X-ray mapping**: identification of mineral phases associated phase boundaries. Importantly, the mineral identification through X-ray analysis requires use of a mineral library, constructed before an automated run by collection of X-ray spectra for each mineral in the sample. This ensures that measurement conditions are satisfied, *e.g.*, appropriate beam energy (keV) [252].

For the case of flame-spheroidised microsphere samples, following sieving and sectioning, chemical investigation was performed *via* backscattered electron (BSE) imaging and SEM-based mineral liberation analysis (MLA; FEI Quanta600 MLA, 20 kV; spot size 7), equipped with energy-dispersive X-ray spectroscopy (EDS; Bruker software, 12.9 mm working distance) and data acquisition software for automated mineralogy (Bruker/JKTech/FEI).

3.5.4 X-ray diffractometry (XRD)

X-ray diffractometry (XRD) is a non-destructive technique that provides specific information related with crystallographic structure, and by inference, chemical composition and physical properties of materials [253]. X-ray diffraction is the elastic scattering of X-ray photons by atoms in a periodic lattice. Scattered monochromatic X-rays that are in phase give constructive interference (Figure 3.4) and the geometric criterion for constructive interference is given by Bragg's law (Equation 3.1) [254]:

$$n \lambda = 2d \sin \theta \quad (\text{Equation 3.1})$$

where n is an integer; λ is the X-ray wavelength; d is the lattice spacing; and θ is the diffraction angle.

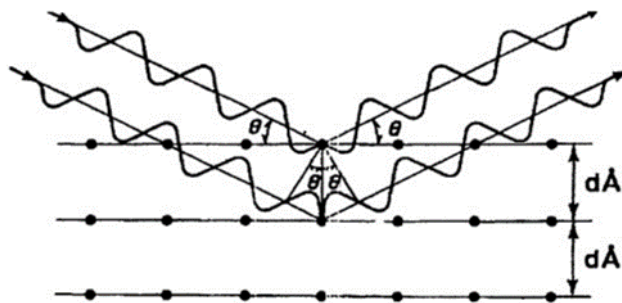


Figure 3.4 Schematic representation of constructive interference [254]

Semiquantitative analysis relates to the estimation of constituent elemental concentrations [255]. XRD may be used to determine semi-quantitatively the weight fractions of constituents.

In this investigation, structural characterisation of the microsphere products was performed by X-ray diffractometry (**XRD**; Bruker D8 Advance, Da Vinci design

with LYNXEYE XE-T detector in 1D mode; Cu K α radiation ($\lambda = 0.15406$ nm); 40 kV and 40 mA; step size 0.02°; total time/step 29.8 s per datapoint; 21°C). High-temperature XRD (**HT-XRD**) (Bruker D8 Advance Series 2 with MRI TC-Basic temperature chamber; Cu K α radiation ($\lambda = 0.15406$ nm); step size 0.050°; step time 2 s; temperatures: 30, 450, 550, 650, 750, 950 and 1050°C; heating rate 10°C/min) was used to investigate starting powders, as a function of heating. Semi-quantitative analysis (Bruker DIFFRAC.EVA software) was used to determine weight fractions of the constituent products.

3.5.5 Superconducting quantum interference device magnetometry (SQUID)

SQUID is a system capable of measuring extremely small magnetic fields with high precision. A typical SQUID system consists of two superconductors separated by an insulating material, forming two parallel Josephson junctions (Figure 3.5).

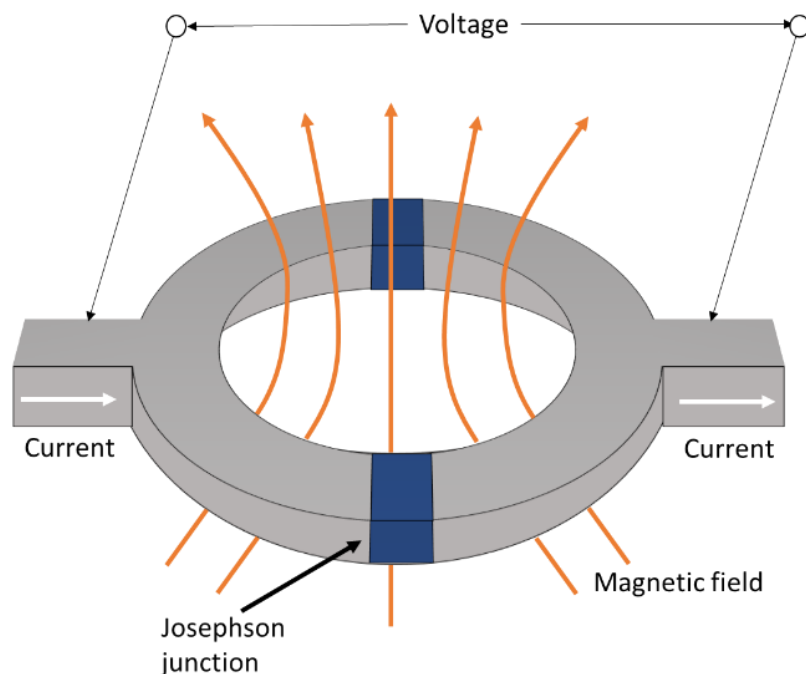


Figure 3.5. Typical dual junction for SQUID magnetometer.

A bias current (I_b), as applied, locates the I - V curve midway between the superconducting and normal state (*i.e.*, resistivity) (Figure 3.6a). Insulating materials (*i.e.*, resistors) prevent hysteresis in the I - V curve. A magnetically coupled field into the SQUID loop generates screening currents that will increase or decrease I_c (*i.e.*, critical current), as a function of the magnetic field direction. Hence, as the external field increases/decreases, the voltage will change in a periodic manner, corresponding to the field (flux) quantum Φ_0 (Figure 3.6b) [256]. Hence, by monitoring the change in voltage, it is possible to determine the magnetic field.

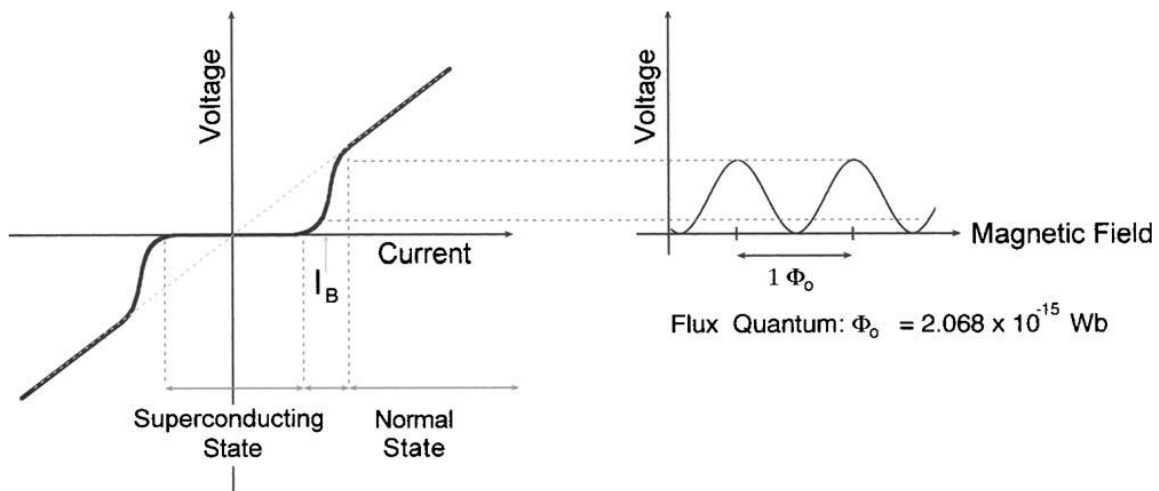


Figure 3.6. (a) Josephson junction bias point (I_b) curve; (b) voltage – magnetic field at constant bias current [256].

Magnetic characterisation of the flame-spheroidised products was performed using **SQUID** (Quantum Design MPMS-3 system; VSM mode; vibration amplitude 1.5 mm; 26.9°C). Before SQUID investigation, the powders were sieved (stainless steel frame; 203 x 50 mm; $\geq 32 \mu\text{m}$ mesh; VWR International) to filter out surplus starting material, and encapsulated within gelatine capsules, before being mounted onto the

sample holder. Magnetic units relevant for this investigation are summarised in Table 3.4. High-temperature SQUID (**HT-SQUID**) (Quantum Design MPMS-3 system; VSM mode; vibration amplitude 1.5 mm; temperatures: 25, 100, 200, 300, 400, 500, 600 and 700°C; heating rate 5°C min⁻¹; ultra-high vacuum) was performed to investigate the magnetic properties of precursor powders, as a function of temperature. Before HT-SQUID measurement, the powder samples were mixed with a non-magnetic cement, to glue them to heating sticks.

Table 3.4. Magnetic units (SI & Gauss) and conversion factors.

Quantity	Gaussian Units	Conversion factor	SI units
Magnetic Field (H)	Oe	$10^3/4\pi$	A/m
Mass magnetization (M)	emu/g	1	Am ² /kg
Magnetic moment (μ)	emu	10^{-3}	J/T

3.5.6 Low frequency induction

Induction heating systems require a conductive coil (in this case a copper-based solenoid). The application of an alternating voltage in the coil circuit generates an alternating current (AC) which results in a time-variable magnetic field. The frequency value for the coil current & magnetic field are equivalent. When a conductive material is positioned in the proximity of the changing magnetic field, eddy currents are induced. These induced currents have the same frequency values as the coil current; nevertheless, their direction is opposite to the coil current. Heat is then generated due to the Joule effect (I^2R) [257]. Figure 3.7 illustrates an induction heating coil circuit.

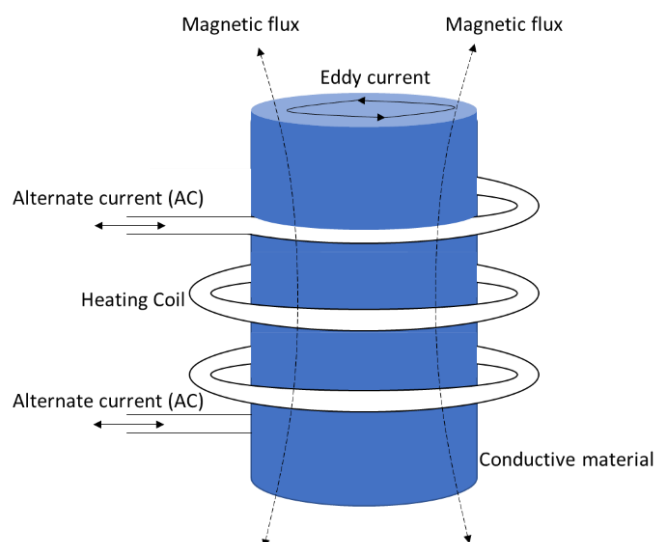


Figure 3.7 Induction coil system.

In this work, the heating of microsphere products was performed *via* low frequency induction (Cheltenham Induction Heating Ltd) (Table 3.5). Glass vials containing the microspheres were placed at the centre of a water-cooled copper coil generating an alternating magnetic field, whilst temperature was measured using a fibre optic sensor *i.e.*, thermocouple (Neoptix Reflex Signal Conditioner). Control samples of processed Fe₃O₄ and P40 dense microspheres were also investigated. All measurements were recorded in triplicate (n=3).

Table 3.5 Induction heating parameters

Sample	Voltage (V)	Power (W)	Current (A)	Frequency (kHz)
P40-Fe ₃ O ₄ porous microspheres	250	350	1.4	204
	100	120	1.2	
Fe ₃ O ₄ :CaCO ₃ porous microspheres (1:1 mass ratio)	150	120	0.8	204
	35	20	0.6	

3.5.7 Complementary techniques

3.5.7.1 Mössbauer spectroscopy

The Mössbauer effect (*i.e.*, recoil-free gamma ray emission and absorption) is the basis of Mössbauer spectroscopy, a technique that measures subtle differences between the hyperfine interactions of a probe nucleus in a solid material and a reference solid material. The high levels of sensitivity of this technique was used to measure the oxidation states of iron, along with its molecular geometries (*e.g.*, tetrahedral, octahedral), and range of site occupancies [258]. In the present work, Mössbauer spectroscopy (room-temperature ^{57}Fe Mössbauer spectroscopy; 26.85°C; Sheffield Hallam University) was used to investigate the magnetic properties, oxidation states and crystallographic sites of Fe_3O_4 powders, prior- and post-flame spheroidisation (*Chapter 4*).

3.5.7.2 Thermogravimetric analysis (TGA)

Thermogravimetric analysis was used to monitor and record sample parameters of mass, temperature and heating time. Typical TGA equipment generates a thermal curve of the sample mass change, as a function of temperature or time [259]. In this investigation, thermogravimetric analysis (TGA, SDT Q600; 40 - 1500°C; heating rate 10°C/min; air) was used to investigate $\text{Fe}_3\text{O}_4:\text{CaCO}_3$ mixed powder powders (1:1 mass ratio; non-spheroidised) as a function of heating (*Chapter 5*).

3.5.7.3 Selected area electron diffraction (SAED) via Transmission electron microscopy (TEM)

TEM provides for imaging & diffraction modalities for specimen characterisation. In the diffraction mode, a sample area is illuminated by the electron beam and an electron diffraction pattern is obtained in the back focal plane of the

objective lens. For single-crystals, spot patterns are produced; for polycrystalline materials, a ring pattern is generated; and for glasses/amorphous materials, a series of diffuse halos are obtained [260]. In this context, the fine-scale structural properties of flame-spheroidised $\text{Fe}_3\text{O}_4:\text{CaCO}_3$ microspheres (1:1 mass ratio; 2:2 gas flow setting) (*Chapter 5*) were investigated *via* using TEM (JEOL 2100+ TEM; 200 kV; operational mode selected area electron diffraction (SAED)), *via* automated acquisition (range of -40 to +40 degrees tilt). Stacked 120 tilted diffraction patterns were loaded and analysed using Crystallographic Tool Box (CrysTBox) software. Prior to TEM investigation, the microsphere samples were ground using a mortar and pestle, dispersed in suspension and deposited onto an amorphous holey carbon film on a Cu TEM support grid.

3.5.7.4 X-ray photoelectron spectroscopy (XPS)

XPS, also known as electron spectroscopy for chemical analysis (ESCA), is a non-destructive technique that uses a monochromatic X-ray source to analyse surface chemical states / bonding, with a sampling depth of 3-10 nm into the surface [261]. In the present work, complementary XPS (VG ESCALab Mark II X-ray Photoelectron and Scanning Auger Spectrometer; Al $\text{K}\alpha$ source; 20 mA; 20 kV; step 1; No. of scans 2; dwell 0.2; pass energy 50 eV, Constant Analyser Energy mode) studies were performed to analyse the surface chemistry of flame-spheroidised $\text{Fe}_3\text{O}_4:\text{CaCO}_3$ microspheres (1:1 mass ratio; 2:2 gas flow setting) (*Chapter 5*).

3.6 Cytocompatibility investigations

3.6.1 Cell culturing

Microsphere products were sterilised by washing in ethanol (100%) followed by complete evaporation overnight in a sterile environment at room temperature. The

human osteoblast-derived cell line MG-63 (European collection of authenticated cell cultures – ECACC) was seeded onto the microspheres at a density of 10,000 cells/cm² in 300 µL of standard cell culture medium; comprising Dulbecco's Modified Eagle Medium (DMEM) supplemented with 10% foetal calf serum, 1% penicillin and streptomycin, 1% L-Glutamine, 1% of non-essential amino acids and 1.5% ascorbic acid. Cells were seeded on 10 mg of sterile microspheres in low-adherent 48-well plates previously coated with 1% (w/v) solution of poly(2-hydroxyethyl methacrylate) (poly-HEMA, Merck) and Ethanol 95% in standard cell culture medium. Cells were incubated at 37°C and 5% CO₂, with media refreshed every 48 h. Two independent experiments were performed, with 3 experimental replicates for each condition.

3.6.2 Cell metabolic activity and statistical analysis

MG-63 cell metabolic activity was evaluated using an Alamar Blue assay at days 2 and 7. Following removal of standard cell culture medium and washing with phosphate-buffered saline, 300 µL of Alamar Blue solution (1:9 Alamar blue:Hanks Balanced Salt Solution) was added to each well plate and incubated for 90 minutes at 37°C and 5% CO₂, followed by a further 10 minutes on a shaker at 150 rpm. Three aliquots of 100 µL were transferred to a 96-well plate. An FLx800 fluorescence microplate reader (BioTek Instruments Inc.) was used to measure fluorescence at 530-nm excitation and 590-nm emission wavelengths.

Two independent cell culture experiments were performed with results shown as “*mean ± standard error of mean*” (unless otherwise stated). Statistical analysis was performed using Prism software (version 9.2.0, GraphPad Software, San Diego, CA). Two-way analysis of variance was calculated followed by a Tukey's multiple comparison test. Mean difference was considered to be significant at $P = 0.05$ corresponding to a 95% confidence level.

At day 7, cells decorating P40-Fe₃O₄ porous microspheres were fixed using 4% paraformaldehyde, prior to ESEM characterisation (as outlined in S3.5.1).

3.7 Summary

In the present Chapter, the general preparation steps for dense and porous microspheres have been outlined. For the case of **dense microspheres**, feedstock Fe₃O₄ powders, and phosphate-based glass (denominated as P40) / Fe₃O₄ mixtures were manufactured *via* the flame spheroidisation process. **Porous microspheres** were prepared by combining porogen (CaCO₃) with **(i)** large (*i.e.*, ≤ 45 μm) and small (*i.e.*, ≤ 5 μm) Fe₃O₄ powders; and **(ii)** P40-Fe₃O₄ mixtures. The precursor-porogen mixtures were flame spheroidised, as a function of mass ratios and gas flow setting.

Furthermore, the characterisation techniques applied have been outlined. The microspheres were investigated *via* SEM and XRD to appraise product topographies and structural properties, respectively, followed by magnetic investigations using SQUID. For EDS and MLA compositional studies, magnetic microsphere samples were sieved and cross-sectioned. Induction heating investigations were performed on microspheres using a high-frequency inductive coil system. Complementary Mössbauer spectroscopy, TGA, SAED *via* TEM, and XPS techniques were also utilised. Cytocompatibility investigations were performed using MG-63 cells seeded onto microsphere products. Additionally, the effect of heat was investigated on starting powders using HT-XRD and HT-SQUID.

4.0 Flame spheroidisation of magnetic microspheres using Fe_3O_4 ($\leq 45 \mu\text{m}$) precursors

4.1 Introduction

The present Chapter initially studies structural transformations and magnetic properties for ($\leq 45 \mu\text{m}$) ***Fe₃O₄ precursor powder*** using high-temperature X-ray diffractometry (HT-XRD) and high-temperature superconductive quantum interference device (HT-SQUID) magnetometry, both under conditions of slow heating rate compared to the rapid, flame spheroidisation-process. The formation of ***Fe₃O₄ dense microspheres*** manufactured *via* the rapid, single-stage, flame spheroidisation method, using large sized magnetite ($\leq 45 \mu\text{m}$) Fe_3O_4 feedstock powders, is then investigated. Later, this Chapter reports on ***Fe₃O₄ porous microspheres***. In this context, the effects of adding non-magnetic calcium carbonate (CaCO_3) porogen for the production of porous microspheres, are explored as a function of mass ratios ($\text{Fe}_3\text{O}_4:\text{CaCO}_3$ 3:1, 1:1, and 1:3 mass ratios) and oxygen-acetylene gas flow settings (2:2, 2.5:2.5, and 3:3).

Scanning electron microscopy (SEM) based techniques, including energy dispersive X-ray spectroscopy (EDS) and mineral liberation analysis (MLA), were used to characterise the flame-spheroidised products. The structures of the magnetite precursor and microsphere products were evaluated using X-ray diffractometry (XRD). Superconductive quantum interference device (SQUID) and Mössbauer spectroscopy measurements provided insights into the magnetic properties of the starting powders and spheroidised products.

4.2 Fe₃O₄ precursor powder

Complementary HT-XRD ($10^{\circ}\text{C min}^{-1}$), and HT-SQUID ($5^{\circ}\text{C min}^{-1}$) measurements, both acquired for slowly increasing temperature, provided insights into the oxidation pathways and magnetic properties of the starting non-spheroidised Fe₃O₄ powders.

4.2.1 Structural transformation as a function of temperature

Comprehensively, HT-XRD data (Figure 4.1) demonstrated a progressive transformation of Fe₃O₄ to a mixture of Fe₃O₄ (weak peaks) and Fe₂O₃ (strong peaks).

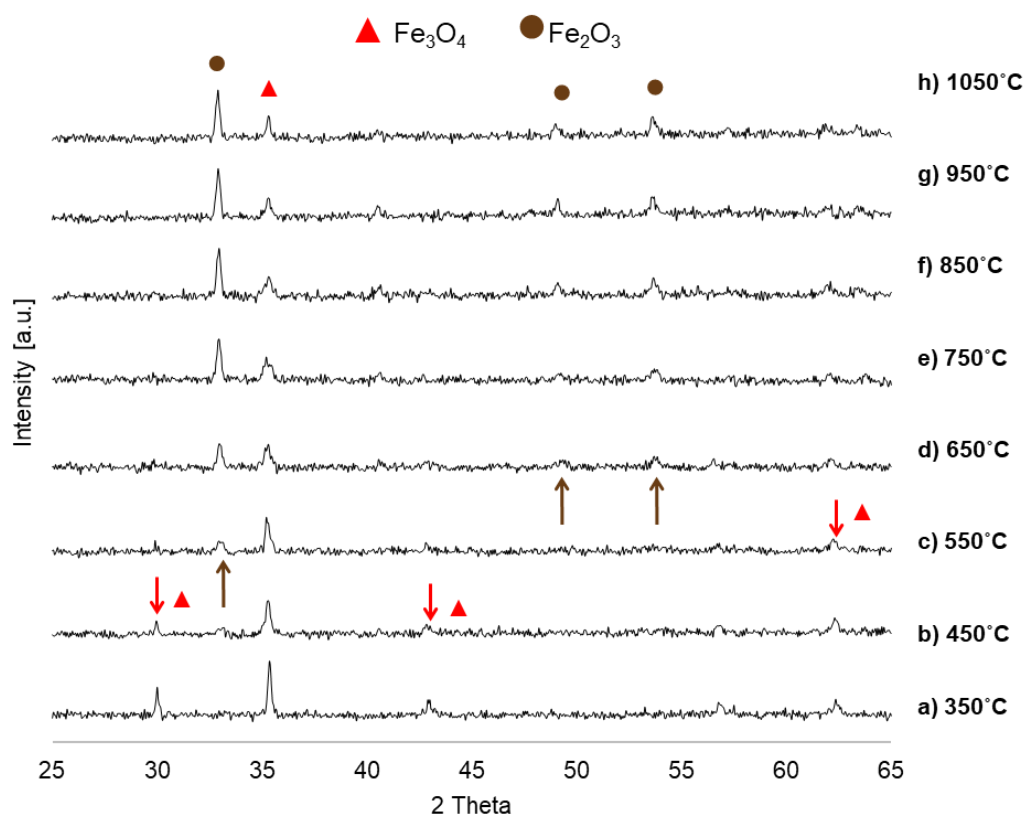


Figure 4.1 XRD diffractograms illustrating the structural transformation of large ($\leq 45 \mu\text{m}$) Fe₃O₄ precursor powders, as a function of increasing temperature.

In particular, Figures 4.1b,c illustrate magnetite crystalline peaks progressively diminishing with increasing temperature, up to 550°C (red arrows). Small peaks

started to emerge at 550°C which were attributed to Fe₂O₃ formation (brown arrows). A summary of the constituent products, as a function of temperature, is presented in Table 4.1 (whilst noting the possibility of systematic error affecting absolute values).

Table 4.1 Wt% constituents of Fe₃O₄ (≤ 45 µm) powder with increasing temperature measured *via* semi-quantitative analysis.

Phase	350°C/ wt%	450°C/ wt%	550°C/ wt%	650°C/ wt%	750°C/ wt%
Fe ₃ O ₄	85.5	54.3	49.1	13.6	7.7
Fe ₂ O ₃	14.5	45.7	50.9	86.4	92.3

4.2.2 Magnetisation as a function of temperature

Complementary HT-SQUID investigations were performed to investigate magnetic expression of the Fe₃O₄ powder as a function of increasing temperature (Figure 4.2). At room temperature, the Fe₃O₄ powders exhibited high saturation magnetisation (95.1 Am²/kg), which progressively started to decrease with increasing temperature to 500°C (50.94 Am²/kg). At 600°C, the magnetisation decreased significantly to 13.05 Am²/kg, and at 700°C the magnetisation reached a low of 1.47 Am²/kg. Summaries of magnetisation values, as a function of temperature, are presented in Table 4.2 and Figure 4.3.

Table 4.2 Magnetic measurements for Fe₃O₄ starting powders ($\leq 45 \mu\text{m}$) as a function of increasing temperature.

Temperature	°C	25	100	200	300	400	500	600	700
Magnetic saturation	Am²/kg (emu/g)	95.08	90.64	82.27	71.71	64.86	50.94	13.05	1.47
Remanent magnetisation	Am²/kg (emu/g)	10.6	9.4	7.9	4.9	2.5	0.4	0	0
Coercive field	kA/m	9.5	8.3	6.7	4.4	2.9	0.4	0	0
	Oe	119	104	84	55	36	4	0	0

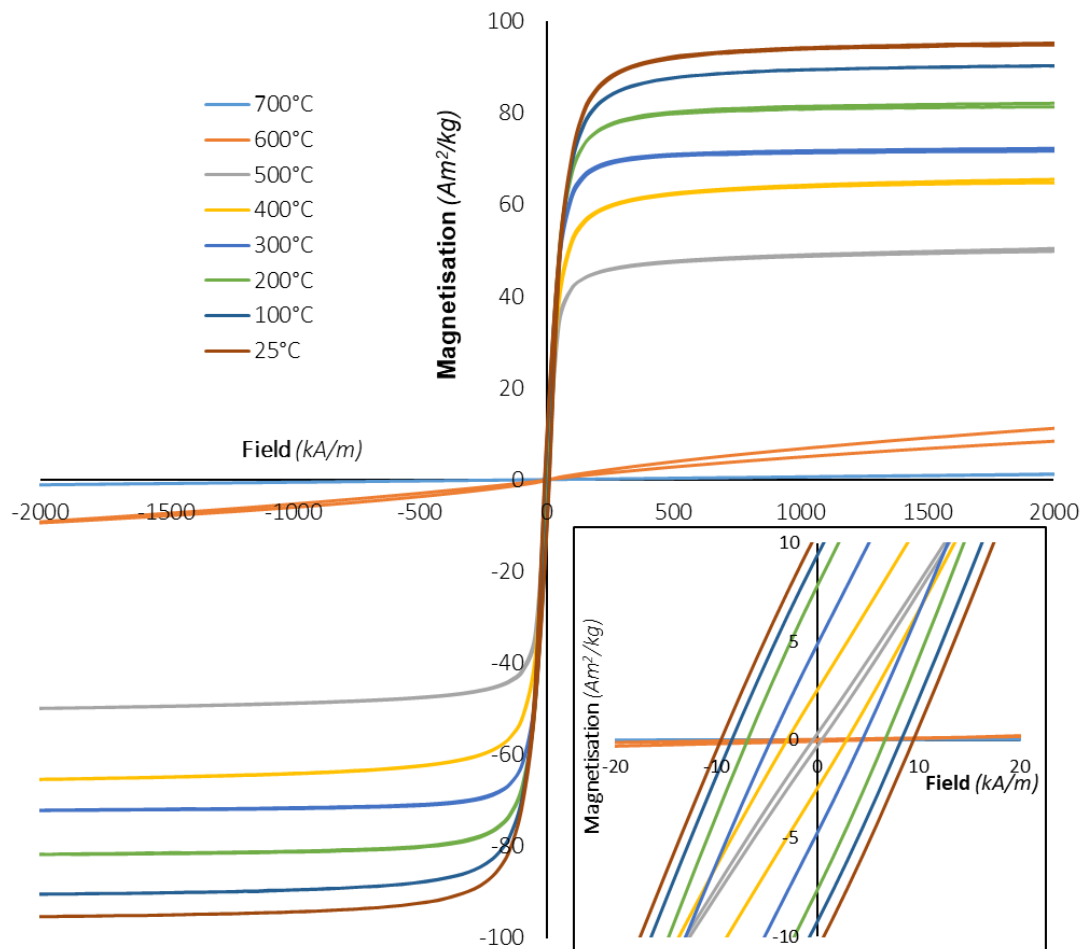


Figure 4.2 Hysteresis loops for magnetite precursor powder, as a function of temperature. Inset figure illustrates a progressive decrease of remanent magnetisation with increasing temperature.

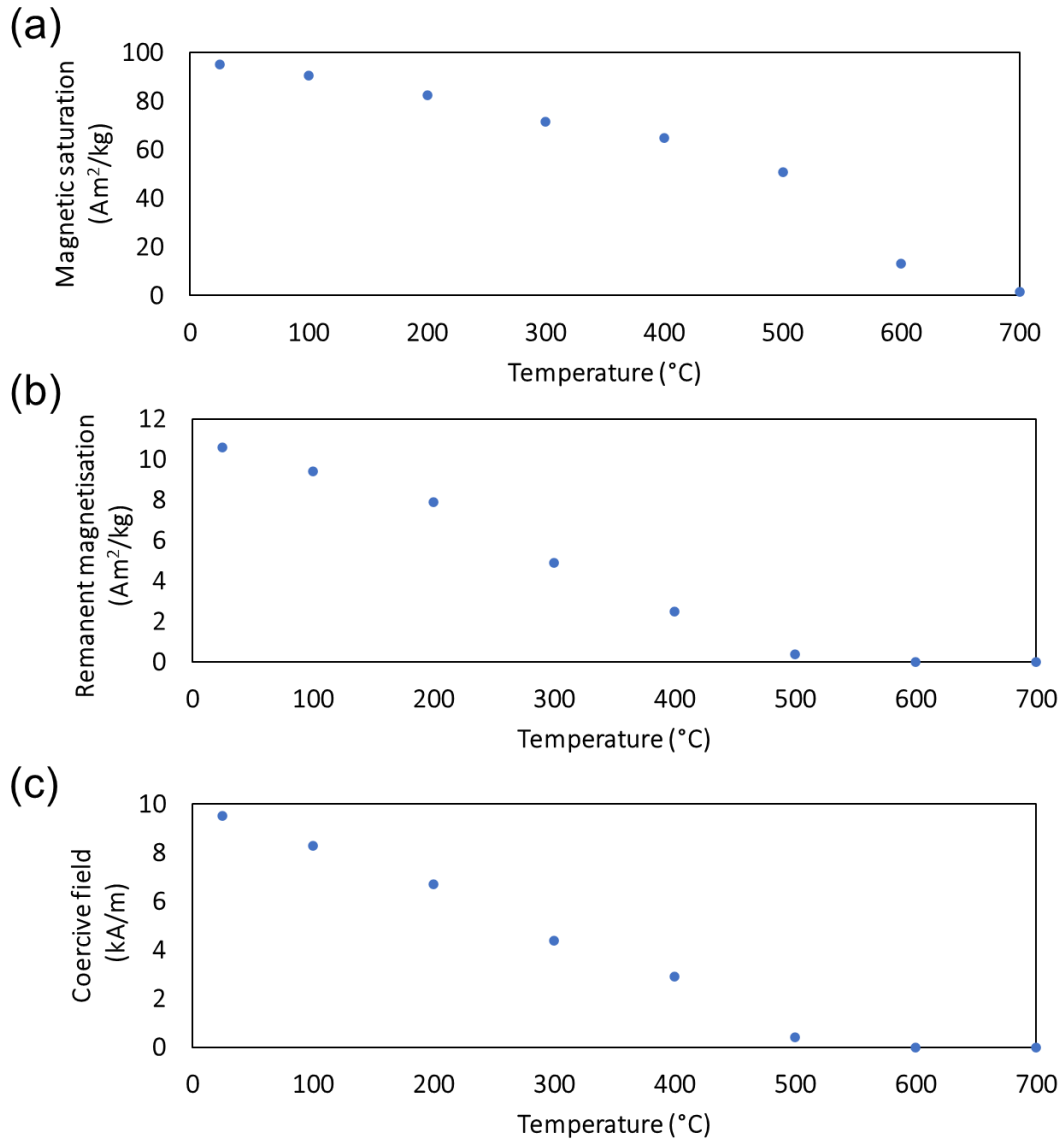


Figure 4.3 Graphs showing: **(a)** magnetic saturation, **(b)** remanent magnetisation, and **(c)** coercive field values for Fe_3O_4 powders ($\leq 45 \mu m$) as a function of increasing temperature, revealing a decrease of magnetic performance.

Having studied Fe_3O_4 precursor powders as a function of temperature, the following section presents characterisation of the Fe_3O_4 flame-spheroidised microspheres.

4.3 Dense Fe₃O₄ microspheres

Large magnetite ($\leq 45 \mu\text{m}$) powders were used for the manufacture of dense, magnetic microspheres. Figure 4.4 presents a summary of the methodology used for flame spheroidisation processing and characterisation of the microspheres produced.

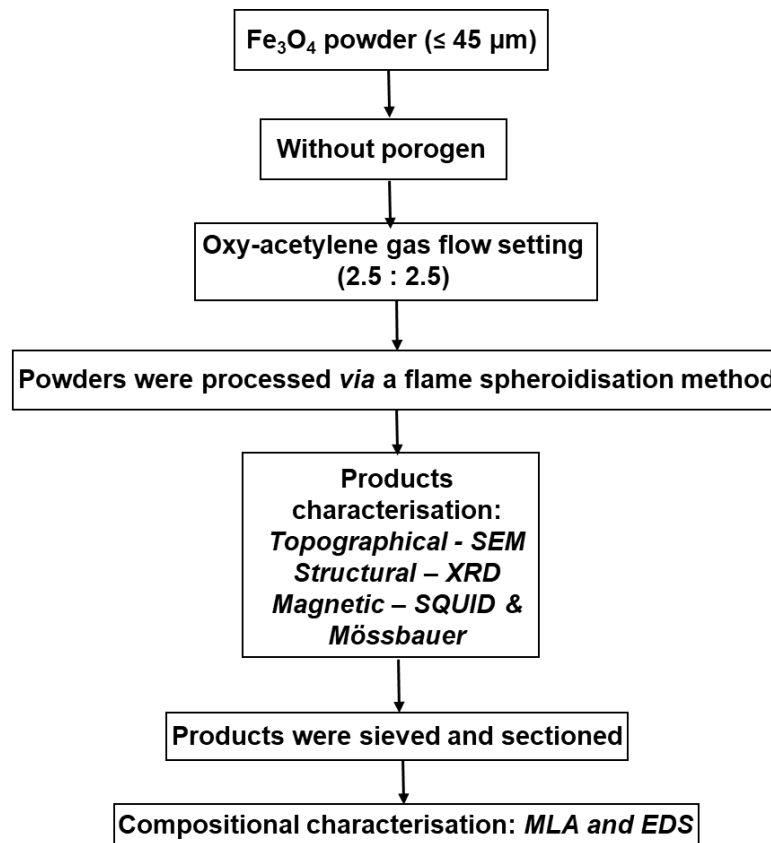


Figure 4.4 Flow diagram summarising the processing steps followed for the manufacture and characterisation of dense, magnetic Fe₃O₄ microspheres.

4.3.1 Fe₃O₄ microsphere topography (*unsieved*)

SEM was used to investigate the starting feedstock powders and physical size and form of the spheroidised products. Figures 4.5(a,b) present low magnification secondary electron (SE) images of the large ($\leq 45 \mu\text{m}$) Fe₃O₄ starting feedstock powder and the resultant dense microsphere products (gas flow setting 2.5:2.5),

respectively, highlighting the morphological transformation of the magnetite precursors into dense microspheres (20 - 104 μm) *via* flame-spheroidisation. Fig. 4.5c presents a size distribution histogram of the microspheres produced.

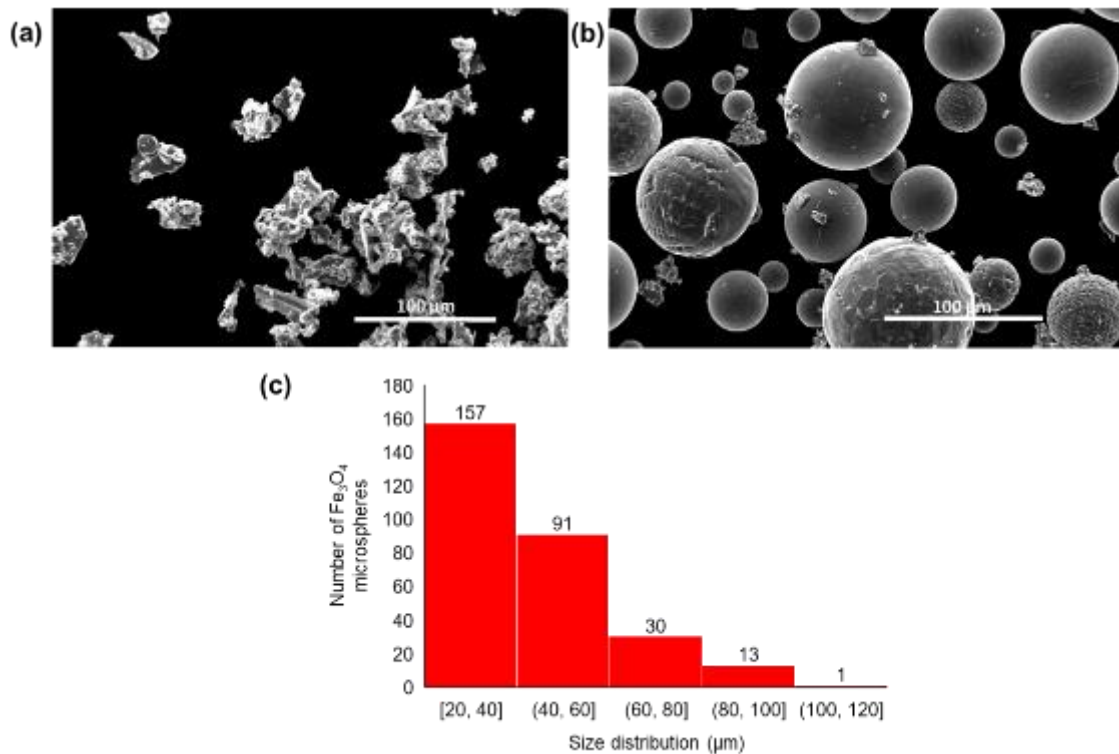


Figure 4.5 SE images of: **(a)** starting Fe_3O_4 powder (before flame spheroidisation-processing), and **(b)** dense microspheres, post flame-spheroidisation. **(c)** Size distribution of the flame-spheroidised, dense, Fe_3O_4 microspheres.

Structural investigations of the Fe_3O_4 precursors and microspheres are presented as follows.

4.3.2 Structural characterisation (*unsieved microspheres*)

Figures 4.6(a,b) presents XRD diffractograms for the starting, $\leq 45 \mu\text{m}$ sized, magnetite feedstock powder and the resultant dense microsphere products (unsieved), corresponding to the particle samples shown in Figures 4.5(a,b). The XRD

data confirmed the presence of the magnetite crystalline structure prior to and post flame-spheroidisation. Characteristic peaks at $2\theta = 18.3^\circ, 30.1^\circ, 35.5^\circ, 37.1^\circ, 43.1^\circ, 53.5^\circ, 57.1^\circ$ and 62.7° correspond to the $\{111\}, \{220\}, \{311\}, \{222\}, \{400\}, \{422\}, \{511\}$ and $\{440\}$ lattice planes of Fe_3O_4 (PDF 01-087-0246), respectively [262]. In addition, Figure 4.6a revealed the presence of a small peak at 33.4° , attributable to the $\{104\}$ spacing for hematite (Fe_2O_3), suggesting slight oxidation of the powders during flame-processing, distinct from the mixture of Fe_2O_3 (strong peaks) and Fe_3O_4 (weak peaks) signatures shown for the slowly heated precursors (Figure 4.1h). Further, it is noted that the distinction between magnetite and maghemite by XRD is difficult, as both phases exhibit a spinel structure and almost identical lattice parameters. In order to validate the iron oxide phase, the XRD pattern corresponding to Fe_3O_4 microspheres was investigated further by stripping the $\text{K}\alpha_2$ component (Bruker DIFFRAC.EVA software) for more accurate $\text{K}\alpha_1$ peak positions identification. Figures 4.6(c-j) show XRD diffractograms, with magnified peak positions, corresponding to the flame-spheroidised Fe_3O_4 products used to compare Fe_3O_4 and $\gamma\text{-Fe}_2\text{O}_3$ phases. Notably, for the cases of $2\theta = 18.3^\circ, 30.1^\circ, 35.5^\circ, 37.1^\circ, 43.1^\circ, 53.5^\circ$ peaks, the Fe_3O_4 phase is confirmed, as shown in Figures 4.6(c-h). Conversely, for $2\theta = 57.1^\circ$ and 62.7° (Figures 4.6(i-j), respectively) the peaks were shifted slightly, in between Fe_3O_4 and $\gamma\text{-Fe}_2\text{O}_3$ positions. However, maghemite has additional peaks to magnetite, the most intense ones being at $15.0^\circ, 23.8^\circ$ & 26.1° , but these were not present in this case. Hence, the XRD evidence indicates a strong dominance of the Fe_3O_4 phase in the flame processed products.

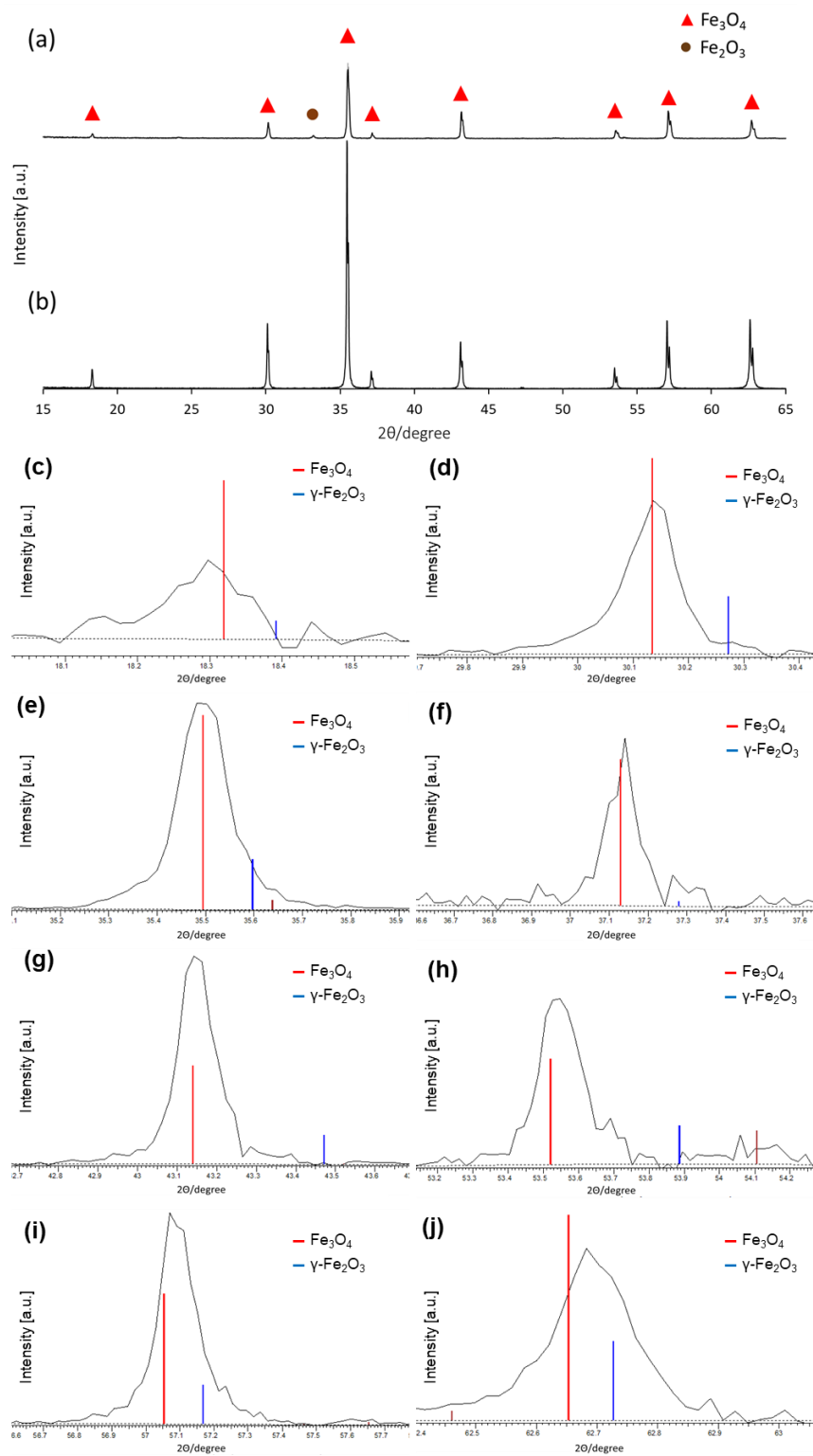


Figure 4.6 XRD diffractograms for: **(a)** Fe₃O₄ microspheres, as compared with **(b)** the starting Fe₃O₄ powder. **(c-j)** Fe₃O₄ microspheres high-magnification XRD diffractograms comparing Fe₃O₄ & γ -Fe₂O₃ peak positions: **(c)** 18.3°; **(d)** 30.1°; **(e)** 35.5°; **(f)** 37.1°; **(g)** 43.1°; **(h)** 53.5°; **(i)** 57.1°; **(j)** 62.7°

4.3.3 Magnetic characterisation (*unsieved microspheres*)

Figure 4.7 presents magnetic hysteresis data for the precursor powder and the flame-spheroidised Fe_3O_4 microspheres. Interestingly, both starting magnetite and processed microspheres revealed similar, strong magnetic saturation values (Table 4.3), whilst noting that the Fe_3O_4 microspheres exhibited significantly lower levels of remanent magnetisation. Nevertheless, these results are indicative of the retention of strong magnetic properties for magnetite, processed by the rapid, flame spheroidisation method at very high temperatures of $\sim 3100^\circ\text{C}$ [63], distinct from the steady decrease in magnetic properties shown by the slowly heated precursors (Figure 4.2).

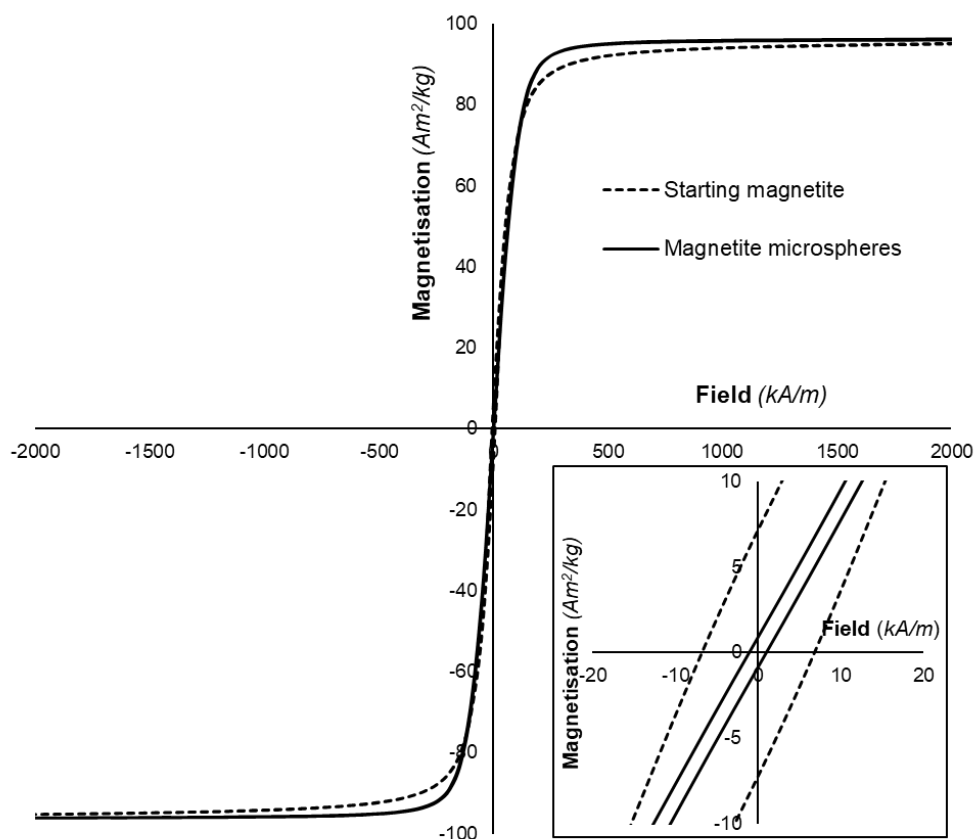


Figure 4.7 Hysteresis loop curves of starting Fe_3O_4 powder and flame-spheroidised Fe_3O_4 microspheres (recorded at 26.85°C). Inset figure provides evidence for starting powder and microspheres remanent magnetisation.

Table 4.3 Magnetic saturation, remanent magnetisation and coercive field values of Fe_3O_4 precursor powder and flame-spheroidised microsphere products (sieved).

Sample	Magnetic saturation	Remanent magnetization	Coercive Field / Hc	
	Am^2/kg (emu/g)	Am^2/kg (emu/g)	(kA/m)	(Oe)
Starting magnetite powder	95.1	7.6	6.9	87
Magnetite microspheres	96.3	0.8	0.5	6.7

Complementary Mössbauer spectroscopy was used to analyse the magnetic moments and types of magnetic order. Figures 4.8(a,b) presents Mössbauer spectra for Fe_3O_4 precursors and flame-spheroidised microspheres, showing two sextets corresponding to iron sites: tetrahedral A (Fe^{3+})_A and octahedral B ($\text{Fe}^{2.5+}$)_B [174, 263].

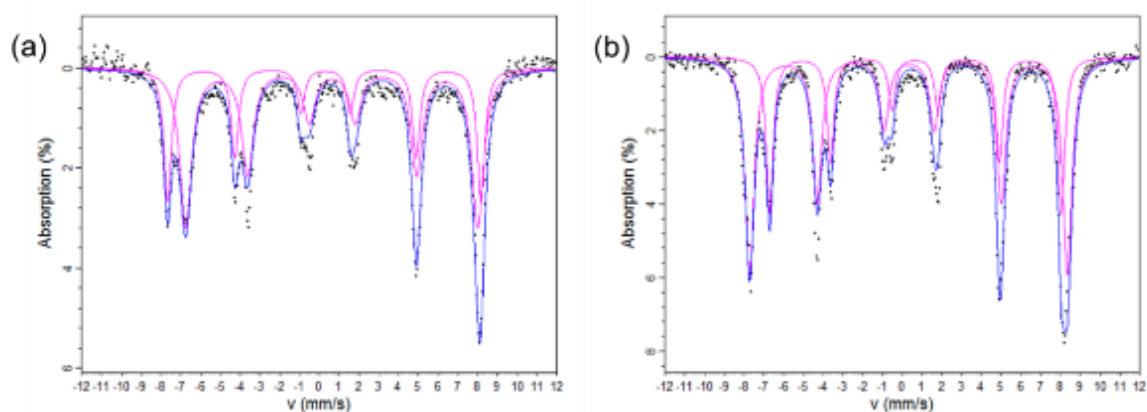


Figure 4.8 Mössbauer spectra for: (a) starting Fe_3O_4 powder; and (b) flame-spheroidised Fe_3O_4 microspheres. Pink sextets: two typical A-sites; Blue sextets: B-sites. (Data acquired by Paul A. Bingham)

Table 4.4. Mössbauer parameters for Fe₃O₄ precursor powder and dense microspheres. B_{hf} hyperfine field; δ isomer shift relative to αFe.

Sample	Valence & Site	B _{hf} / T	δ / mm s ⁻¹	Area ratio
Magnetite precursor	(Fe ³⁺) _A	49.1	0.29	1
	(Fe ^{2.5+}) _B	45.7	0.65	1.9
Magnetite microspheres	(Fe ³⁺) _A	49.8	0.28	1.9
	(Fe ^{2.5+}) _B	45.7	0.66	1

The hyperfine magnetic splitting (B_{hf}) and centre shift (δ) of the fits summarised in Table 4.4 are consistent with those for Fe₃O₄ from the literature [174, 264]. The relative area ratios indicated spectral areas of 33 % for the 49 T sextet, and 66 % for the 46 T sextet. The Fe₃O₄ precursor powder spectrum is consistent with this area ratio, whereas the Fe₃O₄ microsphere spectrum appears to have these areas reversed. This may suggest that: *(i)* the tetrahedral A site is being formed preferentially; *(ii)* the octahedral B site is not being formed as readily in the flame-processed sample; *(iii)* the B site has been doped with non-iron cations, *i.e.*, nonstoichiometric magnetite or *(iv)* maghemite phase or magnetite/maghemite mixtures have been formed [265].

The Fe₃O₄ microsphere products were then sieved (<32 µm) and sectioned, in advance of investigation of their compositional properties.

4.3.4 Compositional analysis (*sieved and sectioned microspheres*)

4.3.4.1 Mineral liberation analysis

Figure 4.9a presents BSE images of a representative sieved, resin embedded and sectioned, flame-spheroidised Fe₃O₄ sample, confirming a high yield of dense microspheres. Notably, mineral mapping analysis (Figures 4.9b and 4.10)

demonstrated very high levels of homogeneity for these microspheres. Associated modal mineralogy and mineral reference data are summarised in Table 4.5.

Table 4.5. Modal mineralogy and mineral reference for Fe_3O_4 microspheres.

Mineral	Modal mineralogy		Mineral reference (wt%)	
	Particles	Weight %	Fe	O
Magnetite (Fe_3O_4)	8385	99.9	72.4	27.6

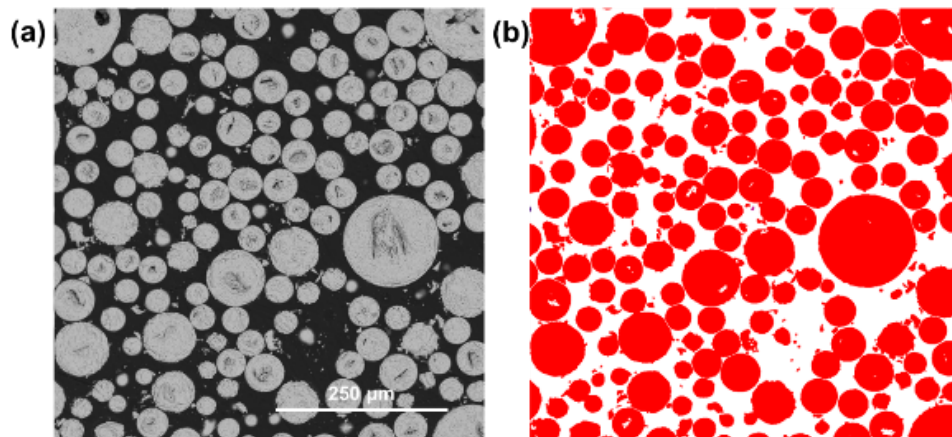


Figure 4.9. (a) BSE image and (b) MLA compositional analysis of dense Fe_3O_4 microspheres, following sieving and sectioning, demonstrating very high levels of Fe_3O_4 compositional homogeneity (red).

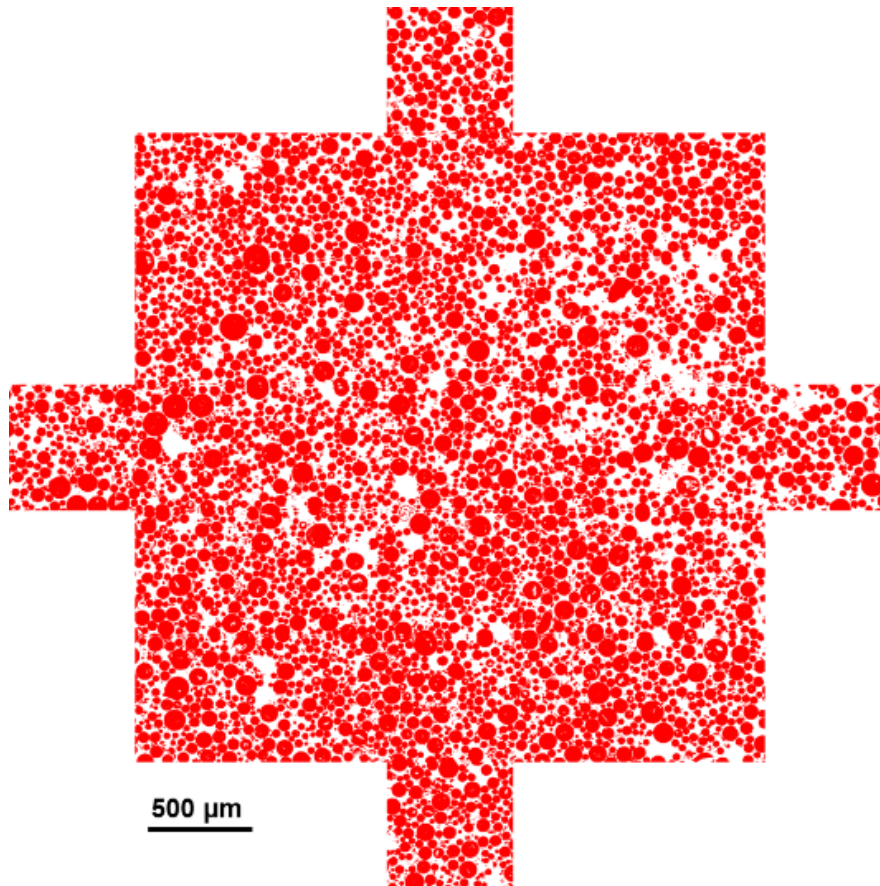


Figure 4.10 Full MLA compositional analysis of flame-spheroidised magnetite ($\leq 45 \mu\text{m}$ starting powder), following sieving and sectioning, demonstrating very high levels of compositional homogeneity.

Having noted the uniform composition of flame spheroidised microspheres, the following section describes, in more detail, the elemental distribution of the products, as assessed using EDS.

4.3.4.2 Energy-dispersive X-ray analysis

Figure 4.11 presents an EDS analysis performed on the sectioned, dense, Fe_3O_4 microspheres, confirming the elemental distribution of the products. Elemental quantification was returned as: $\text{Fe} - 75.95 \pm 0.38 \text{ wt}\%$ and $\text{O} - 24.05 \pm 0.38 \text{ wt}\%$. (Pure magnetite $\text{Fe} - 72.4 \text{ wt}\%$ and $\text{O} - 27.6 \text{ wt}\%$, webmineral.com).

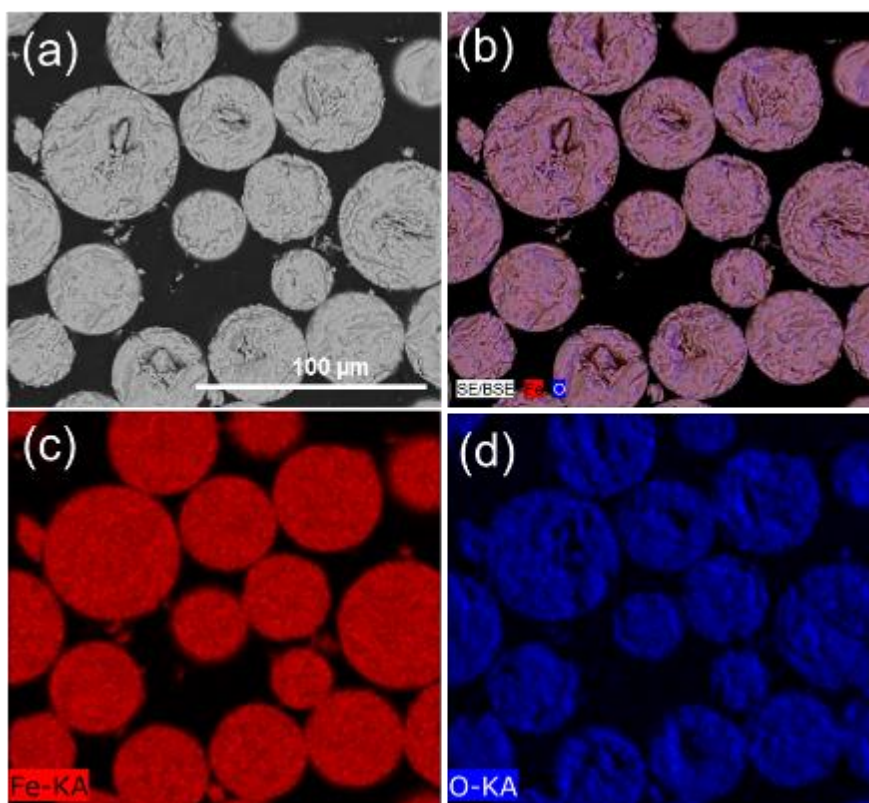


Figure 4.11. (a) BSE image, and (b-d) associated EDS elemental maps for flame-spheroidised Fe_3O_4 microspheres ($\leq 45 \mu\text{m}$ starting powder), following sectioning, illustrating elemental distributions for (b) Fe and O (c) Fe, and (d) O.

Having characterised the Fe_3O_4 starting powders ($\leq 45 \mu\text{m}$) and their products as a consequence of rapid flame-spheroidisation ($\sim 3100^\circ\text{C}$) and comparatively slow rate of heating ($10^\circ\text{C min}^{-1}$ up to 1050°C), it was evident that rate of heating has a significant effect on the product structural and magnetic properties. The flame spheroidised microspheres retained strong magnetisation and an Fe_3O_4 crystalline structure, as distinct from the slow heating of Fe_3O_4 feedstock powders where magnetic properties were degraded as a consequence of Fe_2O_3 formation. The next section investigates the development of Fe_3O_4 porous microspheres, as a function of precursor-to-porogen mass ratios and gas flow settings.

4.4 Fe₃O₄ porous microspheres

4.4.1 Effect of mass ratio

This section describes the effect of CaCO₃ incorporation into the magnetite powders on porosity development. Three different precursor-to-porogen mass ratios, *i.e.* Fe₃O₄:CaCO₃, 3:1, 1:1, and 1:3, were prepared and processed *via* the flame spheroidisation technique. Figure 4.12 summarises the processing steps followed for the manufacture of magnetic microspheres with differing levels of calcium and porosity.

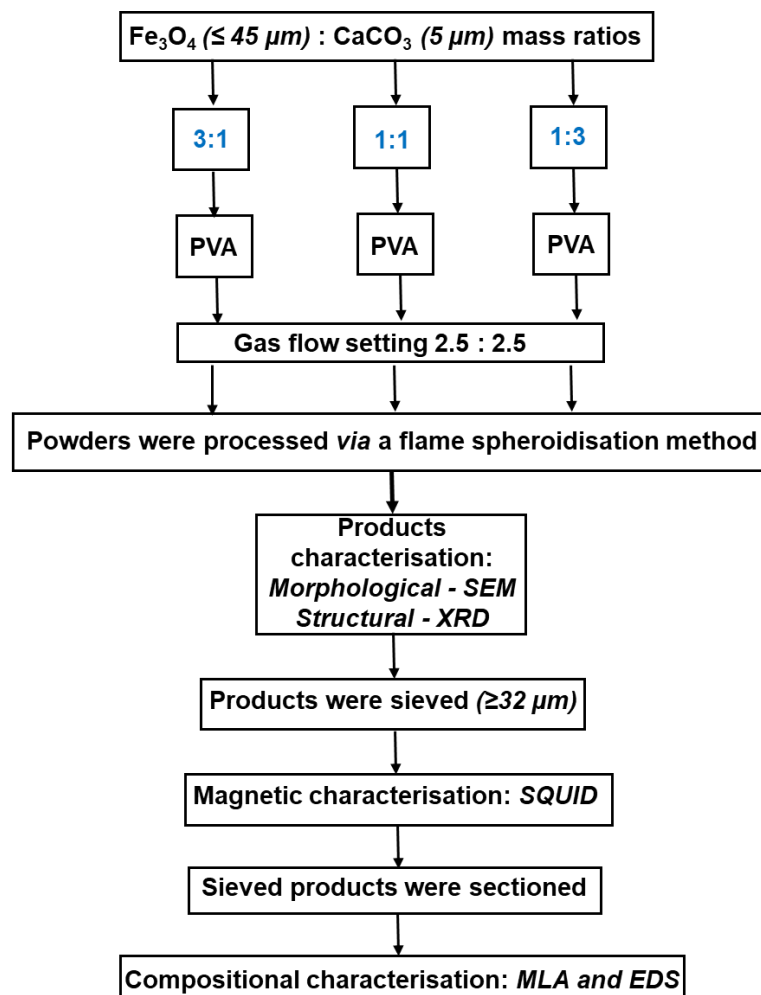


Figure 4.12 Flow diagram summarising the processing steps followed for the manufacture of porous microspheres, as a function of Fe₃O₄:CaCO₃ mass ratio.

The data showed significant differences across the sample products in terms of composition, structure and magnetic expression, directly related to the excess / deficit of iron or calcium incorporated into the microspheres. Surface morphology differences, in regards of shape and size, were noted among manufactured $\text{Fe}_3\text{O}_4:\text{CaCO}_3$ (3:1, 1:1, and 1:3 mass ratios) microspheres, as shown in the following section.

4.4.1.1 Microsphere topography (*unsieved*)

Figures 4.13(a-c) present low magnification SE images of flame-spheroidised $\text{Fe}_3\text{O}_4:\text{CaCO}_3$ (*unsieved*), using starting $\leq 45 \mu\text{m}$ sized magnetite particles, and magnetite to porogen mass ratios of (a) 3:1, (b) 1:1 and (c) 1:3, all samples at a gas flow setting 2.5:2.5.

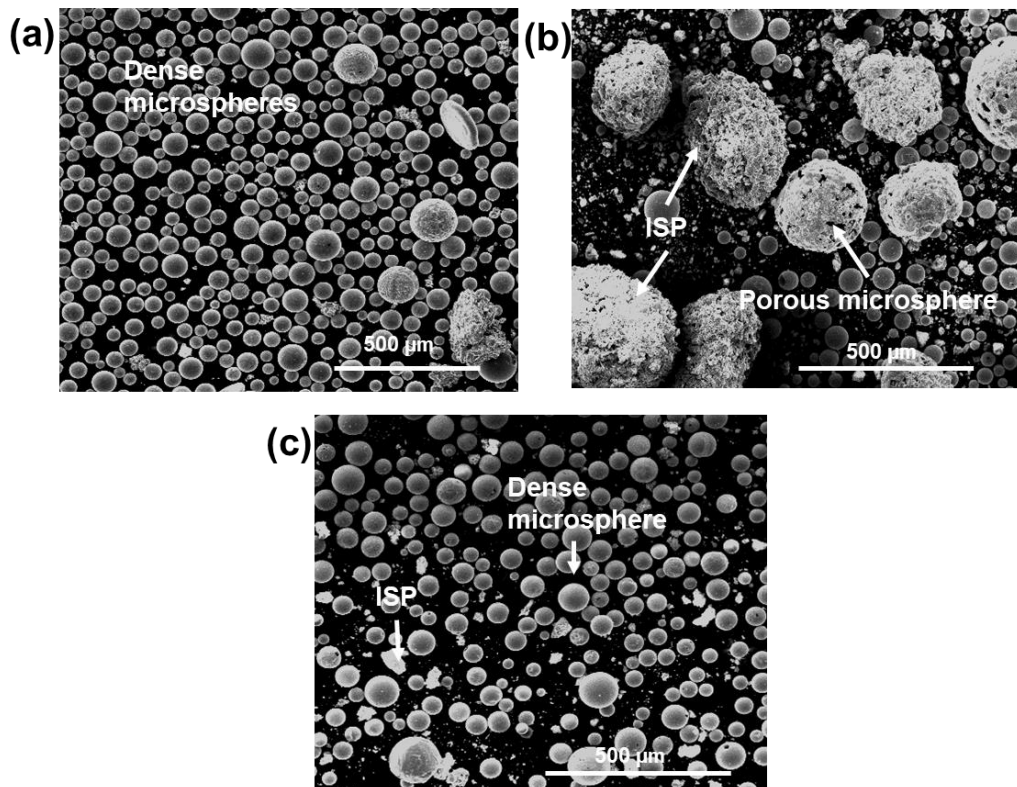


Figure 4.13. SE images of flame-spheroidised $\text{Fe}_3\text{O}_4:\text{CaCO}_3$, using starting $\leq 45 \mu\text{m}$ magnetite particles. Mass ratios: **(a)** 3:1, **(b)** 1:1 and **(c)** 1:3. (*Unsieved*). (ISP: irregular shaped particles)

Table 4.6 Flame-spheroidised reaction product size range (dense microspheres, irregular shaped particles & porous microspheres), as a function of magnetite to porogen mass ratio.

Mass ratio $\text{Fe}_3\text{O}_4:\text{CaCO}_3$	Dense microspheres / μm	ISP / μm	Microspheres with surface porosity / μm
3:1	35 - 180	90 - 260	no
1:1	40 - 130	230 - 360	230 - 290
1:3	30 - 180	30 - 115	no

As summarised in Table 4.6, a 1:1 mass ratio produced a mixture of dense microspheres and irregular-shaped particles (ISP), along with larger microspheres showing clear evidence of porosity (Figure 4.13b). A 3:1 mass ratio created a high yield of dense microspheres with very few irregular-shaped particles (Figure 4.13a), whilst a 1:3 mass ratio produced a similar yield of smaller dense microspheres and few irregular-shaped particles (Figure 4.13c).

4.4.1.2 Structural characterisation (*unsieved microspheres*)

XRD investigations were performed to appraise the structural integrity of these (unsieved) reaction products, as a function of the flame-processing conditions. Figure 4.14 presents XRD patterns for unsieved flame-spheroidised products, formed from $\leq 45 \mu\text{m}$ magnetite precursor particles, for porogen mass ratios of 3:1, 1:1 and 1:3; corresponding to the sample sets imaged in Figures 4.13(a-c). Structural analyses confirmed the presence of varying proportions of $\text{Ca}_2\text{Fe}_2\text{O}_5$ (srebrodolskite) (ICDD PDF no. 00-047-1744), Fe_3O_4 (magnetite) (ICDD PDF no. 01-087-0244), Fe_2O_3 (hematite) (ICDD PDF 00-033-0664) and CaCO_3 (calcium carbonate) (ICDD PDF no. 00-047-1743).

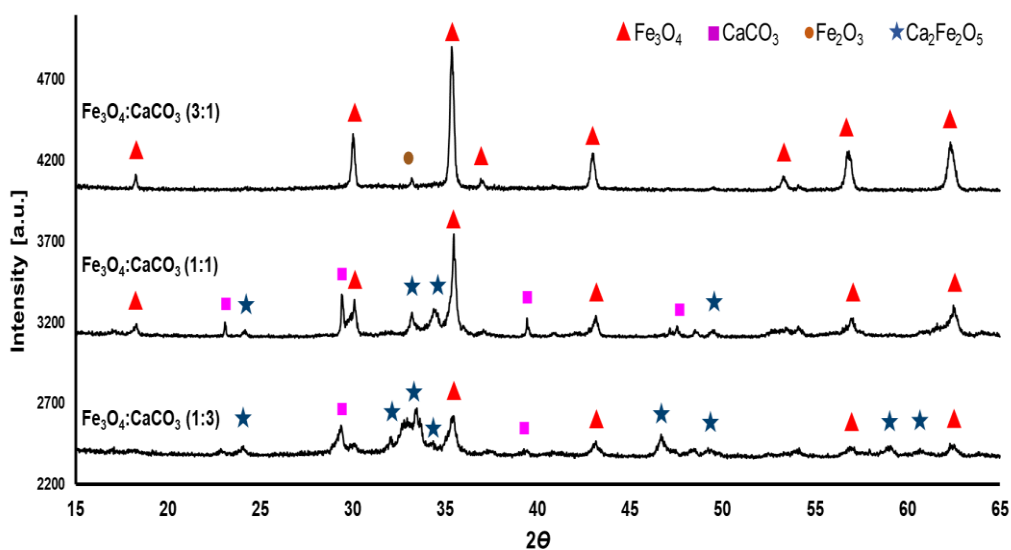


Figure 4.14. XRD patterns for flame-spheroidised $Fe_3O_4:CaCO_3$ (mass ratios 3:1, 1:1 and 1:3), processed using large $\leq 45 \mu m$ magnetite powder.

As summarised in Table 4.7, a mass ratio of 1:1 produced a strong signature for Fe_3O_4 , with medium signatures for $Ca_2Fe_2O_5$ and $CaCO_3$. A mass ratio of 3:1 (Fe_3O_4 rich) revealed a strong Fe_3O_4 signature, with a weak presence for Fe_2O_3 ; whereas a mass ratio of 1:3 ($CaCO_3$ rich) showed medium signatures for $Ca_2Fe_2O_5$ and Fe_3O_4 , and a weak signature for $CaCO_3$.

Table 4.7. Summary of the relative proportion of products, as a function of magnetite to porogen mass ratio.

Mass ratio $Fe_3O_4:CaCO_3$	Microsphere products (strong / medium / weak)			
	Fe_3O_4	Fe_2O_3	$Ca_2Fe_2O_5$	$CaCO_3$
3:1	s	w	-	-
1:1	s	-	m	m
1:3	m	-	m	w

In particular, the progression towards higher porogen content (mass ratio from 3:1 to 1:3) was associated with a reduction in magnetite (Fe_3O_4) and hematite (Fe_2O_3) peak intensities and a consolidation of intensities attributable to *srebrodolskite* ($\text{Ca}_2\text{Fe}_2\text{O}_5$) and CaCO_3 . For magnetic investigations, the Fe_3O_4 : CaCO_3 microsphere products were sieved in order to remove excess un-reacted porogen and magnetite precursor powders.

4.4.1.3 Magnetic characterisation (*sieved*)

Magnetisation measurements revealed information on the magnetic properties of flame-processed microspheres and clarified the effect of Fe_3O_4 : CaCO_3 mass ratio on product magnetic expression. Figure 4.15 shows hysteresis loops for flame-spheroidised products produce with magnetite precursor to porogen mass ratios of 3:1, 1:1 and 1:3. As summarised in Table 4.8, large magnetite powders processed with a 3:1 porogen mass ratio showed the highest magnetisation saturation value. Interestingly, the progression towards increased porogen content (mass ratio from 3:1 to 1:3) showed a decrease in magnetisation values.

Table 4.8. Magnetisation, remanent magnetisation and coercive field values of flame-spheroidised Fe_3O_4 : CaCO_3 , as a function of mass ratio.

Mass ratio Fe_3O_4 : CaCO_3	Magnetic saturation	Remanent magnetisation	Coercive Field / H_c	
	Am^2/kg (emu/g)	Am^2/kg (emu/g)	(kA/m)	(Oe)
3:1	95.1	3.0	3.8	47.9
1:1	38.4	2.6	6.8	87.5
1:3	14.6	1.0	7.2	89.8

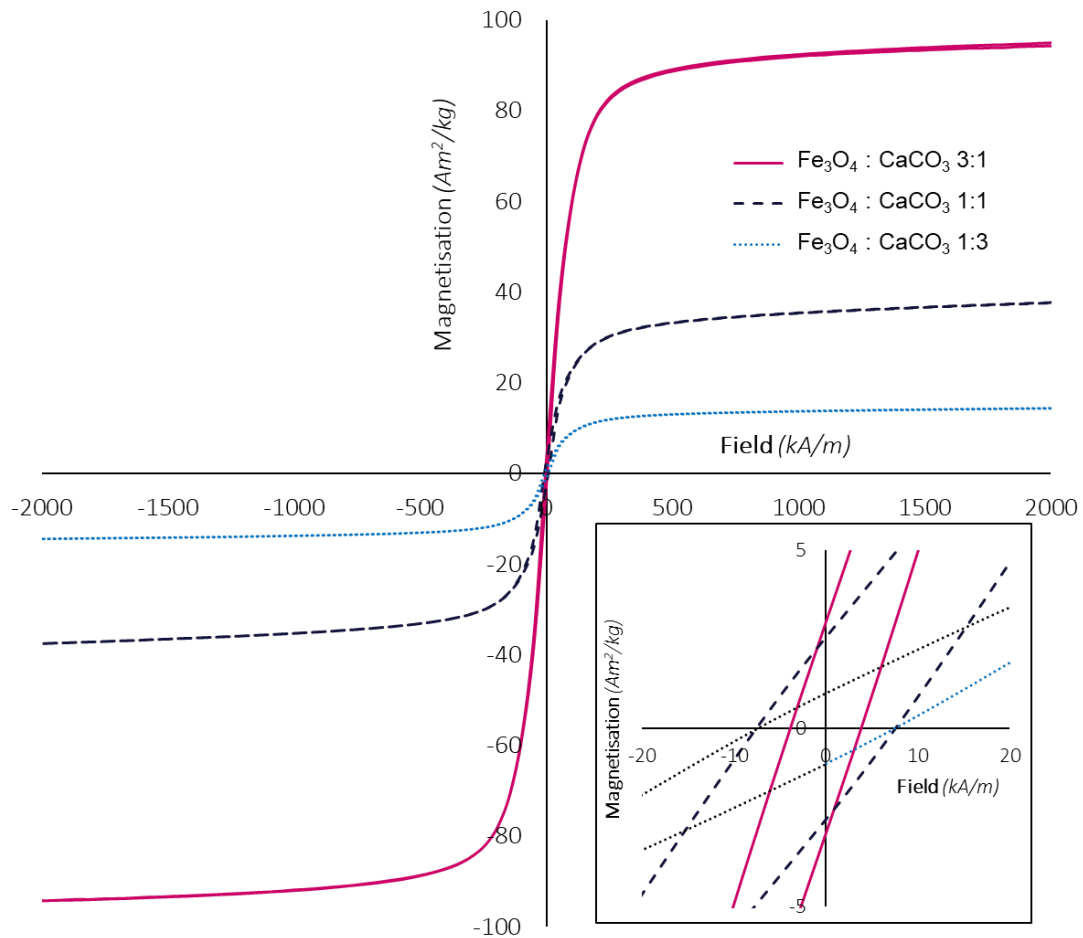


Figure 4.15. Hysteresis loop measurements of flame spheroidised products obtained using $\text{Fe}_3\text{O}_4:\text{CaCO}_3$ mass ratios 3:1, 1:1 and 1:3, at 26.85°C . Inset figure provides evidence for microsphere remanent magnetisation.

The next section presents details of the chemical characterisation of the microspheres, as a function of magnetite-to-porogen mass ratio, following sectioning and polishing.

4.4.1.4 Compositional analysis (*sieved and sectioned*)

4.4.1.4.1 Mineral liberation analysis

Correlated BSE imaging and MLA analyses revealed fine details of the microsphere morphologies and helped clarify their dependencies on the magnetite-to-

porogen mass ratios. Figure 4.16 presents BSE images and mineral mapping analyses for **sieved**, resin embedded and cross-sectioned microsphere samples, prepared using $\leq 45 \mu\text{m}$ magnetite precursor particles; again, corresponding to the sample sets presented in Figure 4.13. As highlighted in Table 4.9, compositional differences, as returned using MLA, were evident across the sample set, with a strong trend towards the development of banded calcium iron oxide (CFO) compositions.

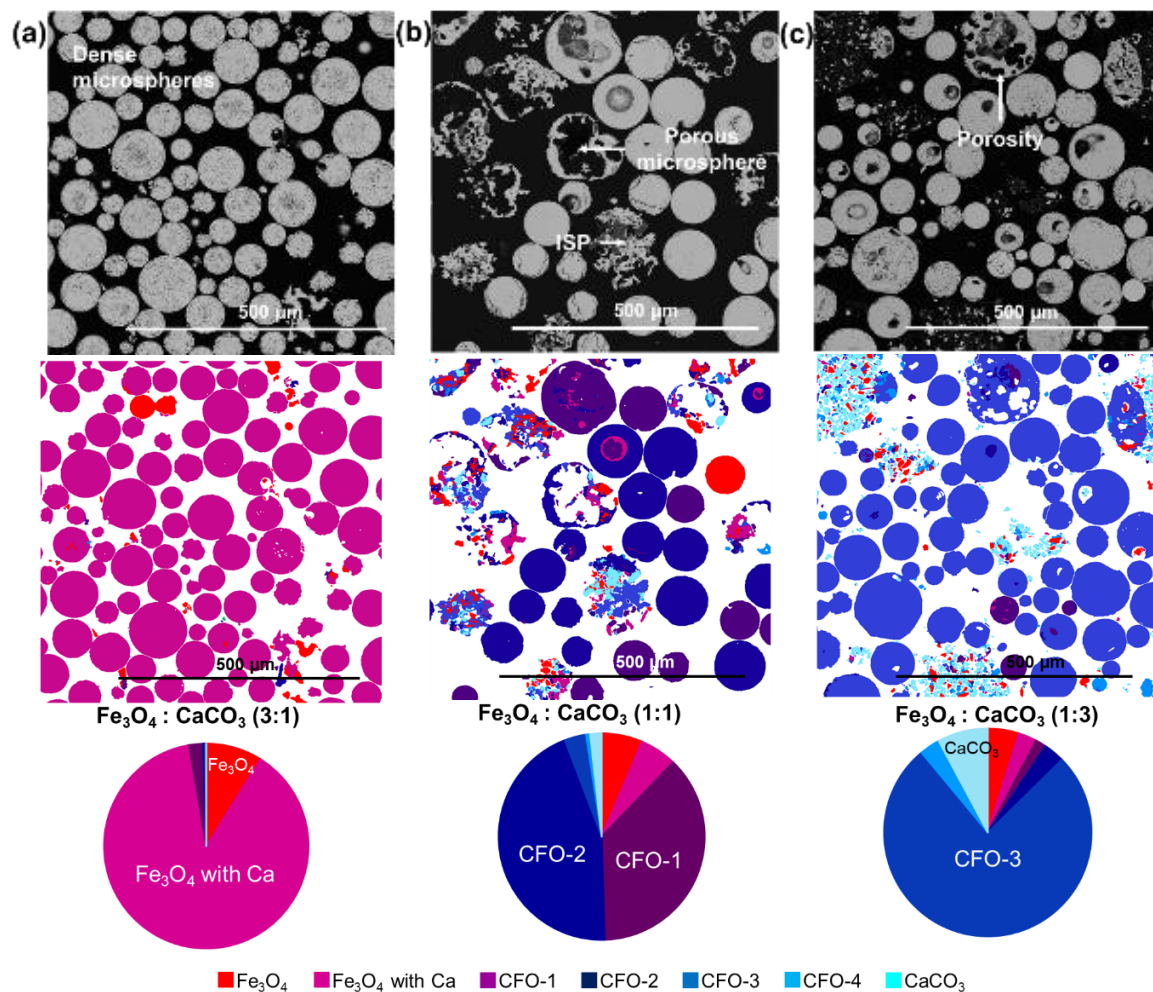


Figure 4.16. BSE images, MLA compositional analyses and charts showing mineral proportions (wt%) of flame-spheroidised $\text{Fe}_3\text{O}_4:\text{CaCO}_3$ using $\leq 45 \mu\text{m}$ magnetite particles: **(a)** 3:1, **(b)** 1:1, and **(c)** 1:3, following sieving and sectioning, illustrating the developed microspheres, particles and associated minerals obtained. (ISP: irregular shaped particles; CFO: calcium iron oxide)

Table 4.9 Mineral proportion (wt%) of flame-spheroidised products, as a function of precursor to porogen mass ratio.

Mass ratio Fe ₃ O ₄ :CaCO ₃	Fe ₃ O ₄ / wt%	Fe ₃ O ₄ with Ca / wt%	CFO-1 / wt%	CFO-2 / wt%	CFO-3 / wt%	CFO-4 / wt%	CaCO ₃ / wt%	Number of particles analysed
3:1	8.9	88.4	2.2	0.3	0.2	0.0	0.0	6,157
1:1	6.4	5.8	37.3	44.6	3.4	0.6	1.8	8,327
1:3	4.8	2.9	1.7	3.2	76.3	3.2	7.9	35,626

Associated molar concentrations and mineral references data, and colour codes (as a function of Fe/Ca excess/deficit) are summarised in Figure 4.17 and Table 4.10, respectively.



Figure 4.17. Mineral colour code as a function of Fe/Ca excess/deficit

Table 4.10 Molar concentrations and mineral references (weight percentage).

Mineral	Molar constituents (wt%)		Mineral reference (wt%)			
	CaO	Fe ₂ O ₃	Ca	Fe	O	C
Fe ₃ O ₄	N/A	N/A	0	72.4	27.6	0
Fe ₃ O ₄ with Ca	12	88	3.6	73.8	22.6	0
CFO-1	28.5	71.5	9.6	67.3	23.1	0
CFO-2	40.7	59.3	15.1	61.3	23.6	0
CFO-3	48.3	51.7	19.1	57	23.9	0
CFO-4	82.4	17.6	48.4	28.9	22.6	0
CaCO ₃	N/A	N/A	40	0	48	12

Figures 4.16(a-c) present BSE images and MLA analyses of **sieved**, resin embedded and sectioned, flame-spheroidised products formed from large magnetite precursors ($\leq 45 \mu\text{m}$). A 1:1 mass ratio (Figures 4.16b, 4.18, and Table 4.11) revealed a mixture of two dominant CFO levels (denominated as CFO-1 and CFO-2, Table 4.9) throughout the flame-spheroidised products, comprising dense and porous microspheres. Interestingly, the porous microspheres revealed more than one mineral (non-uniform), distinct from the dense microspheres (uniform). Comparatively, the porogen-rich sample (1:3 mass ratio, Figures 4.16c, 4.19, and Table 4.12) developed a more uniform sample composition with a high concentration of CFO-3 (Table 4.9), with a mixture of dense microspheres and, interestingly, a few microspheres with tentative signs of porosity (not visible on the surface), and residual (unreacted) porogen. In contrast, precursor-rich products (mass ratio of 3:1, Figures 4.16a, 4.20, and Table 4.13) showed a strong yield of dense microspheres with highly uniform composition (Fe_3O_4 with Ca, Table 4.9), and some residual large magnetite powder ($\leq 45 \mu\text{m}$).

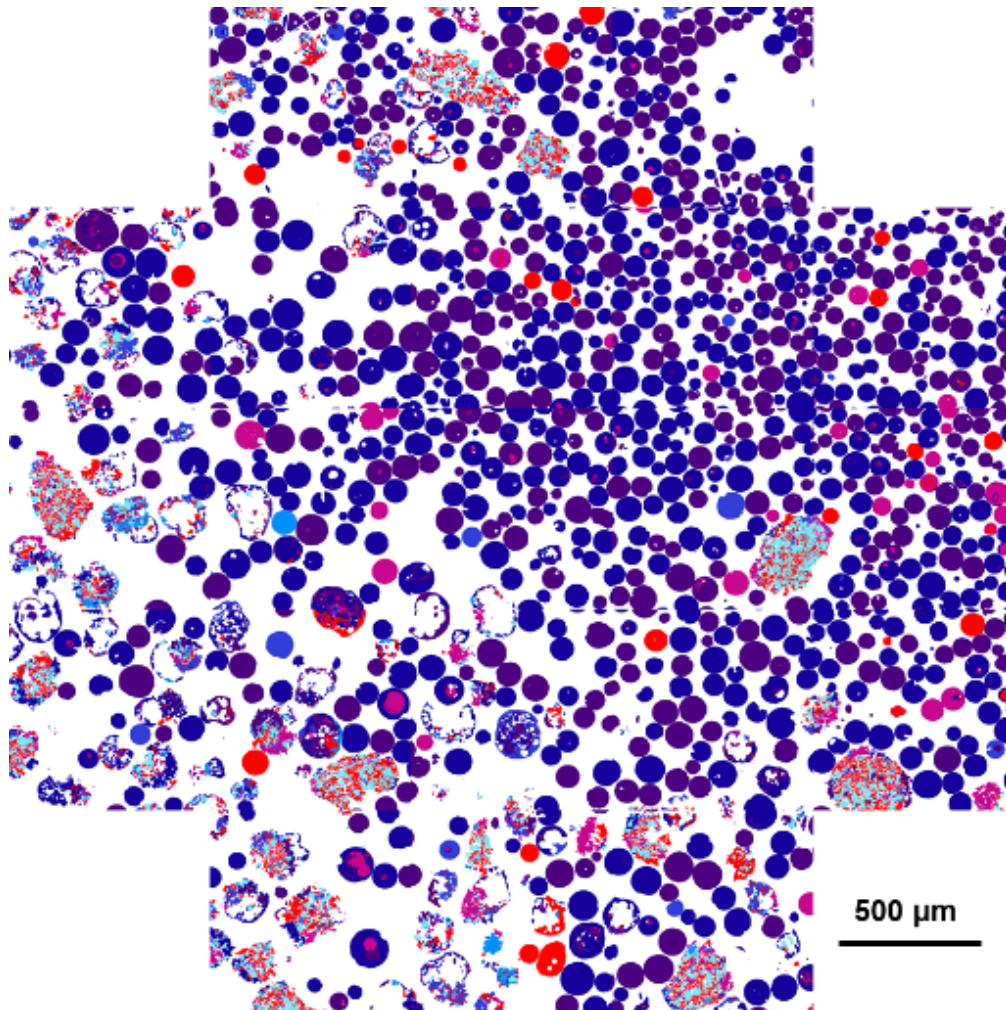
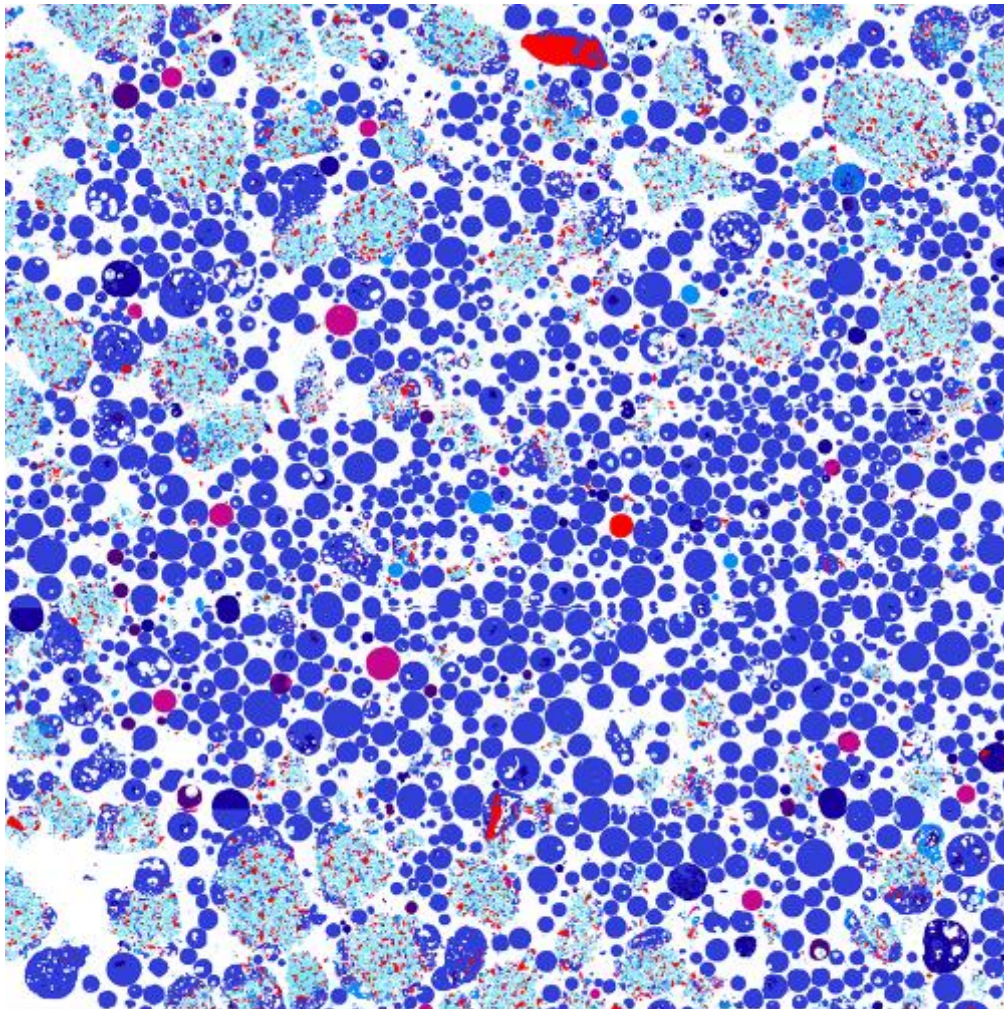


Figure 4.18. Full MLA compositional analysis of flame-spheroidised $\text{Fe}_3\text{O}_4:\text{CaCO}_3$ (mass ratio 1:1), following sieving and sectioning, demonstrating high levels of CFO-1 and CFO-2.

Table 4.11 Modal mineralogy for flame spheroidised- $\text{Fe}_3\text{O}_4:\text{CaCO}_3$ (mass ratio 1:1).

Mineral	Particles	Weight %
Magnetite (Fe_3O_4)	2129	6.4
Magnetite with Ca	1313	5.8
CFO-1	1455	37.3
CFO-2	1407	44.6
CFO-3	729	3.4
CFO-4	435	0.6
CaCO_3	859	1.8



500 μm

Figure 4.19. Full MLA compositional analysis of flame-spheroidised $\text{Fe}_3\text{O}_4:\text{CaCO}_3$ (mass ratio 1:3, **CaCO₃ rich**), following sieving and sectioning, demonstrating high levels of CFO-3.

Table 4.12 Modal mineralogy for flame spheroidised- $\text{Fe}_3\text{O}_4:\text{CaCO}_3$ (mass ratio 1:3).

Mineral	Particles	Weight %
Magnetite (Fe_3O_4)	3681	4.8
Magnetite with Ca	4489	2.9
CFO-1	2907	1.7
CFO-2	1728	3.2
CFO-3	5533	76.3
CFO-4	4281	3.2
CaCO₃	13006	7.9

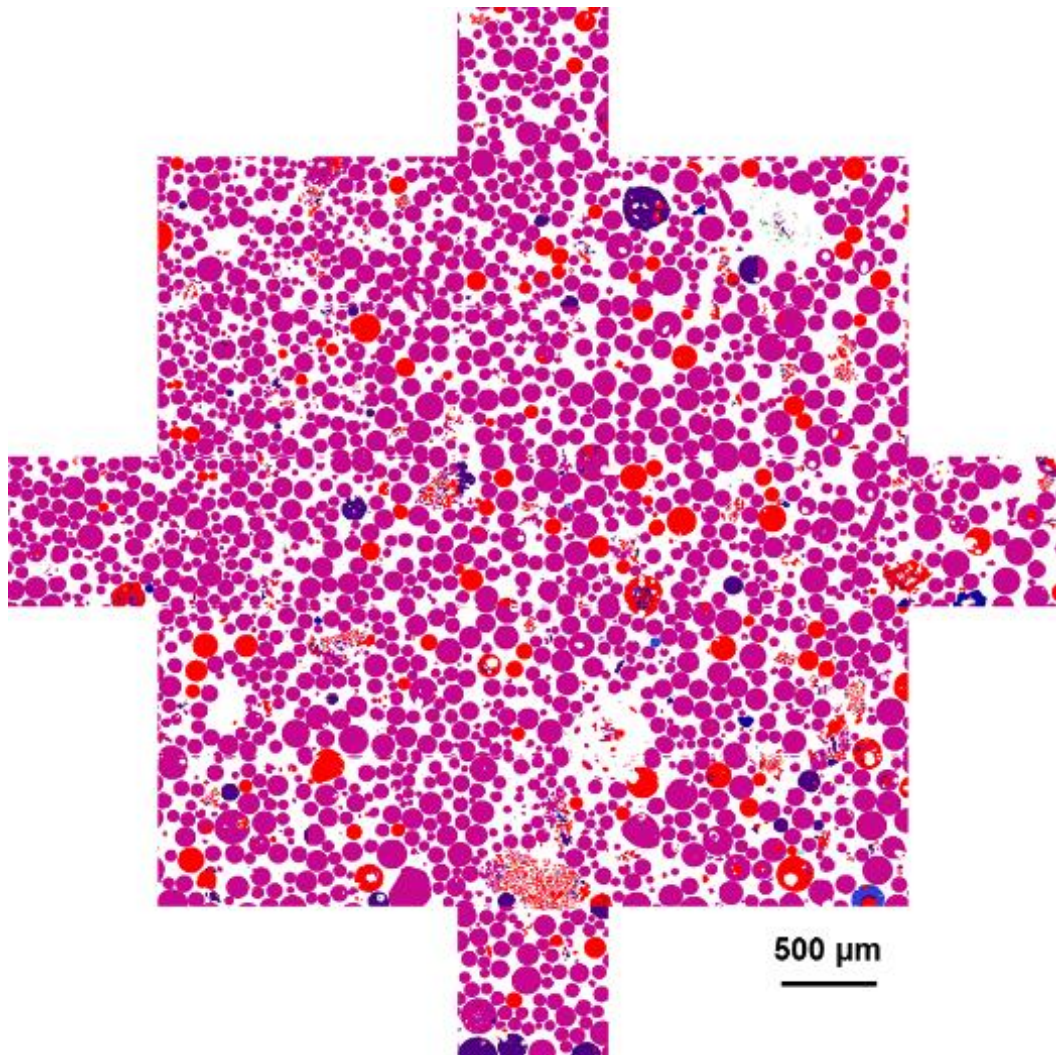


Figure 4.20. Full MLA compositional analysis of flame spheroidised $Fe_3O_4:CaCO_3$ (mass ratio 3:1, **Fe_3O_4 rich**), following sieving and sectioning, demonstrating high levels of Fe_3O_4 with Ca.

Table 4.13 Modal mineralogy for flame spheroidised- $Fe_3O_4:CaCO_3$ (mass ratio 3:1).

Mineral	Particles	Weight %
Magnetite (Fe_3O_4)	2115	8.9
Magnetite with Ca	3185	88.4
CFO-1	520	2.2
CFO-2	124	0.3
CFO-3	151	0.2
CFO-4	34	0.0
CaCO₃	28	0.0

In particular, it is noted that progressive increment of porogen content (*magnetite to porogen mass ratio from 3:1 to 1:3*) consistently resulted in elevated levels of Ca and lower levels of Fe throughout these microsphere products. In the following section, elemental mappings confirming Fe/Ca distributions within the magnetic microspheres, as a function of precursor-to-porogen mass ratio, are presented.

4.4.1.4.2 Energy dispersive X-ray analyses

Complementary energy dispersive X-ray analysis investigations were performed to appraise the Fe/Ca elemental distribution among the $\text{Fe}_3\text{O}_4:\text{CaCO}_3$ microsphere samples (mass ratios 3:1, 1:1 and 1:3). Figure 4.21 presents cross-sectioned, BSE images and elemental maps for the $\text{Fe}_3\text{O}_4:\text{CaCO}_3$ mass ratio 1:1 microsphere specimen. Table 4.14 summarises the molar concentrations (CaO and Fe_2O_3) of the products. The porous microsphere of Figure 4.16b also indicated the Fe / Ca concentration variabilities.

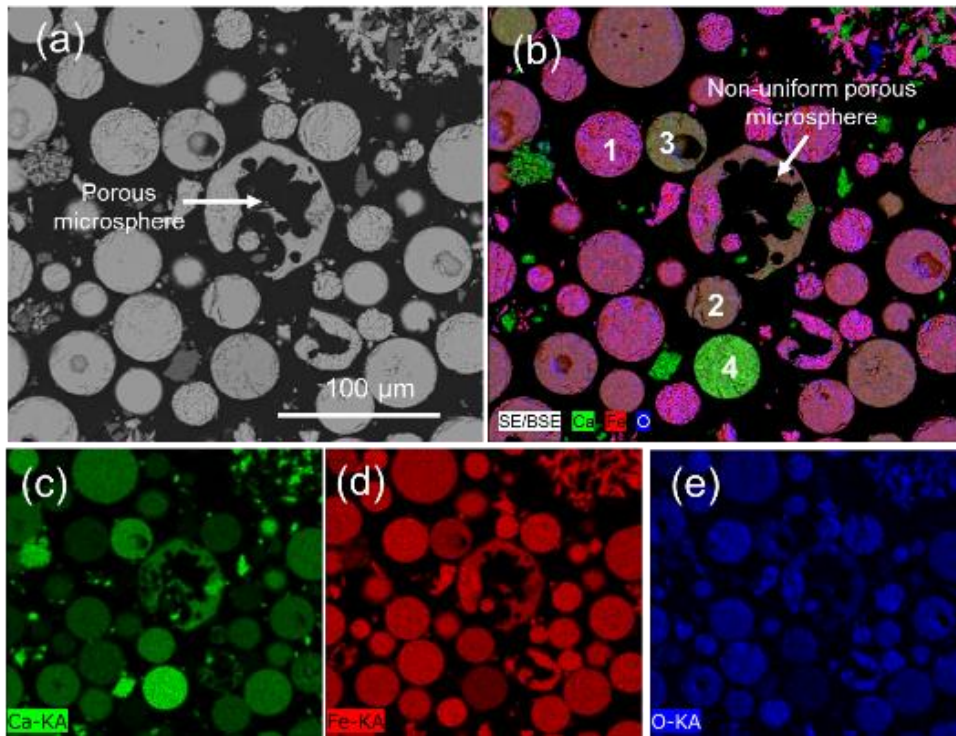


Figure 4.21. (a) BSE image and (b) elemental maps showing (c) calcium, (d) iron, and (e) oxygen for $Fe_3O_4:CaCO_3$ microspheres (mass ratio 1:1), following sieving and sectioning, illustrating porous and dense microspheres, comprising a mixture of Fe / Ca compositions.

Table 4.14. Weight percentage constituents and suggested equilibrium phases for $Fe_3O_4:CaCO_3$ microspheres (mass ratio 1:1).

Number	Name	CaO wt%	Fe_2O_3 wt%	Equilibrium phases
1	Fe excess	27.0 ± 8.4	73.0 ± 8.4	$Ca_2Fe_2O_5 + CaFe_2O_4$
2	Fe rich	48.7 ± 4.6	51.3 ± 4.6	CaO + $Ca_2Fe_2O_5$
3	Ca rich	58.9 ± 0.8	41.1 ± 0.8	CaO + $Ca_2Fe_2O_5$
4	Ca excess	71.2 ± 7.8	28.8 ± 7.8	CaO + $Ca_2Fe_2O_5$

For the case of **porogen-rich** samples, $\text{Fe}_3\text{O}_4:\text{CaCO}_3$ mass ratio 1:3 (Figure 4.22), BSE and elemental maps showed evidence for both, dense and porous, highly uniform microspheres. Despite the presence of few un-reacted, magnetite particles embedded within porous microspheres (Figure 4.22b), this sample provided higher-levels of compositional uniformity when compared to the mass ratio 1:1 sample. As summarised in Table 4.15, the sample comprises un-reacted magnetite and porogen powders and reacted “Ca rich” regions.

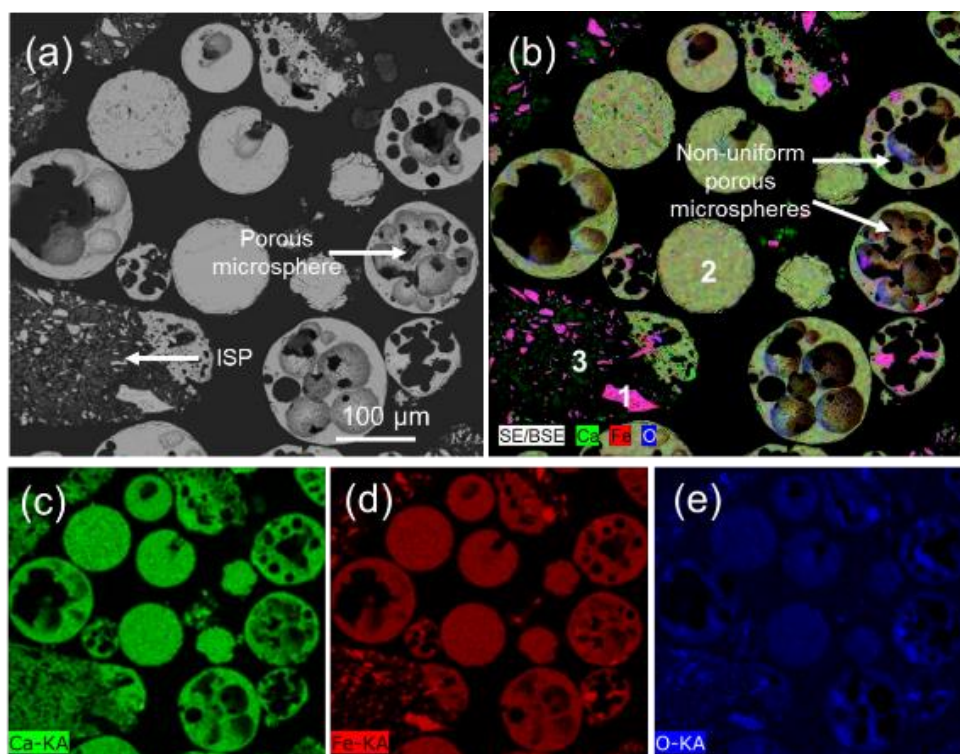


Figure 4.22. (a) BSE image and (b) elemental maps showing (c) calcium, (d) iron, and (e) oxygen of $\text{Fe}_3\text{O}_4:\text{CaCO}_3$ microspheres (mass ratio 1:3; CaCO_3 rich), following sieving and sectioning. (ISP: irregular shaped particle)

Table 4.15. Weight percentage constituents and suggested equilibrium phases for $\text{Fe}_3\text{O}_4:\text{CaCO}_3$ microspheres (mass ratio 1:3).

Number	Name	CaO wt%	Fe_2O_3 wt%	Equilibrium phases
1	Magnetite	3.4 ± 2.3	96.6 ± 2.3	$\text{Fe}_3\text{O}_4 + \text{Fe}_2\text{O}_3$
2	Ca rich	57.6 ± 4.4	42.4 ± 4.5	$\text{CaO} + \text{Ca}_2\text{Fe}_2\text{O}_5$
3	Porogen	86.3 ± 10.1	13.7 ± 10.1	$\text{CaO} + \text{Ca}_2\text{Fe}_2\text{O}_5$

Figure 4.23 shows BSE and elemental maps of the sectioned *precursor-rich* $\text{Fe}_3\text{O}_4:\text{CaCO}_3$ sample (mass ratio 3:1), indicating improved levels of compositional uniformity (Table 4.16). Interestingly, low levels of calcium (Figure 4.22b, green dots) are observed within the dense magnetite microsphere bodies.

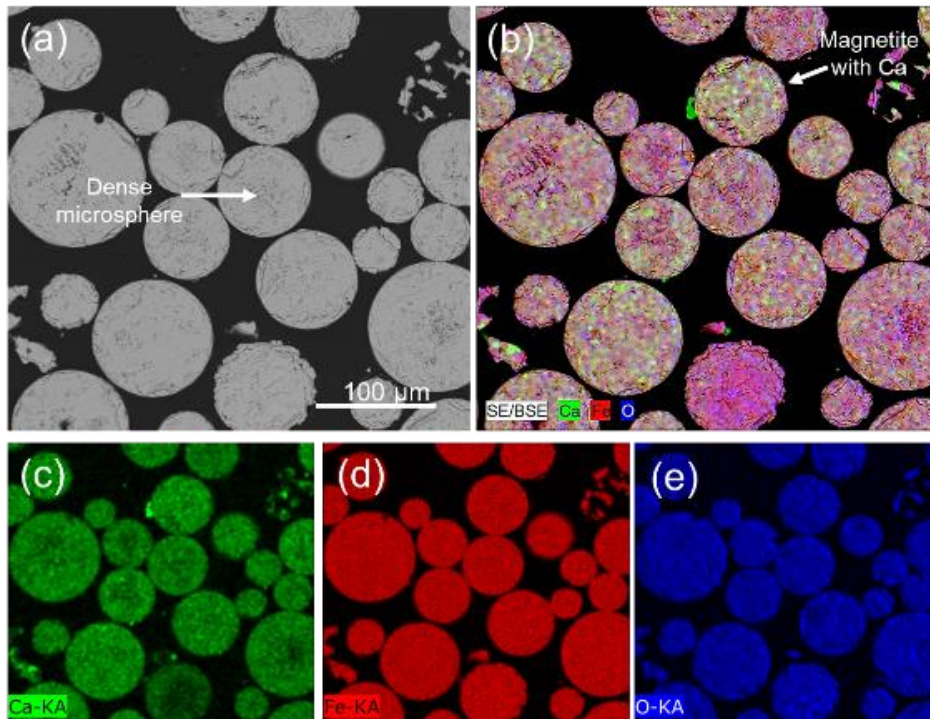


Figure 4.23. (a) BSE image and (b) elemental maps showing (c) calcium, (d) iron, and (e) oxygen in $\text{Fe}_3\text{O}_4:\text{CaCO}_3$ microspheres (mass ratio 3:1; Fe_3O_4 rich), following sieving and sectioning, revealing calcium distributed within the iron oxide microspheres.

Table 4.16. Weight percentage constituents and suggested equilibrium phases for $\text{Fe}_3\text{O}_4:\text{CaCO}_3$ microspheres (mass ratio 3:1).

CaO wt%	Fe_2O_3 wt%	Equilibrium phases
14.0 ± 1.8	85.9 ± 1.8	CaFe_2O_4 + Hematite

Having studied the effect of precursor-to-porogen mass ratio on microsphere properties, the next section is concerned with the effect of gas flow setting (2:2, 2.5:2.5, and 3:3) on porous microsphere formation ($\text{Fe}_3\text{O}_4:\text{CaCO}_3$ mass ratio 1:1).

4.4.2 Effect of gas flow setting

$\text{Fe}_3\text{O}_4:\text{CaCO}_3$ (mass ratio 1:1) microsphere products manufactured using two additional gas flow settings of 2:2 and 3:3 were compared. Figure 4.24 summarises the key steps followed for the manufacture of $\text{Fe}_3\text{O}_4:\text{CaCO}_3$ porous microspheres, as a function of gas flow setting.

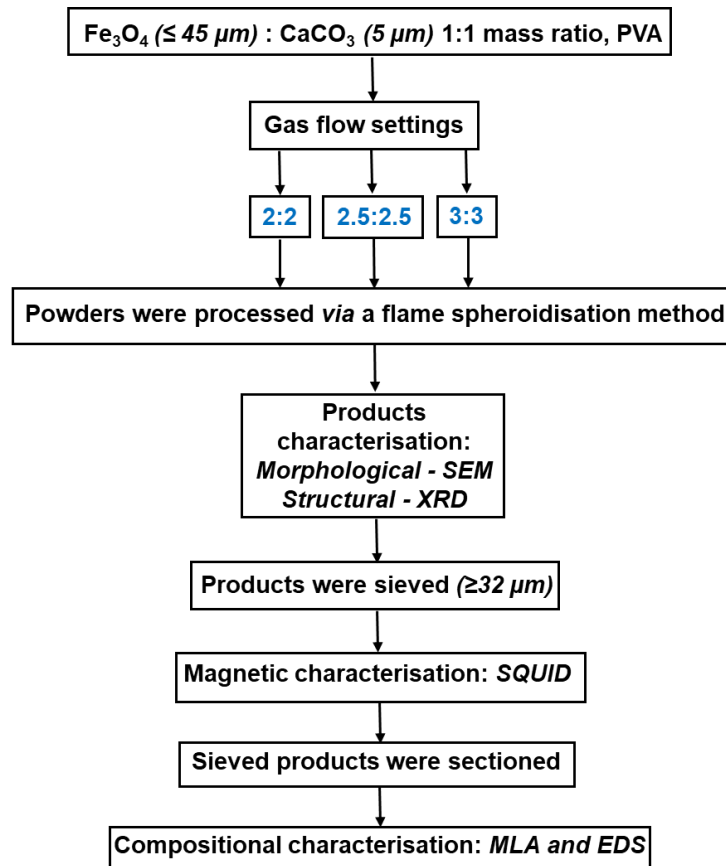


Figure 4.24 Flow diagram summarising the processing steps followed for the manufacture of Fe_3O_4 porous microspheres, as a function of gas flow setting

4.4.2.1 Microsphere topography (*unsieved microspheres*)

Figures 4.25(a,b) show low magnification SE images of flame-spheroidised $Fe_3O_4:CaCO_3$, formed using starting $\leq 45 \mu m$ sized magnetite particles, with gas flow settings of (a) 2:2 and (b) 3:3, respectively. As summarised in Table 4.17, a gas flow setting of 2:2 produced predominantly dense microspheres, with few porous microspheres and irregular particles (Figure 4.25a). A higher gas flow setting 3:3 produced a more consistent yield of porous microspheres, mixed with few smaller dense microspheres and irregular shaped particles (Figure 4.25b). In both cases, for this sample set, there was visible evidence for porosity.

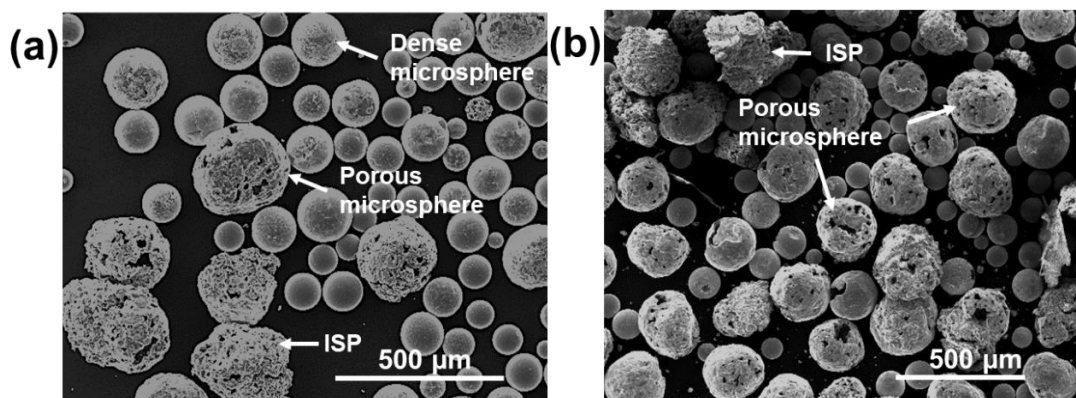


Figure 4.25. SE images of flame-spheroidised $\text{Fe}_3\text{O}_4:\text{CaCO}_3$ (1:1 mass ratio) using starting $\leq 45 \mu\text{m}$ magnetite particles. Gas flow settings: **(a)** 2:2, **(b)** 3:3 (unsieved).

ISP: Irregular shaped particles.

Table 4.17. Size range of flame spheroidised reaction products (dense microspheres, irregular shaped particles and porous microspheres), as a function of gas flow setting.

Mass ratio $\text{Fe}_3\text{O}_4:\text{CaCO}_3$	Gas flow setting / arb. unit.	Dense microspheres / μm	ISP / μm	Microspheres with surface porosity / μm
1:1	2:2	40 - 175	220 - 295	235 - 270
	3:3	60 - 120	180 - 375	190 - 270

4.4.2.2 Compositional analysis (sieved and sectioned)

Mineral analyses revealed fine details of the porous microsphere morphologies and provided supporting evidence for the microsphere formation mechanism. Figure 4.26 shows BSE images and MLA analyses for sieved, resin embedded and cross-sectioned microsphere samples, flame-spheroidised at 2:2 and 3:3 gas flow settings; commensurate with the sample sets presented in Figure 4.25. Mineral mappings highlight porous microspheres. Notably, Fe_3O_4 , CaCO_3 and CFO minerals were

distinct constituents of these porous microspheres. Hence, a formation mechanism distinct from that of dense microspheres is indicated.

As highlighted in Table 4.18, compositional similarities were evident across the sample set, with CFO-1 and CFO-2 as dominant minerals for both cases. Importantly, a 2:2 gas flow setting (Figure 4.27 and Table 4.19) was associated with the highest levels of consumption, as demonstrated by low weight proportions of Fe_3O_4 and CaCO_3 , as compared to gas flow settings of 3:3 (Figure 4.28 and Table 4.20) and 2.5 : 2.5 (Figure 4.18 and Table 4.11).

Table 4.18. Mineral proportion (wt%) of flame-spheroidised products, as a function of gas flow setting.

Gas flow setting / arb. unit.	Fe_3O_4 / wt%	Fe_3O_4 with Ca / wt%	CFO-1 / wt%	CFO-2 / wt%	CFO-3 $\text{Ca}_2\text{Fe}_2\text{O}_5$ / wt%	CFO-4 / wt%	CaCO_3 / wt%	Number particles analysed
2:2	2.5	3.2	44.6	48.4	1	0.1	0.2	3,412
3:3	5.7	5.6	43.7	38.5	4.5	0.5	1.5	13,906

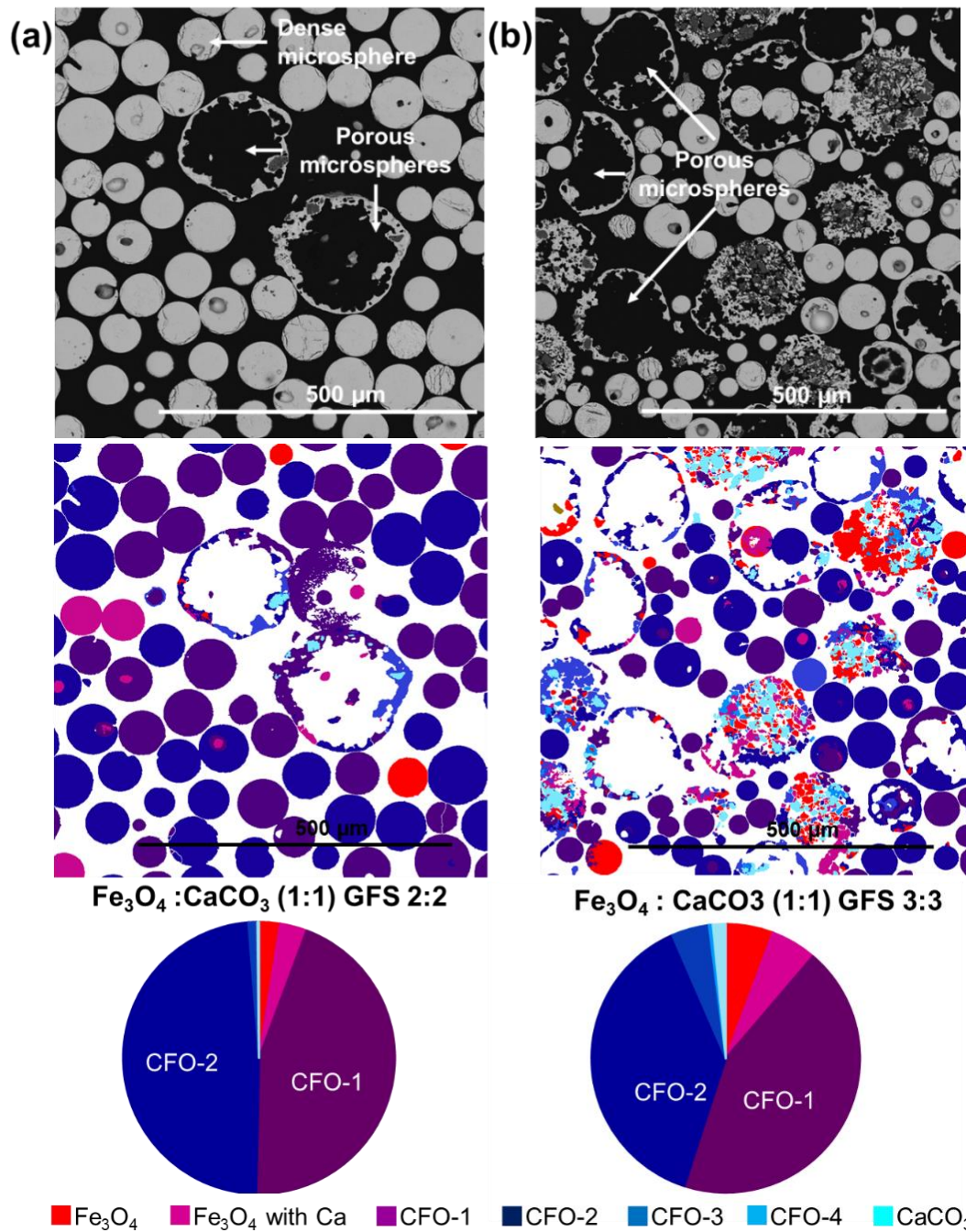


Figure 4.26. BSE images, MLA compositional analysis and associated pie charts showing mineral proportions (weight%) of flame-spheroidised Fe_3O_4 : CaCO_3 microspheres (mass ratio 1:1) prepared using $\leq 45 \mu\text{m}$ magnetite: Gas flow settings (a) 2:2, and (b) 3:3, following sieving and sectioning, illustrating microspheres, particles and minerals obtained. Mineral references shown in Table 4.10.

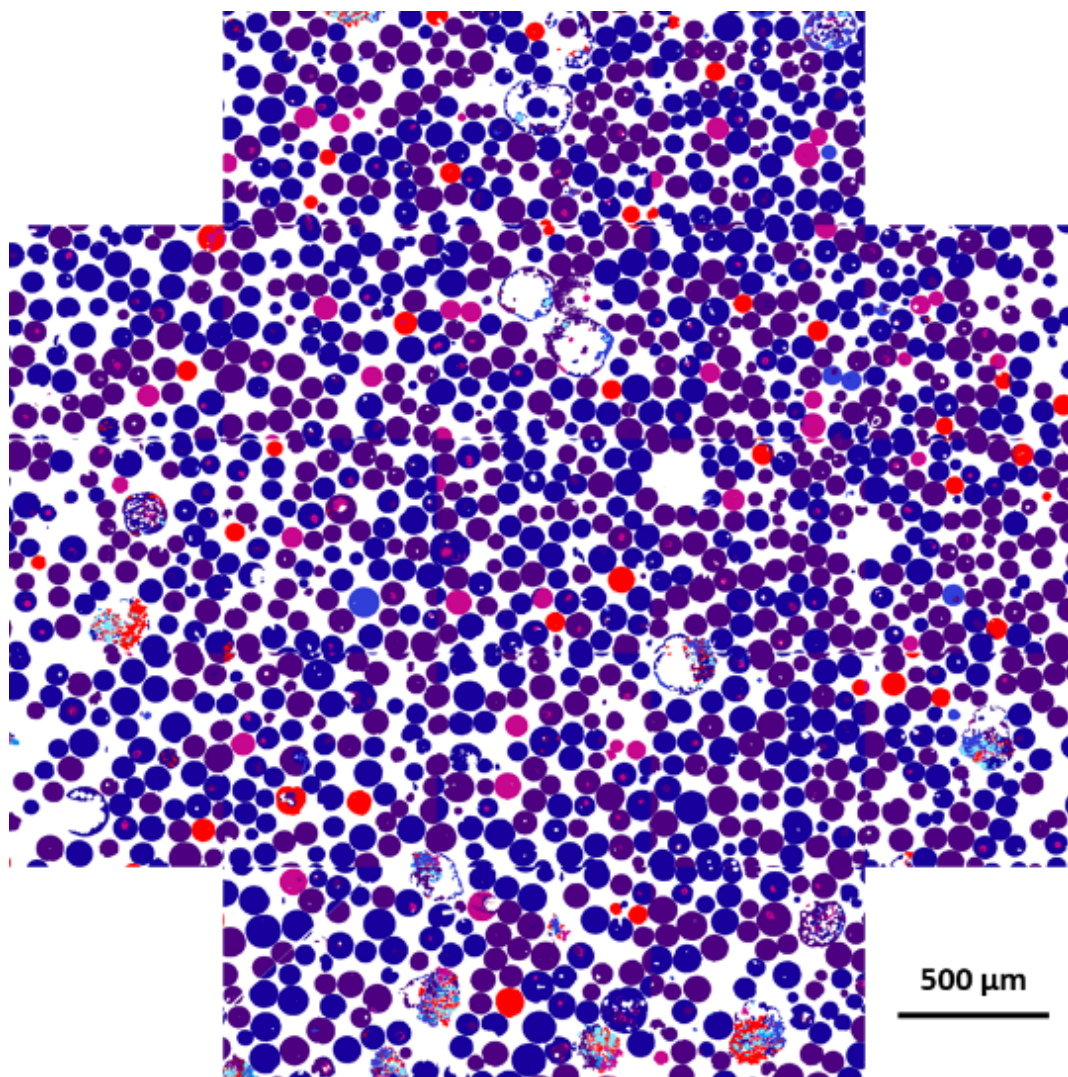


Figure 4.27 Full MLA map for $Fe_3O_4:CaCO_3$ (1:1 mass ratio, 2:2 gas flow setting).

Table 4.19. Modal mineralogy for $Fe_3O_4:CaCO_3$ (1:1 mass ratio, 2:2 gas flow setting).

Mineral	Particles	Weight %
Magnetite (Fe_3O_4)	300	2.5
Fe_3O_4 with Ca	387	3.2
CFO-1	1190	44.6
CFO-2	1126	48.4
CFO-3	211	1.0
CFO-4	77	0.1
$CaCO_3$	121	0.2

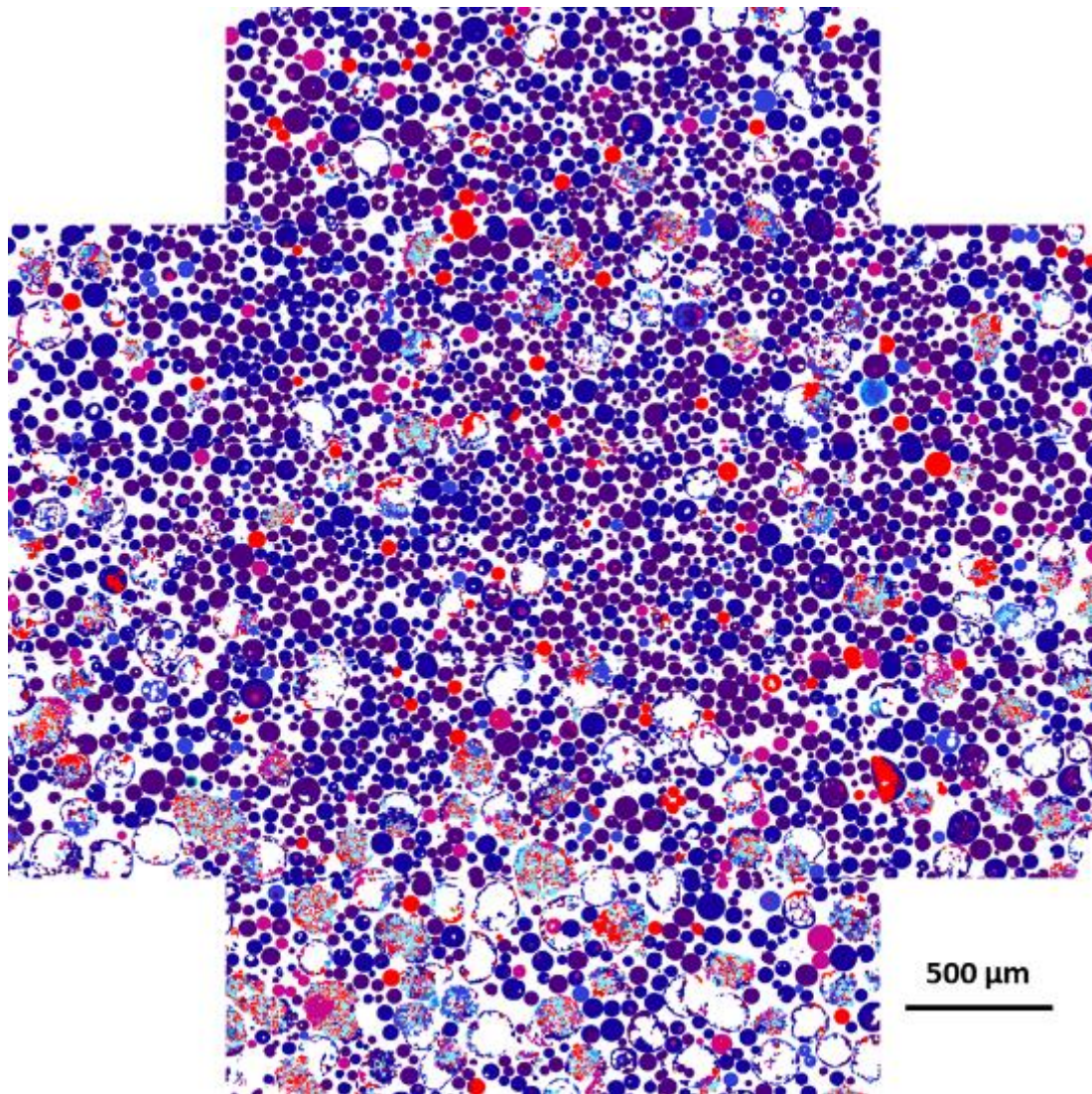


Figure 4.28 Full MLA map for $\text{Fe}_3\text{O}_4:\text{CaCO}_3$ (1:1 mass ratio, 3:3 gas flow setting).

Table 4.20. Modal mineralogy for $\text{Fe}_3\text{O}_4:\text{CaCO}_3$ (1:1 mass ratio, 3:3 gas flow setting).

Mineral	Particles	Weight %
Magnetite (Fe_3O_4)	2931	5.7
Fe_3O_4 with Ca	1840	5.6
CFO-1	3108	43.7
CFO-2	2834	38.5
CFO-3	1321	4.5
CFO-4	592	0.5
CaCO_3	1280	1.5

In summary, the results section of the present Chapter demonstrated the capability of the rapid flame spheroidisation to transform ($\leq 45 \mu\text{m}$) Fe_3O_4 feedstock powders into practical morphologies (*i.e.*, dense Fe_3O_4 microspheres) whilst retaining original ferrimagnetic and compositional properties post-processing. Accordingly, $\text{Fe}_3\text{O}_4:\text{CaCO}_3$ mass ratio combinations led to the formation of $\text{Ca}_2\text{Fe}_2\text{O}_5$ porous microspheres with Fe/Ca excess/deficit and modified ferromagnetic properties. Notably, mineral segregation identified on gas flow setting investigations provided understanding on dynamic evolution of porous products formation whilst flame spheroidised.

4.5 Discussion

4.5.1 Introduction

Magnetic, dense and porous Fe_3O_4 microspheres have been manufactured *via* a rapid, single-stage, flame-spheroidisation method. The novel application of the flame spheroidisation process on ceramic materials (in this case magnetite) enabled the transformation of Fe_3O_4 feedstock powder into Fe_3O_4 dense microspheres with enhanced ferrimagnetic properties, as demonstrated by magnetometry investigations. Further, the flame spheroidisation of $\text{Fe}_3\text{O}_4:\text{CaCO}_3$, as a function of mass ratio and gas flow settings, generated a variety of products in terms of shape (dense microspheres, porous microspheres, irregular shaped particles and mixtures thereof), composition (Fe/Ca excess/deficit) and magnetic properties (the increment in Ca concentration showed a direct effect on the decrease of magnetic saturation). The study of these processing variations has allowed for a comprehensive microsphere formation mechanism to be established.

4.5.2 Formation mechanism of dense microspheres

The suitability of the rapid flame spheroidisation process for the manufacture of Fe_3O_4 dense microspheres, with high levels of compositional uniformity and strong ferrimagnetic expression ($96.3 \text{ Am}^2/\text{kg}$) has been demonstrated. Importantly, flame spheroidisation is a thermal flame spray method, & hence can be classified as a rapid cooling / rapid solidification technology [266]. The formation mechanisms associated with flame spray methods are relevant to explain the development of Fe_3O_4 dense microspheres. The production of microspheres using the flame spheroidisation process has been reported for phosphate [47, 51-53, 237, 241], borate [267], silicate [47, 191, 231, 238] glasses, but remained unexplored for ceramic-based materials until recently [63]. Hence, the application of the flame spheroidisation method for the manufacture of iron oxide-based microspheres is relatively novel. Figure 4.29 schematically illustrates the feeding of precursor Fe_3O_4 powders ($\leq 45 \mu\text{m}$) into a high-temperature oxygen-acetylene flame ($\sim 3100^\circ\text{C}$), where particles rapidly melt and acquire spherical shape, post-flame ejection, due to surface tension and rapid cooling [47, 57, 191, 239, 240, 268, 269].

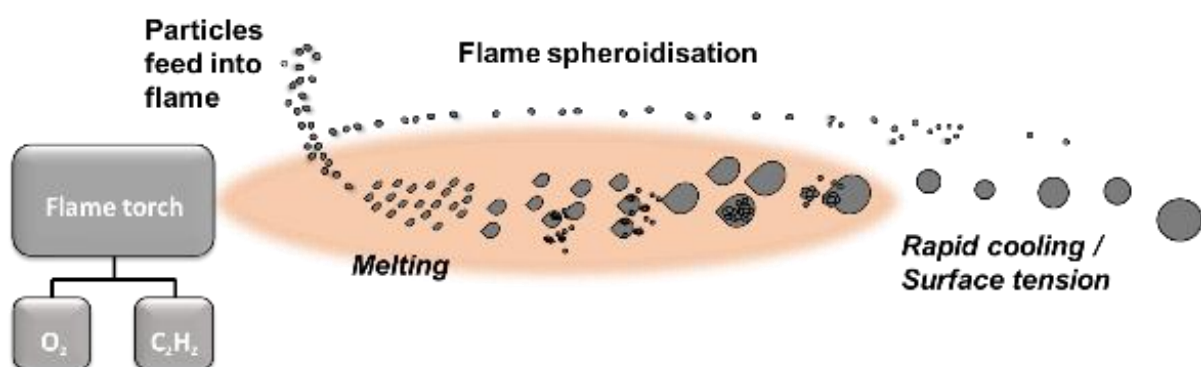


Fig. 4.29. Schematic representation of the flame spheroidisation process for dense Fe_3O_4 microspheres.

To investigate the effect of temperature (noting the caveat of slow heating compared to the rapid, flame spheroidisation process), complementary HT-XRD and HT-SQUID measurements were performed, both with conditions of slowly increasing temperature, to provide insights into the oxidation pathways and magnetic properties of Fe₃O₄ powder (non-spheroidised). HT-XRD revealed a transition of magnetite to hematite between 350°C and 650°C, whilst HT-SQUID showed a progressive decrease in magnetic moment from 25°C to 500°C, with a more significant decrease noted at 600°C. It was interpreted that the Curie point of magnetite was reached between 500°C and 600°C, with the Fe₃O₄ powders losing ferrimagnetic expression [270]. Moreover, the development of Fe₂O₃ revealed by HT-XRD indicated complete consumption of Fe₃O₄, being strongly dependent on time exposure at elevated temperature. Notably, the slow heating process affected strongly the ferrimagnetic properties of Fe₃O₄ precursor powders. In contrast, the rapid, flame spheroidisation process provides an excellent alternative pathway to produce magnetite microspheres retaining their original ferrimagnetic and structural properties.

4.5.3 Formation mechanism of porous microspheres

Figure 4.30 summarises the formation of ferromagnetic microsphere products, with variable calcium iron oxide minerals, developed using the flame spheroidisation process. Microsphere products investigated under gas flow parameter (2:2, 2.5:2.5, and 3:3 arb. unit.), showed no critical variations on composition. Instead, mineral segregation and expansion mechanisms associated with porous microspheres formation were identified. Differently to dense microspheres, porous microsphere products showed **segregated minerals** (magnetite, calcite, calcium ferrites) within the same microsphere system. Since porous microspheres contained fractions of unreacted precursor powders (*i.e.*, magnetite and calcite) mixed with calcium iron

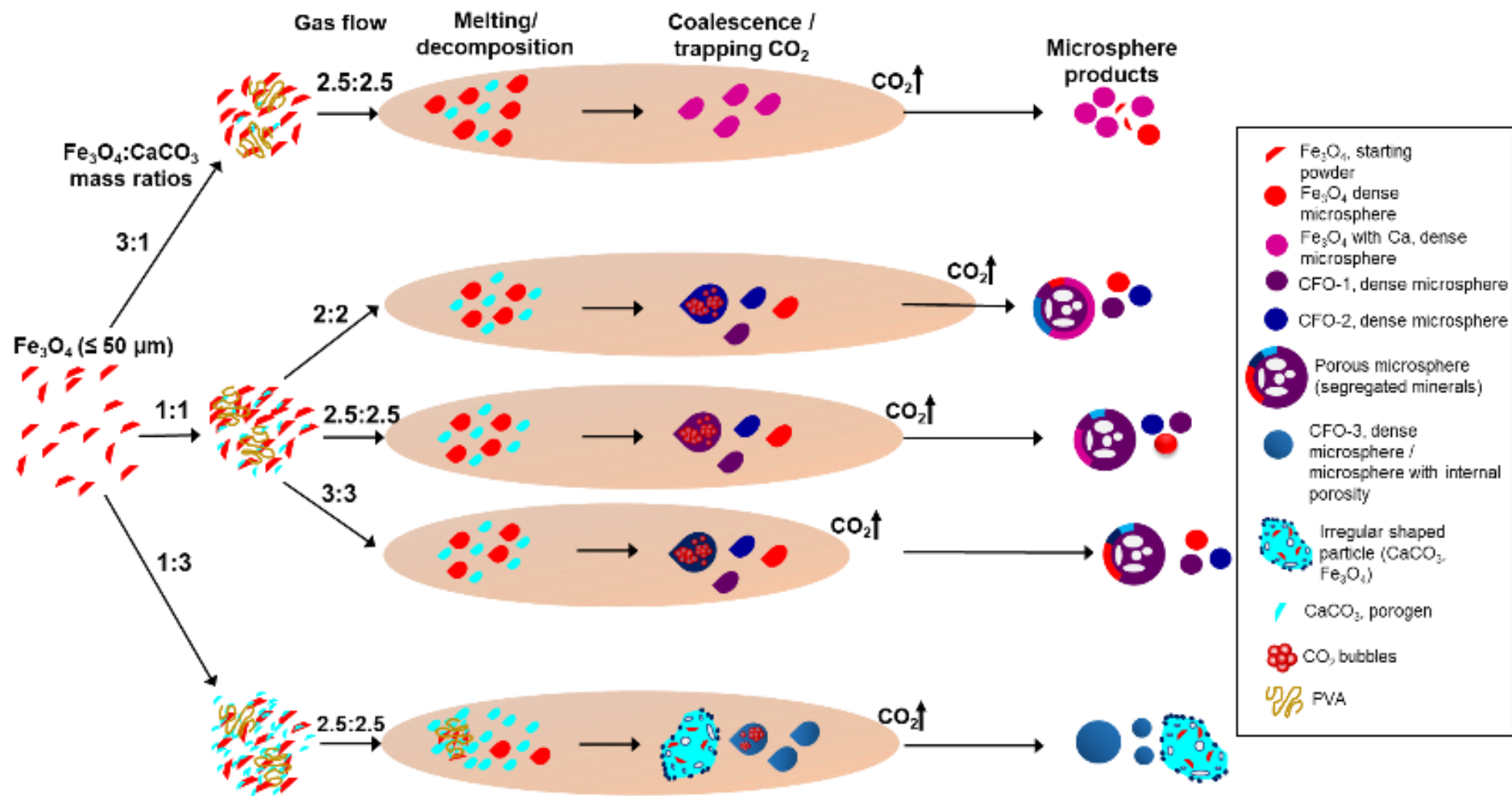


Figure 4.30. Schematic representation of the flame spheroidisation process for $\text{Fe}_3\text{O}_4:\text{CaCO}_3$ microsphere production (mass ratios 3:1, 1:1, and 1:3; and gas flow settings 2:2, 2.5:2.5, and 3:3).

oxides, it was anticipated that a non-equilibrium reaction occurred whilst rapid solidification. Considering the $\text{Fe}_2\text{O}_3\text{:CaO}$ binary phase diagram [188], it was expected that the increase in temperature would enhance diffusion rates of Ca / Fe atoms in liquids. However, flame spheroidisation process cooling was too rapid for atoms to diffuse and produce equilibrium conditions, therefore nonequilibrium structures were produced [266, 271]. This nonequilibrium effect could be associated to the low **residence time** of precursor powders within the flame [272], leading to insufficient time for Ca/Fe atoms within the solid to re-distribute. With regard to the porous microsphere expansion mechanism (detailed in *Chapter 5*), CO_2 gas produced during CaCO_3 porogen decomposition trapped and released from molten drops post-flame ejection whilst rapid solidification occurs, lead to large porous microspheres being formed.

4.5.4 Magnetic properties of Fe_3O_4 dense microspheres

Flame-spheroidised Fe_3O_4 dense microspheres and starting precursor powders both demonstrated similar magnetic saturation levels, with the distinction that the flame spheroidised products showed lower remanent magnetisation ($0.8 \text{ Am}^2/\text{kg}$) as compared to the Fe_3O_4 precursors ($7.6 \text{ Am}^2/\text{kg}$). Mössbauer reversed values (relative area ratio) for Fe_3O_4 microspheres were also indicative of modified magnetic properties [174], as confirmed by low remanence values. Low remanence is important to avoid agglomeration of microspheres in biomedical applications [166], as they would demagnetise quickly upon removal of an alternating magnetic field (AMF). Additionally, remanent magnetisation demonstrated that the microspheres comprise multiple magnetic domains, consistent with a ferrimagnetic type expression [10]. Furthermore, it was recognised that the Fe_3O_4 powders melted at very high temperatures (considerably above the Curie point of magnetite, $\sim 580^\circ\text{C}$) [270], and yet,

ferrimagnetic, chemical and structural properties were retained post flame spheroidisation. Hence, it can be interpreted that high levels of Fe_3O_4 (with very low levels of hematite, Fe_2O_3) were a consequence of the very low residence time of precursor molten particles within the oxygen-acetylene flame. Noting, internal combustion from thermal spraying can generate hypersonic gas velocities of ~ 2000 m/s [266, 273].

Moreover, the possible formation of magnetite / maghemite phase mixture was considered. Fe_3O_4 and maghemite exhibit distinct and characteristic Mössbauer hyperfine magnetic splitting (B_{hf}) and centre shift (δ) values. For the case of maghemite, the expected **centre shift (δ) values** are ~ 0.24 mm/s and ~ 0.36 mm/s for A sites (Fe^{3+}) and B-sites (Fe^{3+}), respectively [274, 275], whereas for magnetite expected values are ~ 0.28 mm/s and ~ 0.66 mm/s for A sites (Fe^{3+}) and B-sites ($\text{Fe}^{2.5+}$), respectively [264, 274]. Notably, the magnetite precursor & magnetite microsphere centre shift values are consistent with those in the literature for Fe_3O_4 . Further, expected maghemite **hyperfine magnetic splitting (B_{hf})** values are 49.8 T for both A and B sites. For the case of magnetite microspheres, the same 49.8 T value is shown for Fe^{3+} A-sites (indistinguishable from maghemite), distinct from the 45.7 T value for $\text{Fe}^{2.5+}$ B-sites (confirming magnetite). Whilst the suggestion of a mixture of maghemite / magnetite phases cannot be fully discounted, it is noted that the **relative area ratio** values for stoichiometric maghemite and magnetite are 1:1.66 [274] and 1:1.9 [174], respectively, with the latter consistent with the data obtained in the present study. This again suggests that magnetite was the dominant phase in the flame processed products. However, it is recognised that this part of the investigation would benefit from further high resolution XPS investigation for definitive iron oxide phase validation.

4.5.5 Fe₃O₄ porous microspheres (1:1 mass ratio)

For the case of **Fe₃O₄:CaCO₃ 1:1** mass ratio, significant changes in morphology, composition, and magnetic properties were observed, as compared to the Fe₃O₄ dense sample. MLA data allowed for compositional distinctions among flame spheroidised products to be established: (i) compositionally uniform, **dense microspheres** were dominated by CFO-1 and CF-2 minerals; (ii) **irregular-shaped particles** were mainly composed of unreacted, CaCO₃ porogen and Fe₃O₄ precursors; and (iii) non-uniform, **porous microspheres** showed segregated minerals within a single microsphere. A suggestion for formation of the two minerals (CFO-1 and CFO-2) relates to a reaction occurring in the proximity of the eutectic point of the binary Fe₂O₃:CaO phase diagram [188]. Therefore, the solidification mechanisms of this sample may be described with reference to the **eutectic reaction** mechanism, L1 → α + β *i.e.*, L1 → CFO-1 + CFO-2. Importantly, the **Ca₂Fe₂O₅ srebrodolskite** phase was consistent for all Fe₂O₃:CaO molar concentrations presented in EDS data (Table 4.13). XRD investigations corroborated the presence of Ca₂Fe₂O₅, a brownmillerite type structure (A₂B₂O₅) that accepts several defects to be incorporated due to its unusual free atomic spaces [186, 276]. For the Fe₃O₄:CaCO₃ 1:1 sample, evidence demonstrated the development of ferromagnetic calcium iron oxide minerals (with Ca/Fe variable concentrations), all constituted by Ca₂Fe₂O₅ crystalline structure. With regards to porosity formation, a certain level of success was achieved at this point, nonetheless, this sample showed the lowest levels of compositional homogeneity so far. Conversely, porogen-rich sample (*i.e.*, Ca-rich microspheres) revealed porous microspheres with higher levels of uniformity.

4.5.6 Ca-rich porous microspheres (1:3 mass ratio)

Ca-rich sample, $\text{Fe}_3\text{O}_4:\text{CaCO}_3$ 1:3 mass ratio, showed improved homogeneity levels among both, porous and dense microspheres. Despite porosity was not shown on SE images, sectioned images revealed internal porosity, attributed to the elevated concentration of CaCO_3 . Internal pores were created as a consequence of porogen decomposition, where CO_2 was stored / unreleased within molten drops whilst rapid solidification (CO_2 produced from CaCO_3 decomposition, detailed in *Chapter 5*). As anticipated, dominant mineral (CFO-3) showed a richer Ca content, as compared to $\text{Fe}_3\text{O}_4:\text{CaCO}_3$ 1:1 sample containing CFO-1 and CFO-2, demonstrating coherence with the increase in CaCO_3 concentration. Also, it was noted that $\text{CaO}:\text{Fe}_2\text{O}_3$ (2:1 molar ratio) binary phase diagram was in good agreement with EDS quantifications, as correlated XRD investigations confirmed, again, $\text{Ca}_2\text{Fe}_2\text{O}_5$ phase. Notably, this sample showed the lowest magnetic saturation levels from the dataset, attributed to Ca occupying atomic spaces within $\text{Ca}_2\text{Fe}_2\text{O}_5$ structure. Further, in order to increase homogeneity, it was desired to remove excess of porogen and magnetite starting powders. For the case of calcite, it was relatively easy by sieving ($\leq 32 \mu\text{m}$). Nonetheless, magnetite unreacted particles were more difficult to separate due to their similar size to small dense microsphere products, whilst nothing some residual large magnetite precursors embedded within porous microspheres.

4.5.7 Fe-rich porous microspheres (3:1 mass ratio)

For the case of **Fe-excess** microsphere sample ($\text{Fe}_3\text{O}_4:\text{CaCO}_3$, mass ratio 3:1), compositional investigations revealed low concentrations of Ca, uniformly distributed across Fe_3O_4 microsphere bodies (e.g. *Fig. 4.23; green dots attributed to calcium incorporation within Fe_3O_4 microspheres*). Hence, it was anticipated that XRD analyses would reveal evidence of the porogen, e.g., signatures for calcium or calcium iron oxide phases. Interestingly, well-defined peaks corresponding to Fe_3O_4 signatures

were obtained, with no structural indicators for the presence of calcium or any related phases. Hence, it is considered that Ca atoms were incorporated within Fe₃O₄ crystalline structure, as a consequence of thermal fluctuations upon solidification of the melt. Additionally, this sample set showed similar magnetic saturation values (95.1 Am²/kg) comparable to dense magnetite microspheres (formed without porogen), demonstrating that low concentrations of non-magnetic calcium atoms have no significant effect on ferrimagnetic expression. However, despite the elevated magnetisation values and high levels of homogeneity achieved, no evidence of porosity was observed, attributed to the low concentration of porogen.

4.5.8 Sample preparation and effect of particle size

Final aspect to consider was the importance of sample preparation. Each individual particle in prepared mixtures may have different Fe₃O₄ / CaCO₃ concentrations, as a consequence of PVA. Considering the thermophoresis force of the particles [272], along with temperature and velocity of these within the oxy-acetylene flame, it was clear that these factors contributed to the final compositions of flame spheroidised microspheres. Morphologies and compositions were also affected by particle size. In *Chapter 5*, a comprehensive description related to porous microsphere formation mechanisms and the effect of particle size were presented. Moreover, knowledge gained in this section was relevant to produce magnetic microspheres with high levels of compositional homogeneity and size control.

4.6 Summary

In order to understand the chemical pathways, thermodynamic effects and morphological transformations associated with calcium iron oxide microspheres

reported here, it was important to consider the materials science related to flame-spray technologies. From a morphological point of view, flame spray methods (e.g., flame spheroidisation) are associated with the formation of non-uniform products as a consequence of high velocity and temperature [277], resulting in molten, semi-molten, and totally un-melted particles [272]. In this Chapter, evidence from SEM micrographs confirmed the presence of dense microspheres, porous microspheres, and irregular-shaped particles. These morphological variations were associated with physical and chemical parameters including flame temperature, residence time of the particles within the flame, and particle size. In concern to structural and chemical properties, flame spray technologies allow for the creation of materials with non-equilibrium characteristics, e.g., materials with a refined grain size, formation of metastable phases and an elevated concentration of point defects, all as a consequence of rapid solidification [266]. Therefore, flame spheroidised products contained modified magnetic, mechanical or chemical properties, as compared with traditionally processed materials.

Initial investigations allowed to recognise the suitability of the flame spheroidisation to manufacture compositionally uniform, Fe_3O_4 magnetic dense microspheres, demonstrating that the transformation of precursor powders into practical spherical morphologies was achieved in a relatively easy and fast way. Moreover, this Chapter explored porogen concentrations and gas flow settings in attempt to develop compositionally uniform microspheres with high levels of porosity. Evidently, by using combinations of $\leq 45 \mu\text{m}$ magnetite with smaller sized porogen, uniform samples were obtained but excess of porogen or Fe_3O_4 precursor materials decreased samples homogeneity. Nonetheless, important evidence and knowledge was obtained in relationship to the nature of the flame-spheroidisation process used

for the manufacture of magnetic microspheres, resulting relevant for the upcoming sections, where parameters control was investigated (*Chapter 5*), and the manufacture of glass-ceramic microspheres with high levels porosity was achieved (*Chapter 6*).

In this context, it was evident that porogen concentration had a direct effect on microsphere composition and magnetic properties, whilst nothing that structural investigations confirmed $\text{Ca}_2\text{Fe}_2\text{O}_5$ phase for all microsphere samples, with Fe and Ca excess / deficit levels. A process control over the flame spheroidisation method would allow for scalability, process mapping, and reproducibility of the manufactured magnetic microspheres, for their potential application in a number of fields, including healthcare, environmental remediation, removal of heavy metals, etc. In particular, due their spherical morphology, strong magnetism, and low remanence, they can be explored for biomedical applications, such as MRI, magnetic hyperthermia, drug-delivery micro-systems, etc.

5.0 Development of compositionally uniform ferromagnetic microspheres using ($\leq 5 \mu\text{m}$) Fe_3O_4 precursors

5.1 Introduction

The single-stage, flame-spheroidisation process, as applied to $\text{Fe}_3\text{O}_4:\text{CaCO}_3$ powder combinations, provided for the rapid production of dense and porous magnetic microspheres with homogeneous composition and high levels of interconnected porosity. In this context, this Chapter examines the parameter space of this flame-processing technique, towards the controllable manufacture of magnetic microspheres using small ($< 5 \mu\text{m}$) Fe_3O_4 precursor particles. The controllability of these factors makes the flame spheroidisation process useful for a range of healthcare applications, including scaffolds for tissue regeneration and drug delivery.

Scanning electron microscopy (SEM) based techniques were used to image and quantify the microsphere products. Structural characterisation was performed using X-ray diffractometry (XRD). Microsphere magnetic properties were investigated *via* SQUID magnetometry. Correlated backscattered electron (BSE) imaging and mineral liberation analysis (MLA) investigations provided insights into the microsphere formation mechanisms, as a function of precursor/porogen **mass ratio** and **gas flow setting**. Optimised conditions for the processing of highly homogeneous **$\text{Ca}_2\text{Fe}_2\text{O}_5$ magnetic microspheres** were identified. Complementary high-temperature X-ray diffractometry (HT-XRD), thermogravimetric analysis (TGA) and high temperature superconductive quantum interference device (HT-SQUID) magnetometry, were used to study precursor powders, providing evidence into the initial process of porogen feedstock decomposition, chemical reaction pathways and structural/magnetic

properties evolution. Furthermore, selected area electron diffraction (SAED) confirmed the identification of $\text{Ca}_2\text{Fe}_2\text{O}_5$ as the dominant phase on microsphere products. Additionally X-ray photoelectron spectroscopy (XPS) was used to study surface chemistry of the microsphere products. Furthermore, induction heating demonstrated a controlled temperature rise to 43.7°C , making flame-spheroidised $\text{Ca}_2\text{Fe}_2\text{O}_5$ microspheres highly promising candidates for magnetic induced hyperthermia applications.

5.2 Effect of mass ratio

Figure 5.1 provides an overview of the key steps followed for the manufacture and characterisation of porous and dense magnetic microspheres using Fe_3O_4 ($\leq 5 \mu\text{m}$) powders, as a function of $\text{Fe}_3\text{O}_4:\text{CaCO}_3$ mass ratio.

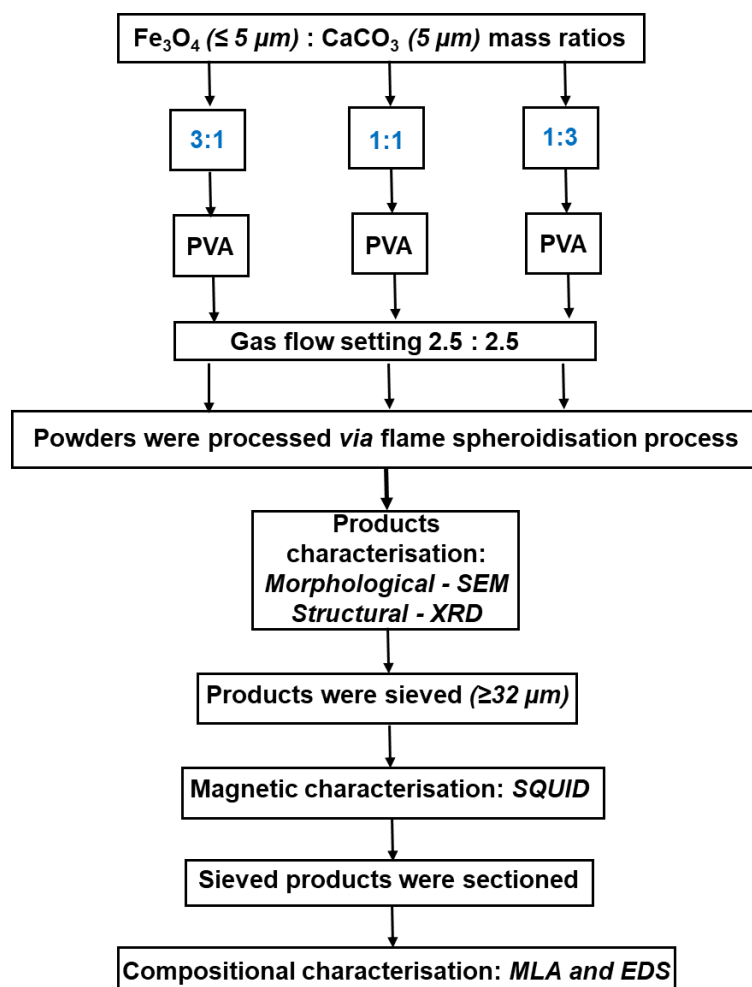


Figure 5.1 Flow diagram summarising the processing steps followed for the manufacture of porous magnetic microspheres using Fe_3O_4 ($\leq 5 \mu\text{m}$) precursor powders, as a function of Fe_3O_4 : CaCO_3 mass ratio (3:1, 1:1, and 1:3).

5.2.1 Microsphere topography (*unsieved*)

Figures 5.2(a-c) present low magnification SE images of flame-spheroidised products formed from Fe_3O_4 : CaCO_3 precursor / porogen materials, with mass ratios of (a) 3:1, (b) 1:1 and (c) 1:3, respectively, using $\leq 5 \mu\text{m}$ sized magnetite starting powders and a gas flow setting of 2.5 : 2.5 in all cases.

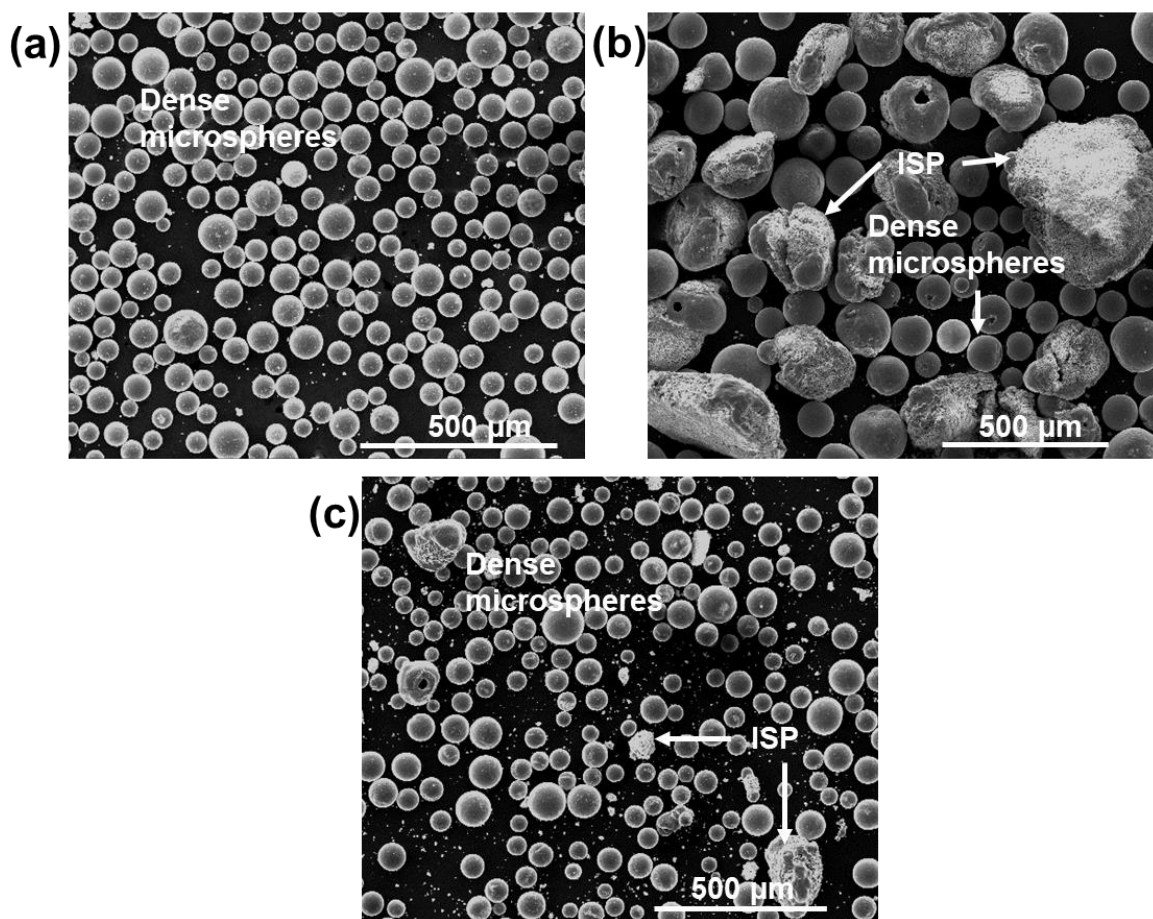


Figure 5.2 SE images of flame spheroidised $Fe_3O_4:CaCO_3$ using starting $\leq 5 \mu m$ magnetite particles. Mass ratios: **(a)** 3:1, **(b)** 1:1, and **(c)** 1:3, respectively (unsieved).

As summarised in Table 5.1, a mass ratio of 1:1 led to the production of a mixture of dense microspheres and larger, irregular shaped particles (ISP) (Figure 5.2b). Notably, a 3:1 mass ratio (**Fe_3O_4 -rich**) generated a consistent yield of dense microspheres with very few ISP (Figure 5.2a), whereas a 1:3 mass ratio (**$CaCO_3$ -rich**) produced a similar mixture of dense microspheres and few ISP (Figure 5.2c).

Table 5.1 Size range of flame-spheroidised reaction products (dense microspheres, irregular shaped particles (ISP), and microspheres with surface porosity), as a function of precursor to porogen mass ratio.

Mass ratio Fe ₃ O ₄ :CaCO ₃	Gas flow setting / arb. unit	Dense microspheres/ µm	ISP / µm	Microspheres with surface porosity / µm
3:1	2.5 : 2.5	35 - 165	75 - 475	No
1:1		65 - 210	205 - 465	
1:3		40 - 145	40 - 195	

Evidently, there were no insights of porosity among the spheroidised samples. The upcoming section presents structural investigations for these unsieved, flame-spheroidised products.

5.2.2 Structural characterisation (*unsieved microspheres*)

Structural investigations were undertaken using XRD to study the crystallography of the flame-spheroidised products as a function of precursor-to-porogen mass ratios. Figure 5.3 shows XRD patterns for flame-spheroidised (*unsieved*) products (mass ratios 3:1, 1:1 and 1:3) corresponding to the sample sets shown in Figures 5.2(a-c). XRD analysis confirmed the presence of the following phases: Ca₂Fe₂O₅ (ICDD PDF no. 00-047-1744), Fe₃O₄ (ICDD PDF no. 01-087-0244), Fe₂O₃ (ICDD PDF 00-033-0664), CaCO₃ (ICDD PDF no. 00-047-1743) and CaO (calcium oxide) (ICDD PDF no. 00-048-1467).

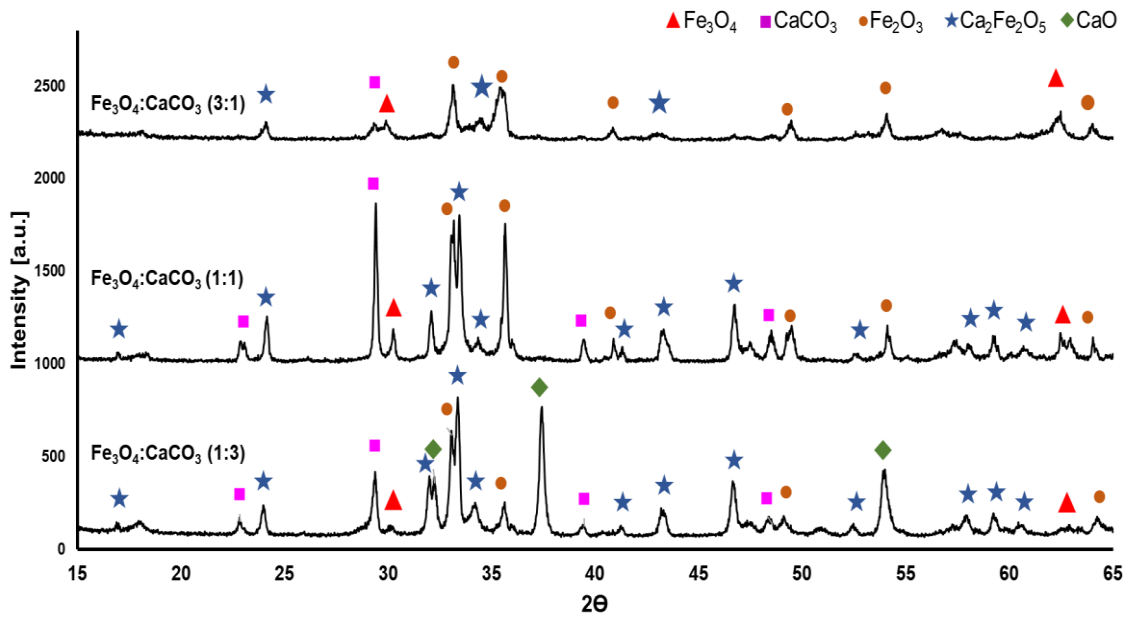


Figure 5.3 XRD patterns for flame-spheroidised $\text{Fe}_3\text{O}_4:\text{CaCO}_3$ (mass ratios 3:1, 1:1 and 1:3) (*unsieved*) using small $\leq 5 \mu\text{m}$ magnetite powders.

Table 5.2 Generalised summary of unsieved microsphere product proportions, as a function of precursor to porogen mass ratio.

Mass ratio $\text{Fe}_3\text{O}_4:\text{CaCO}_3$	Flame spheroidised products (<i>strong / medium / weak</i>)				
	Fe_3O_4	Fe_2O_3	$\text{Ca}_2\text{Fe}_2\text{O}_5$	CaCO_3	CaO
3:1	<i>m</i>	<i>s</i>	<i>m</i>	<i>w</i>	-
1:1	<i>m</i>	<i>s</i>	<i>s</i>	<i>s</i>	-
1:3	<i>w</i>	<i>m</i>	<i>s</i>	<i>m</i>	<i>s</i>

As outlined in Table 5.2, a mass ratio of 1:1 showed strong signatures for Fe_2O_3 , $\text{Ca}_2\text{Fe}_2\text{O}_5$ and (unreacted) CaCO_3 , along with a medium signature for (unreacted) Fe_3O_4 . A mass ratio of 3:1 (**Fe_3O_4 -rich**) revealed a dominant Fe_2O_3 signature, with medium Fe_3O_4 and $\text{Ca}_2\text{Fe}_2\text{O}_5$ signatures, and a weak signature for

CaCO₃. A mass ratio of 1:3 (**CaCO₃-rich**) showed strong signatures for Ca₂Fe₂O₅ and CaO, medium signatures for Fe₂O₃ and CaCO₃, and a weak signature for Fe₃O₄. After these initial structural investigations, the microsphere products were sieved ($\geq 32 \mu\text{m}$) in order to remove any excess Fe₃O₄ and CaCO₃ unreacted powders, prior to magnetic characterisation.

5.2.3 Magnetic characterisation (*sieved microspheres*)

Figure 5.4 presents magnetisation curves for the sieved flame-spheroidised products (mass ratios 3:1, 1:1 and 1:3). For all samples, the magnetisation curves were indicative of typical ferrimagnetic behaviour. As summarised in Table 5.3, progression towards increased porogen (mass ratio from 3:1 to 1:3) was accompanied by a decrease in magnetisation, consistent with a lowering of iron content.

Table 5.3. Magnetic measurements of flame-spheroidised products as a function of precursor to porogen mass ratio.

Mass ratio Fe ₃ O ₄ :CaCO ₃	Gas flow setting	Magnetic saturation / M _s	Remanent Magnetisation / M _r	Coercive Field / H _c	
	Arb. units	Am ² /kg (emu/g)	Am ² /kg (emu/g)	(kA/m)	(Oe)
3:1	2.5:2.5	36	3.3	9.1	115
1:1		10.1	0.6	7.0	87.5
1:3		3.6	0.3	7.2	90

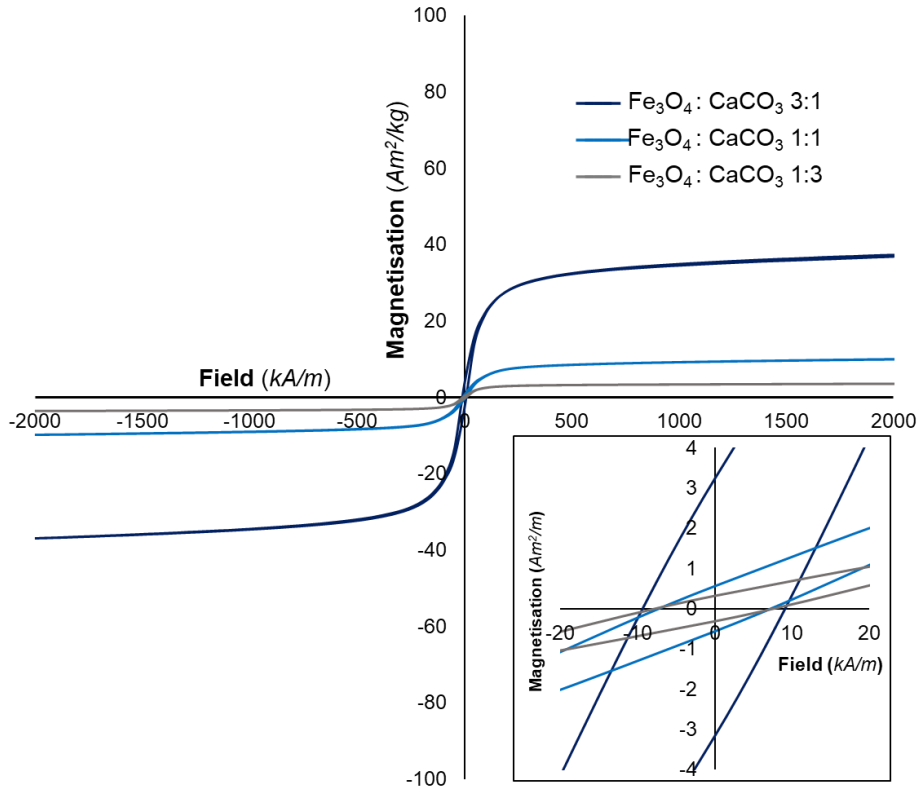


Figure 5.4 Magnetisation curves for flame spheroidised $\text{Fe}_3\text{O}_4:\text{CaCO}_3$ (mass ratios 3:1, 1:1 and 1:3; gas flow setting 2.5:2.5) at 26.85°C , using Fe_3O_4 ($\leq 5 \mu\text{m}$) powders.

Inset figure provides evidence of remanent magnetisation in all cases.

The upcoming section presents compositional analyses for the manufactured microspheres as a function of mass ratio, following mechanical grinding and sectioning.

5.2.4 Chemical analysis (*sieved and sectioned microspheres*)

5.2.4.1 Mineral liberation analysis

Figures 5.5(a-c) presents BSE images and MLA mappings showing fine-scale morphological details and minerals of the sieved microsphere products, manufactured using $\leq 5 \mu\text{m}$ Fe_3O_4 precursor powders; extracted from the sample sets presented in Figure 5.2. Table 5.4 highlights mineral proportions of the reacted products, revealing

clear compositional differences. As anticipated, a progressive decrement in precursor content or increment in porogen content (mass ratio 3:1 to 1:3) was directly accompanied by a lowering of Fe levels and elevation of Ca levels throughout the flame-spheroidised products.

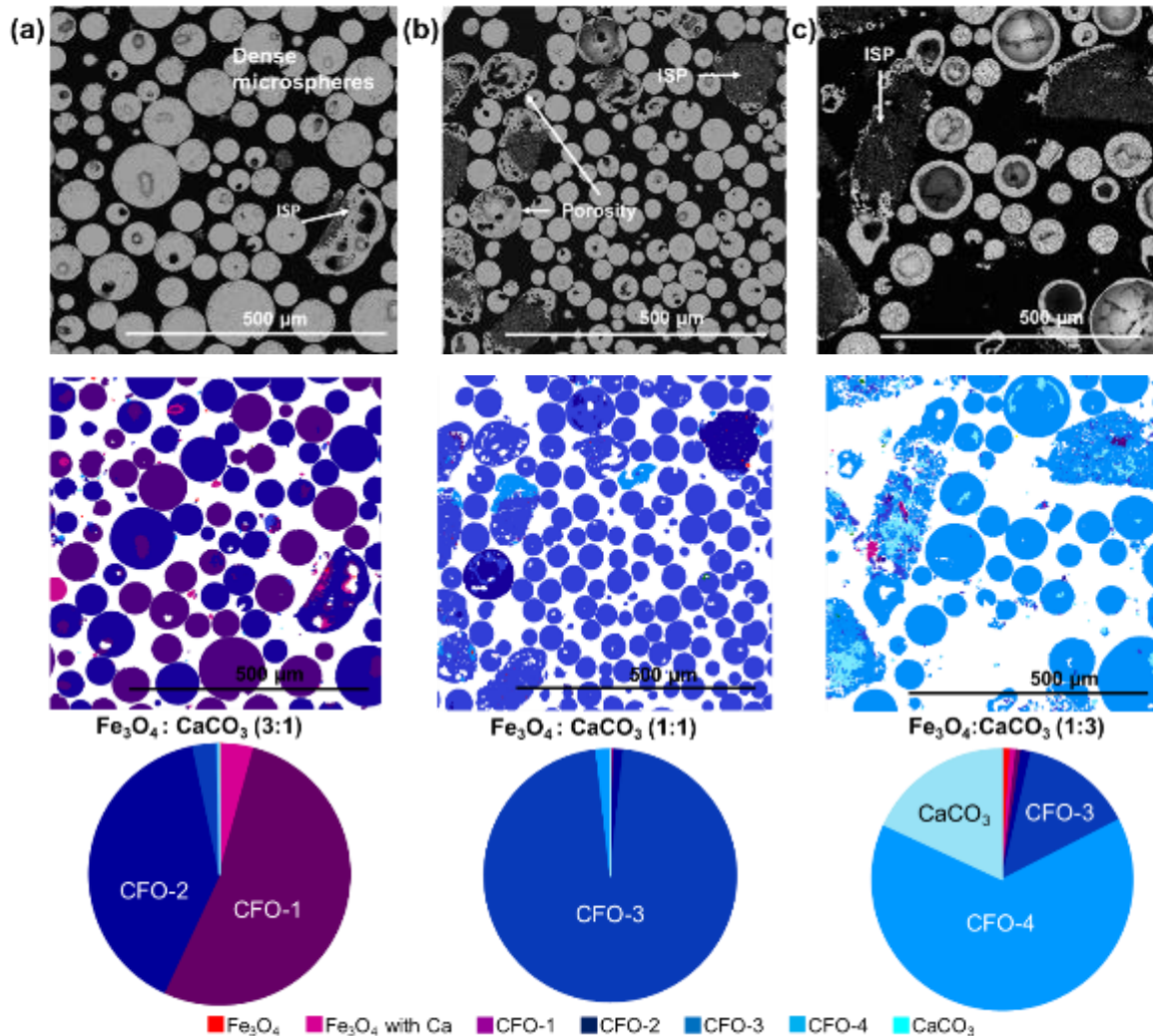


Figure 5.5 BSE images, MLA compositional analyses and associated pie-charts showing the mineral proportions (wt%) of flame spheroidised Fe_3O_4 : CaCO_3 using $\leq 5 \mu\text{m}$ magnetite particles, as a function of mass ratio: **(a)** 3:1, **(b)** 1:1, and **(c)** 1:3; following sieving and sectioning, illustrating microsphere porosity, ISP, and dense microspheres. Mineral references shown in Table 4.10. (ISP: Irregular-shaped particles; CFO: calcium iron oxide)

Table 5.4 Mineral proportion (weight percentage) of magnetic microsphere products, as a function of Fe₃O₄:CaCO₃ mass ratio.

Mass ratio Fe ₃ O ₄ :CaCO ₃	Fe ₃ O ₄ / wt%	Fe ₃ O ₄ with Ca / wt%	CFO- 1 / wt%	CFO- 2 / wt%	CFO-3- Ca ₂ Fe ₂ O ₅ / wt%	CFO- 4 / wt%	CaCO ₃ / wt%	Number of particles analysed
3:1	0.3	3.9	52.7	39.7	3.0	0.2	0.1	9544
1:1	0.1	0.3	0.1	1.2	96.5	1.8	0	4064
1:3	1.0	0.7	0.7	1.2	13.9	64.4	18.1	23851

Flame-spheroidised Fe₃O₄:CaCO₃ with mass ratio 1:1 (Figure 5.5b), upon sectioning, provided direct evidence for the development of low and high levels of internal porosity within dense microspheres and larger irregular-shaped particles, respectively. MLA mapping provided direct evidence for high levels of homogeneity of CFO-3 (Figure 5.6; Table 5.5). In addition, EDS analysis (Table 4.17) showed the elemental composition to be consistent with srebrodolskite (*i.e.*, brownmillerite Ca₂Fe₂O₅; Ca – 19.1%, Fe – 57%, O – 23.9%) [63]. Hence, mineral CFO-3 was denominated as Ca₂Fe₂O₅. For the case of flame-spheroidised **precursor-rich** powder (mass ratio 3:1; Figure 5.5a), the evidence showed the development of comparatively lower levels of internal porosity within dense microspheres and few irregular-shaped particles. The MLA data comprised two dominant CFO levels (denoted CFO-1 and CFO-2; Table 5.6, Figure 5.7). Both these samples (Figures 5.5 a,b) showed complete consumption of the precursor and porogen, with no evidence for residual Fe₃O₄ nor CaCO₃ (Table 5.4). Conversely, for the case of flame-spheroidised **porogen-rich** powder (mass ratio 1:3; Figure 5.5c), a variety of dense and irregular-shaped morphologies with significantly higher levels of internal porosity were revealed. MLA data also showed a mixture of CFO compositions dominated by

Ca excess (CFO-4, Table 5.7; Figure 5.8), along with larger ISP comprising unreacted porogen.

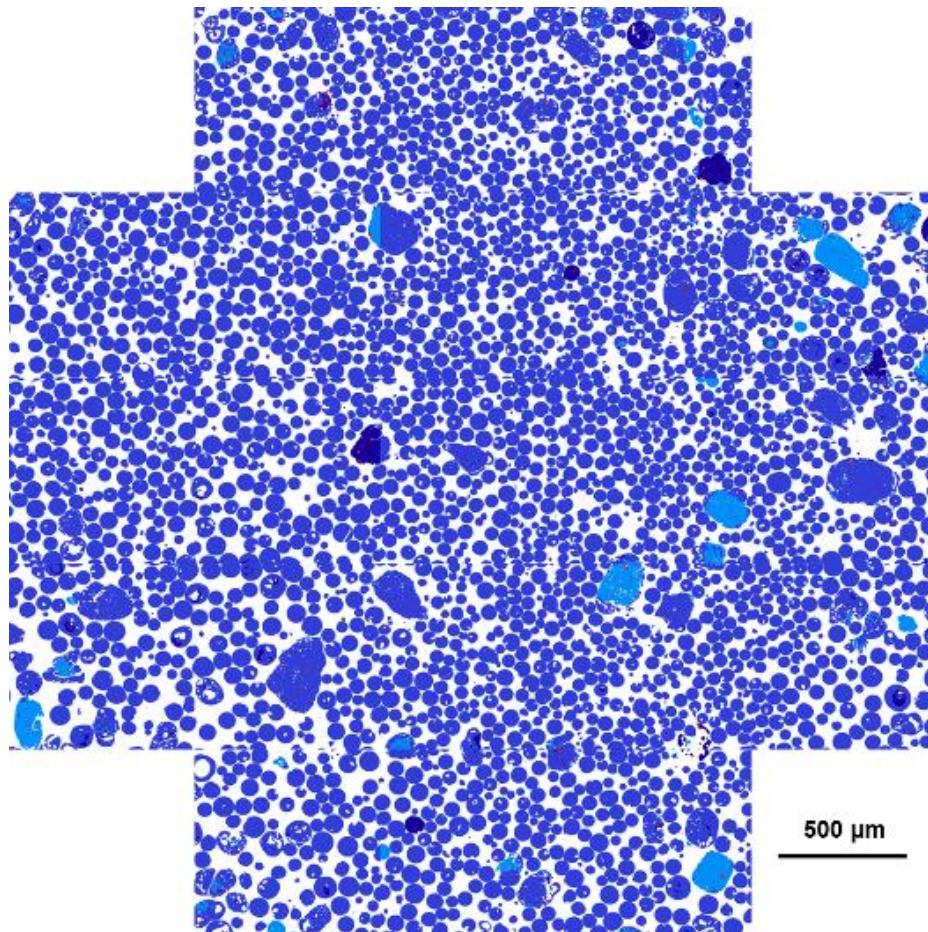


Figure 5.6 Full MLA compositional analysis of flame-spheroidised Fe_3O_4 - $CaCO_3$ (mass ratio 1:1; gas flow setting 2.5 : 2.5), following sieving and sectioning, demonstrating high levels of CFO-3.

Table 5.5. Modal mineralogy for flame spheroidised- Fe_3O_4 : $CaCO_3$ (mass ratio 1:1)

Mineral	Particles	Weight %
Fe_3O_4	78	0.1
Fe_3O_4 with Ca	95	0.3
CFO-1	125	0.1
CFO-2	203	1.2
CFO-3- $Ca_2Fe_2O_5$	3311	96.5
CFO-4	231	1.8
$CaCO_3$	21	0.00

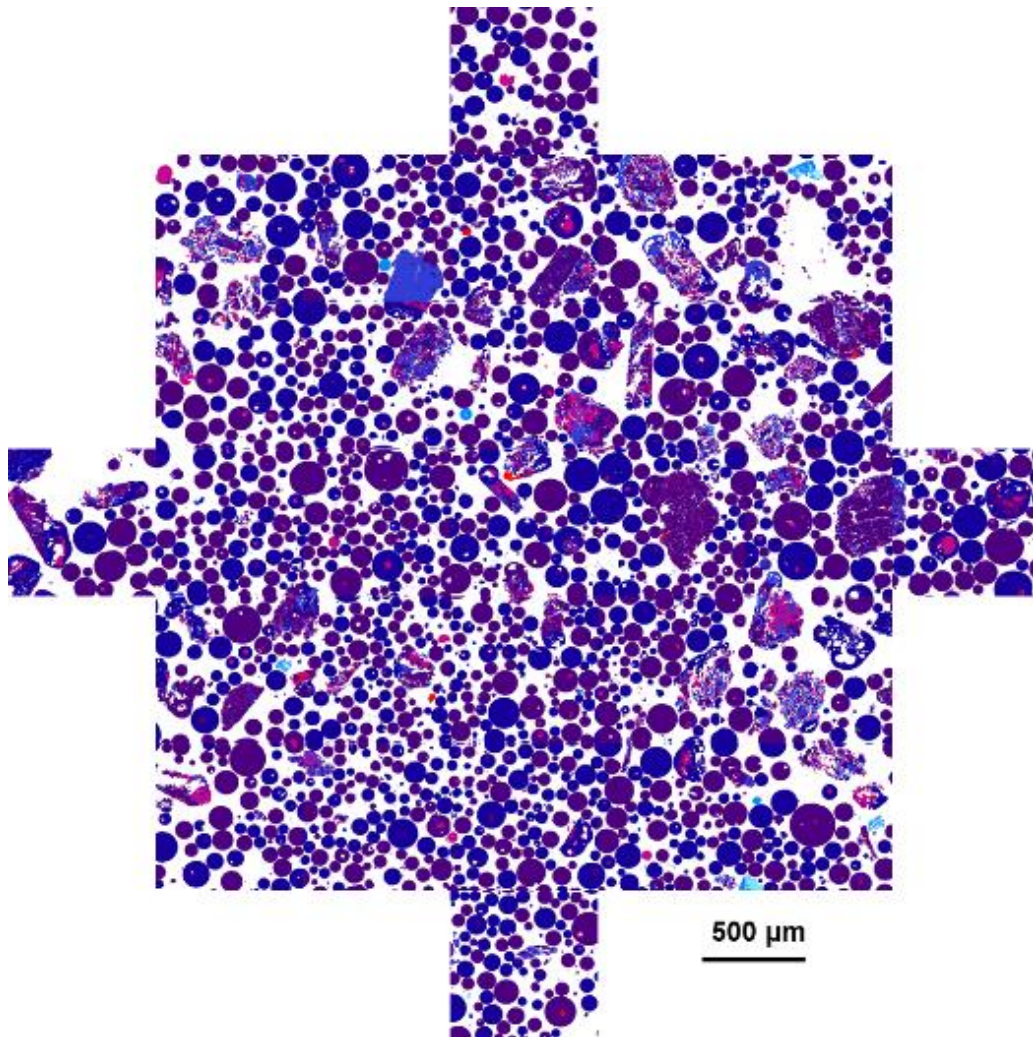


Figure 5.7 Full MLA compositional analysis of flame-spheroidised $Fe_3O_4:CaCO_3$ (mass ratio 3:1; gas flow setting 2.5 : 2.5), following sieving and sectioning, demonstrating high levels of CFO-1 and CFO-2.

Table 5.6. Modal mineralogy for flame spheroidised- $Fe_3O_4:CaCO_3$ (mass ratio 3:1)

Mineral	Particles	Weight %
Fe_3O_4	573	0.3
Fe_3O_4 with Ca	2056	3.9
CFO-1	3250	52.7
CFO-2	2030	39.7
CFO-3	1199	3.0
CFO-4	278	0.2
$CaCO_3$	158	0.1

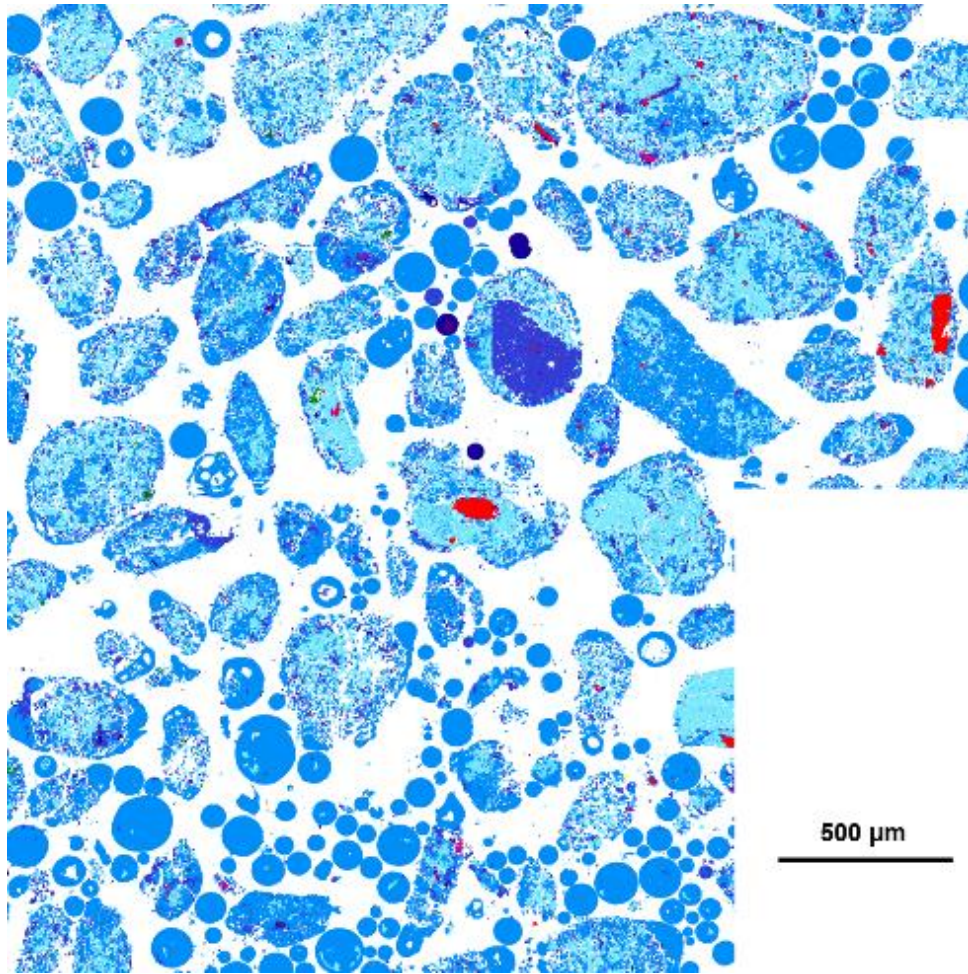


Figure 5.8. Full MLA compositional analysis and modal mineralogy table of flame-spheroidised Fe_3O_4 - $CaCO_3$ (mass ratio 1:3; gas flow setting 2.5 : 2.5), following sieving and sectioning, demonstrating high levels of CFO-4.

Table 5.7. Modal mineralogy for flame-spheroidised Fe_3O_4 : $CaCO_3$ (mass ratio 1:3)

Mineral	Particles	Weight %
Fe_3O_4	96	1.0
Fe_3O_4 with Ca	548	0.7
CFO-1	1103	0.7
CFO-2	1271	1.2
CFO-3- $Ca_2Fe_2O_5$	4955	13.9
CFO-4	9283	64.4
$CaCO_3$	6595	18.1

Notably, the highest levels of homogeneity were achieved using a $\text{Fe}_3\text{O}_4:\text{CaCO}_3$ mass ratio of 1:1, whilst noting complete precursor consumption. In the next section, EDS analysis revealed insight into the elemental distributions within magnetic microspheres as a function of precursor-to-porogen mass ratio.

5.2.4.2 Energy dispersive X-ray (EDS) analyses

EDS investigations provided evidence on the Fe/Ca elemental distributions within the sectioned, resin embedded $\text{Fe}_3\text{O}_4:\text{CaCO}_3$ (mass ratios 3:1, 1:1, 1:3) magnetic microsphere products. Figure 5.9 presents a BSE image and elemental mappings of the $\text{Fe}_3\text{O}_4:\text{CaCO}_3$ (mass ratio 1:1) flame-spheroidised products, illustrating porous and dense microspheres with high levels of uniformity ($\text{Ca}_2\text{Fe}_2\text{O}_5$, Table 5.8).

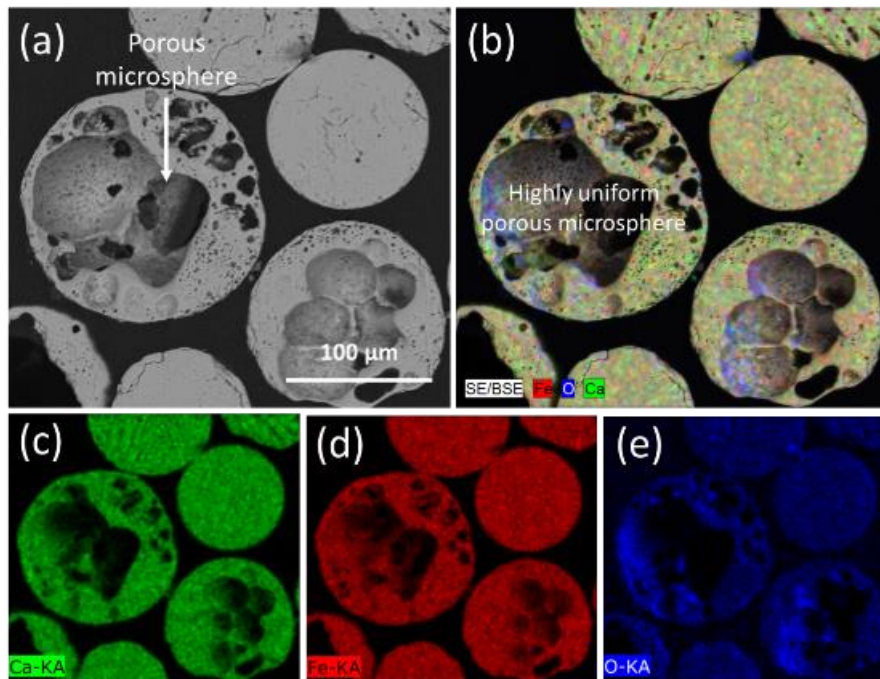


Figure 5.9 (a) BSE image and (b) elemental mapping showing (c) calcium, (d) iron, and (e) oxygen for $\text{Fe}_3\text{O}_4:\text{CaCO}_3$ microspheres (mass ratio 1:1), following sieving and sectioning, illustrating porous and dense microspheres, and high levels of homogeneity.

Table 5.8 EDS molar concentrations (wt%) and proposed equilibrium phases for flame spheroidised $\text{Fe}_3\text{O}_4:\text{CaCO}_3$ (mass ratio 1:1)

Name	CaO wt%	Fe_2O_3 wt%	Proposed phases
Ca rich	66.06 ± 1.84	33.93 ± 1.84	CaO + $\text{Ca}_2\text{Fe}_2\text{O}_5$

For the case of *precursor-rich* $\text{Fe}_3\text{O}_4:\text{CaCO}_3$ samples (mass ratio 1:3), Figure 5.10 shows a strong yield of dense microspheres comprising two different levels of Fe/Ca (Table 5.9).

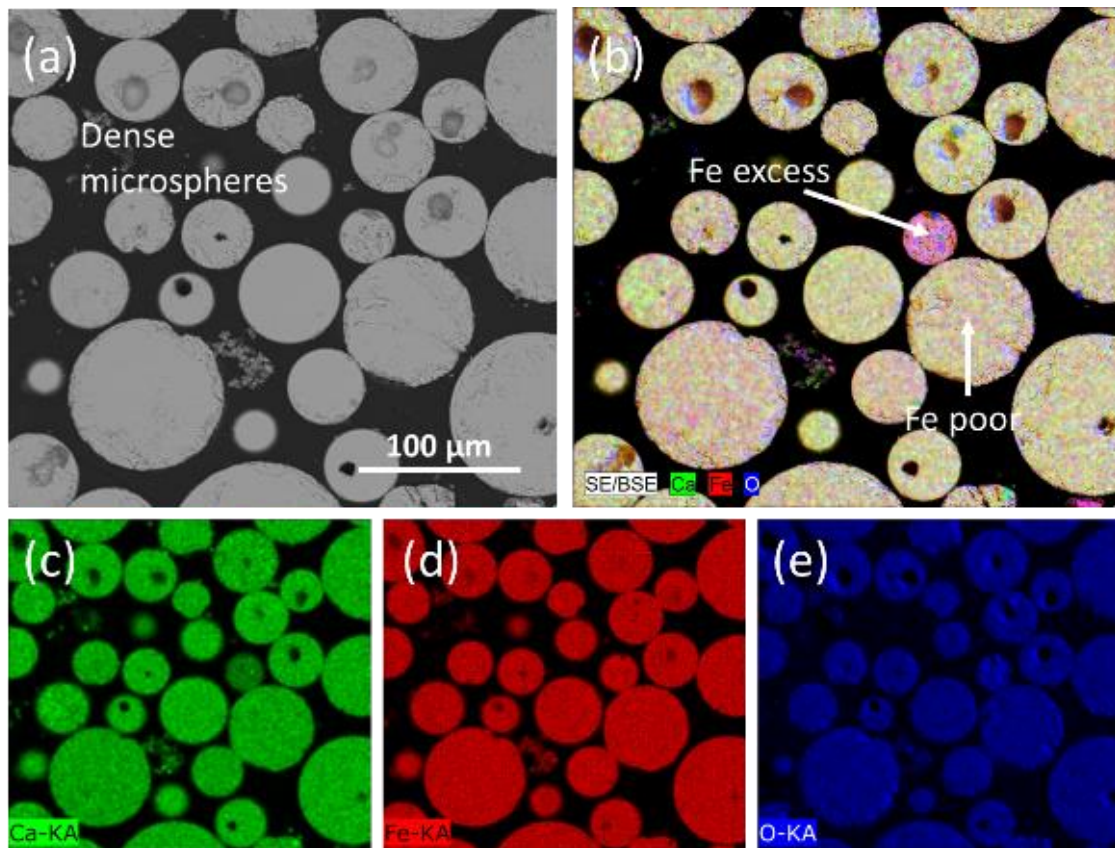


Figure 5.10 (a) BSE image and (b) elemental mapping showing (c) calcium, (d) iron, and (e) oxygen for $\text{Fe}_3\text{O}_4:\text{CaCO}_3$ microspheres (mass ratio 3:1), following sieving and sectioning, illustrating dense microspheres, and a mixture of two different levels of iron / calcium.

Table 5.9 EDS molar concentrations (wt%) and proposed equilibrium phases for flame spheroidised $\text{Fe}_3\text{O}_4:\text{CaCO}_3$ (mass ratio 3:1).

Name	CaO wt%	Fe_2O_3 wt%	Proposed phases
Fe excess	29.57 ± 2.10	70.42 ± 2.10	$\text{Ca}_2\text{Fe}_2\text{O}_5 + \text{CaFe}_2\text{O}_4$
Fe rich	42.71 ± 1.54	57.28 ± 1.54	$\text{CaO} + \text{Ca}_2\text{Fe}_2\text{O}_5$

For the case of porogen-rich samples, Figure 5.11 shows BSE image and EDS mappings highlighting **Ca-excess** irregular-shaped particles, containing unreacted CaCO_3 porogen and reacted CaO (Table 5.10). Notably, certain levels of porosity were also evident in these irregular-shaped particles.

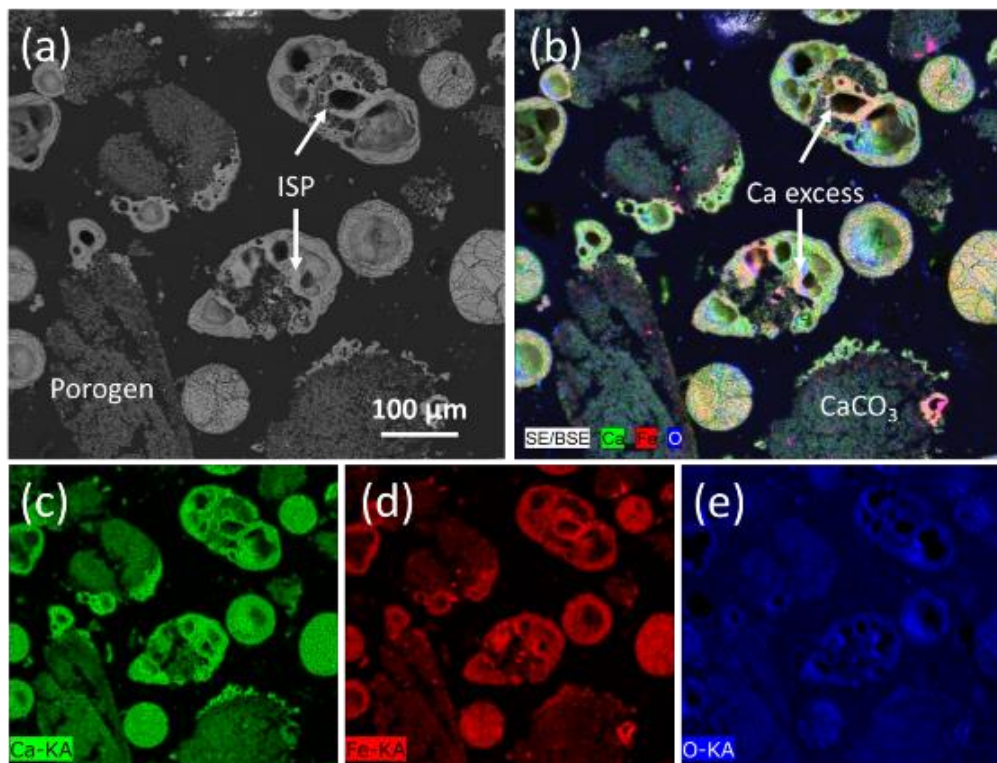


Figure 5.11 (a) BSE image and (b) elemental mappings showing (c) calcium, (d) iron, and (e) oxygen for $\text{Fe}_3\text{O}_4:\text{CaCO}_3$ microspheres (mass ratio 1:3), following sieving and sectioning, illustrating dense microspheres, and elevated levels of calcium.

Table 5.10 EDS molar concentrations (wt%) and proposed equilibrium phases for flame spheroidised Fe₃O₄:CaCO₃ (mass ratio 1:3).

Name	CaO wt%	Fe ₂ O ₃ wt%	Proposed phases
Ca excess	77.34 ± 5.62	22.65 ± 5.62	CaO + Ca₂Fe₂O₅

Characterisation of the microsphere products allowed investigation of property dependencies on the precursor-to-porogen mass ratio, whilst noting that Fe₃O₄:CaCO₃ (1:1 mass ratio) samples showed the highest levels of compositional uniformity (Ca₂Fe₂O₅) among all the samples investigated. The next section explores the effects of gas flow setting on samples of Fe₃O₄:CaCO₃ (1:1 mass ratio).

5.3 Effect of gas flow setting

Fe₃O₄:CaCO₃ (mass ratio 1:1) powders were flame-spheroidised using **2:2** and **3:3** gas flow settings, for comparative morphological investigation (Figure 5.12).

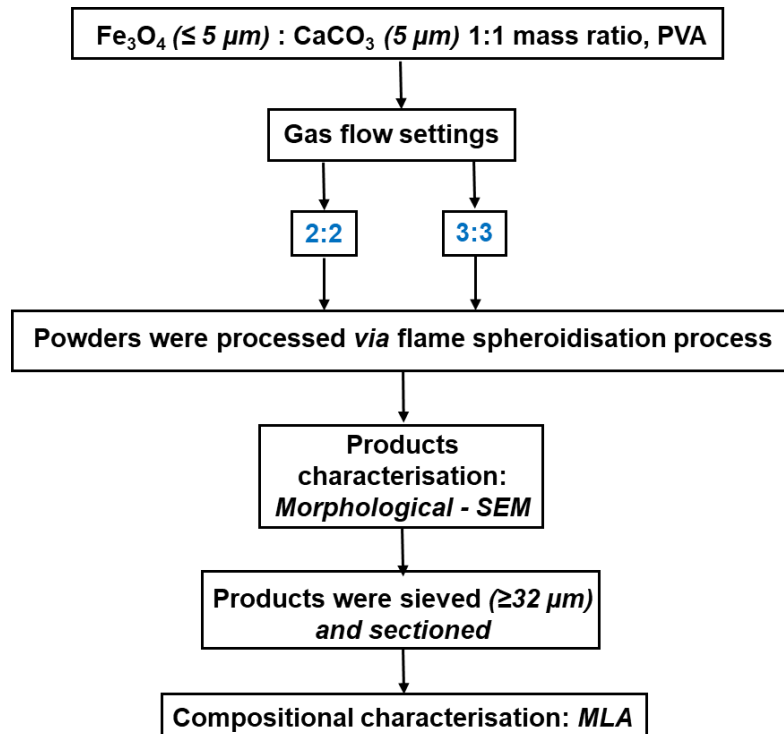


Figure 5.12 Flow diagram summarising the processing steps followed for the manufacture of porous magnetic microspheres using Fe_3O_4 ($\leq 5 \mu m$) precursor, as a function of gas flow setting (2:2 and 3:3)

5.3.1 Microsphere morphologies (*unsieved*)

Figures 5.13(a,b) present low magnification SE images of flame-spheroidised $Fe_3O_4:CaCO_3$ products, for precursor to porogen ($Fe_3O_4:CaCO_3$) mass ratio of 1:1, with gas flow settings of **(a)** 2:2 and **(b)** 3:3, respectively.

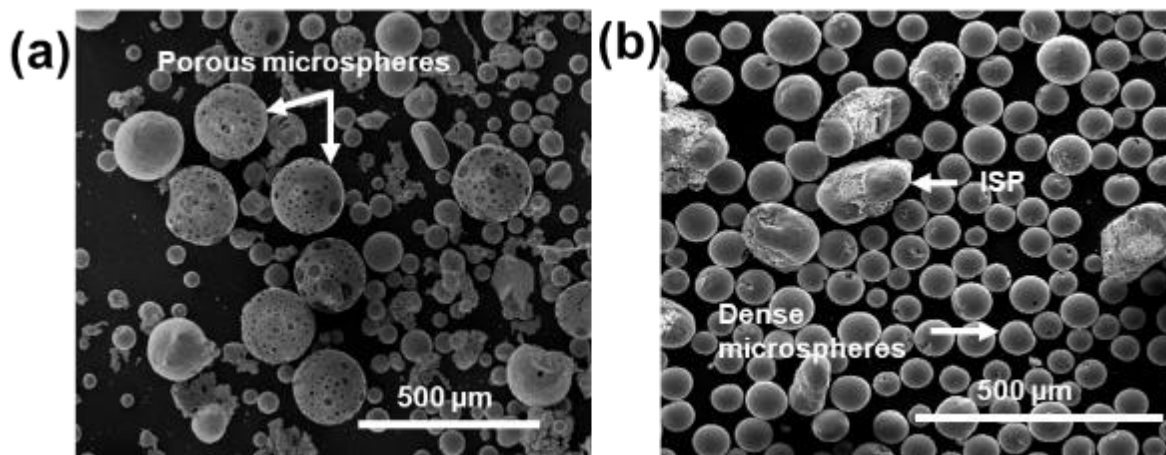


Figure 5.13. SE images of flame-spheroidised $\text{Fe}_3\text{O}_4:\text{CaCO}_3$ (1:1 mass ratio) using starting $\leq 5 \mu\text{m}$ magnetite particles. Gas flow settings: (a) 2:2 and (b) 3:3 (unsieved). (ISP: Irregular shaped particles.)

Table 5.11 Size range of flame-spheroidised reaction products (dense microspheres, irregular shaped particles (ISP), and microspheres with surface porosity), as a function of gas flow setting.

Mass ratio $\text{Fe}_3\text{O}_4:\text{CaCO}_3$	Gas flow setting / arb. unit	Dense microspheres / μm	ISP / μm	Microspheres with surface porosity / μm
1:1	2:2	35 - 80	15 – 105	125 - 180
	3:3	55 - 150	175 - 210	-

As detailed in Table 5.11, an increased gas flow setting of 3:3 presented dense microspheres and few irregular-shaped particles (Figure 5.13b), whilst a lower gas flow setting of 2:2 resulted in a consistent yield of **highly porous microspheres**, along with small dense microspheres and very few irregular-shaped particles (Figure 5.13a). Notably, only the gas flow setting 2:2 (mass ratio 1:1) processing conditions resulted

in the production of microspheres with visible evidence for surface porosity (pore size range 1.8 – 64.5 μm ; mean pore size 13.1 μm , SD 12.6 μm) (porosity measurements *via* ImageJ software).

5.3.2 Microsphere compositions (*sieved and sectioned*)

Figures 5.14(a,b) present BSE images and MLA mineral mapping analyses, extracted from the sample sets presented in Figure 5.13, showing fine-scale morphological details of the sieved microsphere products and clarifying the compositional dependencies on gas flow setting. Interestingly, significant levels of internal porosity were revealed for both sample sets. For the case of higher gas flow setting 3:3, moderate levels of internal porosity were associated with the microspheres and few irregular-shaped products (Figure 5.14b). Whereas, for gas flow setting 2:2, a variety of developed porosities was evident, including high levels of interconnected porosity for the case of the larger microspheres (125 – 180 μm) (Figure 5.14a).

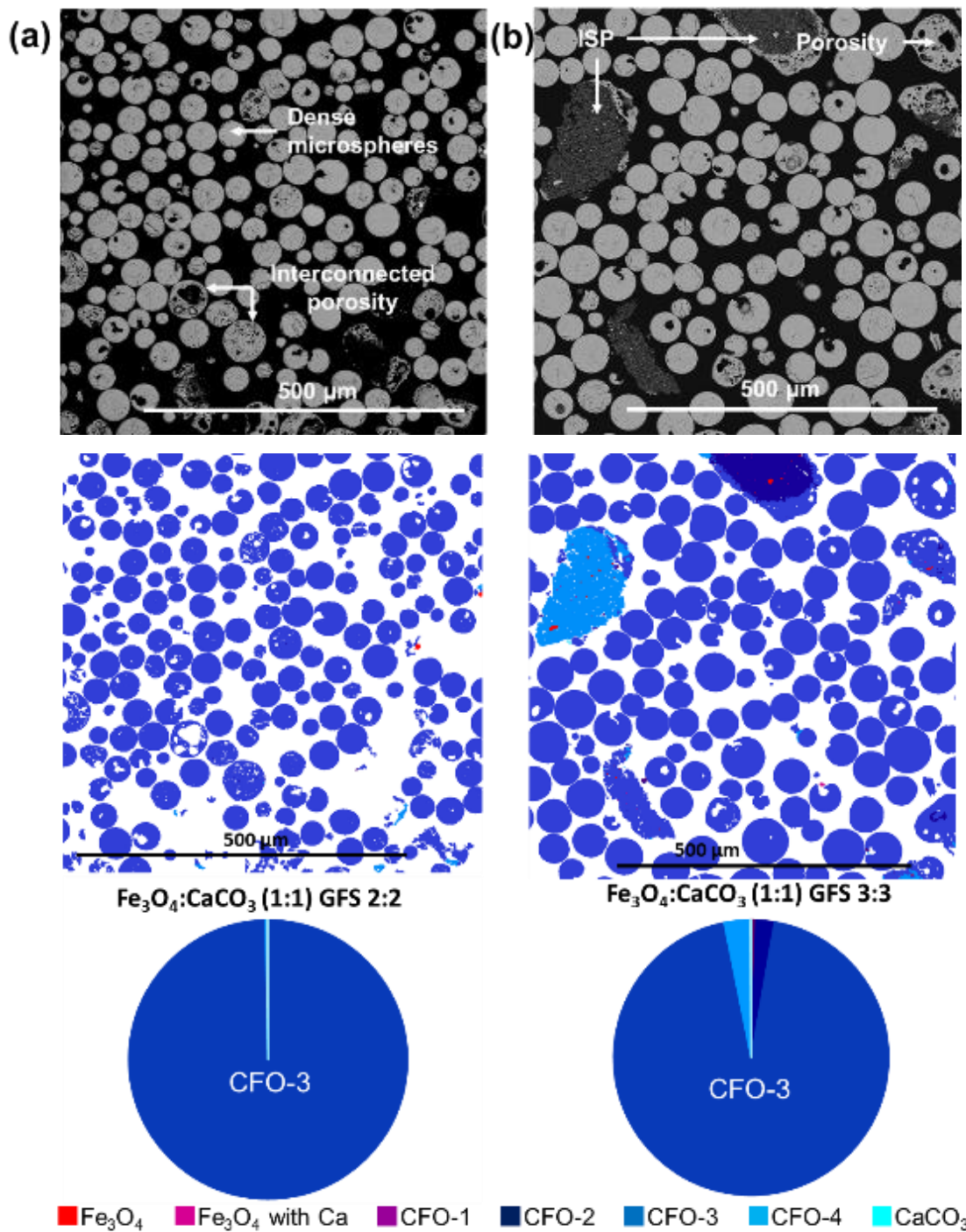


Figure 5.14. BSE images, MLA compositional analyses and associated pie-charts showing the mineral proportions (wt%) of flame-spheroidised $\text{Fe}_3\text{O}_4:\text{CaCO}_3$ microspheres (mass ratio 1:1) prepared using $< 5 \mu\text{m}$ magnetite: (a) 2:2, and (b) 3:3, following sieving and sectioning, illustrating microspheres, particles and minerals obtained. Mineral references shown on Table 4.10. (GFS: Gas flow setting; ISP: Irregular-shaped particles)

Table 5.12 Mineral proportion (wt%) of microsphere products, as a function of gas flow setting.

Gas flow setting	Fe ₃ O ₄ / wt%	Fe ₃ O ₄ with Ca / wt%	CFO-1 / wt%	CFO-2 / wt%	CFO-3 / wt%	CFO-4 / wt%	CaCO ₃ / wt%	Number particles analysed
2:2	0.0	0.0	0.0	0.1	99.6	0.1	0.1	1560
3:3	0.1	0.1	0.4	2.1	94.1	3.0	0.1	4127

As highlighted in Table 5.12, high levels of sample homogeneity were maintained, as a function of gas flow setting, with CFO-3, *i.e.*, srebrodolskite (Ca₂Fe₂O₅) the dominant mineral for all mass 1:1 sample sets. For the case of gas flow setting 3:3, the Ca₂Fe₂O₅ proportion decreased slightly compared to gas flow setting 2.5 : 2.5 (96.5wt%, Table 5.5), whilst a small amount of CFO-2 and CFO-4 was evident (Figure 5.15; Table 5.13). Notably, for the case of gas flow setting 2:2, the highest level of Ca₂Fe₂O₅ homogeneity (99.6 wt%) was returned (Figure 5.16; Table 5.14).

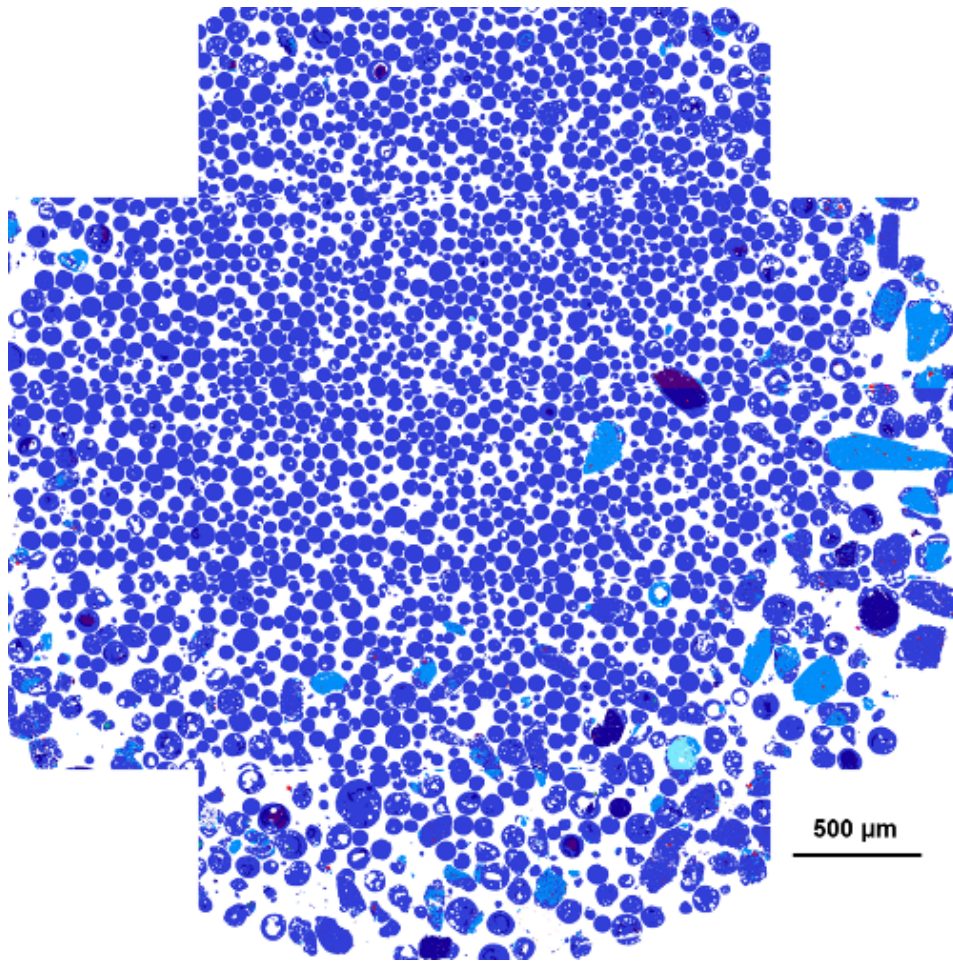


Figure 5.15. Full MLA compositional analysis and modal mineralogy for flame-spheroidised $\text{Fe}_3\text{O}_4\text{-CaCO}_3$ (mass ratio 1:1; **gas flow setting 3:3**), following sieving and sectioning, demonstrating high levels of CFO-3.

Table 5.13 Modal mineralogy for flame-spheroidised $\text{Fe}_3\text{O}_4\text{:CaCO}_3$ (mass ratio 1:1; gas flow setting 3:3).

Mineral	Particles	Weight %
Fe_3O_4	119	0.1
Fe_3O_4 with Ca	148	0.1
CFO-1	192	0.4
CFO-2	343	2.1
CFO-3- $\text{Ca}_2\text{Fe}_2\text{O}_5$	2946	94.1
CFO-4	343	3.0
CaCO_3	36	0.1

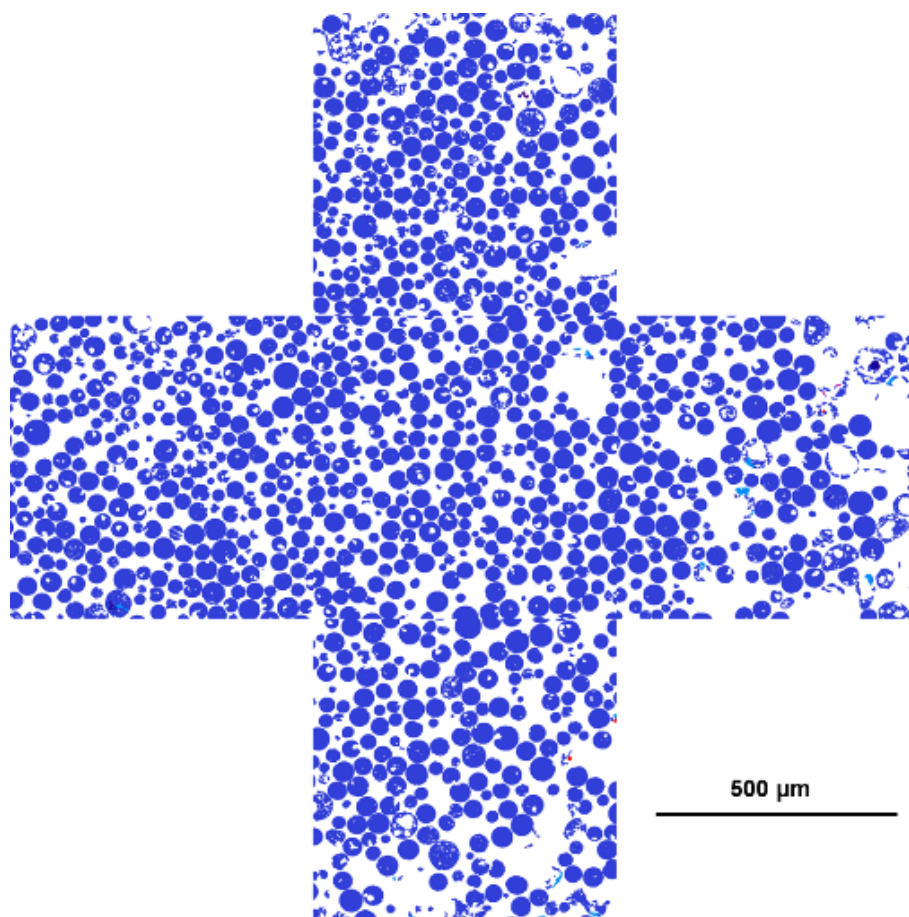


Figure 5.16 Full MLA compositional analysis and modal mineralogy for flame-spheroidised Fe_3O_4 - $CaCO_3$ (mass ratio 1:1; **gas flow setting 2:2**), following sieving and sectioning, demonstrating the highest levels of homogeneity (CFO-3) amongst all the samples investigated.

Table 5.14 Modal mineralogy for flame spheroidised- Fe_3O_4 : $CaCO_3$ (mass ratio 1:1; gas flow setting 2:2).

Mineral	Particles	Weight %
Fe_3O_4	5	0.0
Fe_3O_4 with Ca	2	0.0
CFO-1	3	0.0
CFO-2	24	0.1
CFO-3- $Ca_2Fe_2O_5$	1501	99.6
CFO-4	25	0.1
$CaCO_3$	0	0.1

Having investigated the gas flow setting parameter and its effect on microsphere morphology and mineralogy, the $\text{Fe}_3\text{O}_4:\text{CaCO}_3$ (1:1 mass ratio; 2:2 gas flow setting) sample exhibited the highest levels of compositional uniformity combined with good levels of interconnected porosity. The upcoming section focusses on further characterisation and induction heating investigations of these materials.

5.4 Compositionally uniform, $\text{Ca}_2\text{Fe}_2\text{O}_5$ magnetic microspheres

This section presents complementary investigations of optimised, $\text{Ca}_2\text{Fe}_2\text{O}_5$ dense and porous, magnetic microspheres (Fe_3O_4 size ($<5\ \mu\text{m}$); mass ratio (1:1); gas flow setting (2:2); with PVA used to bind the starting Fe_3O_4 and CaCO_3 powders). The effects of temperature on the precursor/porogen (1:1) powders (non-spheroidised) are explored initially, followed by structural, morphological, magnetic and compositional investigations of these flame-spheroidised microspheres. Finally, induction heating studies demonstrate the suitability of compositionally uniform $\text{Ca}_2\text{Fe}_2\text{O}_5$ magnetic microspheres (as compared to Fe_3O_4 precursor powders) for magnetic-mediated hyperthermia investigations.

5.4.1 $\text{Fe}_3\text{O}_4:\text{CaCO}_3$ (1:1 mass ratio) precursor powder

5.4.1.1 Thermal analysis

Thermogravimetric analysis (TGA) was used to profile wt% changes of the starting $\text{Fe}_3\text{O}_4:\text{CaCO}_3$ powder mix (non-spheroidised starting powders), as a function of increasing temperature. The TGA curve of Figure 5.17 demonstrated an initial 2.5 wt% increment from 40°C to 611°C, consistent with the oxidation of Fe_3O_4 to Fe_2O_3 , followed by a drop of 11 wt%, from 611°C to 712°C, which was attributed to decomposition of the CaCO_3 porogen within the sample.

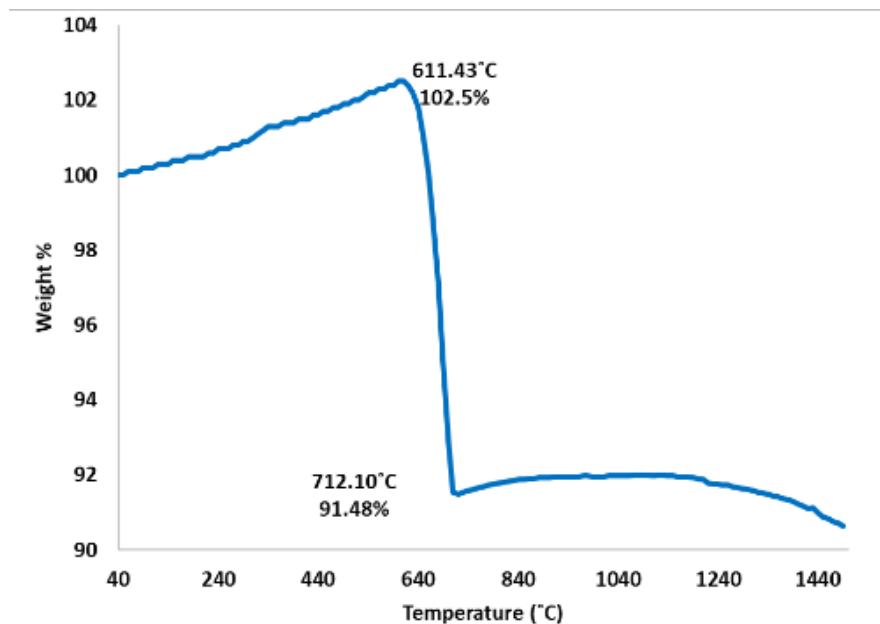


Figure 5.17 T-wt% curve for $\text{Fe}_3\text{O}_4:\text{CaCO}_3$ (1:1 mass ratio) precursor powders

After noting a temperature effect on the $\text{Fe}_3\text{O}_4:\text{CaCO}_3$ precursor powders (mass ratio 1:1), details of these structural transformations, at different temperature points, were investigated.

5.4.1.2 Structural transformations as a function of temperature

High temperature (HT) - XRD investigations were performed to profile structural changes of the starting powder mix, as a function of slowly increasing temperature ($10^\circ\text{C}/\text{min}$), revealing insights into the chemical transformation pathway. Overall, the evidence demonstrated a progressive transformation of $\text{Fe}_3\text{O}_4:\text{CaCO}_3$ to a mixture of CaCO_3 , Fe_2O_3 and $\text{Ca}_2\text{Fe}_2\text{O}_5$ (Figure 5.18). Figure 5.18a confirmed the starting powder to be a mixture of Fe_3O_4 precursor and CaCO_3 porogen, whilst their defining crystalline peaks progressively diminished with increasing temperature up to 550°C (Figure 5.18c, red arrows). A small peak attributable to the onset of Fe_2O_3 formation emerged at 450°C (Figure 5.18b, brown arrow). At 650°C and 750°C more intense and

sharper peaks indicative of the development of $\text{Ca}_2\text{Fe}_2\text{O}_5$ became evident (Figures 5.18d,e, blue arrows). A summary of the constituent products, as a function of temperature, is given in Table 5.15.

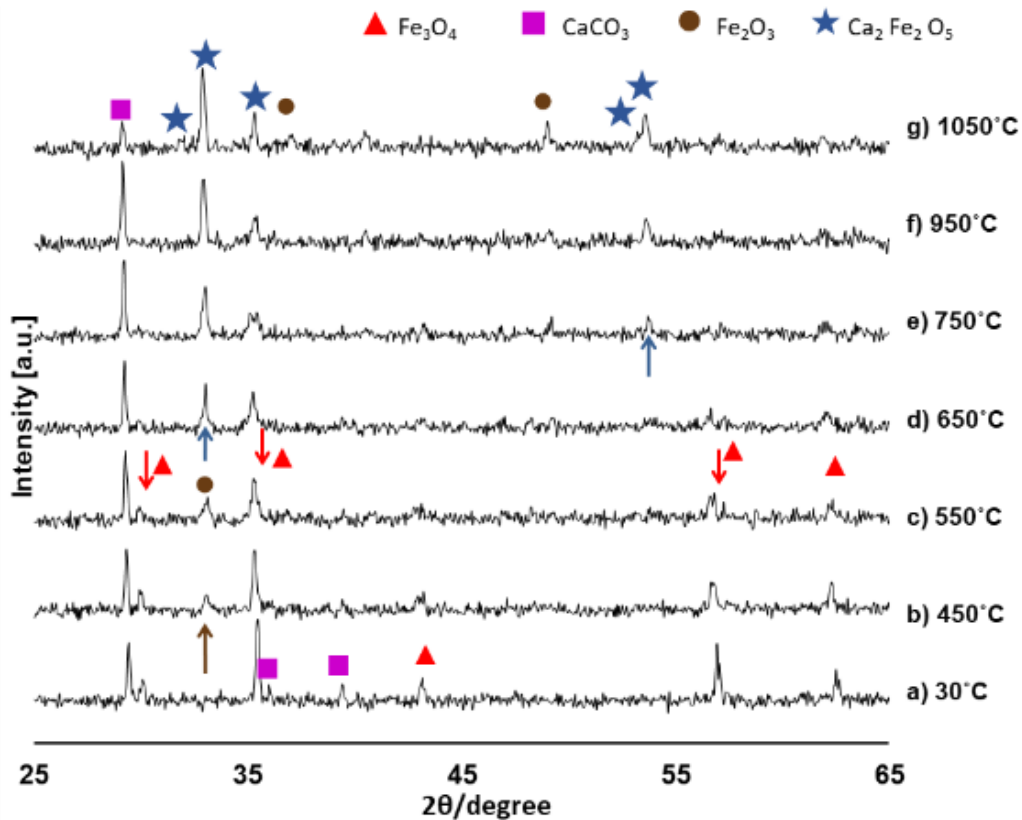


Figure 5.18 XRD patterns illustrating $\text{Fe}_3\text{O}_4:\text{CaCO}_3$ starting powder structural transformation, as a function of increasing temperature.

Table 5.15 Wt% constituents of mixed $\text{Fe}_3\text{O}_4:\text{CaCO}_3$ powders, as a function of increasing temperature measured by semi-quantitative analysis.

Phase	30 °C	450 °C	550 °C	650 °C	750 °C	950 °C	1050 °C
Fe_3O_4	30.2	11.9	11	6.1	-	-	-
CaCO_3	69.8	61.5	74.6	41.1	43.7	41.2	14.4
Fe_2O_3	-	26.6	14.4	20.4	21.7	26.2	38.1
$\text{Ca}_2\text{Fe}_2\text{O}_5$	-	-	-	32.5	34.6	32.6	47.4

To conclude the investigations of the $\text{Fe}_3\text{O}_4:\text{CaCO}_3$ (1:1) powders, the next section is concerned with magnetic saturation, as a function of slowly increasing temperature.

5.4.1.3 Magnetic properties as a function of temperature

Figure 5.19 presents evidence of a thermal effect on the magnetic expression of prepared $\text{Fe}_3\text{O}_4:\text{CaCO}_3$ mixed powders. At room temperature, the starting mixed powders showed a saturation magnetisation of $47.93 \text{ Am}^2/\text{kg}$. Hysteresis loops showed a significant decrease in magnetisation at 600°C ($2.65 \text{ Am}^2/\text{kg}$) and by 700°C the magnetisation was extremely low ($0.46 \text{ Am}^2/\text{kg}$). Magnetisation values, as a function of temperature, are summarised in Figure 5.20 and Table 5.16.

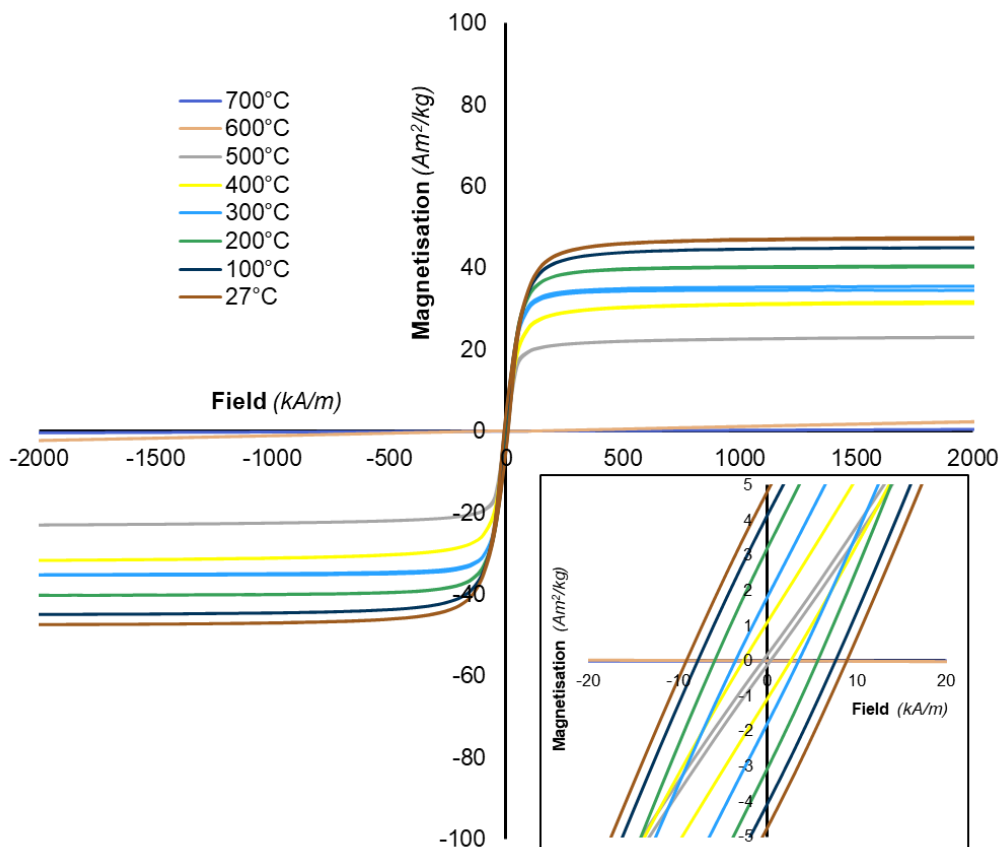


Figure 5.19 Magnetisation curves for $\text{Fe}_3\text{O}_4:\text{CaCO}_3$ (1:1) powders, as a function of temperature. Inset figure provides evidence of remanent magnetisation in all cases.

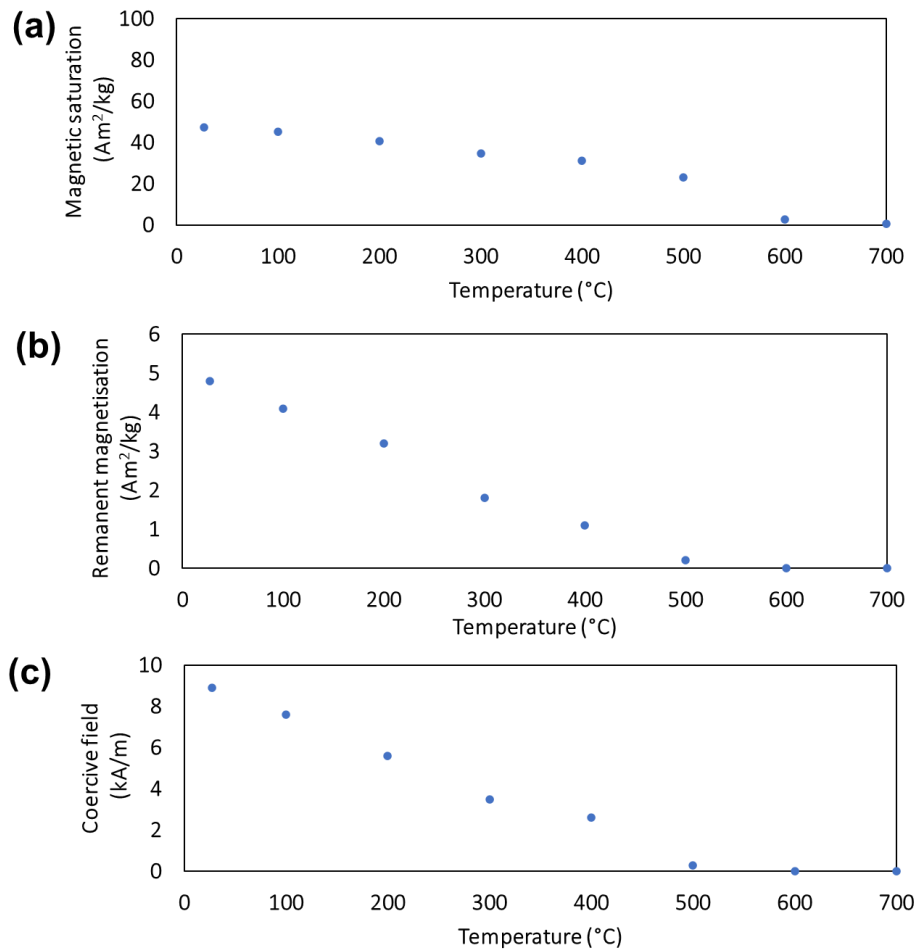


Figure 5.20 Graphs showing (a) magnetic saturation, (b) remanent magnetisation, and (c) coercive field for $Fe_3O_4:CaCO_3$ (mass ratio 1:1) powder mixtures, as a function of increasing temperature, revealing a decrease of magnetic properties.

Table 5.16 Magnetisation values for Fe_3O_4 ($\leq 5 \mu m$) : $CaCO_3$ prepared powders, as a function of increasing temperature.

Temperature	°C	27	100	200	300	400	500	600	700
Magnetic saturation	Am ² /kg (emu/g)	47.2	45.1	40.5	34.5	31.3	23.1	2.6	0.5
Remanent magnetisation	Am ² /kg (emu/g)	4.8	4.1	3.2	1.8	1.1	0.2	0	0
Coercive field	kA/m	8.9	7.6	5.6	3.5	2.6	0.3	0	0
	Oe	111	95	71	43	32	4	0	0

It was evident that magnetic saturation, remanent magnetisation and coercive field values progressively decreased, as a function of slowly increasing temperature.

In the next section, structural investigations of rapidly processed, flame-spheroidised $\text{Fe}_3\text{O}_4:\text{CaCO}_3$ (mass ratio 1:1, gas flow setting 2:2) microsphere products, is presented.

5.4.2 Structural characterisation of $\text{Ca}_2\text{Fe}_2\text{O}_5$ microspheres

5.4.2.1 X-ray diffraction (*unsieved microspheres*)

Figure 5.21 presents an XRD pattern for rapidly processed $\text{Fe}_3\text{O}_4:\text{CaCO}_3$ (mass ratio 1:1, gas flow setting 2:2) flame-spheroidised products (unsieved), confirming the presence of $\text{Ca}_2\text{Fe}_2\text{O}_5$ (srebrodolskite) (Table 5.17), Fe_3O_4 (magnetite), Fe_2O_3 (hematite) and CaCO_3 (calcite), being distinct from the CaCO_3 , Fe_2O_3 and $\text{Ca}_2\text{Fe}_2\text{O}_5$ products for the case of slowly-heated powders (Figure 5.18) where full consumption of Fe_3O_4 occurred.

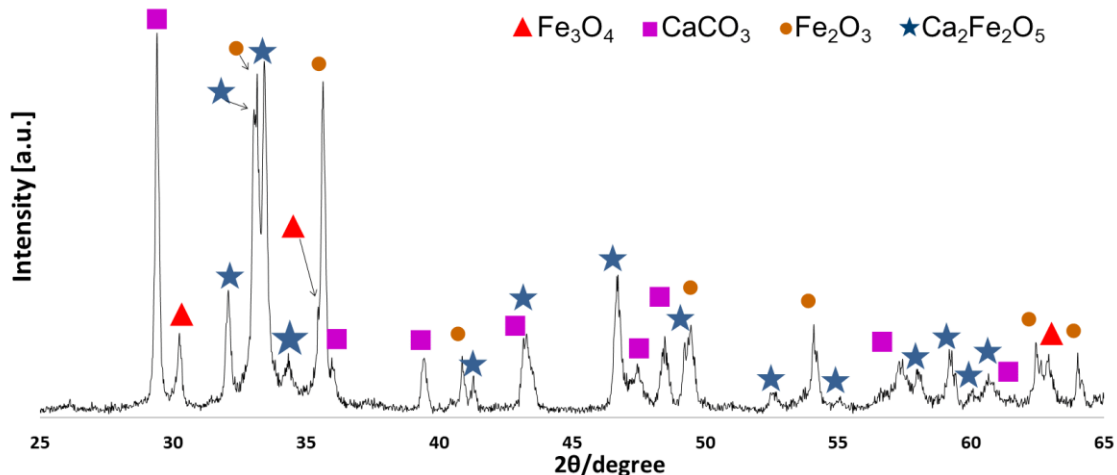


Figure 5.21 XRD pattern for flame-spheroidised $\text{Fe}_3\text{O}_4:\text{CaCO}_3$ (1:1 mass ratio; gas flow setting of 2:2).

Table 5.17 Srebrodolskite ($\text{Ca}_2\text{Fe}_2\text{O}_5$) Miller indices and correlated diffraction angles [278]

KHL	002	200	141	051	231	161	202
2θ	31.9	33.0	33.4	34.3	41.3	43.5	46.6
KHL	080	033	181	143	341	082	302
2θ	49.4	52.4	55.1	57.9	59.2	60.0	60.1

For the purpose of electron diffraction investigation, the microsphere products were sieved ($> 32 \mu\text{m}$) to remove excess unreacted (Fe_3O_4 and CaCO_3) and reacted (Fe_2O_3) particles, in advance of grinding and dispersion on a grid for investigation in the TEM.

5.4.2.2 Selected area electron diffraction (SAED) (*sieved microspheres*)

Compositionally uniform, flame-spheroidised $\text{Fe}_3\text{O}_4:\text{CaCO}_3$ products (mass ratio 1:1; gas flow setting 2:2), dominated by $\text{Ca}_2\text{Fe}_2\text{O}_5$ microspheres, were ground using mortar and pestle, dispersed in suspension and deposited onto an amorphous holey carbon film on a Cu TEM support grid, to create fragments sufficiently thin for investigation by electron diffraction. Figure 5.22a presents a cumulative selected area electron diffraction (SAED) pattern from these fine-scale, $\text{Ca}_2\text{Fe}_2\text{O}_5$ microsphere fragments. Well-defined rings are evident, indicative of a dispersion of fine-grained material. Identification of inner diffraction rings was consistent with crystal plane spacings of $\{020\}$, $\{200\}$ and $\{141\}$, corresponding to $\text{Ca}_2\text{Fe}_2\text{O}_5$. As highlighted in Table 5.17, Miller indices $\{200\}$ and $\{141\}$ correspond to the two more intense peaks. For the case of $\{020\}$, for which 2θ is found at 11.98, it was not observed on Figure 5.21 as it was out of the analysed range.

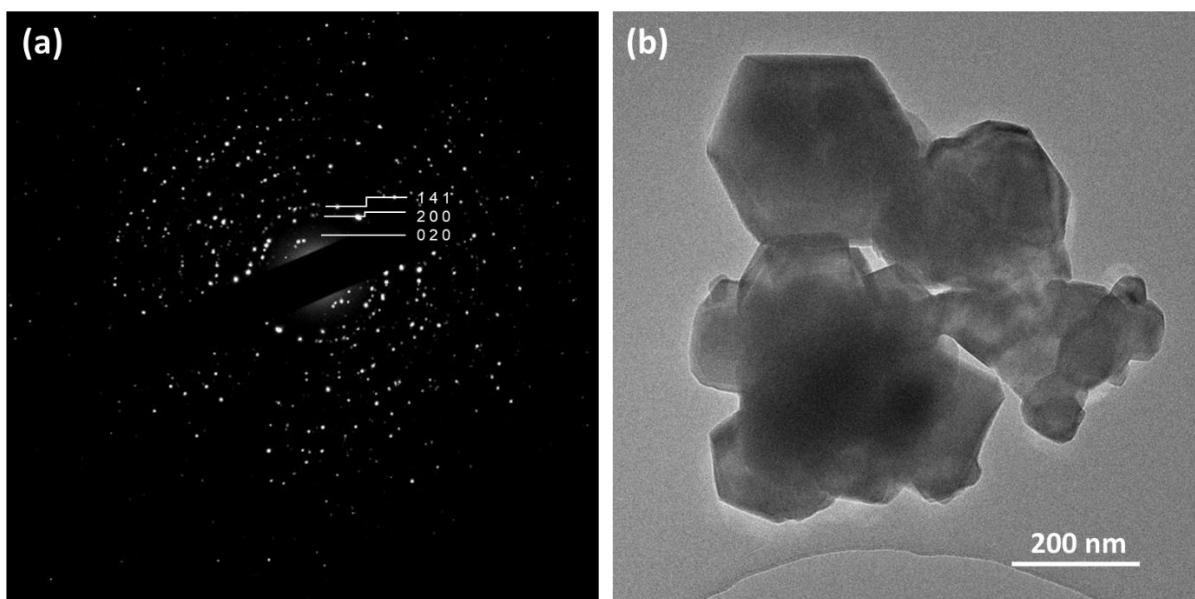


Figure 5.22. (a) Cumulative selected area electron diffraction (SAED) pattern for 120 stacked tilted fields of view, corresponding to compositionally uniform, flame-spheroidised $\text{Fe}_3\text{O}_4:\text{CaCO}_3$ (mass ratio 1:1; gas flow setting 2:2), i.e. $\text{Ca}_2\text{Fe}_2\text{O}_5$ microsphere fragments, following grinding; (b) Bright field diffraction contrast TEM image of a $\text{Ca}_2\text{Fe}_2\text{O}_5$ microsphere fragment.

Figure 5.22b shows a TEM image from a polycrystalline, $\text{Ca}_2\text{Fe}_2\text{O}_5$ microsphere fragment showing a range of grains sizes, with average crystallite size ~ 38 nm (estimated from associated XRD patterns using the Scherrer equation; FWHM = 0.225; $2\theta_{002} = 31.9^\circ$; $\lambda = 0.15406$ nm; Figure 5.21). These complementary structural investigations indicated a fine-scale crystallographic nature for these flame-spheroidised magnetic microsphere products, whilst also supporting the identification of $\text{Ca}_2\text{Fe}_2\text{O}_5$ as the dominant phase.

The following section looks at the microsphere morphologies in more detail, with particular attention given to the interconnective porosity of the microspheres.

5.4.3 $\text{Ca}_2\text{Fe}_2\text{O}_5$ microsphere topography (*unsieved*)

Figure 5.23a presents a low magnification SE image of these $\text{Ca}_2\text{Fe}_2\text{O}_5$ products, demonstrating a mixture of large porous (125 - 180 μm) and smaller dense (35 - 80 μm) microspheres, along with some small irregular-shaped particles. A total of 124 pores measured from five different porous microspheres showed a size range between 1.8 μm and 64.5 μm , respectively, with mean pore size of 13.1 μm (SD of 12.6 μm). Figure 5.23b shows a typical spheroidised porous microsphere in detail, whilst the magnified boxed region of Figure 5.23c demonstrates the interconnected porous microstructure. The prepared $\text{Fe}_3\text{O}_4:\text{CaCO}_3$ powders mixed with PVA, prior to flame-spheroidisation, are shown in Figure 5.23d. Comparatively, Figure 5.23e illustrates a large, porous microsphere (centre) and small dense microspheres (background).

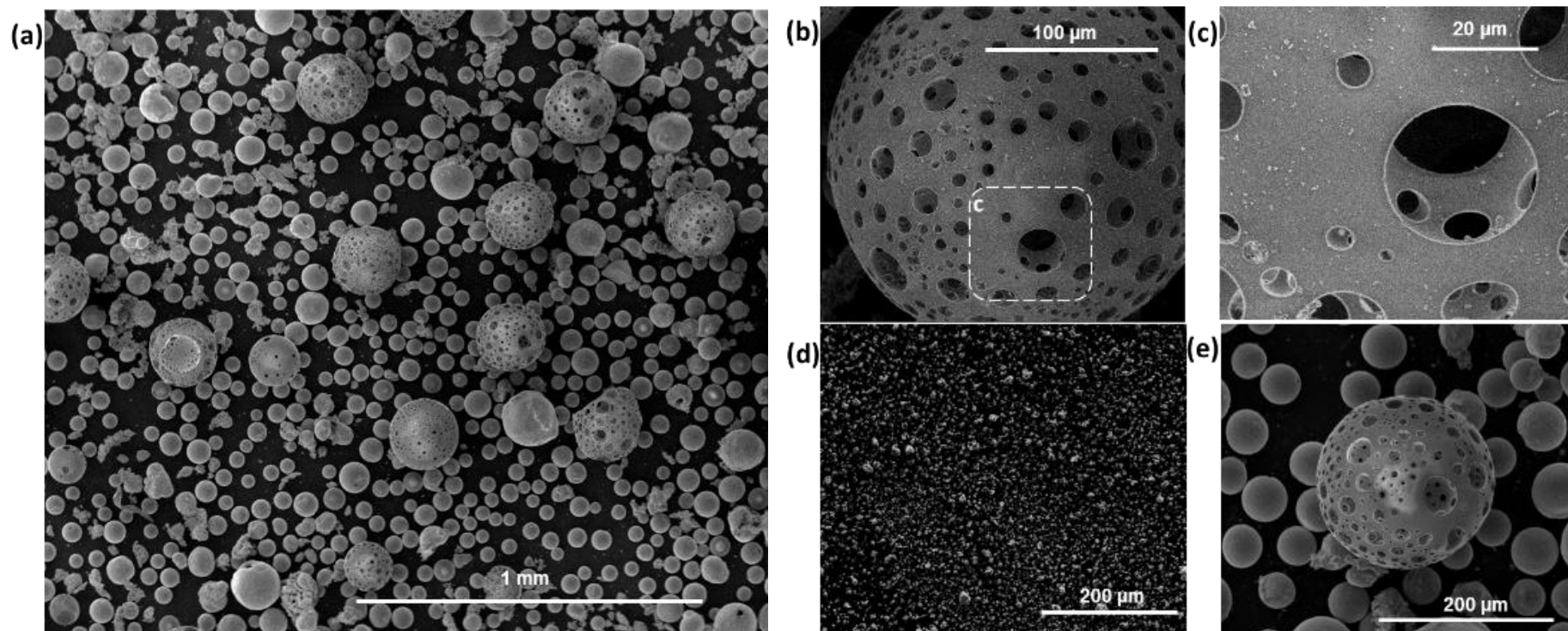


Figure 5.23. SE images of flame-spheroidised $\text{Ca}_2\text{Fe}_2\text{O}_5$ showing: (a) Small, dense and large, porous microspheres; (b) details of a porous microsphere; (c) microsphere interconnected porosity (boxed in region (b)). (d) Prepared $\text{Fe}_3\text{O}_4:\text{CaCO}_3$ starting powder mixture with PVA, as used for both flame spheroidisation (fast heating) and high temperature (slow heating) analyses. (e) $\text{Ca}_2\text{Fe}_2\text{O}_5$ porous microsphere (centre) and dense microspheres (background) following flame-processing.

The next section presents complementary surface chemistry characterisation data for these flame-spheroidised $\text{Ca}_2\text{Fe}_2\text{O}_5$ microspheres.

5.4.4 Surface chemical analysis of $\text{Ca}_2\text{Fe}_2\text{O}_5$ microspheres (*sieved*)

Complementary X-ray photoelectron spectroscopy studies were performed, to analyse the surface chemistry of the flame-spheroidised $\text{Ca}_2\text{Fe}_2\text{O}_5$ porous and dense microspheres. Figure 5.24a presents a survey spectrum of the srebrodolskite microspheres.

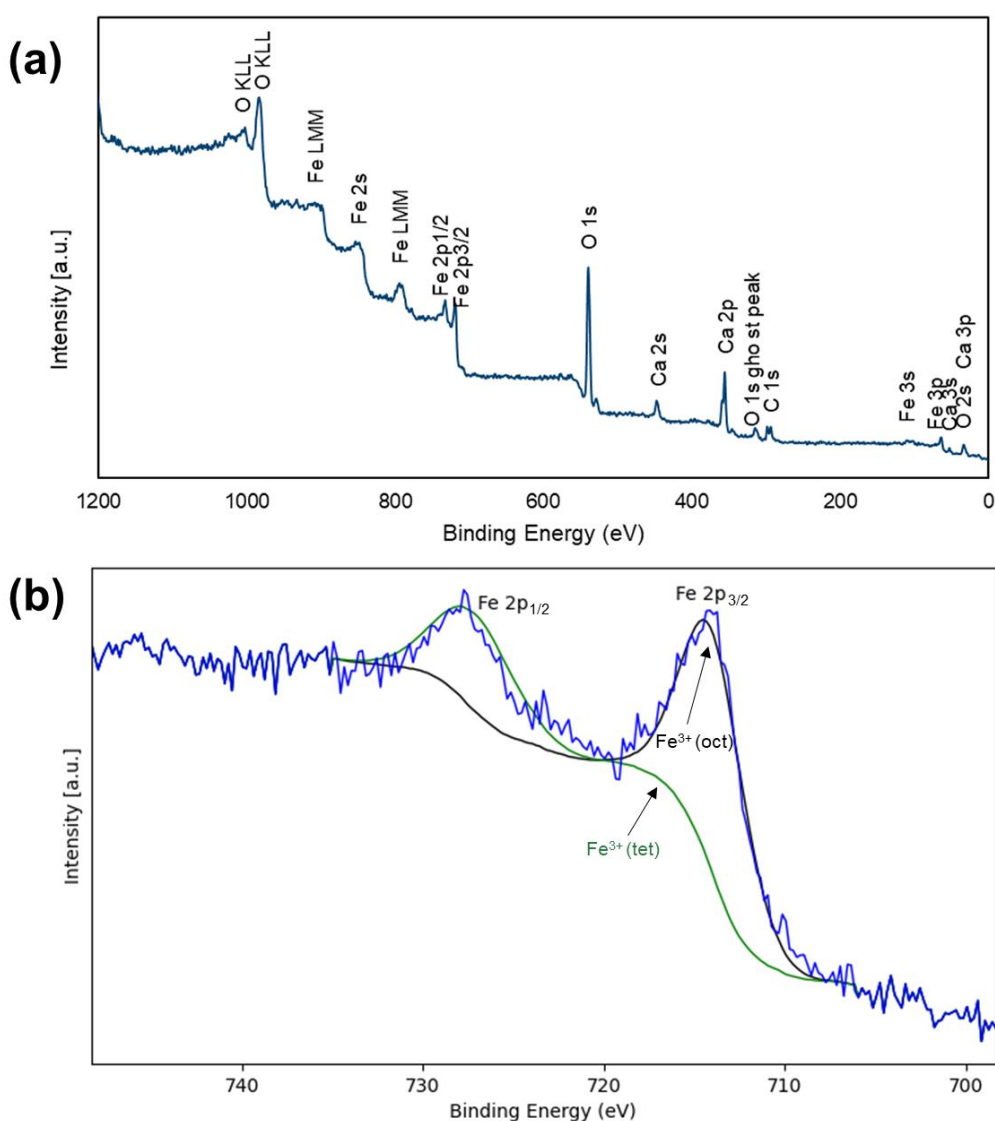


Figure 5.24 (a) XPS of flame-spheroidised $\text{Ca}_2\text{Fe}_2\text{O}_5$ porous and dense microspheres (1:1 mass ratio; 2:2 gas flow setting); **(b)** High-resolution XPS of Fe 2p

XPS spectra for the $\text{Ca}_2\text{Fe}_2\text{O}_5$ microspheres highlighted Ca 2p (355 eV), O 1s (539 eV) and Fe 2p (718 and 733 eV) peaks, with the latter splitting into two spin orbits (Fe $2p_{1/2}$ and Fe $2p_{3/2}$, Figure 5.24b) suggesting the presence of Fe^{3+} oxidation state in both tetrahedral and octahedral sites, characteristic for Fe-based brownmillerite minerals [279, 280].

The next section presents magnetic characterisation data for $\text{Fe}_3\text{O}_4:\text{CaCO}_3$ (1:1 mass ratio) both prior- and post- flame spheroidisation, as compared to Fe_3O_4 dense microspheres.

5.4.5 Magnetic characterisation of $\text{Ca}_2\text{Fe}_2\text{O}_5$ microspheres (*sieved*)

Figure 5.25 presents magnetisation curves for small ($\leq 5 \mu\text{m}$) precursor / porogen mixtures (1:1 $\text{Fe}_3\text{O}_4:\text{CaCO}_3$), prior and post flame spheroidisation, compared to Fe_3O_4 microspheres (Chapter 4). As summarised in Table 5.18, incorporation of porogen into the mixture led to a decrease of magnetisation saturation values. Nevertheless, it was noted that $\text{Fe}_3\text{O}_4:\text{CaCO}_3$ flame-spheroidised products showed significant magnetic saturation values around $8.9 \text{ Am}^2/\text{kg}$, clearly different from that exhibited by slowly-heated $\text{Fe}_3\text{O}_4:\text{CaCO}_3$ precursors (Figure 5.19).

Table 5.18 Magnetic saturation, remanent magnetisation and coercive field values for Fe_3O_4 dense microspheres, and $\text{Fe}_3\text{O}_4:\text{CaCO}_3$ (mass ratio 1:1) mixtures using ≤ 5 μm precursors, before and after flame-processing

Sample	Magnetic saturation	Remanent magnetization	Coercive Field / H_c	
	Am^2/kg (emu/g)	Am^2/kg (emu/g)	(kA/m)	(Oe)
Fe_3O_4 dense microspheres	96.3	0.8	0.5	6.7
$\text{Fe}_3\text{O}_4:\text{CaCO}_3$ (1:1) starting powders	47.0	3.6	6.7	84.9
$\text{Fe}_3\text{O}_4:\text{CaCO}_3$ (1:1) microspheres	8.9	0.9	8.7	109

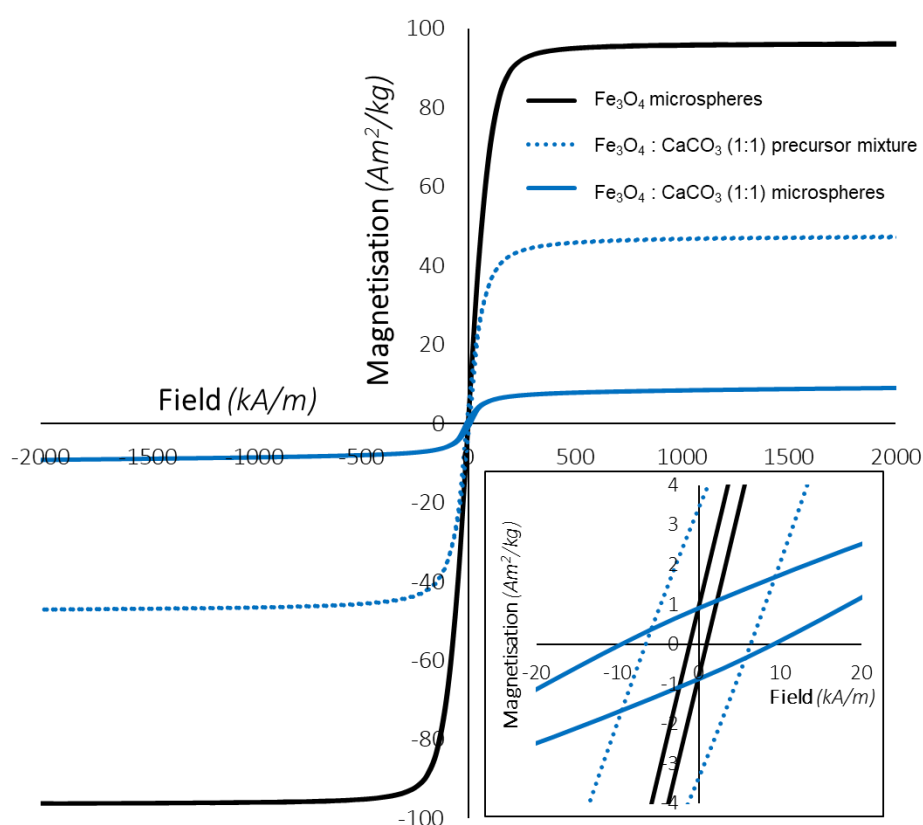


Figure 5.25 Hysteresis loop measurements for flame-spheroidised Fe_3O_4 microspheres, compared to $\text{Fe}_3\text{O}_4:\text{CaCO}_3$ (mass ratio 1:1) precursor powders and microsphere products, at 26.85°C . Inset figure provides evidence of remanent magnetisation in all cases.

Having investigated the $\text{Ca}_2\text{Fe}_2\text{O}_5$ microsphere morphologies and magnetic properties, the following section is concerned with the material's suitability for magnetic hyperthermia applications *via* induction heating.

5.4.6 Induction heating of $\text{Ca}_2\text{Fe}_2\text{O}_5$ microspheres

The potential of $\text{Ca}_2\text{Fe}_2\text{O}_5$ microspheres for magnetic mediated hyperthermia was evaluated *via* induction heating (Table 5.19). Figure 5.26 presents the evolution of temperature for the most homogeneous flame-spheroidised $\text{Ca}_2\text{Fe}_2\text{O}_5$ microsphere (mass ratio 1:1, gas flow setting 2:2), along with Fe_3O_4 and CaCO_3 starting powders in isolation, by way of control. The Fe_3O_4 powder showed high levels of induction heating, up to $\sim 130^\circ\text{C}$, but with evidence for lack of heating control, whilst CaCO_3 powder showed no induction heating as anticipated. Notably, homogeneous $\text{Ca}_2\text{Fe}_2\text{O}_5$ microspheres exhibited highly controlled heating to a constant level of 43.7°C which remained stable upon voltage decrease (150 to 35 V). Std. errors for induction heating measurements are shown in Table 5.20.

Table 5.19 Experimental parameters for the induction heating experiments.

Voltage / V	Power / W	Current / A	Magnetic field / kA/m (Oe)	Frequency / kHz
150	120	0.8	0.10 (1.2)	204
35	20	0.6	0.07 (0.9)	204

Table 5.20 Statistical analysis on induction heating measurements.

Std. Error	$\text{Ca}_2\text{Fe}_2\text{O}_5$ microspheres	Fe_3O_4 powder	CaCO_3 porogen
Slope	0.006150	0.02827	0.0009041
Y-intercept	0.4288	1.971	0.06303

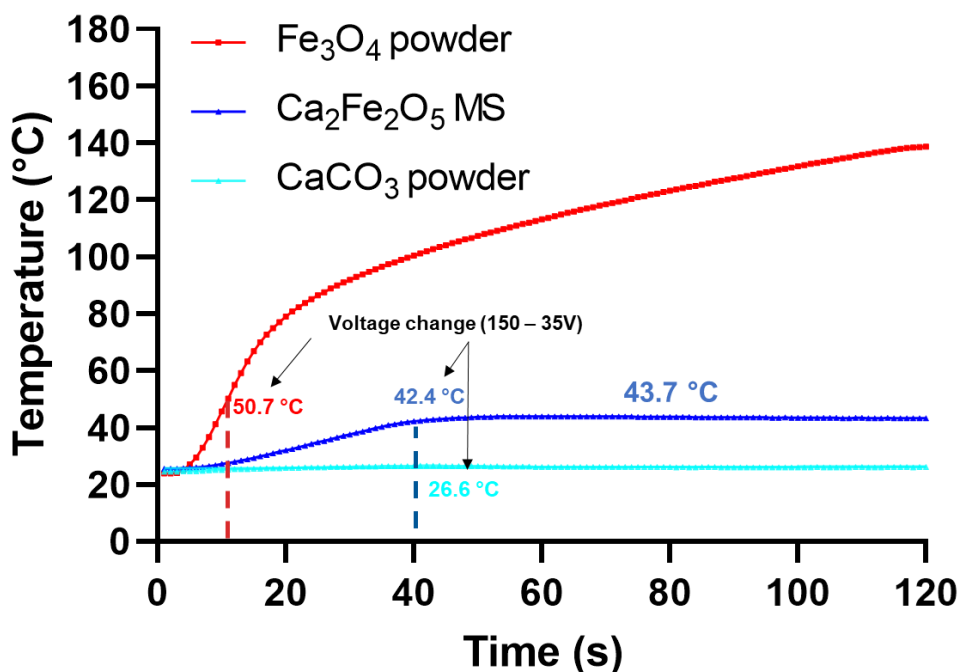


Figure 5.26 Induction heating curves for flame-spheroidised $\text{Ca}_2\text{Fe}_2\text{O}_5$ microspheres, compared with Fe_3O_4 and CaCO_3 starting powders, in isolation. Homogenous $\text{Ca}_2\text{Fe}_2\text{O}_5$ microspheres exhibited highly stabilised temperature control. (All curves display averages of triplicate measurements) (MS: Microspheres).

In summary, the flame spheroidisation of small ($\leq 5 \mu\text{m}$) magnetite precursor / porogen mixtures generated porous and dense microspheres, along with irregular shaped particles. Fine-scale details of microsphere products were observed on sectioned samples, revealing internal porosity for flame-spheroidised products. Moreover, variations in porosity levels (e.g., internal pores, interconnected pores) were observed as a function of gas flow setting. Compositional variations were noted on flame-spheroidised $\text{Ca}_2\text{Fe}_2\text{O}_5$, with excess / deficit of Fe / Ca, depending on porogen concentration. The highest levels of compositional uniformity, along with microspheres

with surface porosity and interconnected porosity, were observed on $\text{Ca}_2\text{Fe}_2\text{O}_5$ 1:1 mass ratio; 2:2 gas flow setting sample. High-temperature investigations (HT-XRD, HT-SQUID, and TGA) performed on $\text{Fe}_3\text{O}_4:\text{CaCO}_3$ (1:1) mixture, provided insights into the chemical reaction pathways, feedstock powder decomposition, and magnetic properties transformation, all acquired under slow heating conditions, different to the rapid, flame spheroidisation process. Finally, induction heating demonstrated the suitability of $\text{Ca}_2\text{Fe}_2\text{O}_5$ compositional uniform products for magnetic hyperthermia.

5.5 Discussion

5.5.1 Introduction

The present Chapter reports on the optimisation of the flame spheroidisation process (parameters of particle size, mass ratio of magnetite / porogen, gas flow setting and product sieving) for the production of magnetic microspheres using small ($<5 \mu\text{m}$) Fe_3O_4 precursors. Modification of these parameters produced a variety of products in terms of size (small and large), shape (dense and porous microspheres, and irregular-shaped particles), or a mixture of these, with distinct magnetic properties and compositions (depending on Fe or Ca excess/deficit). A schematic illustration (Figure 5.27) provides a detailed summary description of the development of magnetic microspheres using small ($<5 \mu\text{m}$) Fe_3O_4 precursors, as a function of particle size, mass ratio and gas flow setting.

5.5.2 Effect of precursor size

Firstly, the use of small ($<5 \mu\text{m}$) Fe_3O_4 precursors / CaCO_3 porogen combinations led to the development of improved products in terms of compositional uniformity, as compared to the large magnetite ($\leq 45 \mu\text{m}$) / CaCO_3 microspheres described in

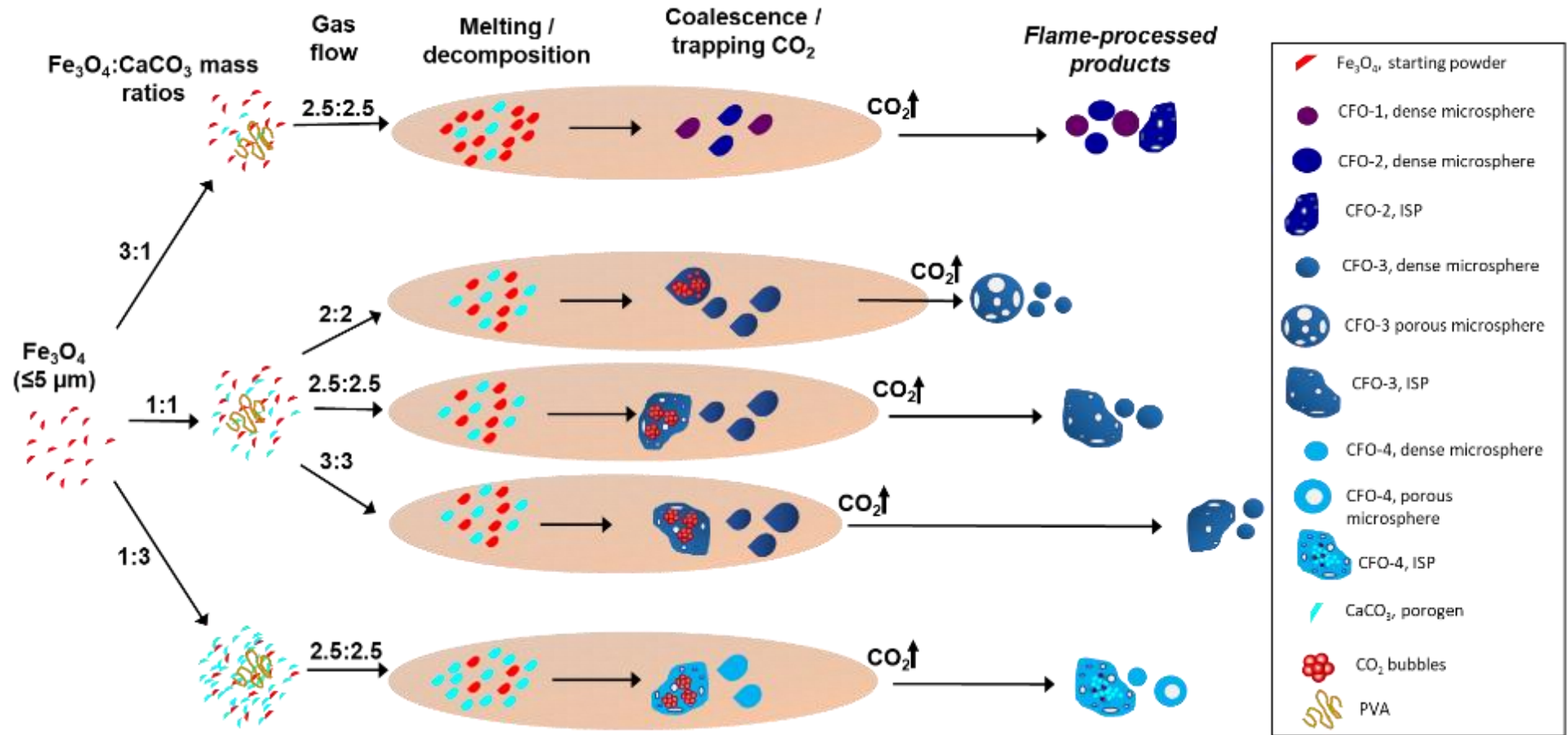


Figure 5.27. Flame spheroidisation of Fe_3O_4 (<math>< 5 \mu\text{m}</math>) : CaCO_3 microsphere products, as a function of mass ratio and gas flow setting.

Chapter 4. It is also noted that using Fe_3O_4 / CaCO_3 (1:1) precursors within the **same size range (both $\leq 5 \mu\text{m}$)** generated microsphere products with high levels of compositional uniformity, at all gas flow settings of 2:2, 2.5 : 2.5, and 3:3.

5.5.3 Effect of particle size distribution

Secondly, an important observation relates to the **heat transfer and rapid melting associated with** small particles. For flame-spray technologies, the volume fraction of unmelted/unreacted particles generally increases with increasing average particle size [272]; however, it also correlates with the particle size distribution [281, 282]. For example, it is noted that small Fe_3O_4 ($<5 \mu\text{m}$) powders produced larger quantities of **reacted materials**, *i.e.*, Fe_2O_3 (oxidised Fe_3O_4) and CaO (from CaCO_3 decomposition) (XRD data, Figure 5.3); as compared with larger ($\leq 45 \mu\text{m}$) Fe_3O_4 powders (*Chapter 4*), the flame-processed products of which exhibited larger amounts of remanent Fe_3O_4 and CaCO_3 **unreacted powders**. In this case, it is suggested that a broad particle size distribution (below $45 \mu\text{m}$) results in larger variations of particle heating during flame-processing, as distinct from small Fe_3O_4 precursors. Additional factors influencing small precursor powder collisions and chemical transformations may include particle thermophoretic forces [272, 283] and turbulence [266, 272, 284] generated within the flame.

5.5.4 Effect of mass ratio

Thirdly, the mass ratio parameter as applied to small magnetite / porogen combinations revealed a direct effect on the resultant mineral **composition** and **magnetic properties**. $\text{Ca}_2\text{Fe}_2\text{O}_5$ (srebrodolskite) was the only **calcium iron oxide phase** revealed for all ($<5 \mu\text{m}$) Fe_3O_4 : CaCO_3 flame-spheroidised samples investigated, similar to ($\leq 45 \mu\text{m}$)

$\text{Fe}_3\text{O}_4:\text{CaCO}_3$ microspheres (*Chapter 4*). Again, the suggestion is that rapid cooling and solidification mechanisms associated with the flame spheroidisation method allow for the formation of $\text{Ca}_2\text{Fe}_2\text{O}_5$ microsphere structures with modified compositions (excess / deficit of Fe / Ca atoms), *i.e.*, the microsphere products retained structural integrity for all mass ratio cases, but presented some Fe / Ca variations according to elemental availability. This could also be related to the unusual capacity of $\text{Ca}_2\text{Fe}_2\text{O}_5$ to support a number of defects [285, 286]. Indeed, this phenomenon was reinforced by compositional analyses of sieved samples. MLA mappings highlighted a clear trend towards iron deficit / calcium excess, as the mass ratio progressed from 3:1 towards 1:3; with a mass ratio 1:1 showing the highest levels of homogeneity (CFO-3, denominated as $\text{Ca}_2\text{Fe}_2\text{O}_5$). This compositional trend emphasised the importance of **maximum consumption** of the starting materials, occurring for a mass ratio of 1:1 & gas flow setting of 2.5 : 2.5; in which case the MLA data showed no evidence for any unreacted Fe_3O_4 and CaCO_3 from this sample. It should also be noted that **sieving** acts as simple way to improve sample homogeneity, by removing excess, small, unreacted Fe_3O_4 and CaCO_3 , and Fe_2O_3 reacted powders. In contrast, **Fe rich samples (mass ratio 3:1)** showed poor compositional uniformity, with two banded calcium iron oxide minerals observed (CFO-1 and CFO-2). Similarly, **Ca rich samples (mass ratio 1:3)** were associated with low porogen consumption, along with irregular shaped particles containing an excess of unreacted CaCO_3 and reacted CaO. In addition, the mass ratio parameter also influenced strongly the microsphere magnetic properties. An increase in porogen content (from $\text{Fe}_3\text{O}_4:\text{CaCO}_3$ 3:1 to 1:3) was directly related to a decrease of magnetic saturation and remanent magnetisation. This was attributed to the **incorporation of paramagnetic**

calcium atoms within the brownmillerite structure ($\text{Ca}_2\text{Fe}_2\text{O}_5$) as a function of mass ratio. As detailed in *Chapter 4*, the flame spheroidisation process leading to the formation of metastable materials, and hence products with modified ferromagnetic properties.

5.5.5 Effect of gas flow setting

Fourthly, the parameter of **gas flow setting** also influenced the development of porosity within the microspheres. Two types of porosity were identified for the sample set: *i.e.* internal pores (either interconnected or not) and surface pores. It is considered that surface pores were formed by molten droplets trapping and releasing CO_2 gas bubbles produced during porogen decomposition ($\text{CaCO}_3 \rightarrow \text{CaO} + \text{CO}_2$). In contrast, internal pores were created within molten drops as a consequence of unreleased CO_2 gas bubbles, during rapid solidification. Hence, it is noted that incremental porogen concentration (from $\text{Fe}_3\text{O}_4:\text{CaCO}_3$ 3:1 to 1:3 mass ratios) combined with an elevated gas flow setting *i.e.*, 3:3, is associated with higher internal porosity levels. Conversely, surface pores (with interconnected porosity) were more strongly associated with increased porogen content (from $\text{Fe}_3\text{O}_4:\text{CaCO}_3$ 3:1 and 1:3 mass ratios), but at a 2:2 gas flow setting. This effect is attributed to increased **residence time** of molten droplets within the oxy-acetylene flame, as a determining factor for the development of microsphere porosity. Considering that particle temperature is directly related to residence time of the particle within the flame [287, 288], a gas flow setting of 2:2 would facilitate CO_2 trapping and release, maximise the number of fully reacted precursor / porogen powders, thereby producing **fewer irregular shaped particles**. Furthermore, flame length can be controlled by adjusting the gas flow ratio [284]. As illustrated in Figure 5.27, the flame length decreased with increasing the gas flow setting (from 2:2 to 3:3), consequently

influencing particle residence time within the flame. In addition, the addition of **polyvinyl alcohol (PVA)** promoted binding of Fe_3O_4 precursors with CaCO_3 porogen particles and helped hold the agglomerated masses together. Accordingly, it is considered that porous microspheres are produced from the agglomeration of $\text{Fe}_3\text{O}_4:\text{CaCO}_3$ particles, with rapid melting and coalesce leading to the production of melt pools rendered spherical by surface tension, in advance of rapid solidification and phase separation, as appropriate.

5.5.6 Compositionally uniform, $\text{Ca}_2\text{Fe}_2\text{O}_5$ microsphere

5.5.6.1 Formation mechanism

Accordingly, to produce porous microspheres with interconnected porosity and high values of compositional homogeneity, the data suggested that optimised flame spheroidisation process conditions should be at the gas flow setting of 2:2 using a magnetite ($<5\ \mu\text{m}$) to porogen mass ratio 1:1. A detailed investigation of $\text{Fe}_3\text{O}_4:\text{CaCO}_3$ starting powders (mass ratio 1:1; gas flow setting 2:2), and a mixture of porous and dense flame-spheroidised $\text{Ca}_2\text{Fe}_2\text{O}_5$ magnetic microspheres (with smaller, unreacted particles of Fe_3O_4 , CaCO_3 and reacted Fe_2O_3 removed by sieving), allowed for a comprehensive formation mechanism to be established. Figure 5.28 schematically summarises the key stages of dynamic evolution proposed for these flame-spheroidised powders.

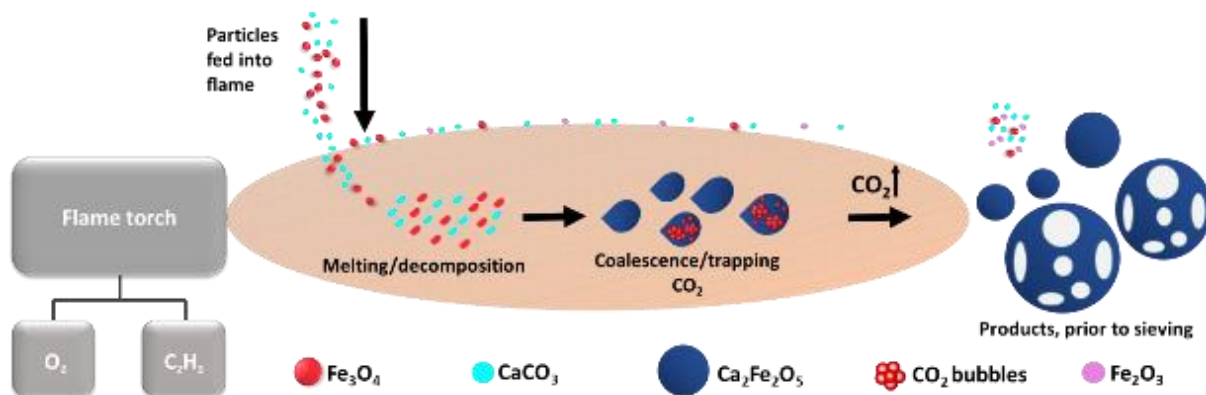


Figure 5.28 Schematic representation of dense and porous $\text{Ca}_2\text{Fe}_2\text{O}_5$ microsphere formation, via oxy-acetylene flame-processing (products prior to sieving).

Formation mechanisms associated with porosity development during flame-spheroidisation have been described previously for glass microspheres [53, 237, 240, 289] and, more recently, for ceramic [63, 64] and glass-ceramic microspheres [65]. For the case of the present magnetic microspheres, prepared $\text{Fe}_3\text{O}_4:\text{CaCO}_3$ particles were fed into a high-temperature flame ($\sim 3100^\circ\text{C}$) [290] where rapid melting and droplet coalescence occurred. The molten particles acquired spherical shape post exiting the flame due to surface tension. The development of compositionally uniform, dense and porous $\text{Ca}_2\text{Fe}_2\text{O}_5$ microspheres, upon rapid cooling and solidification, is consistent with the $\text{CaO}:\text{Fe}_2\text{O}_3$ (2:1 molar ratio) section of Ca-Fe-O phase diagram (Figure 5.29, 1:1 mass ratio) [188].

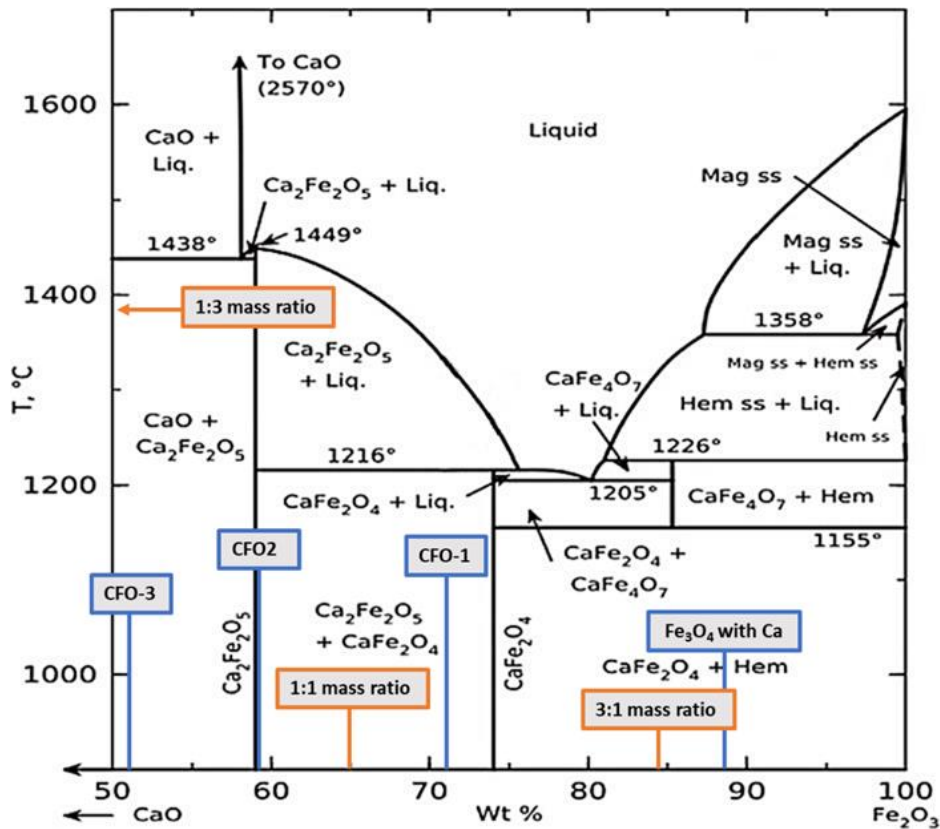


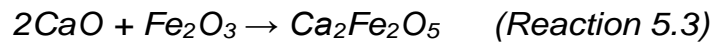
Figure 5.29 CaO-Fe₂O₃ phase diagram showing starting mass ratio positions (orange) and developed mineral codes (blue)

Fine scale diffraction patterns (SAED data) acquired from Ca₂Fe₂O₅ microsphere fragments, confirmed their resultant polycrystalline structure. It is considered that CO₂, produced during CaCO₃ decomposition, became trapped in the form of gas bubbles within molten droplets, and escaped rapidly at the point of solidification, and hence was responsible for the production of the larger Ca₂Fe₂O₅ microspheres exhibiting high levels of interconnected porosity (Figures 5.23b,c). The high compositional uniformity of these microspheres (Figure 5.16) indicated that product composition was established before the development of porosity.

5.5.6.2 High-temperature investigations

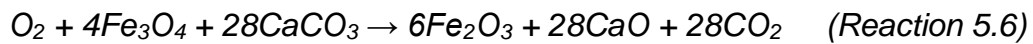
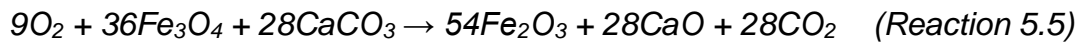
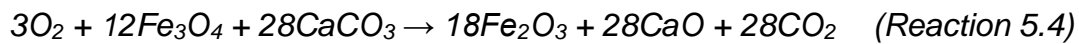
The evidence from HT-XRD, TGA and HT-SQUID investigations, all acquired under conditions of controlled heating rate, provided complementary information relating to particle decomposition and chemical pathways. The HT-XRD data (Figure 5.18, Table 5.15) showed a transition of magnetite to hematite upon slow heating between 30°C and 650°C, whilst TGA data (Figure 5.17) showing a 2.5% weight increment between 40 and 611°C; consistent with the initial stage of Fe_3O_4 oxidation (Reaction 5.1) [291]. Nonetheless, a complete conversion from Fe_3O_4 to Fe_2O_3 should produce a theoretical 3.3% weight increment [292]. The TGA study was performed on air, hence, it is suggested that the oxidation rate and oxidation kinetics of Fe_3O_4 precursors were influenced by ambient temperature [293] and particle size [294], and, consequently, partially oxidised (~ 76%). For the case of HT-SQUID data (Figure 5.19), a substantial drop of magnetic saturation, from 500°C to 600°C, was evident, attributable to transition across the Curie point of magnetite (~580°C). The TGA curve also showed substantial weight loss of 11%, between 611 and 712°C, consistent with the decomposition of CaCO_3 porogen to CaO and CO_2 evolution (Reaction 5.2). Indeed, it is noted that $\text{Ca}_2\text{Fe}_2\text{O}_5$ brownmillerite-type phase (srebrodolskite) formation can occur as a consequence of Fe_2O_3 and CaO reaction (Reaction 5.3), whilst the formation of mineral srebrodolskite is in agreement with previous work on $\text{CaO}:\text{Fe}_2\text{O}_3$ thermal processing [295, 296]. In particular, the formation of calcium ferrites ($\text{Ca}_2\text{Fe}_2\text{O}_5$ and CaFe_2O_4) in the range of 900 to 1200°C, as investigated by HT-XRD, indicated complete consumption of $\text{CaO}:\text{Fe}_2\text{O}_3$ by 1200°C [296]. This helps to explain the presence of residual Fe_2O_3 peaks at 1050°C in Figure 5.18g, with the absence of CaO peaks in Figure 5.18 being attributed to immediate reaction between

Fe₂O₃ and CaO once CaCO₃ had decomposed (Reaction 5.3). Figure 5.18 also showed that, above 750°C, Ca₂Fe₂O₅ peaks gradually become more intense, evidencing Ca₂Fe₂O₅ formation, whilst CaCO₃ peaks became less intense. Table 5.15 suggests a significant 26.8% loss of weight of CaCO₃ from 950°C (41.2%) to 1050°C (14.4%).



Conversely, XRD peaks attributable to Fe₃O₄ and CaCO₃ in Figure 5.21 were attributed to small particles of unmelted magnetite and porogen, with the suggestion that these particles were pushed to the periphery and coldest part of the flame, either elevated by the oxy-acetylene gas-pressure (Figure 5.28), or due to collision with other particles. Similarly, Fe₂O₃ XRD peaks identified within the flame spheroidised reaction products (Figure 5.21) suggests a reacted portion of Fe₃O₄ that was also pushed to the periphery of the flame. It is likely that the temperature at the periphery of the flame was sufficient to oxidise small particles of magnetite. A flame-generated melt composed of CaO:Fe₂O₃ (2:1 molar ratio) is consistent with the formation of Ca₂Fe₂O₅ upon rapid droplet cooling and solidification. Further, the CaO:Fe₂O₃ phase diagram (Figure 5.29) shows the starting Fe₃O₄:CaCO₃ 1:1 and 3:1 **mass ratio positions** (whilst noting that the 1:3 mass ratio corresponding to Fe₂O₃ 37.8wt% / CaO 62.2wt% would be off the scale to the left of the diagram), for comparison with the actual mineral products developed in practice (Table

4.10). The positions were calculated based on the molecular weights of reactants and products: Fe₃O₄ (231.5 g/mol), CaCO₃ (100.0 g/mol), Fe₂O₃ (159.7 g/mol) and CaO (56.07 g/mol). Importantly, it is considered that the following reactions occurred prior to Ca₂Fe₂O₅ formation (Reaction 5.3), and Fe₃O₄:CaCO₃ mass ratios 1:1 (Reaction 5.4), 3:1 (Reaction 5.5) and 1:3 (Reaction 5.6).



Notably, the starting Fe₃O₄ particle size has a significant effect on the Fe/Ca excess/deficit levels for the products (as detailed in section 5.5.3), along with the sieving of remanent, small particles (Fe₃O₄, CaCO₃, Fe₂O₃ and CaO) post-flame spheroidisation.

5.5.6.3 Magnetic properties

Magnetic characterisation for Ca₂Fe₂O₅ microspheres revealed a lower magnetic saturation value (8.9 Am²/kg, Table 5.18) as compared to magnetite powder (96.3 Am²/kg) and the magnetite/porogen powder mix (1:1) (47 Am²/kg). The ferromagnetic expression of the flame spheroidised Ca₂Fe₂O₅ microsphere products was attributed to their structural arrangements, comprising ordered oxygen vacancies with alternating layers of corner-sharing FeO₄ tetrahedra and FeO₆ octahedra [285, 297, 298]. This structure provided for two types of magnetic moment, arising from FeO₄ and FeO₆ [299],

corresponding to antiferromagnetic and weak ferromagnetic behaviour, respectively [285, 299].

5.5.6.4 Induction heating investigations

Having thoroughly characterised the $\text{Ca}_2\text{Fe}_2\text{O}_5$ microspheres, induction heating investigations were performed to test the suitability of these materials for magnetic hyperthermia applications. To address one of the main limitations related to magnetic hyperthermia which is controlling the temperature increase to between 40-45°C [300] induction heating measurements demonstrated the ability of $\text{Ca}_2\text{Fe}_2\text{O}_5$ microspheres to address this issue. It is considered that the mechanism of heat generation used in our study was *via* hysteresis loss, as revealed by magnetisation curves showing remanence. This mechanism is typical for multi-domain, ferro- and ferrimagnetic materials [10, 301]. Additionally, it was noted that the frequency used in our experiment (204 kHz) was within the clinical magnetic hyperthermia accepted range [11, 18, 130, 300, 302-304]. Magnetic particles used in magnetic-hyperthermia applications should heat rapidly in order to prevent patient discomfort [18]. Notably, the desired temperature was achieved in ~ 40 seconds. With regards to the low magnetic field reported here, it is noted that the magnetic hyperthermia effect can be achieved through the application of weak magnetic fields (<7.95 kA/m) [18]. Hence, these induction heating measurements show promising results for the $\text{Ca}_2\text{Fe}_2\text{O}_5$ magnetic microspheres developed in the present study. However, for formal validation, this part of the investigation would require further research using alternating magnetic fields, suitable for a clinical environment.

5.5.6.5 Biomedical applications

It is noted that manufactured, uniform $\text{Ca}_2\text{Fe}_2\text{O}_5$ microspheres have particular relevance in healthcare applications *e.g.*, as MRI contrast agents [305, 306] due their ferromagnetic expression. Alternatively, porous magnetic microspheres offer the key advantage of enabling drug delivery to specific tissues [307]. Nonetheless, only a modest number of large porous microspheres were developed, as compared to large numbers of dense microspheres. Hence, there is a need for improvement in porosity yields.

The next Chapter reports on the development of highly-porous, glass-ceramic ferromagnetic microspheres, towards cell viability investigations.

5.6 Summary

The manufacture of magnetic microsphere products using small ($<5\ \mu\text{m}$) Fe_3O_4 precursor can be achieved through control of particle size, mass ratio and $\text{O}_2/\text{C}_2\text{H}_2$ gas flow setting parameters associated with the facile, rapid, single-stage, flame spheroidisation process. In the present Chapter, optimised conditions for the processing of highly homogeneous $\text{Ca}_2\text{Fe}_2\text{O}_5$ porous (large, 125 - 180 μm) and dense (small, 35 - 80 μm) microspheres were identified. Direct evidence from structural, morphological and compositional investigations, along with complementary high-temperature studies (HT-XRD, TGA and HT-SQUID), have enabled a $\text{Ca}_2\text{Fe}_2\text{O}_5$ microsphere formation mechanism to be established, describing the dynamic evolution of starting 1:1 $\text{Fe}_3\text{O}_4:\text{CaCO}_3$ feedstock powder during the rapid flame spheroidisation process. It is proposed that the development of interconnected porosity during $\text{Ca}_2\text{Fe}_2\text{O}_5$ rapid solidification was a

consequence of the production of CO₂ gas bubbles (arising from decomposition of the CaCO₃ porogen), trapped within coalescing molten droplets. The compositionally uniform Ca₂Fe₂O₅ ferromagnetic microspheres (Fe₃O₄:CaCO₃ 1:1 mass ratio / 2:2 gas flow setting) showed relevance for magnetic hyperthermia applications as demonstrated with a simple induction heating experiment, as these flame spheroidised Ca₂Fe₂O₅ products delivered a controlled temperature increase (43.7°C).

6.0 Development of ferromagnetic porous and dense glass-ceramic microspheres for biomedical applications

6.1 Introduction

The first part of the present Chapter demonstrates the formation of **dense, glass-ceramic microspheres** manufactured *via* the flame spheroidisation process. Combinations of Fe_3O_4 ($\leq 45 \mu\text{m}$) precursor powder and phosphate-based glass (40P₂O₅-16CaO-24MgO-20Na₂O in mol%) denoted as P40, were investigated as a function of **1:1, 4:1 and 16:1 mass ratios** in the absence of CaCO₃ porogen. Building upon initial knowledge gained, the second part of this Chapter reports on **highly porous, ferromagnetic glass ceramic P40-Fe₃O₄ microspheres** (125 – 200 μm) also developed *via* the flame spheroidisation process.

Scanning electron microscopy (SEM) was used for the observation of microsphere topography. Structural investigations were performed using X-ray diffractometry. Magnetic investigations of the glass-ceramic products were performed via SQUID magnetometry. Fine-scale details (*e.g.*, porosity, phase separation) of sectioned microsphere samples were visualised using backscattered electron (BSE) imaging. Compositional investigations were performed *via* mineral liberation analysis (MLA) & energy dispersive X-ray spectroscopy (EDS). The suitability of the microsphere products for controlled delivery of heat was evaluated using an induction heating coil system. Complementary, cytocompatibility investigations of the P40-Fe₃O₄ porous microspheres

were conducted, and compared with Fe_3O_4 dense microspheres (*Chapter 4*), $\text{Ca}_2\text{Fe}_2\text{O}_5$ microspheres (*Chapter 5*), and P40 dense microspheres, all as controls.

6.2 P40- Fe_3O_4 dense microspheres (*no porogen*)

The quaternary phosphate-based glass 40- P_2O_5 -16CaO-24MgO-20 Na_2O (mol%), denoted P40, was produced using the melt-quench technique (*Chapter 3 – Materials and Methods*). The P40 (63 – 25 μm) and Fe_3O_4 (≤ 45 μm) powders (1:1, 4:1 and 16:1 mass ratios) were then processed *via* the flame spheroidisation method (2.5 : 2.5 gas flow setting). Figure 6.1 shows a summary of the key steps for sample preparation, flame spheroidisation and characterisation of the P40- Fe_3O_4 dense microspheres.

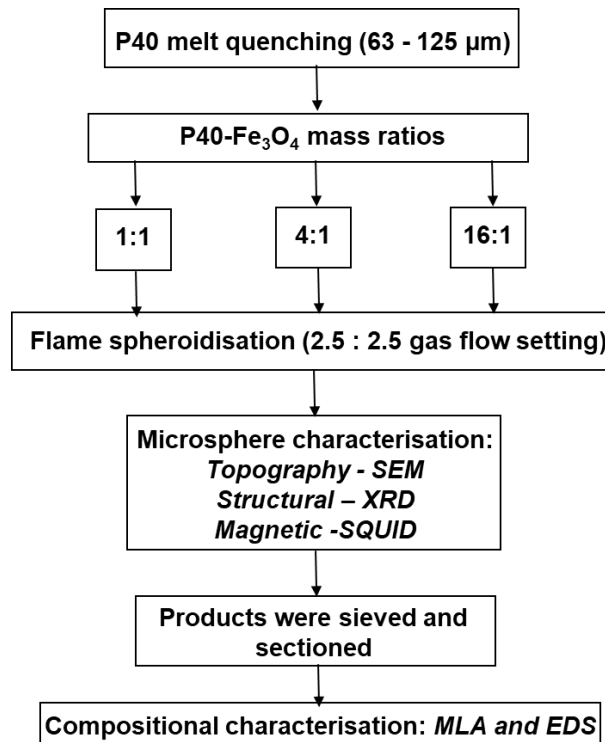


Figure 6.1 Flow diagram summarising the key steps followed for the manufacture of P40- Fe_3O_4 dense microspheres.

6.2.1 Microsphere topography (*unsieved*)

Figures 6.2(a-c) show low-magnification secondary electron (SE) images of flame-spheroidised P40-Fe₃O₄, for mass ratios of (a) 1:1, (b) 4:1 and (c) 16:1. For all cases, well-defined spherical morphologies were revealed. Notably, no irregular-shaped particles were present, attributed to the phosphate-based glass low melt temperatures and hence high viscosity. As anticipated, no surface porosity was observed. As the absence of irregular-shaped particles among the microsphere samples was noted, the products were not sieved or sectioned until compositional investigations had taken place.

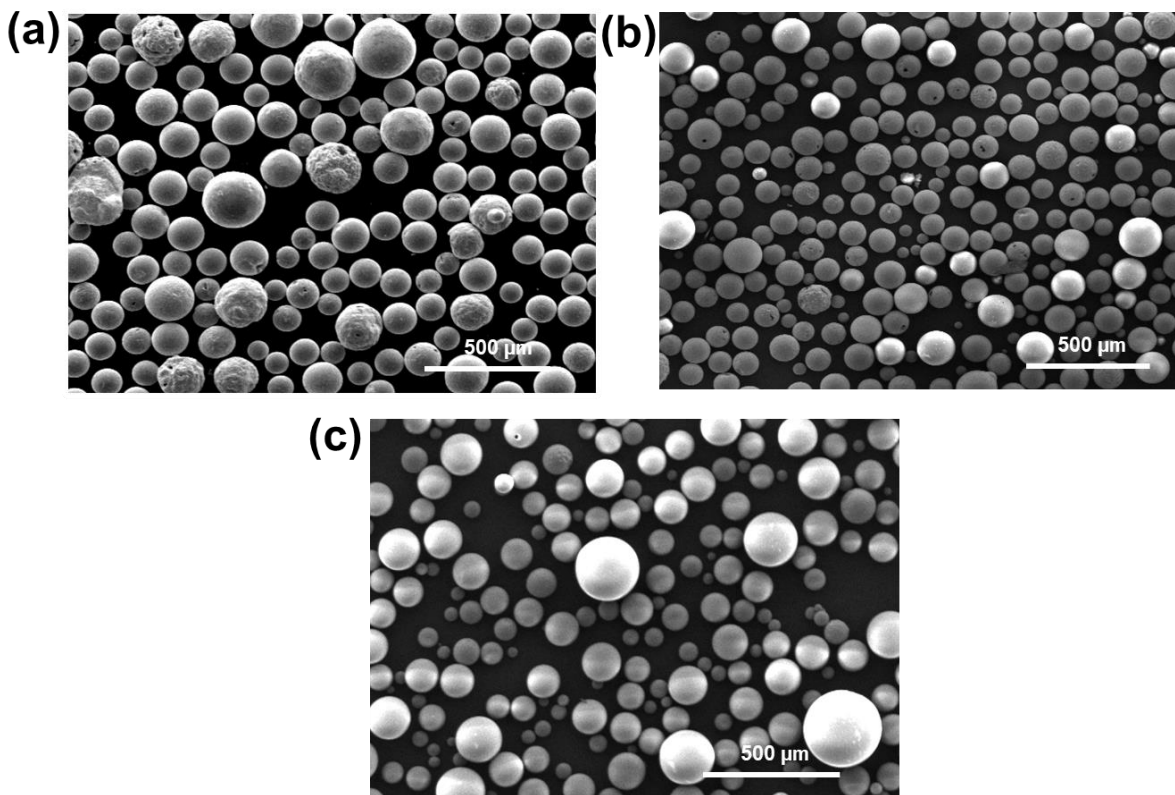


Figure 6.2 SE images for flame-spheroidised microspheres P40-Fe₃O₄, for different mass ratios (a) 1:1 (~120 – 265 μm), (b) 4:1 (~50 – 250 μm), and (c) 16:1 (~50 – 300 μm).

6.2.2 Structural characterisation (*unsieved*)

XRD investigations were performed to appraise the structural properties of the flame-spheroidised P40:Fe₃O₄ microspheres produced, as a function of mass ratio. Figure 6.3 shows XRD patterns for flame-spheroidised products (mass ratios of 1:1, 4:1 and 16:1) corresponding to the sample sets imaged in Figures 6.2(a-c). Structural analysis for P40:Fe₃O₄ (mass ratio 1:1) confirmed the presence of MgFeO (magnetite, magnesian) (ICDD PDF no. 01-076-2587) and Na₃Fe₂(PO₄)₃ (sodium iron phosphate) (ICDD PDF no. 00-045-0319). For the case of 4:1 mass ratio, weaker peaks for MgFeO were revealed and a slight curvature peak was noted, akin to an amorphous hump, most likely due to the P40 amorphous structure. Comparatively, a more prominent curvature of the baseline consistent with amorphous P40 glasses was noted for the 16:1 mass ratio samples.

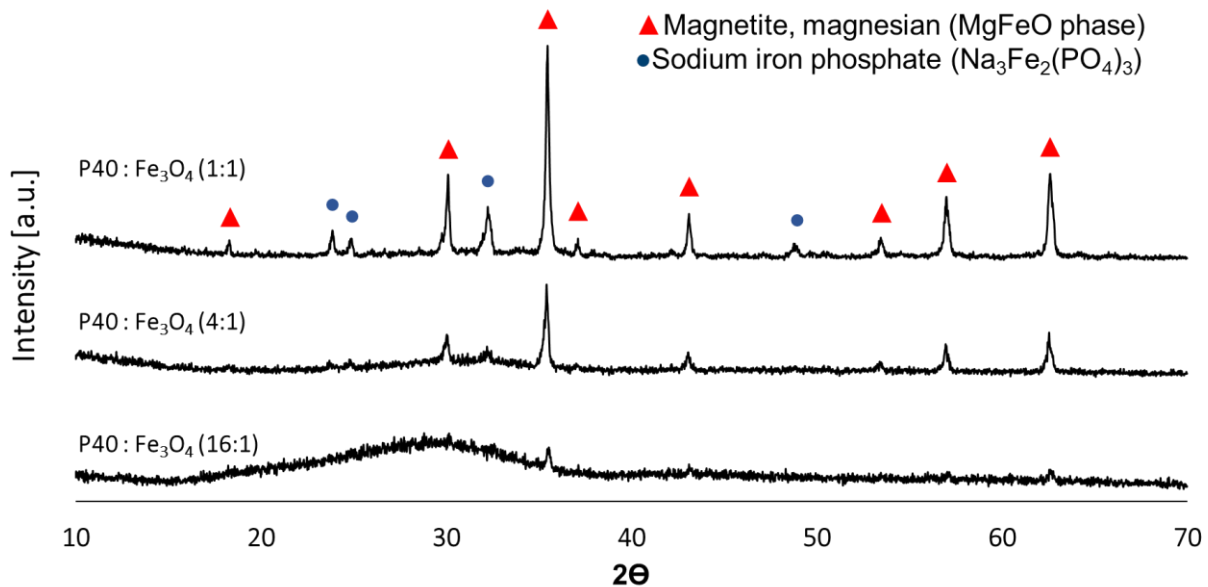


Figure 6.3 XRD patterns for flame-spheroidised P40:Fe₃O₄ (mass ratios 1:1, 4:1 and 16:1).

Evidently, the progression towards higher P40 content (mass ratio from 1:1 to 16:1) was associated with a reduction in magnesian (MgFeO) and sodium iron phosphate ($\text{Na}_3\text{Fe}_2(\text{PO}_4)_3$) peak intensities, whilst a prominent curvature typical of amorphous materials emerged (noting that amorphous hump shifted as a function of mass ratio, an indicative of different species forming). Importantly, no structural evidence corresponding to Ca-based phases was shown in XRD attributed to the allocation of calcium atoms in the amorphous phase of the products or within the interstitial sites of MgFeO (detailed in 6.4.2.4). The following section presents magnetic investigations of these P40- Fe_3O_4 dense microspheres.

6.2.3 Magnetic characterisation via SQUID magnetometry (*unsieved*)

Magnetic characterisation provided information on magnetic saturation, remanent magnetisation and coercive fields for these P40- Fe_3O_4 dense microspheres, whilst noting the effect of mass ratio on magnetic properties. Figure 6.4 presents hysteresis loops for flame-spheroidised P40 glass to Fe_3O_4 precursors mass ratios of 1:1, 4:1 and 16:1, respectively, compared to Fe_3O_4 dense microspheres (*Chapter 4*) and P40 dense microspheres.

Table 6.2 summarises the magnetic properties of these flame-spheroidised products as a function of mass ratio. As expected, the evolution towards decreased magnetite content (mass ratio from 1:1 to 16:1) revealed a decrease in magnetic saturation values, consistent with the findings of *Chapters 4* and *5*.

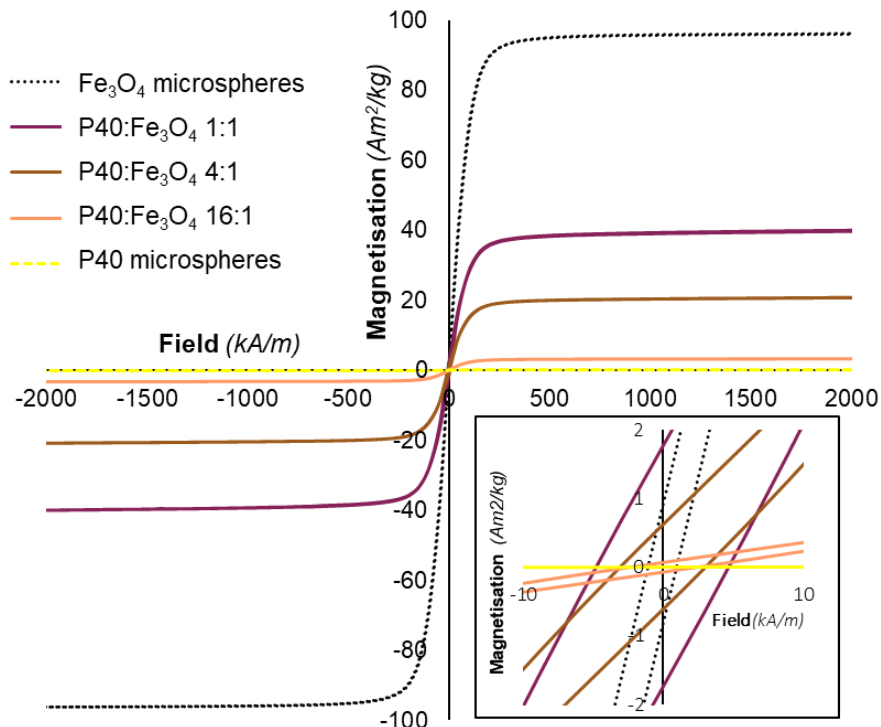


Figure 6.4 Hysteresis curves for P40-Fe₃O₄ dense microspheres (mass ratios 1:1, 4:1 and 16:1) at 26.85°C. Inset figure provides evidence for microsphere remanent magnetisation.

Table 6.2 Magnetic measurements for P40-Fe₃O₄ dense microspheres, as a function of mass ratio, compared to Fe₃O₄ and P40 dense microspheres.

Microsphere sample	Mass ratio P40:Fe ₃ O ₄	Gas flow setting Arb. units	Magnetic saturation / M _s	Remanent Magnetisation / M _r	Coercive Field / H _c	
			Am ² /kg (emu/g)	Am ² /kg (emu/g)	(kA/m)	(Oe)
Fe ₃ O ₄	-	2.5:2.5	96.3	0.8	0.5	6.7
P40:Fe ₃ O ₄	1:1		39.5	1.7	4.4	56
	4:1		20.8	0.6	2.8	36
	16:1		3.2	0.1	1.9	24
P40	-		0.0	0.0	0.0	0.0

The next section presents compositional investigations performed on P40-Fe₃O₄ dense microspheres, as a function of mass ratio, following sample preparation (sieving and sectioning).

6.2.4 Compositional analyses (*sieved and sectioned*)

6.2.4.1 Mineral liberation analysis

Associated BSE imaging and MLA analyses highlighted details of the microsphere morphologies and revealed a compositional transformation as a function of P40-to-Fe₃O₄ mass ratio. Figure 6.5 shows BSE images and mineral mapping analysis for sieved, resin embedded and cross-sectioned P40-Fe₃O₄ microspheres, corresponding to the sample sets shown in Figure 6.2. Table 6.3 summarises compositional differences across the sample set, obtained using MLA, with a strong trend towards the development of banded P40 / Fe-based mineral compositions.

Table 6.3 Mineral proportions (wt%).

Mass ratio P40:Fe ₃ O ₄	P40	P40-Fe	Fe-P40	Fe ₃ O ₄	Fe ₃ O ₄ with Ca	Other	Number of particles analysed
1:1	0.1	0.7	58.8	22.6	15.7	2.1	8,925
4:1	0.7	56.6	29.3	8.6	4.5	0.3	1,202
16:1	79.8	4.5	6.9	5.1	3.1	0.6	1,906

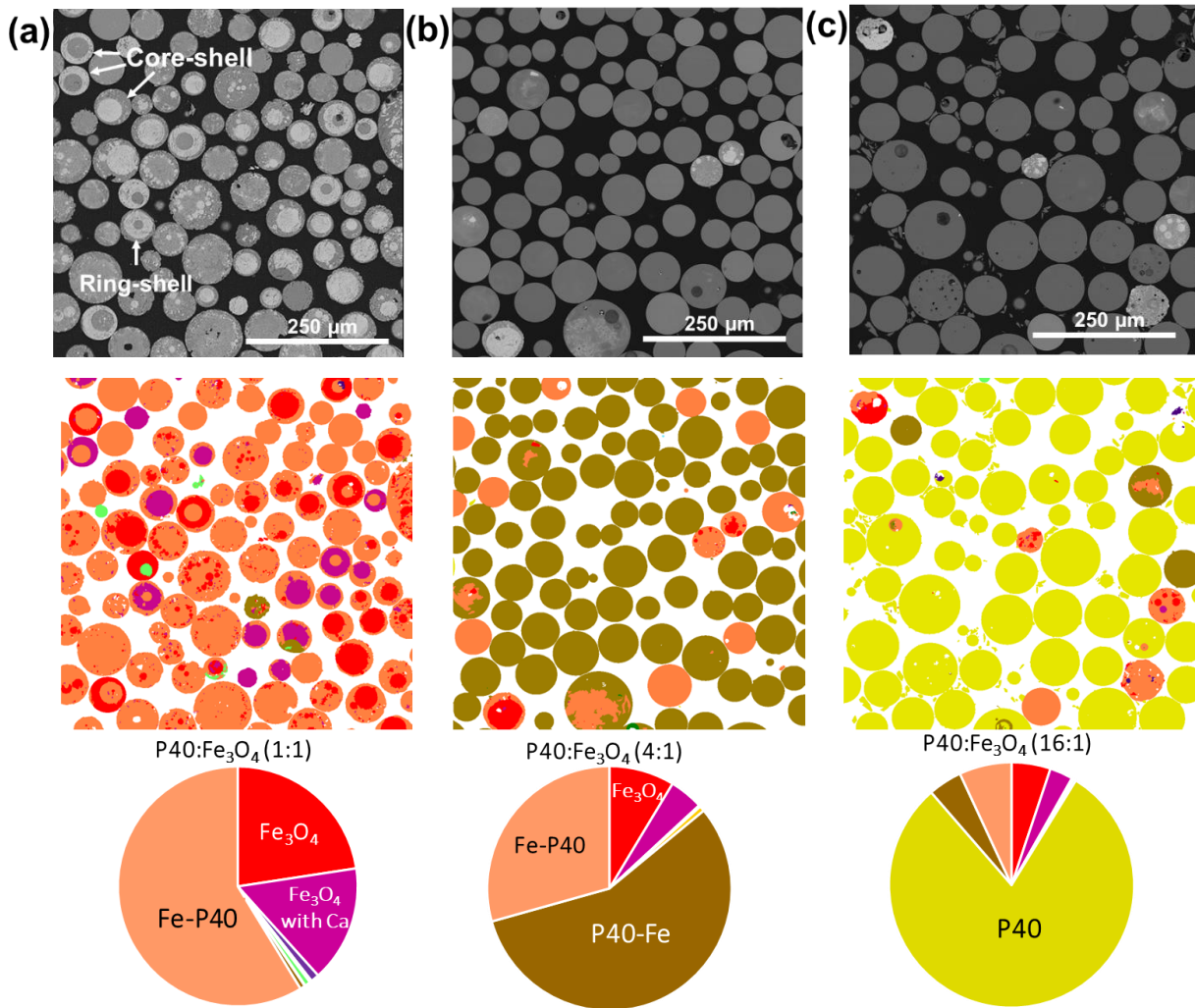


Figure 6.5 BSE and MLA compositional analyses and charts showing mineral proportions (wt%) of flame-spheroidised P40-Fe₃O₄ magnetic microspheres: (a) 1:1, (b) 4:1 and (c) 16:1, following sieving and sectioning, illustrating the developed dense microspheres and associated minerals obtained.

Correlated mineral reference data and colour codes, as a function of Fe/Ca/P variations, are summarised in Table 6.4 and Figure 6.6, respectively. Figures 6.5(a-c) show BSE images and MLA analyses of sieved, resin embedded and sectioned, flame-

spheroidised P40-Fe₃O₄ products. A 1:1 mass ratio (Figures 6.5a, 6.7 and Table 6.5) revealed a mixture of three dominant minerals (Fe-P40, Fe₃O₄ and Fe₃O₄ with Ca) throughout these flame-spheroidised dense microspheres. Interestingly, the dense microsphere revealed ‘ring-shell’ and ‘core-shell’ type structures consisting of varying mineral compositions (non-uniform). Moreover, the P40-Fe₃O₄ 4:1 mass ratio sample (Figures 6.5b, 6.8 and Table 6.6) revealed higher yields of dense microspheres comprising a mixture of two dominant minerals (denoted as P40-Fe and Fe-P40). Comparatively, P40-rich products (mass ratio 16:1, Figures 6.5c, 6.9 and Table 6.7) showed a higher yield of dense microspheres with high concentration of P40.

Table 6.4 Mineral references (wt%) and density.

Mineral	Mineral reference (wt%)							Density g/cm ³
	Ca	Fe	P	Mg	Na	O	C	
P40	9.1	0	28.7	7.2	7.2	47.9	0	1.40
P40-Fe	7.5	10.6	25.1	6.2	6.0	44.6	0	2.08
Fe-P40	8.8	32.0	13.6	7.3	2.4	35.9	0	3.46
Fe₃O₄	0	72.4	0	0	0	27.6	0	5.15
Fe₃O₄ with Ca	3.6	73.8	0	0	0	22.6	0	6.12
CFO-1	9.6	67.3	0	0	0	23.1	0	5.71
CFO-2	15.1	61.3	0	0	0	23.6	0	5.33
CFO-3	19.1	57	0	0	0	23.9	0	5.05
CFO-4	48.4	28.9	0	0	0	22.6	0	3.28
CaCO₃	40	0	0	0	0	48	12	2.71
Ca-P-Fe	36.6	7.7	17.0	0	0	38.7	0	1.92
Ca-P40-Fe	30.4	9.5	15.5	2.3	4.3	37.9	0	2.01
P-Ca-Mg-Fe (no Na)	17.5	8.0	18.2	14.3	0.0	42.1	0	1.95

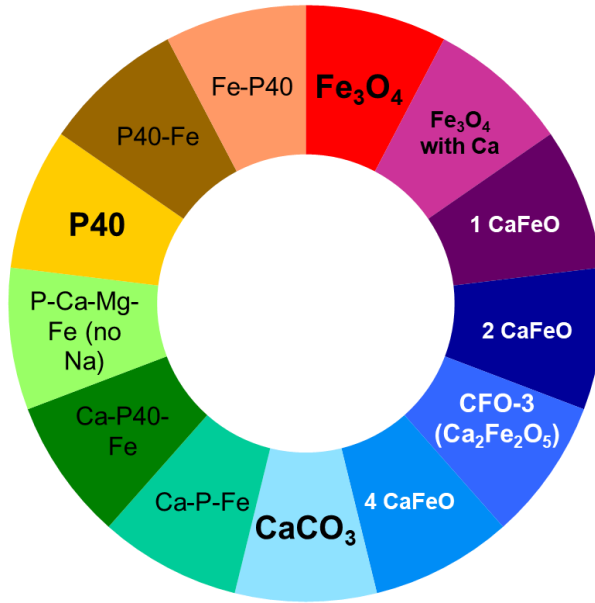


Figure 6.6 Molar colour code as a function of Fe/Ca/P concentrations.

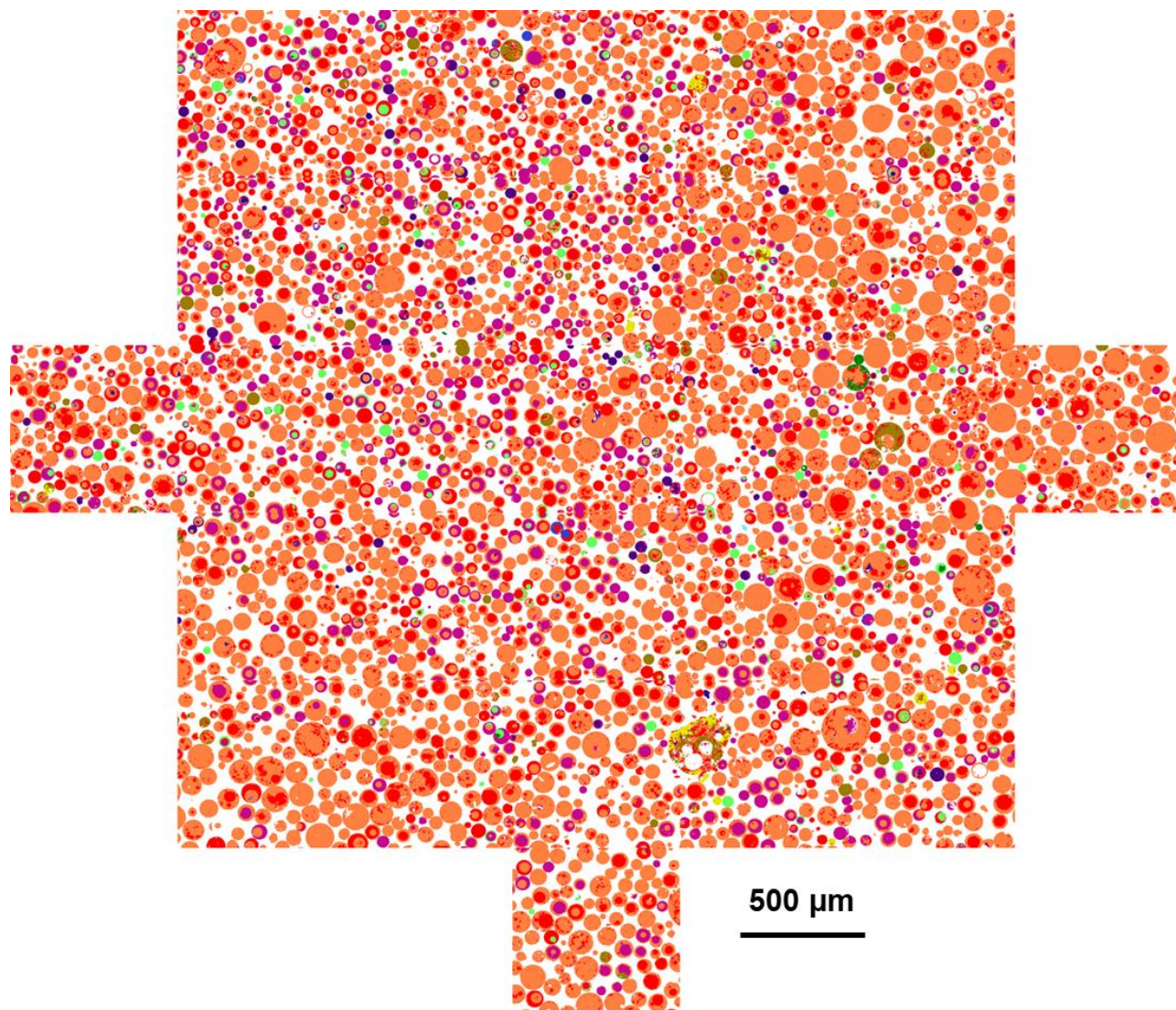
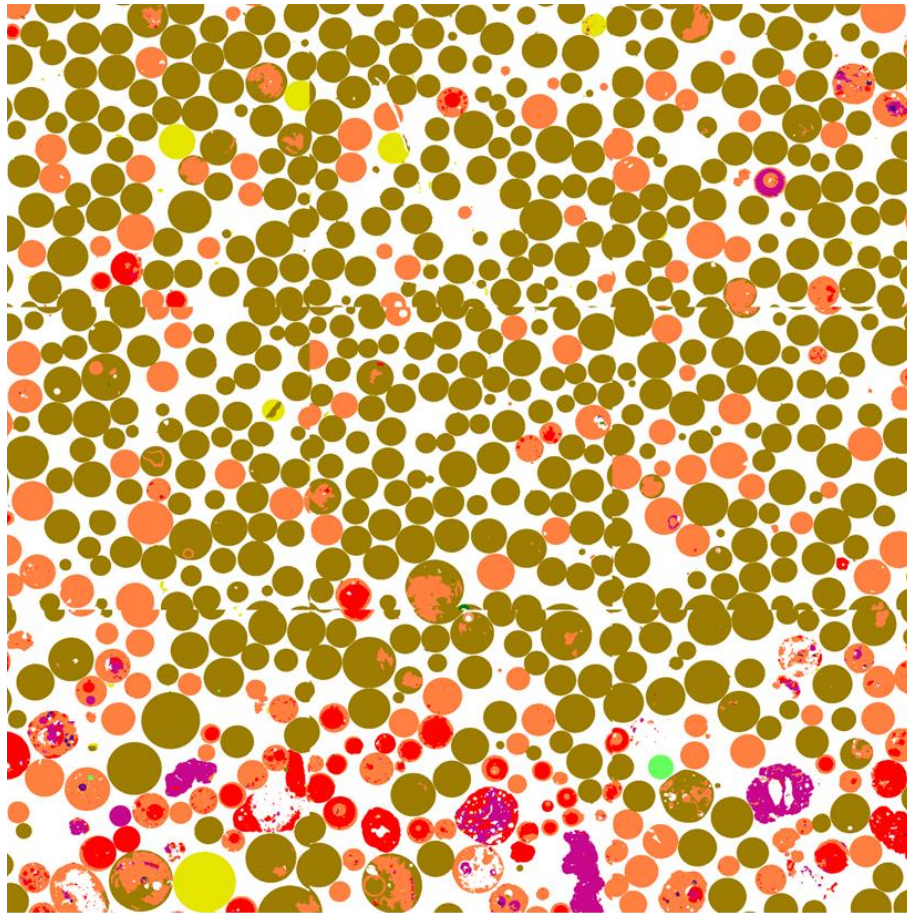


Figure 6.7 Full MLA compositional analysis of flame-spheroidised P40:Fe₃O₄ (mass ratio 1:1), following sieving and sectioning, demonstrating high levels of Fe-P40.

Table 6.5 Modal mineralogy for flame spheroidised P40:Fe₃O₄ (mass ratio 1:1).

Mineral	Particles	Weight %
Fe-P40	3164	58.8
Fe ₃ O ₄	2334	22.6
Fe ₃ O ₄ with Ca	2454	15.7
Other minerals	973	2.9



500 μ m

Figure 6.8 Full MLA compositional analysis of flame-spheroidised P40:Fe₃O₄ (mass ratio 4:1), following sieving and sectioning, demonstrating high levels of P40-Fe and Fe-P40 banded minerals.

Table 6.6 Modal mineralogy for flame spheroidised P40:Fe₃O₄ (mass ratio 4:1).

Mineral	Particles	Weight %
P40-Fe	592	56.6
Fe-P40	274	29.3
Fe ₃ O ₄	146	8.6
Fe ₃ O ₄ with Ca	95	4.5
Other minerals	95	1.3

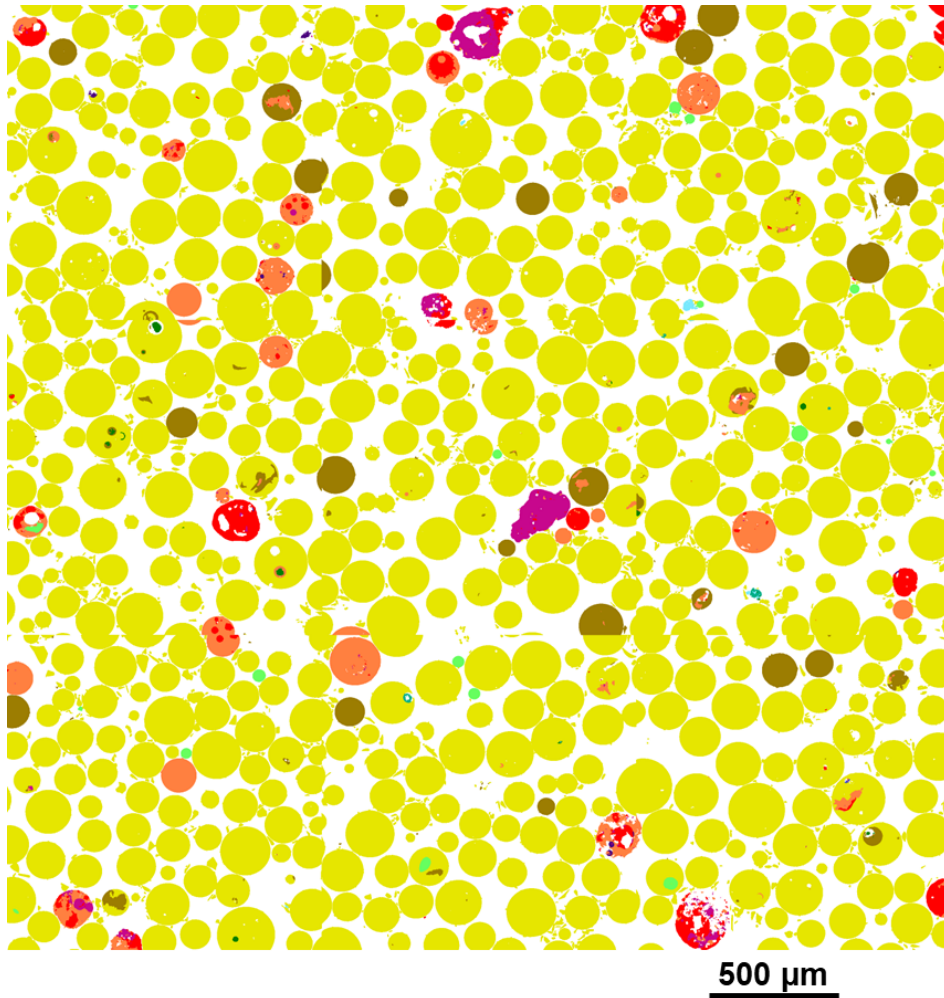


Figure 6.9 Full MLA compositional analysis of flame-spheroidised P40:Fe₃O₄ (mass ratio 16:1), following sieving and sectioning, demonstrating high levels of P40.

Table 6.7 Modal mineralogy for flame spheroidised P40:Fe₃O₄ (mass ratio 16:1).

Mineral	Particles	Weight %
P40	1590	79.8
P40-Fe	99	4.5
Fe-P40	72	6.9
Fe ₃ O ₄	52	5.1
Fe ₃ O ₄ with Ca	37	3.1
Other minerals	56	0.6

As anticipated, it was clear that increases in P40 content (P40:Fe₃O₄ from 1:1 to 16:1) resulted in lower levels of Fe and higher concentrations of P, Mg, Na, and Ca (Table 6.4). The next section presents elemental mappings corresponding to P40-Fe₃O₄ dense products, as a function of mass ratio.

6.2.4.2. Energy dispersive X-ray

Energy dispersive X-ray investigations were performed to appraise elemental distributions among these P40:Fe₃O₄ (mass ratios 1:1, 4:1 16:1) dense microspheres. Figure 6.10 shows cross-sectioned, BSE images and elemental mappings of P40:Fe₃O₄ (mass ratio 1:1) microspheres. Table 6.8 highlights the molar concentrations (Na₂O, MgO, CaO, P₂O₅ and Fe₂O₃) of the products. Core-shell and ring-shell microspheres confirmed variability of the elemental concentrations.

For the case of P40:Fe₃O₄ (mass ratio 4:1; Figure 6.11), BSE and elemental mappings showed evidence of a strong yield of dense microspheres. As summarised in Table 6.9, the samples revealed higher levels of P₂O₅ for all constituents, when compared to mass ratio 1:1 (Table 6.8), as anticipated.

Figure 6.12 shows BSE and elemental mappings of sectioned P40-rich microspheres (P40:Fe₃O₄, mass ratio 16:1), confirming elevated levels of phosphorous, and very low levels of Fe (Table 6.10). Interestingly, only one microsphere exhibited high levels of iron (Figure 6.12e).

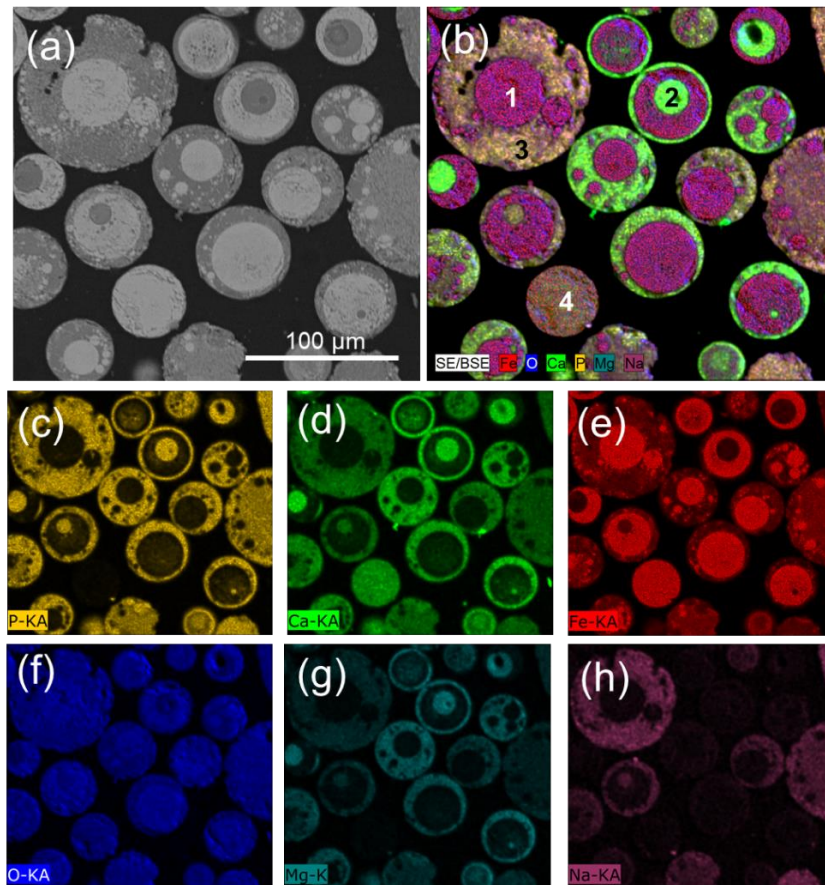


Figure 6.10. (a) BSE image and (b) elemental mapping showing (c) phosphorus (d) calcium, (e) iron, (f) oxygen, (g) magnesium and (h) sodium, of P40:Fe₃O₄ microspheres (mass ratio 1:1), following sieving and sectioning, illustrating core-shell and ring-shell morphologies.

Table 6.8. Molar constituents (wt%) for P40:Fe₃O₄ microspheres (mass ratio 1:1).

Number	Name	Na ₂ O / wt%	MgO / wt%	CaO / wt%	P ₂ O ₅ / wt%	Fe ₂ O ₃ / wt%
1	Fe-rich	0.70 ± 1.57	5.60 ± 3.86	3.24 ± 2.29	5.08 ± 3.35	85.36 ± 9.57
2	Mg-rich	0	30.88 ± 2.60	30.37 ± 4.06	22.4 ± 2.34	16.35 ± 1.36
3	Na-rich	8.47 ± 1.98	14.89 ± 2.20	17.38 ± 4.80	24.36 ± 2.65	34.89 ± 10.37
4	CFO	0	0	27.20	0	72.80

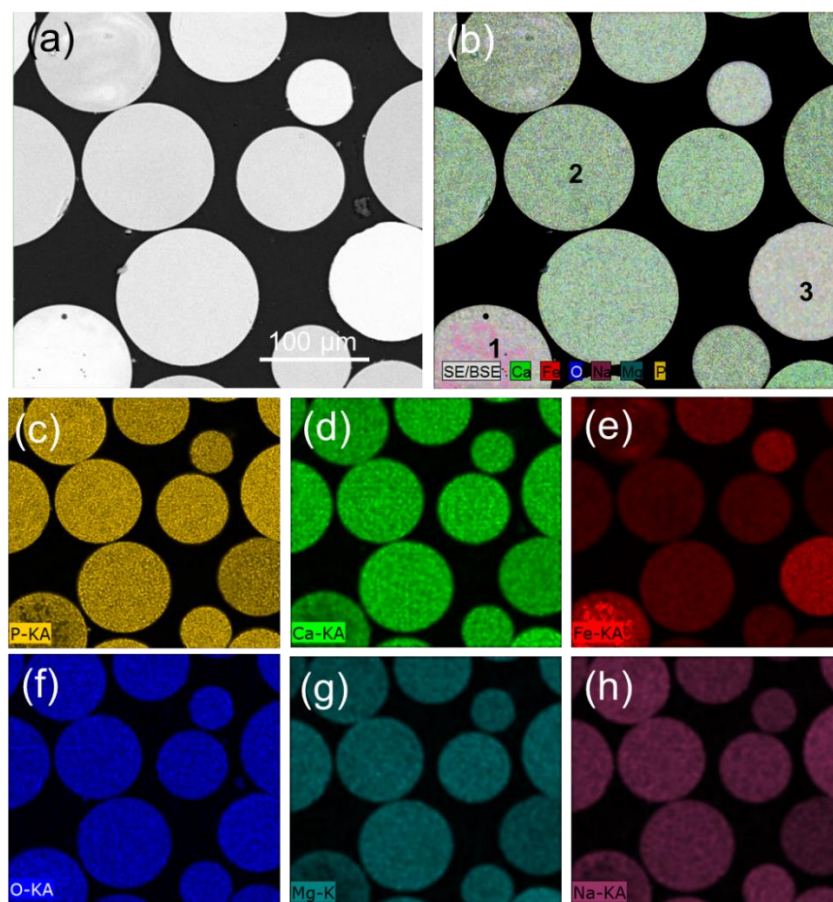


Figure 6.11. (a) BSE image and (b) elemental mapping showing (c) phosphorus, (d) calcium, (e) iron, (f) oxygen, (g) magnesium and (h) sodium, of P40:Fe₃O₄ microspheres (mass ratio 4:1), following sieving and sectioning, illustrating dense microsphere morphologies.

Table 6.9. Molar constituents (wt%) for P40:Fe₃O₄ microspheres (mass ratio 4:1).

Number	Name	Na ₂ O / wt%	MgO / wt%	CaO / wt%	P ₂ O ₅ / wt%	Fe ₂ O ₃ / wt%
1	Fe-rich	12.95 ± 1.15	15.16 ± 0.63	8.02 ± 2.41	17 ± 2.58	46.88 ± 6.78
2	P-rich	15.11 ± 0.48	26.5 ± 0.75	19.15 ± 0.57	30.57 ± 0.93	8.67 ± 2.28
3	P-rich 2	12.71 ± 0.08	23.23 ± 0.10	16.58 ± 0.22	27.06 ± 0.09	20.39 ± 0.14

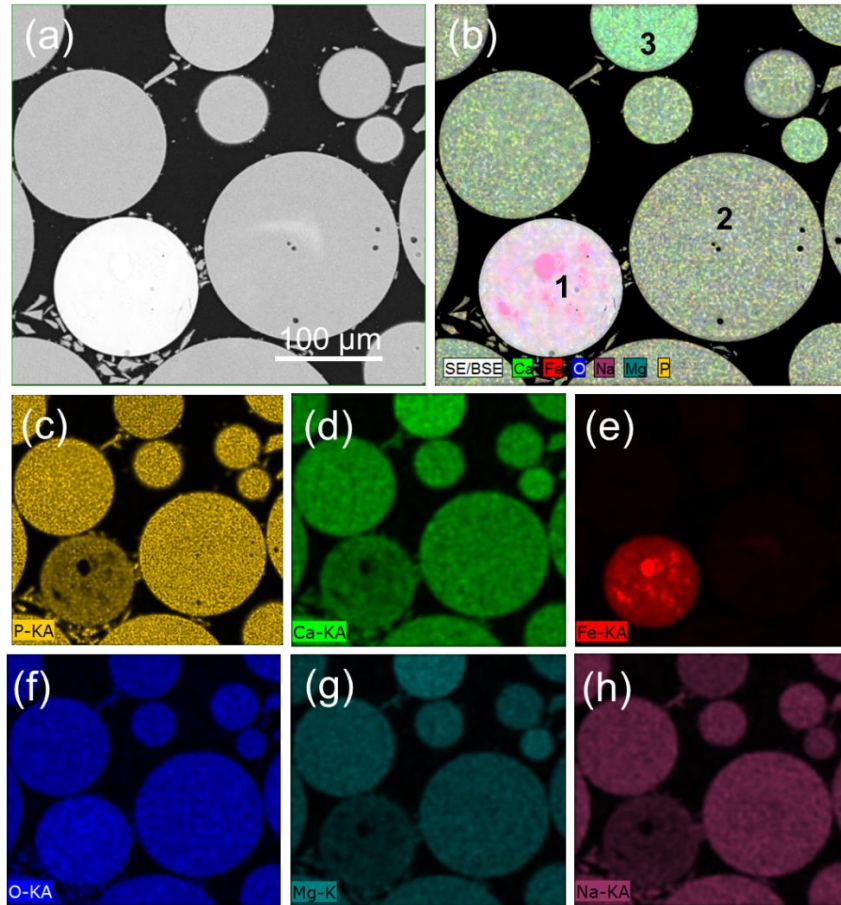


Figure 6.12. (a) BSE image and (b) elemental mapping showing (c) phosphorus, (d) calcium, (e) iron, (f) oxygen, (g) magnesium and (h) sodium of P40:Fe₃O₄ microspheres (mass ratio 16:1), following sieving and sectioning, illustrating dense microsphere morphologies.

Table 6.10. Molar constituents (wt%) for P40:Fe₃O₄ microspheres (mass ratio 16:1).

Number	Name	Na ₂ O / wt%	MgO / wt%	CaO / wt%	P ₂ O ₅ / wt%	Fe ₂ O ₃ / wt%
1	Fe-rich	15.08 ± 0.56	18.65 ± 0.87	13.22 ± 0.79	27.34 ± 0.50	25.68 ± 2.16
2	P-rich	19.64 ± 0.31	25.34 ± 0.24	18.07 ± 0.08	35.82 ± 0.21	1.11 ± 0.05
3	Mg-rich	12.31 ± 0.12	33.78 ± 0.31	24.49 ± 0.13	28.37 ± 0.30	1.04 ± 0.07

Building on the investigation of P40-Fe₃O₄ dense microsphere morphologies, as a function of mass ratio, the next section explores the development of highly **porous, glass-ceramic magnetic microspheres**.

6.3 P40-Fe₃O₄ highly porous microspheres

Figure 6.13 presents a flow diagram, comprising the steps followed for the flame spheroidisation, characterisation and cytocompatibility investigations on highly porous, P40-Fe₃O₄ ferromagnetic microspheres.

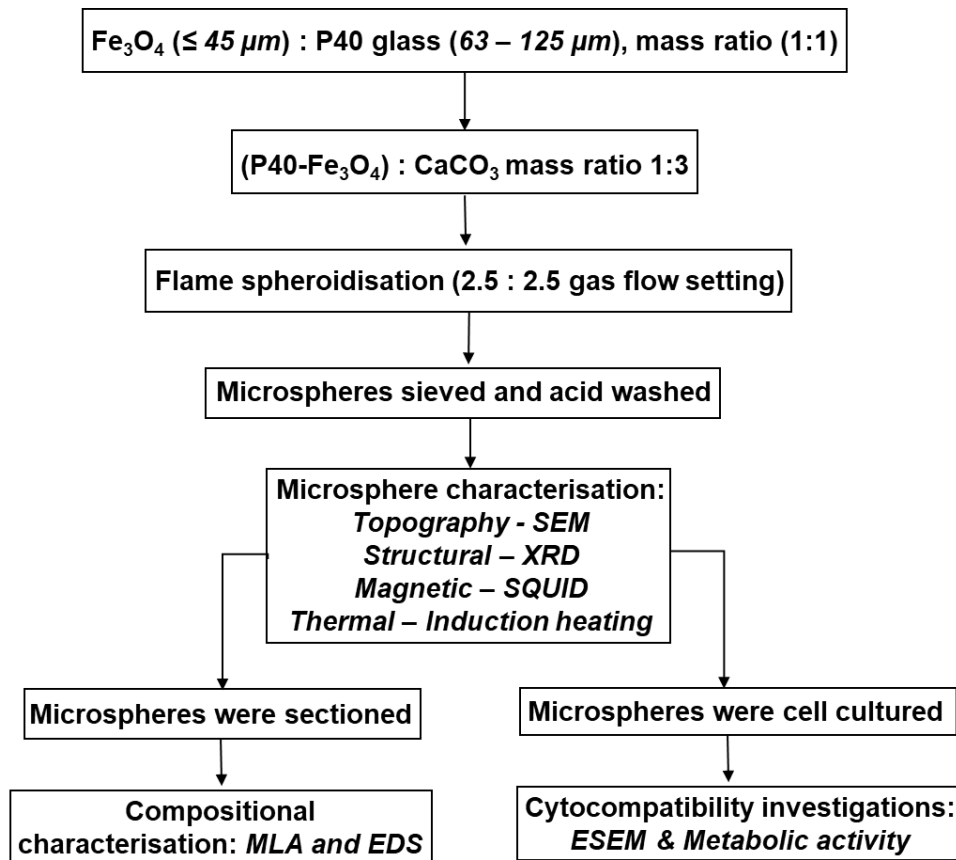


Figure 6.13 Flow diagram summarising the key steps followed for the manufacture of P40-Fe₃O₄ porous microspheres.

The Fe_3O_4 ($\leq 45 \mu\text{m}$) precursor and melt-quenched P40 phosphate-based glass (63 – 125 μm) powders were combined at a mass ratio of 1:1. The P40- Fe_3O_4 powders were then mixed with calcium carbonate (CaCO_3) which was used as a porogen ($\leq 63 \mu\text{m}$) (1:3 mass ratio). The prepared powders were then processed *via* the flame spheroidisation technique (2.5:2.5 gas flow setting), then sieved and acid washed prior to characterisation (SEM, XRD and SQUID). The microsphere products were also cross-sectioned for compositional analyses (*via* MLA and EDS). The heating of porous microspheres was performed *via* high frequency induction, with Fe_3O_4 and P40 dense microspheres used as controls. Finally, cytocompatibility assessment was carried out using the human osteoblast cell line MG-63 seeded directly onto the P40- Fe_3O_4 porous microspheres, with cell metabolic activity evaluated using Alamar Blue at days 2 and 7. The Fe_3O_4 , $\text{Ca}_2\text{Fe}_2\text{O}_5$ and P40 microspheres were used as controls. Finally, fixed cells on the P40- Fe_3O_4 microspheres were imaged using ESEM.

6.3.1 Microsphere topography (*sieved microspheres*)

Figure 6.14a shows a representative, low-magnification SE image of the flame spheroidised P40- Fe_3O_4 microsphere products (size range 125 – 212 μm) with exceptionally high levels of porosity. Figure 6.14b shows P40- Fe_3O_4 porous microspheres, whilst Figure 6.14c highlights the interconnected nature of the porosity. For comparison, Figures 6.14d and 6.14e show SE images of flame spheroidised Fe_3O_4 and P40 dense microspheres, respectively, which were used for magnetometry, induction heating and cytocompatibility control investigations. All samples were manufactured under the same processing conditions as for P40- Fe_3O_4 .

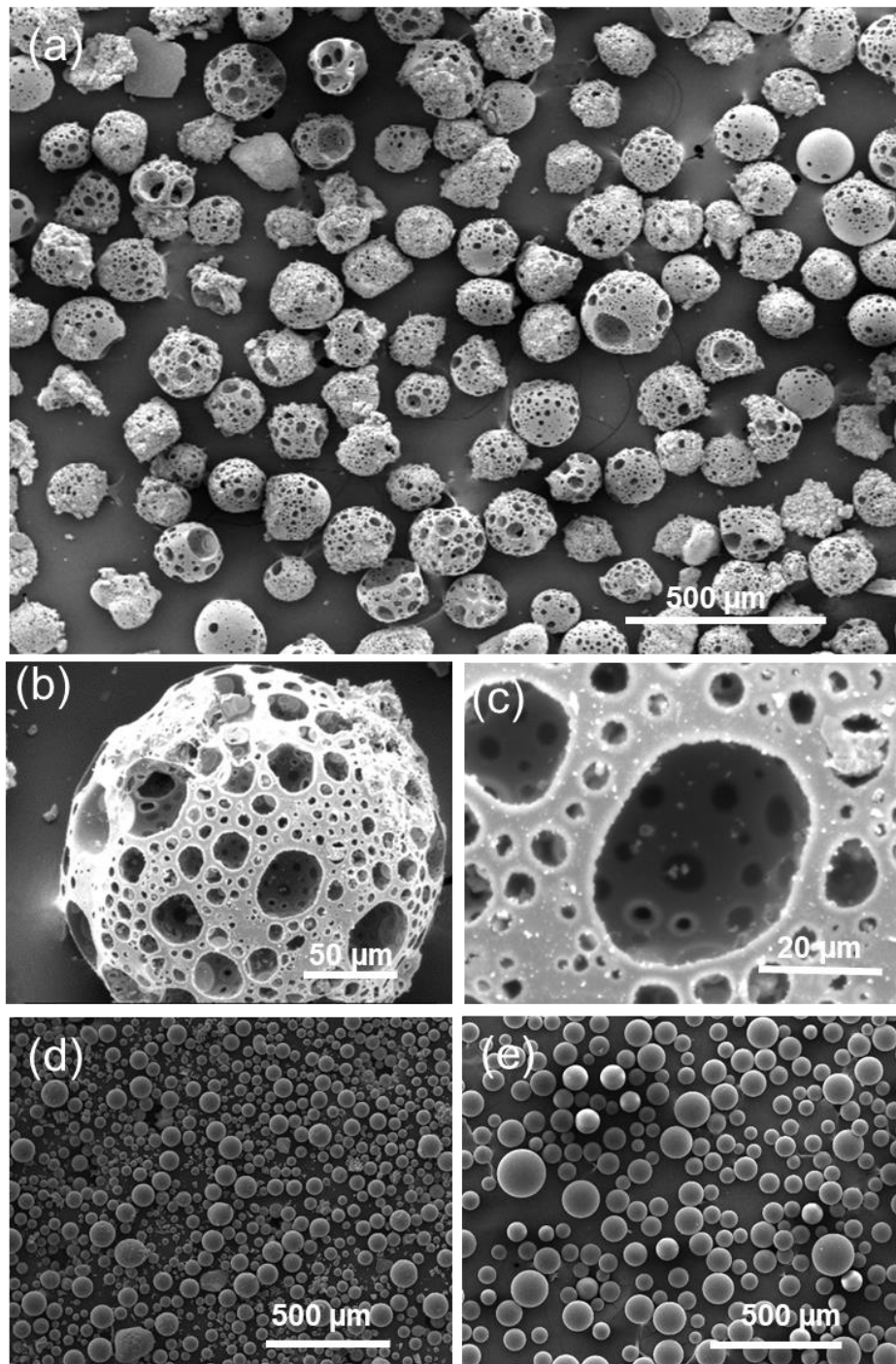


Figure 6.14. SE images of flame spheroidised **(a)** P40-Fe₃O₄ porous microspheres (125 - 212 μm); with **(b)** details of a porous microsphere; and **(c)** highlight of microsphere interconnected porosity. Flame spheroidised, unsieved **(d)** Fe₃O₄ dense microspheres (~ 20 - 100 μm), and **(e)** P40 dense microspheres (~ 30 - 150 μm), used as controls.

These P40-Fe₃O₄ products presented the largest number of highly porous microspheres within the 141– 180 μm size range (Figure 6.15a), whilst dense Fe₃O₄ and P40 controls exhibited smaller microspheres in the range ~ 20 - 100 μm and ~ 30 - 150 μm, respectively. It was noted that smaller P40-Fe₃O₄ products in the 63 - 125 μm size resembled more irregular shaped morphologies exhibiting lower levels of porosity (Figure 6.16). For the case of well-defined P40-Fe₃O₄ porous microspheres (between 125 – 212 μm), the surface pore diameters exhibited values in the range 0.9 to 56.2 μm (Figure 6.15b; mean 2.8 μm; median 1.9 μm; SD 3.79; n = 490 pores measured from three different microspheres). Figure 6.17 compares BSE images of cross sectioned large (125 – 212 μm) and small (63 – 125 μm) P40-Fe₃O₄ microspheres. Evidently, large products presented high levels of interconnected porosity; conversely, small products showed a larger number of irregular-shaped particles.

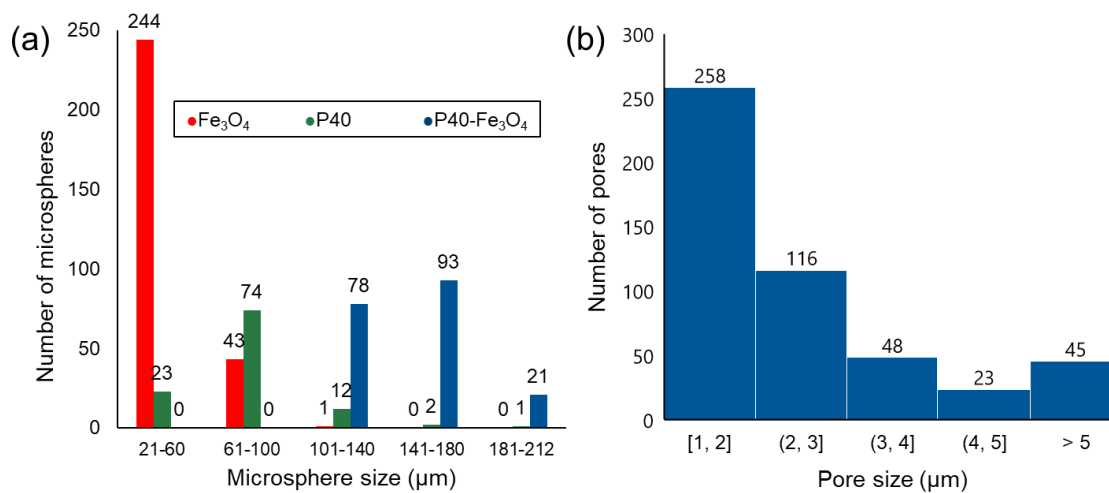


Figure 6.15. Size distributions of (a) flame-spheroidised P40-Fe₃O₄ porous microspheres (125 – 212 μm) (n = 192), as compared to Fe₃O₄ and P40 dense microsphere controls (≤ 212 μm) (n = 288 & n = 112, respectively); and (b) P40-Fe₃O₄ microsphere outer surface pores.

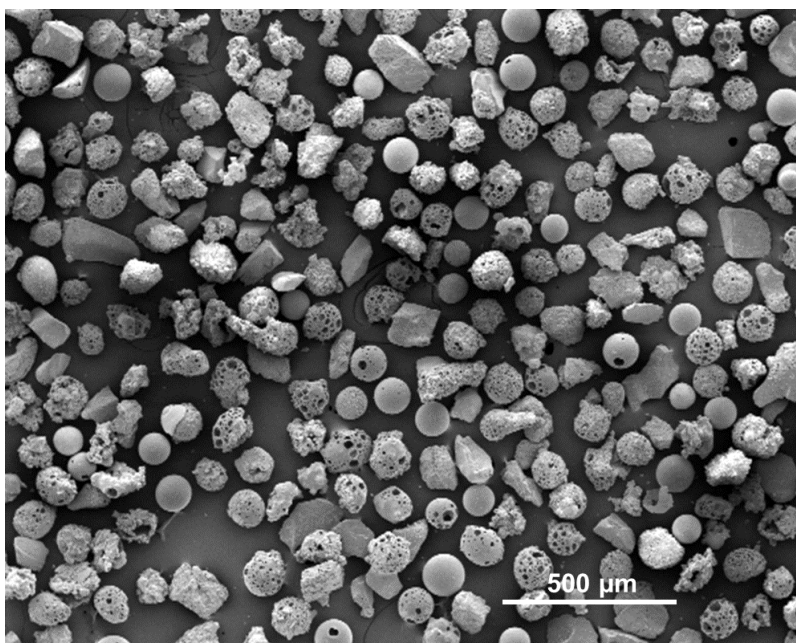


Figure 6.16. SE images of flame spheroidised P40-Fe₃O₄ porous microspheres, within the 63 - 125 μm size range, along with dense microspheres and irregular shaped particles.

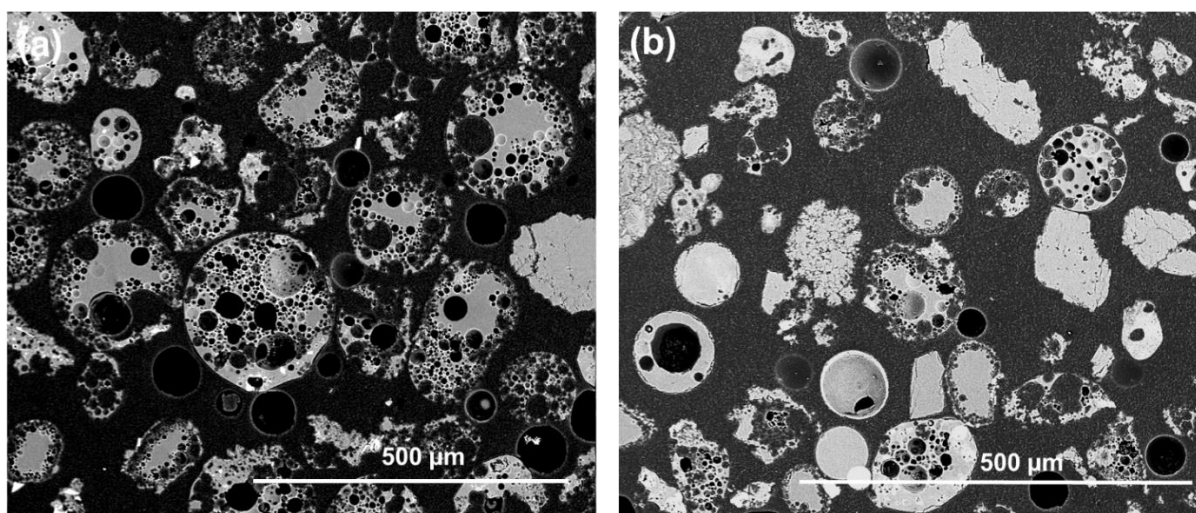


Figure 6.17. Cross-sectioned BSE images of (a) larger (125 - 212 μm) and (b) smaller (63 - 125 μm) P40-Fe₃O₄ microspheres.

The following section reports on the structural properties of highly porous P40- Fe_3O_4 microspheres (125 – 212 μm), as compared to Fe_3O_4 and P40 dense microsphere controls.

6.3.2 Structural characterisation (*sieved microspheres*)

Figure 6.18 shows XRD patterns for the P40- Fe_3O_4 flame spheroidised porous microspheres, compared to dense Fe_3O_4 and P40 microsphere controls. The diffractogram for P40 processed in isolation exhibited a characteristic glass curve consistent with its amorphous nature; whilst that for processed Fe_3O_4 confirmed retention of crystalline Fe_3O_4 along with the presence of a small amount of Fe_2O_3 . Interestingly, the diffractogram for processed P40- Fe_3O_4 revealed the presence of crystalline $\text{Ca}_2\text{Fe}_2\text{O}_5$, along with (unreacted) Fe_3O_4 and CaCO_3 , with slight curvature of the baseline consistent with the presence of amorphous P40.

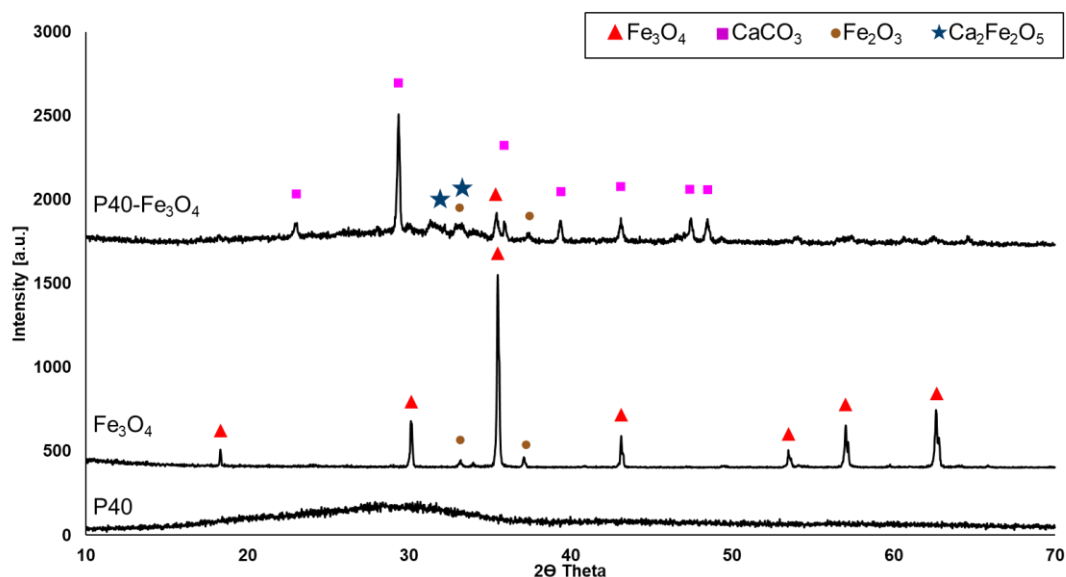


Figure 6.18. X-ray diffractograms for flame spheroidised, highly porous, P40- Fe_3O_4 microspheres, compared to the Fe_3O_4 and P40 dense microsphere control samples.

6.3.3 Magnetic properties of P40-Fe₃O₄ porous microspheres (sieved)

Figure 6.19 presents hysteresis loops for flame-spheroidised P40-Fe₃O₄ porous microspheres, Fe₃O₄ dense microspheres and P40 dense microspheres. Importantly, the P40-Fe₃O₄ porous microspheres and Fe₃O₄ dense microspheres both revealed typical hysteresis loops indicative of ferromagnetic behaviour. As summarised in Table 6.11, the Fe₃O₄ microspheres showed the highest levels of magnetic saturation, whilst the P40 dense microspheres showed no magnetic saturation, as anticipated. Notably, highly porous P40-Fe₃O₄ microspheres exhibited magnetic saturation at 4 Am²/kg and a lower but significant value of remanent magnetisation of 0.2 Am²/kg, as compared to dense Fe₃O₄ microspheres.

Table 6.11. Magnetic measurements for flame-spheroidised reaction products.

Sample	Saturation magnetisation	Remanent magnetisation, Mr	Coercive field, Hc	
	Am ² /kg (emu/g)		kA/m	Oe
Fe ₃ O ₄	96.3	0.8	0.5	6.7
P40- Fe ₃ O ₄	4	0.2	5.8	72.6
P40	0	0	0	0

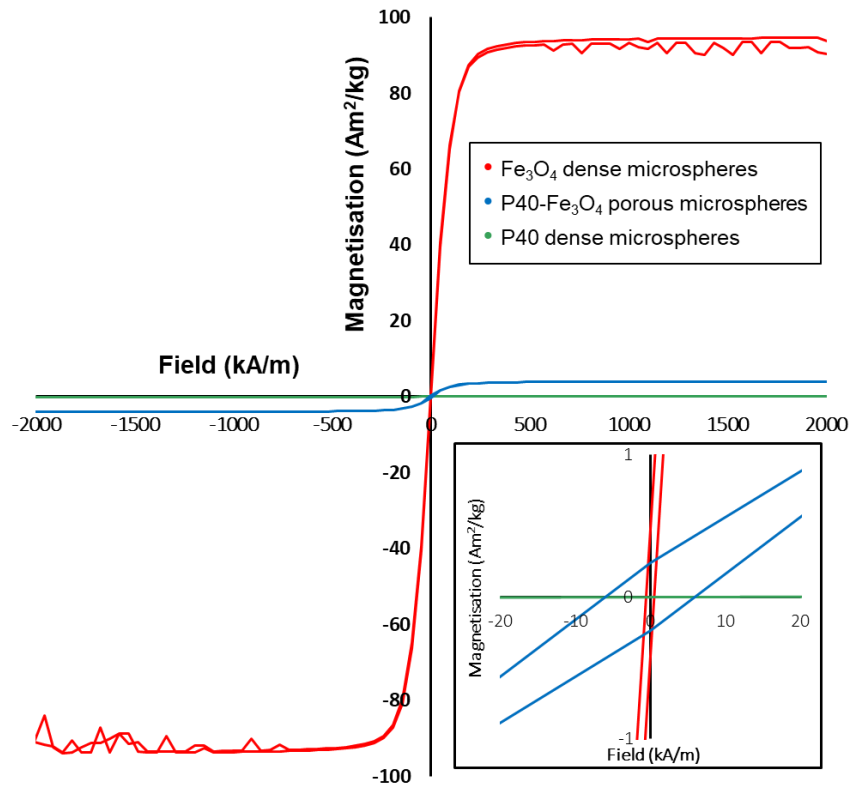


Figure 6.19. SQUID magnetometry measurements for flame-spheroidised P40-Fe₃O₄ porous microspheres, compared to Fe₃O₄ and P40 dense microspheres, at 26.85°C. Inset figure provides evidence for Fe₃O₄ and P40-Fe₃O₄ remanent magnetisation.

6.3.4 Compositional analyses (*sieved and sectioned*)

6.3.4.1 Mineral liberation analysis

Figure 6.20a illustrates a BSE image of resin embedded and sectioned P40-Fe₃O₄ microspheres, evidencing very high levels of interconnected porosity. Mineral mapping (Figure 6.20b and Figure 6.21) revealed a variety of products, dominated by Ca-P40-Fe, P40-Fe and Ca₂Fe₂O₅, along with unreacted P40, CaCO₃ and Fe₃O₄ (Table 6.12). A total

of 24,637 particles were quantified via MLA software using a standard 70% matching threshold.

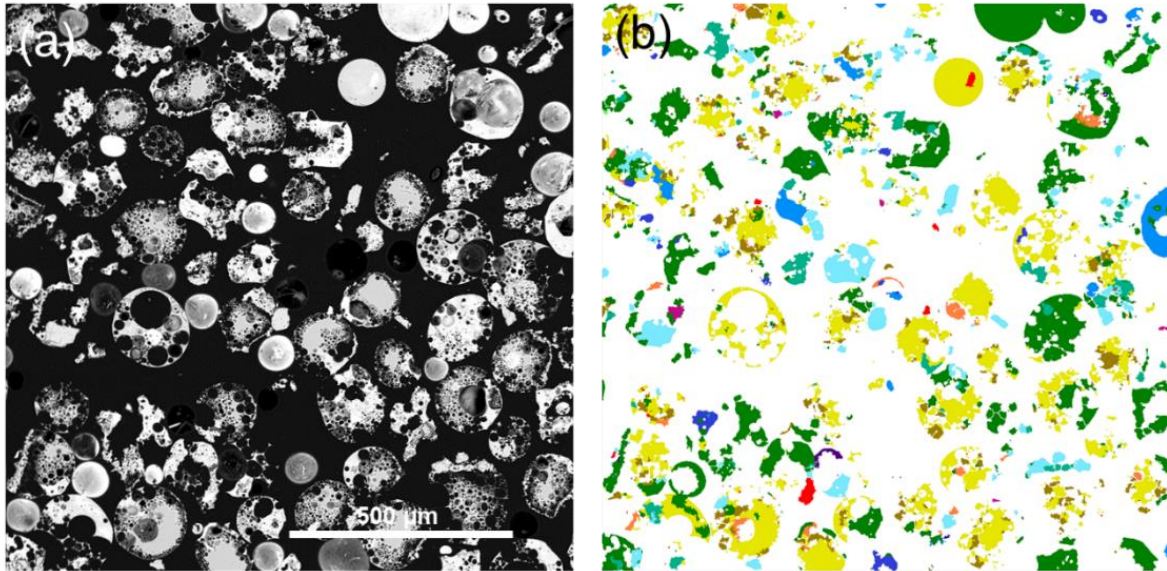


Figure 6.20. Sectioned, flame-spheroidised, P40-Fe₃O₄ porous microspheres: (a) BSE image highlighting microsphere porosity; (b) MLA compositional map demonstrating a mixed phase product comprising primarily iron oxide decorated P40.

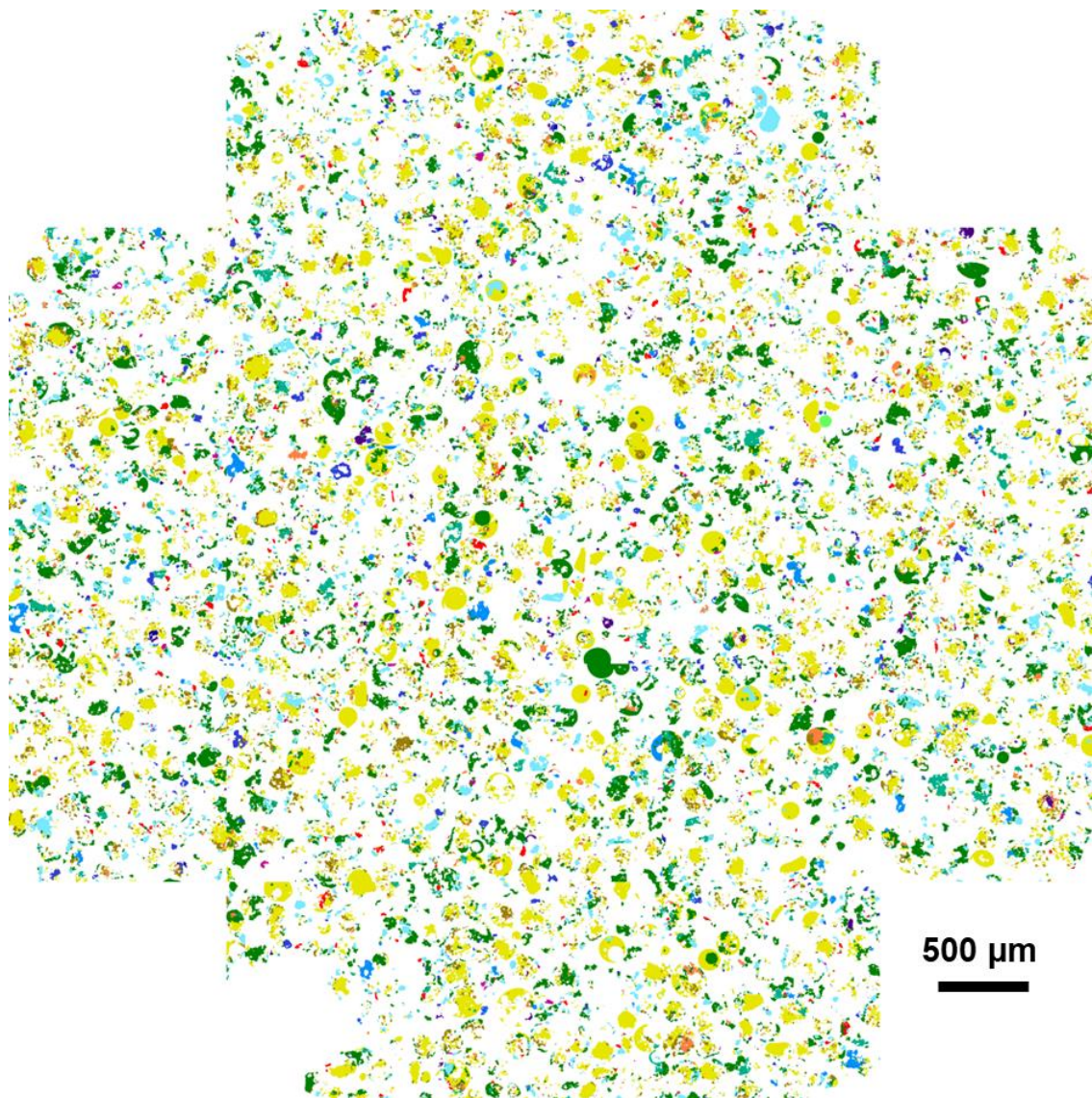


Figure 6.21. MLA data for flame-spheroidised P40-Fe₃O₄ porous microspheres, following sieving and sectioning, showing high levels of P40 and Ca-P40-Fe

Table 6.12. Mineral proportion (weight percentage) of P40:Fe₃O₄ porous microspheres.

Mineral	Particles	Weight %
P40	8270	25.5
P40-Fe	4032	8.8
Fe-P40	925	3.7
Fe ₃ O ₄	479	3.7
Fe ₃ O ₄ with Ca	317	1.4
CFO-1	211	1.5
CFO-2	78	0.3
CFO-3 - Ca ₂ Fe ₂ O ₅	481	5.1
CFO-4	245	3.3
CaCO ₃	2956	14.6
Ca-P-Fe	1347	4.8
Ca-P40-Fe	5202	27.0
P-Ca-Mg-Fe (no Na)	94	0.2

6.3.4.2. Energy dispersive X-ray spectroscopy

Further, Figure 6.22 shows BSE, a detailed EDS elemental map, and elemental mappings corresponding to the sectioned P40-Fe₃O₄ porous microspheres. The elemental map (Figure 6.21b) highlights a distribution of FeO-rich domains (~ 10 μm sized) embedded within the microspheres (125 – 212 μm). A summary of the compositions of FeO-rich and FeO-poor regions of the microspheres is presented in Table 6.13. Notably, elevated levels of CaO were associated with FeO-rich regions, as confirmed in Figure 6.23 that highlights the correlation between BSE and elemental mappings of FeO and CaO regions of individual porous microspheres.

Table 6.13. Molar constituents of highlighted regions of flame-spheroidised P40-Fe₃O₄ microspheres (Figure 6.22).

	Na ₂ O / wt% ± SD	MgO / wt% ± SD	CaO / wt% ± SD	P ₂ O ₅ / wt% ± SD	FeO / wt% ± SD
FeO-rich	9.3 ± 4.8	8.4 ± 3.2	32.2 ± 9.2	44.8 ± 7.4	5.4 ± 5.8
FeO-poor	14.7 ± 0.2	11.6 ± 0.2	11.7 ± 0.2	61.9 ± 0.3	0.1 ± 0.1

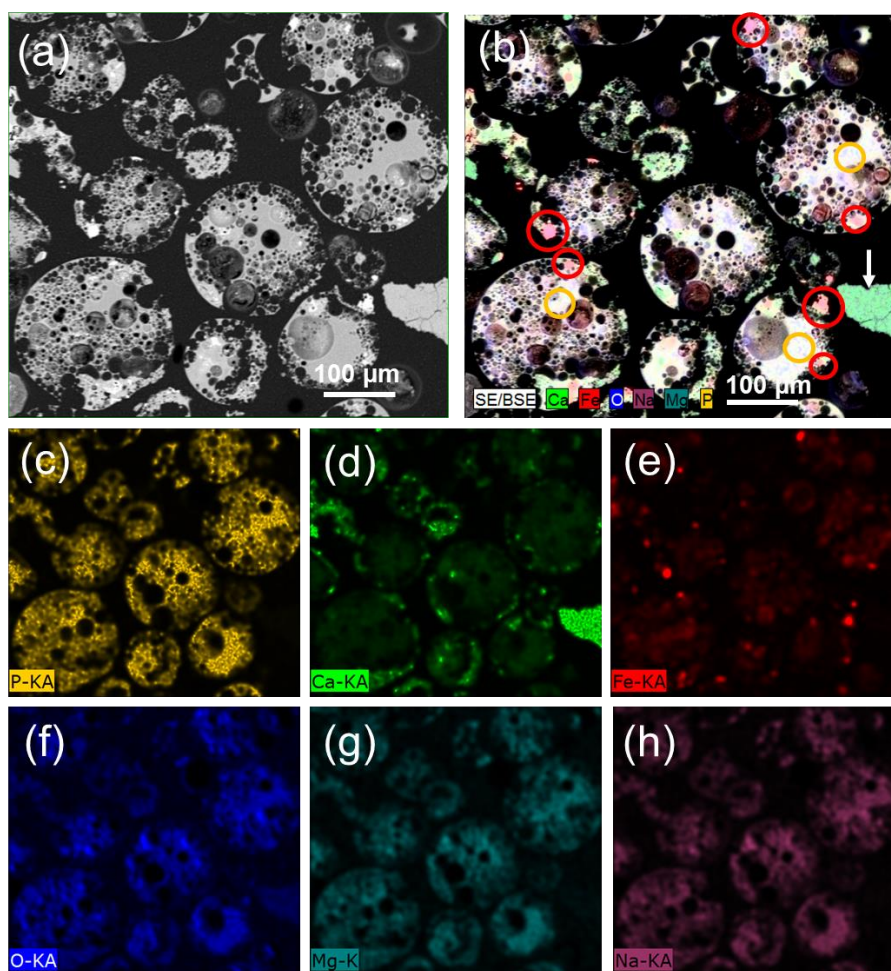
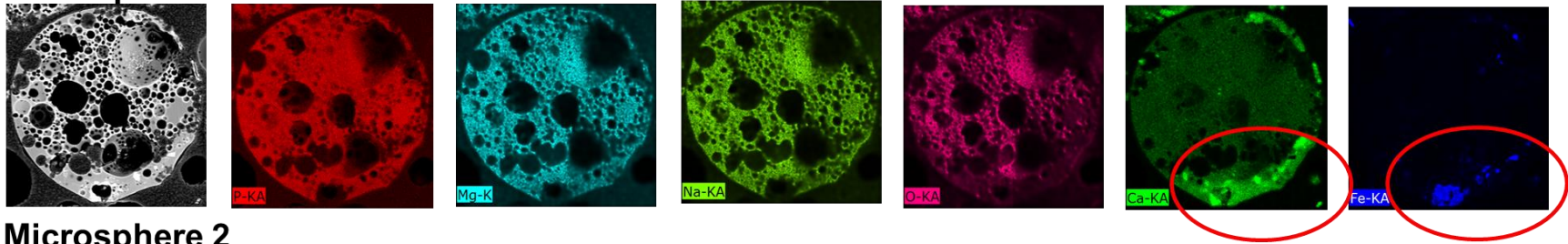
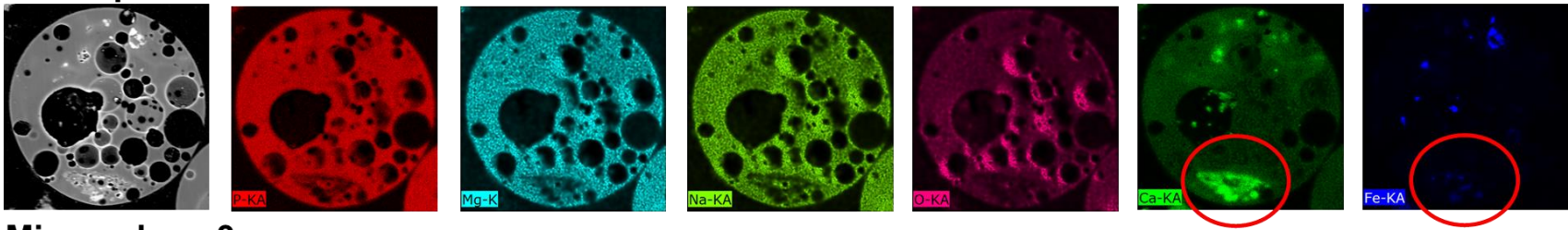


Figure 6.22. (a) BSE image and (b) EDS elemental mapping showing (c) phosphorous (d) calcium, (e) iron, (f) oxygen, (g) magnesium and (h) sodium of P40:Fe₃O₄ porous microspheres (mass ratio 1:1), following sieving and sectioning. Red circles highlight FeO-rich areas, and yellow circles highlight FeO-poor areas.

Microsphere 1



Microsphere 2



Microsphere 3

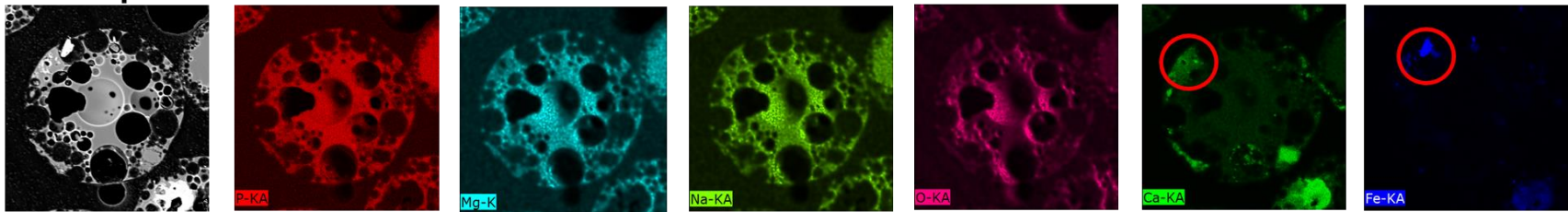


Figure 6.23. EDS analyses for representative P40-Fe₃O₄ porous microspheres showing BSE images and elemental mappings for phosphorous, magnesium, sodium, oxygen, calcium and iron, following sieving and sectioning. Red circles highlight calcium and iron in the same microsphere areas.

6.3.5 Induction heating

Figure 6.24 shows the evolution of temperature of induction heated highly porous P40-Fe₃O₄ microspheres, as compared to dense Fe₃O₄ and P40 microspheres. Experimental parameters for the induction heating investigations are detailed in Table 6.14. The Fe₃O₄ dense microspheres exhibited the highest levels of induction heating, reaching ~ 140°C, but with complete lack of heating control. Conversely, the P40 microspheres showed no induction heating at all, as anticipated. Notably, the P40-Fe₃O₄ highly porous microspheres exhibited highly controlled heating profiles, to a constant level of 41.9°C, which remained stable upon voltage decrease (from 250 down to 100 V after 40 s; Table 6.14). For the case of the Fe₃O₄ samples, the voltage decrease was applied at 10 s and stopped at ~ 80 s due to the uncontrolled temperature rise (Figure 6.24).

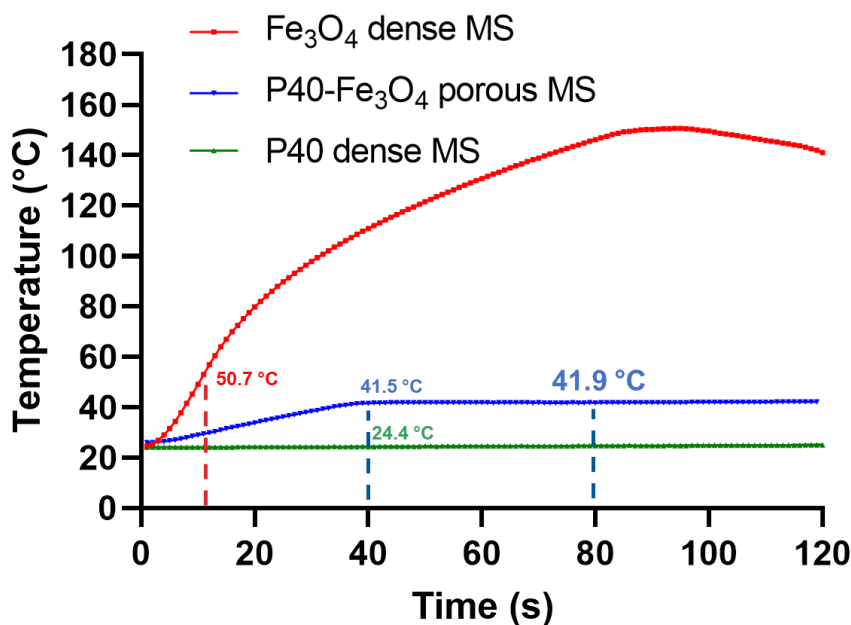


Figure 6.24. Induction heating curves for P40-Fe₃O₄ porous microspheres, compared with Fe₃O₄ and P40 dense microspheres (MS). (All curves display averages of triplicate measurements. Std. errors in Table 6.15).

Table 6.14. Experimental parameters for induction heating experiments.

Voltage / V	Power / W	Current / A	Magnetic field / kA/m (Oe)	Frequency / kHz
250	350	1.4	0.17 (2.2)	204
100	120	1.2	0.15 (1.9)	204

It is noted that the application of lower voltages of 50 and 150 V, respectively, to the P40-Fe₃O₄ microspheres resulted in slower heating rates (Figure 6.25).

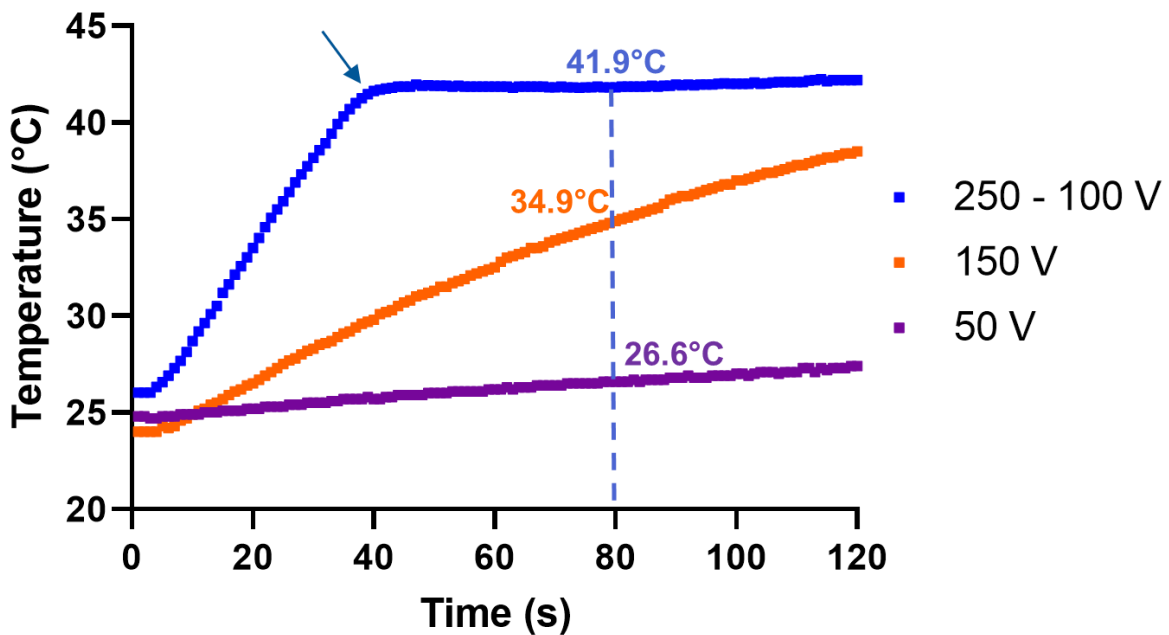


Figure 6.25. Induction heating curves for P40-Fe₃O₄ porous microspheres corresponding to 50 V, 150 V and 250 V (down to 100 V after 40 s, blue arrow) heating regimes. Lower voltages were associated with lower rates of temperature increase.

Table 6.15. Standard errors for induction heating experiments. P40-Fe₃O₄ and P40 triplicate measurements are indicative of good heating stability. Measurements for Fe₃O₄ showed much strong variability.

Std. Error	P40-Fe ₃ O ₄	Fe ₃ O ₄	P40
Slope	0.005096	0.02827	0.0006563
Y-intercept	0.3523	1.971	0.04576

6.3.6 Cytocompatibility

For cytocompatibility assessment, the MG-63 cell line in direct contact response to P40-Fe₃O₄ porous microspheres was evaluated at day 2 and day 7, *via* measurement of cell metabolic activity (Figure 6.26) and compared with the response to Ca₂Fe₂O₅, Fe₃O₄ and P40 microspheres. Analysis at day 2 revealed the metabolic response to be significantly higher for cells exposed to P40-Fe₃O₄ microspheres, compared to the controls ($p < 0.0007$). Notably, no significant difference was returned for cells exposed to P40-Fe₃O₄ microspheres and tissue control plastic (TCP) (control) on day 2.

On day 7, P40-Fe₃O₄ porous microspheres presented no significant difference in cell response compared to day 2. Conversely, Fe₃O₄ dense microspheres revealed lower cellular response, while P40 and Ca₂Fe₂O₅ microspheres showed higher levels of metabolic activity. Evidently, P40-Fe₃O₄ porous microspheres showed higher levels of metabolic activity on day 7, as compared to Fe₃O₄, Ca₂Fe₂O₅ and P40 controls. Additionally, P40-Fe₃O₄ porous microspheres and TCP presented significant differences as a consequence of a TCP cell response increment.

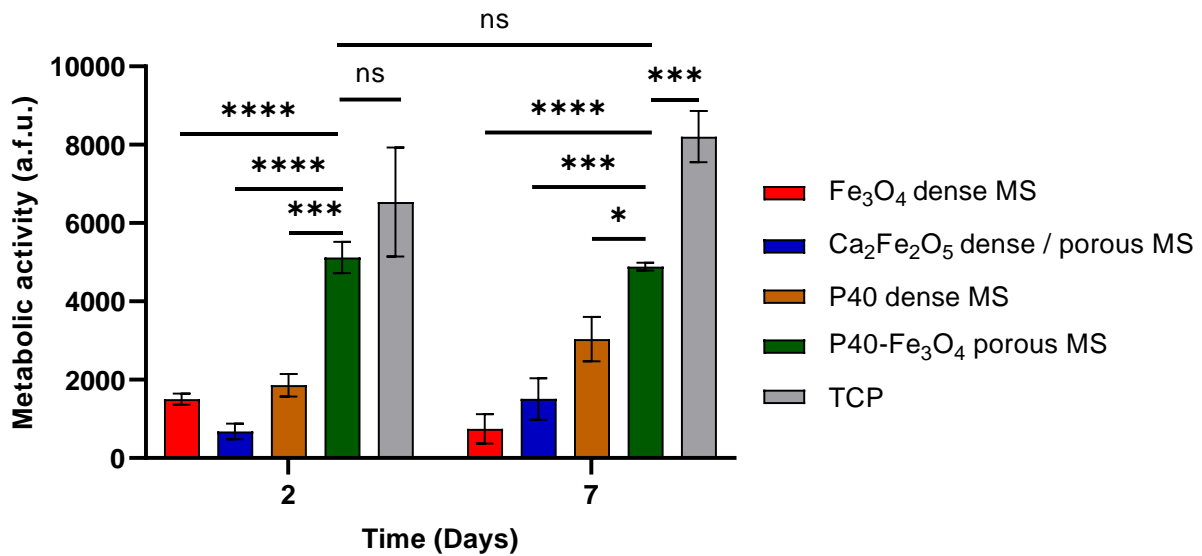


Figure 6.26. Evaluation of cell growth in direct culture, of human osteoblast derived MG-63 adhered to P40-Fe₃O₄ microspheres. Cell metabolic activity on days 2 and 7 for P40-Fe₃O₄ porous microspheres, compared to Fe₃O₄ and P40 dense microspheres (ns = no-significance; *p 0.05; ***p <0.0007; and ****p < 0.0001). (Arbitrary fluorescence units (a.f.u.); Tissue culture plastic (TCP); microspheres (MS))

Figure 6.27 shows low and high-magnification ESEM images for MG-63 cell / P40-Fe₃O₄ porous microsphere interactions at day 7. Yellow dashed lines (Figures 6.27e-l) illustrate cells peripheries, demonstrating that the cells adhered to the microsphere surfaces whilst being guided by surface texture.

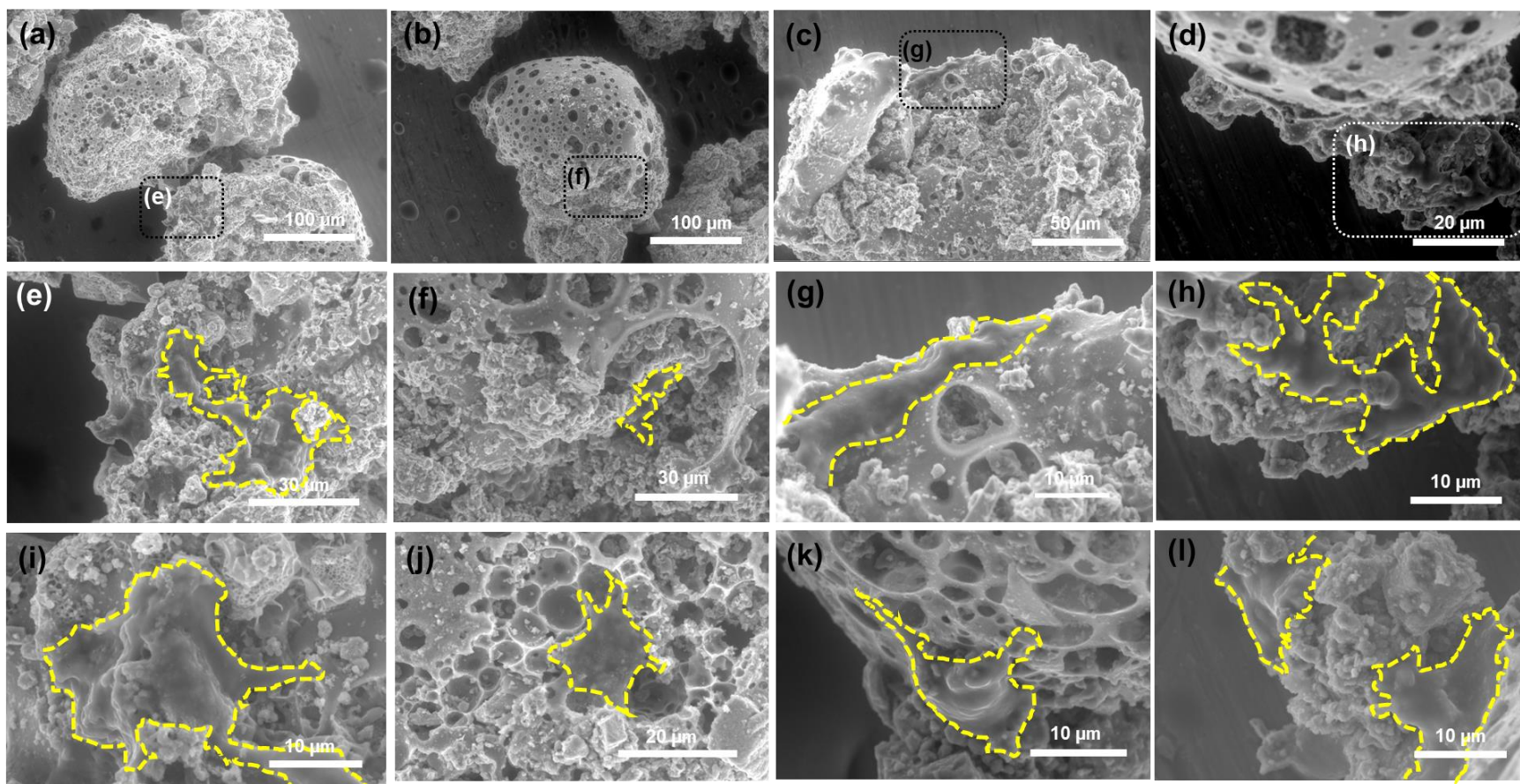


Figure 6.27. High magnification ESEM images of cell seeded P40-Fe₃O₄ porous microspheres on day 7. Yellow dashed lines illustrate cell peripheries.

The highlights of this results section included (for the first time) the novel combination of phosphate-based glasses with magnetite *via* the flame spheroidisation process; the manufacture of cytocompatible, highly porous P40-Fe₃O₄ products composed of a phosphate-glass matrix with embedded ferromagnetic regions; and the controlled delivery of heat within the clinical accepted range for magnetic hyperthermia (~43°C). Further, for the case of P40-Fe₃O₄ dense microspheres, mass ratio investigations revealed insights into the formation mechanisms of phosphate-glass and magnetite in isolation (without CaCO₃ porogen); the retention of ferromagnetic expression of the products post-flame spheroidisation; and the formation of core-shell / ring-shell segregated minerals.

6.4 Discussion

6.4.1 Introduction

P40-Fe₃O₄ dense microsphere mass ratio investigations demonstrated that the rapid, single-stage, flame spheroidisation process enabled the novel combination of phosphate-based glass and magnetite, with the resulting glass-ceramic products retaining ferromagnetic expression. Moreover, the P40-Fe₃O₄ porous microsphere products showed good levels of homogeneity, in terms of size and porosity levels. Comprehensive mineral analysis data showed that P40-Fe₃O₄ porous microspheres comprised a mixture of pure P40 and modified Ca-P40-Fe matrices embedded with Fe minerals (primarily Fe₃O₄ and Ca₂Fe₂O₅). The findings of MLA investigations were reinforced by EDS mapping, highlighting FeO-rich regions (~10 µm) distributed within P40 microsphere matrices (125 - 212 µm). Further, an association of (unreacted) Fe₃O₄ and (reacted)

$\text{Ca}_2\text{Fe}_2\text{O}_5$ with FeO-rich areas dispersed within the glass matrices was confirmed, with these regions considered responsible for ferromagnetic expression and the induction heating profiles of the P40- Fe_3O_4 porous microspheres. It was noted that the highly porous products were able to deliver heat in a controllable way *via* induction heating (to between 40-45°C), thereby targeting one of the main requirements for magnetic hyperthermia [300].

6.4.2 P40- Fe_3O_4 dense microspheres

6.4.2.1 Formation mechanisms of core-shell microspheres

The suitability of the flame spheroidisation process for the rapid manufacture of magnetic core-shell microspheres has been demonstrated (Figure 6.5a and Figure 10b, MLA and EDS mappings respectively, for P40- Fe_3O_4 1:1 sample). It is suggested that the solidification of P40- Fe_3O_4 core-shell microspheres was mediated by surface tension, similar to the calcium ferrite dense microspheres described in *Chapter 4*, however, an important distinction was noted. For the case of core-shell microspheres, the significant difference between P40 and Fe_3O_4 melting points (~765°C and ~1600°C, respectively) is considered a crucial factor for the development of P40 / Fe_3O_4 melt pools. Post-flame ejection, it is suggested that Fe_3O_4 solidifies more rapidly than P40, and engulfs the remaining pool prior to solidification. Notably, particle size is also an important parameter as large, P40 particles (63 – 125 μm) are capable of engulfing smaller, Fe_3O_4 ($\leq 45 \mu\text{m}$) particles.

The formation of magnetic, core-shell / ring-shell microspheres *via* the rapid flame spheroidisation, opens up the opportunity to investigate formation mechanisms associated with these materials in combination, with a range of characterisation

possibilities, *e.g.*, optical and/or laser diagnostics for particle visualisation and measurement of physical parameters such as particle velocity, flame temperature and gas pressure [308]. Notably, the P40-Fe₃O₄ core-shell microspheres manufactured in the present work revealed a non-uniform distribution of Fe₃O₄ / P40 glass, *i.e.*, with some microspheres showing P40 (core) - Fe₃O₄ (shell) or vice versa, or ring-shell structures. Hence, the need for some measure of flame spheroidisation refinement is recognised.

6.4.2.2 Parameter optimisation for P40-Fe₃O₄ core-shell microspheres

Regardless of the core-shell microsphere formation exhibited by rapid, flame spheroidisation, there is a need for process refinement for the controllable manufacture of uniform core-shell and/or ring-shell P40-Fe₃O₄ microspheres. Whilst noting this is out of the scope of the present investigation (the main objective was the manufacture of highly porous, glass/ceramic microspheres) it is appropriate to outline relevant investigations related to the production of core-shell structures. For example, Jegede *et al* [309], developed uniform Co-Cu core-shell structures using a drop-tube technique and studied the effect of cooling rate and particle size/morphology. A fine, uniform dispersion of Co-rich particles within a Cu-rich matrix was achieved, attributed to the metastable liquid phase separation of the products. Moreover, they reported on the effect of particle size range as a critical parameter for the controlled production of core-shell structures. Shi *et al* [310], investigated formation mechanisms of core-shell & core-shell-corona (*i.e.*, ring-shell) microstructures observed in liquid droplets of immiscible Cu-Fe-based alloys produced *via* gas atomisation. They suggested that the phase with the lower volume fraction will preferentially form the core, whereas the phase of the larger volume will form the shell or matrix. Additionally, Wang *et al* [311], studied the formation of core-shell

monotectic alloys and the effect of different compositions. The study demonstrated that core-shell structures tend to form when these are near their critical composition point, resulting in a longer migration time of demixed liquids prior to microstructure solidification.

Importantly, parameters need to be optimised for the controllable manufacture of magnetic core-shell microspheres with uniform dispersions of core / shell matrices. In this context, it is suggested that flame spheroidisation processing conditions could be explored using narrow precursor particle size distributions of magnetite (*e.g.*, 30 – 45 μm , instead of a broad particle size distribution *i.e.*, Fe_3O_4 powders below 45 μm), mixed with larger glass particles (*e.g.*, 45 – 63 μm) to achieve more uniform P40 (shell) / Fe_3O_4 (core) products. Evidently, the microstructure of P40- Fe_3O_4 core-shell microspheres present several levels of complexity due to the range of minerals generated (Table 6.4) with different compositions and differences between the temperature sensitivity of the precursors. Nevertheless, it is anticipated that the controllability of such parameters, as combined with the ability of glasses to be prepared from different formulations and precursors, could enable the manufacture of tailored glass-ceramic, core-shell / ring-shell microspheres *via* a rapid, single stage, flame spheroidisation process. Accordingly, optimised, uniform core-shell magnetic glass-ceramic microstructures could be developed for a range of applications, including biomedical.

6.4.2.3 Applications and manufacturing routes of core-shell structures

The P40: Fe_3O_4 1:1 mass ratio sample (*i.e.*, 50wt% Fe_3O_4 and 50wt% P40) revealed interesting core-shell / ring-shell morphologies. It is noted that such core-shell / ring-shell structures display functional properties of both the core and shell materials [312]. The applications of core-shell structures range from pharmaceutical and biomedical

(e.g., targeted drug delivery [313], controlled drug release [314], cell encapsulation [315]) to food industry [312], catalysis [316], energy storage [317, 318] and environmental remediation [319, 320]. Interestingly, core-shell particles with porosity levels have been developed for liquid chromatography [321] applications. Moreover, manufacturing methods for the production of core-shell microspheres include polymerisation [322], spray drying [323], solvent evaporation [324] and self-assembly methods [325]. Here, the flame-spheroidisation process has shown relevance for the production of core-shell / ring-shell microstructures, as demonstrated by P40:Fe₃O₄ (1:1 mass ratio) sample.

6.4.2.4 Effect of mass ratio

As the flame spheroidisation of phosphate-based glass - magnetite microspheres is novel, there was need to explore high concentrations of P40 (*i.e.*, P40-Fe₃O₄ 4:1 and 16:1 mass ratios) to evaluate the iron oxide phase dispersion within the phosphate-based glass matrix and their magnetic behaviour. In the present investigation, for the manufacture of dense microspheres, P40-Fe₃O₄ mass ratio combinations of 1:1, 4:1 and 16:1 were explored (Figure 6.29).

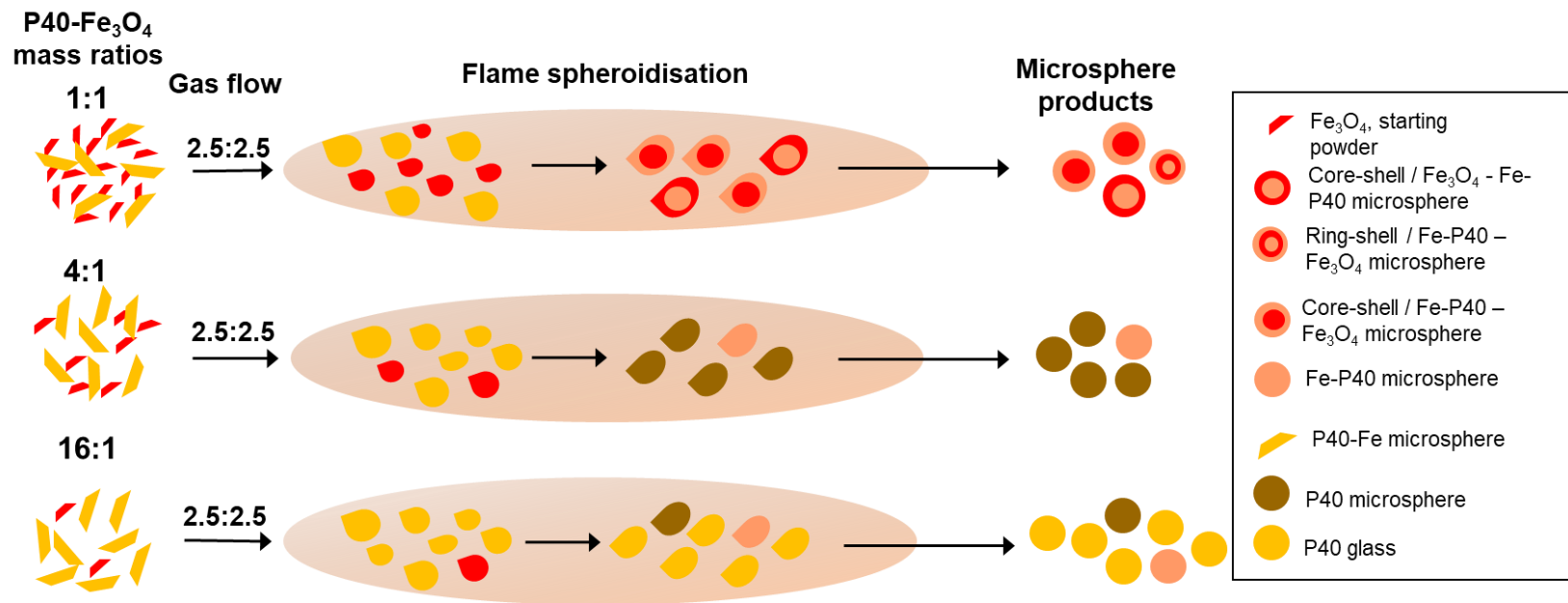


Figure 6.29. Schematic representation of the flame spheroidisation process for P40-Fe₃O₄ microsphere production (mass ratios 1:1, 4:1 and 16:1; gas flow setting 2.5:2.5).

Similar to *Chapters 4* and *5*, structural, chemical and magnetic properties showed variations as a function of mass ratio. **For P40:Fe₃O₄ (1:1)**, X-ray diffractogram (Figure 6.3) revealed two crystallographic phases: MgFeO and Na₃Fe₂(PO₄)₃. Notably, no peaks associated to calcium were matched by the Bruker software system. However, it may be that calcium atoms were incorporated within the magnetite, magnesian **MgFeO** crystal structure. In *Chapter 4*, the Fe-rich structure *i.e.* Fe₃O₄:CaCO₃ (mass ratio 3:1) correlated with well-defined Fe₃O₄ peaks (XRD, Figure 4.14) with no signatures related to calcium phases. Similarly, it is possible that the MgFeO phase found in P40:Fe₃O₄ (mass ratio 1:1) (Figure 6.3) accepted atoms of calcium upon rapid cooling. Hence, XRD provided no evidence related to phases associated with calcium. Supplementary evidence was provided by MLA investigations. The mineral denominated as “Fe₃O₄ with Ca” was present for both, P40:Fe₃O₄ (1:1) (*Chapter 6*, Table 6.5), and Fe-rich sample (3:1) (*Chapter 4*). Hence, it could be interpreted that rapid cooling of the microspheres was too fast and very few calcium atoms were incorporated into the magnetite crystallographic structure (whist noting the possibility that MLA software - *threshold 70%* - may classify two minerals with similar compositions as the same). However, EDS mapping (Figure 6.10d) revealed concentrations of calcium dispersed in a few microsphere shells. Hence, an alternative suggestion is that calcium atoms within the microspheres may be associated with amorphous phases.

Furthermore, a structural signature corresponding to sodium iron phosphate *i.e.*, **Na₃Fe₂(PO₄)₃**, provided evidence for chemical and structural affinity between iron oxide and phosphate-glass. As confirmed by both MLA and EDS, phosphorous and iron co-existed in variant Fe/P concentrations. MLA references (Table 6.4) revealed the presence of iron for most of the phosphate-based minerals, except for pure P40

glass; accordingly, EDS compositions (Table 6.8) denominated as Fe-rich, Na-rich and Mg-rich, also showed Fe/P concentrations (except for CFO). Ta, *et al.*[326] studied sodium phosphate / iron and iron oxides chemical interactions. The study suggested that Na_3PO_4 chemically absorbed Fe and Fe_2O_3 , mediated by covalent bindings and formation of Fe-O-P linkages. Particularly, $\text{Na}_3\text{Fe}_2(\text{PO}_4)_3$ exhibits a three-dimensional structure containing FeO_6 octahedra and PO_4 tetrahedra linked through common corners [327].

As described in *Chapters 4 and 5*, the incorporation of non-magnetic components within the Fe_3O_4 structure resulted in a decrease in magnetic saturation *i.e.*, a dilution effect. In the present Chapter, $\text{Na}_3\text{Fe}_2(\text{PO}_4)_3$ and MgFeO structural signatures progressively diminished and magnetic saturation decreased as a function of P40 glass concentration increase (from 1:1 to 16:1 mass ratio), showing consistency with previous Chapters.

6.4.3 Highly porous P40- Fe_3O_4 microspheres

6.4.3.1 Formation mechanism

The P40- Fe_3O_4 porous microsphere formation pathways were similar to the mechanisms described in *Chapters 4 and 5*. Formation mechanisms associated with porosity development during flame-spheroidisation have been described previously for glass-ceramic microspheres [65]. The highly porous P40- Fe_3O_4 ferromagnetic microspheres were produced by feeding prepared powders into a high-temperature oxygen-acetylene flame ($\sim 3100^\circ\text{C}$) where they melted and coalesced, and acquired spherical form due to surface tension and rapid cooling upon ejection from the flame (Figure 6.30).

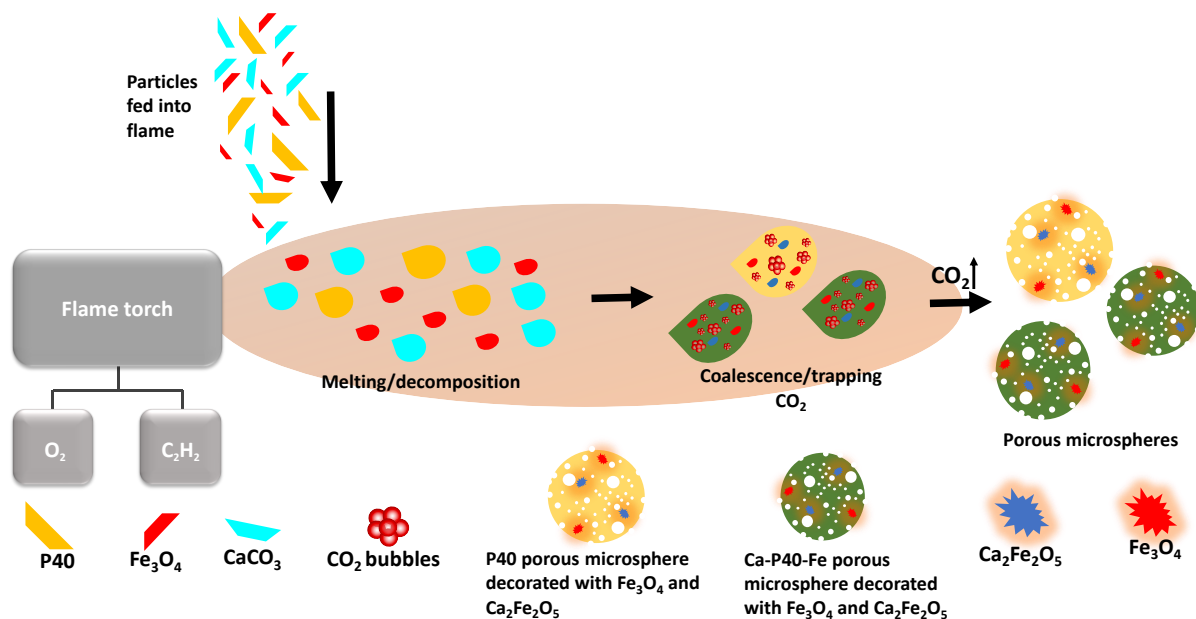


Figure 6.30 Schematic representation of the flame spheroidisation process for ferromagnetic glass-ceramic porous microsphere production.

Again, it is considered that high levels of porosity arose from a combination of physical and chemical parameters, *i.e.* precursor melting point, viscosity and porogen concentration [237, 241]. The melting points for P40 glass ($\sim 765^\circ C$) [237] and magnetite ($\sim 1600^\circ C$) were sufficiently low for molten droplet formation within the flame, whilst levels of melt viscosity were appropriate for CO_2 entrapment and release. $CaCO_3$ porogen decomposition ($CaCO_3 \rightarrow CaO + CO_2$) was considered responsible for CO_2 production and release prior to particle cooling and solidification, leading to development of the microsphere interconnected porosity observed [63]. Moreover, correlation of FeO-rich areas with high levels of CaO was consistent with the chemical affinity of Fe_3O_4 and $CaCO_3$ to develop $Ca_2Fe_2O_5$. Accordingly, it is suggested that FeO-rich areas here comprise a ferromagnetic $Ca_2Fe_2O_5$ perovskite type structure [285], and within $Ca_2Fe_2O_5$ there is evidence also on the incorporation of P_2O_5 , Na_2O and MgO upon solidification (Table 6.13). In the case of flame-spheroidised Fe_3O_4 and

P40 control samples, in the absence of CaCO_3 , topographical evidence confirmed the development of dense microspheres, thereby emphasising the importance of CaCO_3 on porosity formation.

6.4.3.2 Induction heating and ferromagnetic properties

The highly porous P40: Fe_3O_4 microspheres demonstrated their ability to deliver heat in a controllable way *via* induction heating, whilst noting that magnetic properties emanated from $\text{Ca}_2\text{Fe}_2\text{O}_5$ and Fe_3O_4 phases impregnated within the phosphate glass. The P40- Fe_3O_4 porous products revealed remanent magnetisation (*i.e.*, residual magnetisation) (Figure 6.19), hence, it was interpreted that the mechanism to produce heat within was mediated by hysteresis loss (same mechanism described in *Chapter 5*, for $\text{Ca}_2\text{Fe}_2\text{O}_5$ compositionally uniform microspheres). This mechanism is typical for multi-domain, ferro- and ferrimagnetic materials [10, 109], and distinct from single-domain particles (*i.e.*, superparamagnetic nanoparticles) that produce heat *via* Néel and Brownian relaxation [109].

For magnetic hyperthermia applications, mediated by an internal heat source near to or inside a tumour (for example), microscale ferromagnetic bioactive glasses become an attractive option because agglomeration of the magnetic species (embedded in a solid matrix) is no longer an issue [328]. In the past, different types of implants have been explored as an internal heat source for magnetic hyperthermia. For example, Tonthat, *et al* [329] developed micro-magnetic implants ($\sim 83.6 \mu\text{m}$) and a wireless temperature measurement system (frequency and field, 500 kHz and 4.73 kA/m, respectively) for magnetic hyperthermia. Renard, *et al* [330] developed silica microbeads implants with superparamagnetic iron oxide nanoparticles embedded, for localised magnetic hyperthermia on solid tumours. In addition to magnetic hyperthermia, brachytherapy is a therapeutic approach that consists of implanting

radioactive material within tumour tissue. Brachytherapy produces high levels of radiation *in situ*, reducing patient side effects when compared to external radiotherapy [97].

Similarly, P40-Fe₃O₄ porous microspheres could be implanted within or in the proximity of the tumour, with a significant advantage over brachytherapy as magnetic hyperthermia is non-radioactive (whilst noting that implanted radioactive beads have been only used for prostate cancer). Moreover, phosphate-glasses possess the ability to bond to bone. Hence, implanted P40-Fe₃O₄ porous microspheres could remain at a target site (e.g., bone tumours), enabling repeated hyperthermia heat cycles at later stages of the treatment. Additionally, high levels of porosity could be explored for the incorporation and release of drugs at localised sites. Ahmed *et al* [203] investigated degradation rates and biocompatibility of iron-phosphate glasses as a function of Fe₂O₃ content. Biocompatibility was achieved with increasing the iron concentration, attributed to an improvement in chemical durability (due to the replacement of P–O–P bonds in the glass by Fe–O–P bonds). Hence, it is noted that iron-phosphate glasses have been shown to be cytocompatible.

Induction heating parameters used for P40-Fe₃O₄ measurements were similar to Ca₂Fe₂O₅ microspheres (*Chapter 5*) with the distinction that induced magnetic field was higher for P40-Fe₃O₄ products (Table 6.16). As noted for the different magnetic saturation levels between P40-Fe₃O₄ (4 Am²/kg) and Ca₂Fe₂O₅ (8.9 Am²/kg), there was a requirement to adjust the field in order to reach the target temperature (*via* induction coil heating). Importantly, the relatively low fields for both P40-Fe₃O₄ and Ca₂Fe₂O₅ showed relevance for the present investigation, as magnetic hyperthermia effects can be readily achieved through the application of weak magnetic fields (<7.95 kA/m) [18], as mentioned in *Chapter 5*. With regards to the experimental frequency

(204 kHz) it was within the clinical accepted range for hyperthermia [11, 18, 130, 300, 302-304] and, notably, the same value used for both P40-Fe₃O₄ and Ca₂Fe₂O₅ measurements. Again, the magnetic hyperthermia temperature (43.7°C) was rapidly achieved (only 40 s) making these porous microspheres promising for reduced periods of therapy exposure, thus improving patient comfort.

Table 6.16. Experimental parameters for induction heating experiments on P40-Fe₃O₄ porous microspheres, and Ca₂Fe₂O₅ microspheres (*Chapter 5*).

Sample	Voltage / V	Power / W	Current / A	Magnetic field / kA/m (Oe)	Frequency / kHz
P40-Fe ₃ O ₄	250	350	1.4	0.17 / 2.2	204
	100	120	1.2	0.15 / 1.9	
Ca ₂ Fe ₂ O ₅	150	120	0.8	0.09 / 1.2	204
	35	20	0.6	0.07 / 0.9	

Hence, it was evident that induction heating profiles for highly porous P40-Fe₃O₄ ferromagnetic microspheres are highly promising for magnetic hyperthermia applications, whilst noting for validation this would need formal investigation in a clinical alternating magnetic field environment in the future.

6.4.3.3 Cytocompatibility

Cytocompatibility studies indicated the general suitability of P40-Fe₃O₄ porous microspheres for healthcare applications. The MG-63 cells evaluated on days 2 and 7 showed P40-Fe₃O₄ porous microspheres exhibited sustained, higher levels of metabolic activity compared to control Fe₃O₄, Ca₂Fe₂O₅ and P40 microsphere samples. Complementary ESEM investigations for day 7 samples revealed evidence for good conformation of MG-63 cells on P40-Fe₃O₄ microspheres, guided by surface texture, suggesting that these cells would colonise porous glass-ceramics preferentially [331]. P40 porous microspheres have been shown previously to be cytocompatible [53] and biocompatible via *in vivo* studies [94]. It was evident that the P40 matrix increased considerably the cytocompatibility of P40-Fe₃O₄ microsphere products compared to the sample controls. The initial low metabolic activity of P40 dense microspheres, on day 2, was attributed to the presentation of a low surface area compared to porous microspheres. Nonetheless, P40 microspheres showed a significantly increase in metabolic activity by day 7, demonstrating cytocompatibility for phosphate-based glass used in this investigation. Hence, the enhanced cytocompatibility associated with magnetite incorporated within larger, porous P40 microspheres suggests enhanced surface area provided a significant advantage for cell proliferation. Further, it is suggested that P40-Fe₃O₄ porous products could be used for hyperthermic treatment and drug release in bone tumours, and also as bone grafting substitutes.

6.4.3.4 Role of iron oxide in influencing degradation

Altering the phosphate-glass composition imparts control of the degradation rate over several orders of magnitude [332]. For the case of iron-phosphate glasses, Fe 3-5 mol% reduces the degradation rate (by two orders of magnitude), improving

the chemical durability of the glass [333]. Fe(II) and Fe(III) are capable to incorporate into the phosphate-glass structure with the distinction that Fe(II) acts to **cross link** (*i.e.*, a network modifier) the phosphate chains, with replacement of P-O-P bonds in the glass by Fe-O-P bonds. Whereas Fe(III) incorporates into the phosphate backbone and hence acts as a **network former** rather than network linking [203]. The Fe(III) ions are arranged at either tetrahedral or octahedral sites, conversely, Fe(II) ions are found only in octahedral coordinations between the network formed by the Fe(III) polyhedral and the PO₄ groups [334]. In the present investigation, different concentrations of iron-phosphate coexist in more than one mineral (MLA data, Table 6.4), suggesting the formation of P/Fe cross-links & networks. For example, the Na₃Fe₂(PO₄)₃ crystal structure consists of PO₄ tetrahedra and FeO₆ octahedra units sharing their corners with intrinsic Na defects (as detailed in section 6.4.2.4) [335]. Furthermore, microsphere porosity is another factor that influences the degradation rate. Islam *et al* [237] compared the degradation levels between porous and dense phosphate-based microspheres with Mg and Ca variations. The results showed that the introduction of porosity lead to an increase in mass loss (2.5 times higher) and ion release profiles (Na, Ca, Mg and P) when compared to dense microspheres. Similarly, Hossain *et al* [53] studied the degradation rates of porous calcium phosphate microspheres and compared with dense CaP microspheres by way of control. Again, increased mass loss and ion release for the case of porous microspheres were observed. Importantly, both investigations concluded that the increased mass loss and ion release profiles were attributable to the increased surface area of porous microspheres. In this context, it is recognised that degradation studies for P40-Fe₃O₄ porous microspheres would be required in the future.

6.4.3.5 Routes of delivery

Depending on the target tissue, it is noted that porous microspheres may be delivered *via* oral, inhalation (*e.g.*, *via* aerosol [48]), implantation or intratumoral approaches. For bone tissue repair and/or cancer therapy, bone cements and hydrogels have been explored in combination with porous microspheres, providing important benefits such as the encapsulation and controlled delivery of drugs/cells. For example, injectable **bone cements** in conjunction with porous microspheres have been investigated for osteogenic applications [336] and drug-delivery [337]. Luo *et al* [338] reported injectable TiO₂ porous microspheres added into calcium sulphate cement for controlled and sustained drug release applications. Zhao *et al* [339] developed injectable macroporous magnesium phosphate-based bone cement / gelatine microsphere composites for sustained drug release. Similarly, **hydrogels** embedded with bioactive glasses, have been reportedly delivered *via* minimally invasive injection (cannulated needle or catheter) [340]. Sun *et al* [341] reported injectable calcium alginate hydrogels to block pores of protein loaded porous microspheres for controlled protein delivery, and demonstrated that proteins maintained their structural integrity post-preparation. Notably, it was recognised that injectable biomaterials are desired over implanted biomaterials since these may cause secondary effects *e.g.*, inflammation, infection, and/or tissue growth inhibition [342]. Hence, injectable hydrogels and bone cements (as combined with porous microspheres) have been proposed as alternatives for minimally invasive treatments.

For the case of **osteosarcoma**, locally delivered strategies combining therapeutic approaches have been reported, *e.g.*, hydrogels embedded with porous microspheres for drug delivery *via* patch implantation [343]; thermosensitive hydrogels in combination with chemotherapeutics delivered by intratumoral injection [344]; or

Fe_3O_4 and CaO_2 nanoparticles loaded into a 3D printed akermanite scaffolds for synergistic magnetic hyperthermia with catalytic suppression therapy, delivered *via* implantation [345]. Additionally, composite bone cements loaded with ferrimagnetic bioactive glass-ceramic particles for controlled delivery of heat in magnetic hyperthermia for bone tumours have been reported. Takegami *et al* [346] developed a bioactive bone cement, with a portion of the bioactive glass ceramic component replaced by magnetite micro-particles. The bone cements were implanted in a rabbit tibia and exposed to an external magnetic field (100 kHz). Similarly, Miola *et al* [347] prepared and characterised poly(methyl methacrylate)-based cement loaded with a bioactive glass (45S5) and iron oxide (Fe_2O_3 and FeO) particles. Regardless of the controlled delivery of heat shown in both investigations, the materials used were non-porous, irregular-shaped particles [346, 348]. Importantly, both investigations demonstrated the general suitability of glass-ceramic materials for bone cancer therapeutics.

In this context, it is proposed that P40- Fe_3O_4 porous microspheres could be utilised as a novel bone graft substitute for bone tumours, with magnetic hyperthermia and drug release potential. Alternatively, there is potential for the development of P40- Fe_3O_4 porous ferromagnetic microspheres, in combination with hydrogels or bone cements, for magnetic hyperthermia. In particular, high porosity levels could provide an opportunity for the incorporation and delivery of various payloads (drugs, biologics, cells, *etc.*) to specific tissue and/or location.

6.5 Summary

Highly porous, cytocompatible, glass-ceramic ferromagnetic microspheres have been manufactured *via* a facile, rapid, single-stage flame spheroidisation process, using ground powder mixtures of P40, Fe₃O₄ and CaCO₃. Complementary SEM, XRD, EDS and MLA investigations confirmed a distribution of ~10 µm sized Fe₃O₄ and Ca₂Fe₂O₅ phases embedded within 125 – 212 µm sized P40-based microsphere glass-matrices, with evolution of CO₂ from the porogen considered responsible to the development of interconnected porosity upon solidification. SQUID magnetometry provided evidence for remanent magnetisation (0.2 Am²/kg) of the P40-Fe₃O₄ porous microspheres, whilst the dispersion of embedded ferromagnetic Fe₃O₄ and Ca₂Fe₂O₅ phases was attributed to the effective application of inductive heat, to a constant level of 41.9°C, making these products highly appropriate for magnetic hyperthermia applications. Further, human osteoblast-derived cell-culture investigations confirmed cytocompatibility and hence general suitability of these P40-Fe₃O₄ porous microspheres for healthcare applications, with complementary ESEM evidence showing good conformation of MG-63 cells on the microsphere surfaces. It is suggested that the demonstration of highly porous, bioactive, glass-ceramic microspheres, incorporating ferromagnetic expression, opens up new opportunities for the development of synergistic biomaterials, *e.g.* for localised magnetic hyperthermia treatments, combined with the potential to deliver therapeutics incorporated within the pore structures. Furthermore, the flame spheroidisation of dense P40-Fe₃O₄ microspheres provided understanding related to glass-ceramic interactions, chemical transformations, and magnetic saturation variations as a function of mass ratio. The formation of core-shell / ring-shell ferromagnetic microstructures demonstrated the capability of the flame spheroidisation to develop such products. Nonetheless, there

is a need for process refinement for the controllable production of these materials. Finally, the rapid, single-stage, flame spheroidisation process showed relevance developing unique glass-ceramic combinations, with enhanced magnetic properties and strong porosity yields suitable for biomedical applications.

7.0 Conclusions and future work

7.1 Conclusions

The purpose of the present work was to develop novel, porous and dense, magnetic microspheres *via* a rapid, single-stage, flame spheroidisation method, for their application in healthcare.

In Chapter 4, dense (20 - 104 μm) Fe_3O_4 ferrimagnetic microspheres were produced *via* a facile, rapid, single-stage, flame spheroidisation process from large Fe_3O_4 precursors (<45 μm). Direct evidence from XRD, SEM, SQUID, Mössbauer, EDS and MLA characterisation, along with complementary HT-XRD and HT-SQUID investigations, demonstrated the formation of Fe_3O_4 dense microspheres and a retention of their ferrimagnetic properties post-flame spheroidisation. The combination of strong levels of magnetic saturation (96.3 Am^2/kg) and low remanent magnetisation (0.8 Am^2/kg) opens up new opportunities. For example, it is considered flame spheroidised Fe_3O_4 microspheres could be functionalised with appropriate polymers & chemotherapeutics to achieve cytocompatibility and, hence, be explored *e.g.*, as chemoembolization agents.

For the case of calcium ferrites, Chapter 4 and Chapter 5 investigated Fe_3O_4 / CaCO_3 combinations, using two Fe_3O_4 precursor sizes: small (<5 μm) and large (<45 μm). Morphological, structural and compositional investigations provided evidence on the effects of Fe_3O_4 precursor size, $\text{Fe}_3\text{O}_4:\text{CaCO}_3$ mass ratio, and $\text{O}_2/\text{C}_2\text{H}_2$ gas flow setting parameters. Further, dense (small, 35 - 80 μm) and porous (large, 125 - 180 μm) $\text{Ca}_2\text{Fe}_2\text{O}_5$ (srebrodolskite) ferromagnetic microspheres, with very high levels of compositional uniformity, were manufactured *via* rapid flame spheroidisation. The data

obtained from XRD, SEM, EDS and MLA characterisation, along with complementary HT-XRD and TGA investigations, allowed a mechanism to be established, describing the morphological development of $\text{Ca}_2\text{Fe}_2\text{O}_5$ microspheres from starting 1:1 Fe_3O_4 : CaCO_3 feedstock powder (Fe_3O_4 , $<5 \mu\text{m}$). It is suggested that the evolution of CO_2 gas bubbles (arising from decomposition of the CaCO_3 porogen), trapped within coalescing molten droplets, was responsible for the development of interconnected porosity during $\text{Ca}_2\text{Fe}_2\text{O}_5$ cooling and rapid solidification. Moreover, complementary SQUID magnetometry confirmed the ferromagnetic properties of the flame-spheroidised products. The potential use of $\text{Ca}_2\text{Fe}_2\text{O}_5$ microspheres (1:1 mass ratio / 2:2 gas flow setting) for magnetic hyperthermia applications was demonstrated via a simple, but significant, induction heating measurement (43.7°C). The combination of compositional control, high levels of porosity and functional properties (*i.e.*, magnetic and thermal) achieved opens up the opportunity to explore the application of magnetic microspheres for a range of biomedical challenges.

In Chapter 6, phosphate-based glass (denoted as P40) / Fe_3O_4 interactions in isolation (no CaCO_3 porogen) were studied. In particular, a formation of Fe_3O_4 / P40 glass melt pools was considered a key aspect for materials evolution and the formation of core-shell structures (1:1 P40: Fe_3O_4). Hence, no PVA was used for the flame spheroidisation of P40- Fe_3O_4 porous microspheres (contrary to Fe_3O_4 : CaCO_3 products); noting that a low glass melting point and low viscosity enabled rapid melting of the P40 glass and facilitated coalescence with Fe_3O_4 particles. In Chapters 4 and 5, increasing porogen concentration was associated with higher levels of porosity. Accordingly, highly porous microspheres 1:1 P40: Fe_3O_4 were flame spheroidised using elevated concentrations of porogen, *i.e.*, glass-ceramic precursors / porogen (1:3 mass ratio). In this context, highly porous, cytocompatible, glass-ceramic

ferromagnetic microspheres were manufactured *via* flame spheroidisation, using ground powder mixtures of P40, Fe₃O₄ and CaCO₃. Complementary SEM, XRD, EDS and MLA investigations confirmed a distribution of ~10 µm sized Fe₃O₄ and Ca₂Fe₂O₅ phases embedded within 125 – 212 µm sized P40-based microsphere glass-matrices, with evolution of CO₂ from the porogen considered responsible to the development of interconnected porosity upon rapid solidification. SQUID magnetometry provided evidence for remanent magnetisation (0.2 Am²/kg) of the P40-Fe₃O₄ porous microspheres, whilst dispersions of embedded ferromagnetic Fe₃O₄ and Ca₂Fe₂O₅ phases were attributed to the effective application of inductive heat, to a constant level of 41.9°C, making these products highly appropriate for magnetic hyperthermia applications.

Further, human osteoblast-derived cell-culture studies confirmed cytocompatibility and hence general suitability of P40-Fe₃O₄ porous microspheres for healthcare applications. Complementary ESEM evidence showing good conformation of MG-63 cells on P40-Fe₃O₄ porous microsphere surfaces. It is suggested that the demonstration of highly porous, bioactive, glass-ceramic microspheres, incorporating ferromagnetic expression, opens up new opportunities for the development of synergistic biomaterials, *e.g.* for localised magnetic hyperthermia treatments, combined with the potential to deliver chemotherapeutics incorporated within the pore structures.

7.2 Contributions

- Development of cytocompatible, P40-Fe₃O₄ ferromagnetic microspheres with high levels of interconnected porosity.
- Development of compositionally uniform, Ca₂Fe₂O₅ porous and dense ferromagnetic microspheres.
- Development of Fe₃O₄ dense microspheres with enhanced ferrimagnetic properties.
- The optimisation of the flame-spheroidisation process for the controllable production of magnetic microspheres and a comprehensive description of material dynamic evolution whilst flame-spheroidised.
- Demonstrated suitability of P40-Fe₃O₄ highly porous microspheres and Ca₂Fe₂O₅ porous and dense microspheres for magnetic hyperthermia applications.

7.3 Future work

- **Formal magnetic hyperthermia investigations.** As detailed in Chapters 5 and 6, formal validation of microsphere product magnetic hyperthermia would be required in a controlled environment using an alternating magnetic field (AFM) system. An *in vitro* evaluation of the heating performance of P40-Fe₃O₄ and Ca₂Fe₂O₅ microspheres applied in tumour cells is proposed for future work. For example, Mamani *et al* [349] evaluated *in vitro* magnetic hyperthermia of magnetic nanoparticles in glioblastoma tumour cells using a commercial AFM system DM100 (nB nanoscale Biomagnetics, 305 - 557 kHz).

- **Cytocompatibility investigations** for prolonged periods, e.g., day 14, day 21, etc. Accordingly, degradation studies on P40-Fe₃O₄ porous microspheres are proposed, to evaluate material bioactivity. Further, it is suggested to study the effect of Ca₂Fe₂O₅ microspheres on different cell types, e.g. T-cells [36].
- **Flame spheroidisation & process conditions.** Refinement of the flame spheroidisation technique is proposed for the controlled production of core-shell P40-Fe₃O₄ microspheres. Additionally, it is suggested to use laser and optical diagnostic techniques [308] for the measurement and analysis of physical parameters (e.g. particle velocity, flame pressure and temperature) associated with microsphere formation mechanisms within the flame.
- **Materials.** In order to develop related bioactive magnetic microspheres with tailored properties, it is suggested to explore additional phosphorous concentrations (e.g., P30, P45) and/or alternative porogens, e.g., sodium carbonate (Na₂CO₃) or combinations of porogens (e.g., CaCO₃ and Na₂CO₃).
- **Additional biomedical investigations,** such as absorption and release studies of P40-Fe₃O₄ highly porous microspheres for drug delivery applications; T1/T2 relaxation measurements on magnetic microspheres developed in the present investigation, for their application in MRI; and bone cements and/or hydrogels incorporating P40-Fe₃O₄ microspheres.

References

- [1] H. Sung, J. Ferlay, R. L. Siegel, M. Laversanne, I. Soerjomataram, A. Jemal, and F. Bray, "Global Cancer Statistics 2020: GLOBOCAN Estimates of Incidence and Mortality Worldwide for 36 Cancers in 185 Countries," *CA: A Cancer Journal for Clinicians*, vol. 71, no. 3, pp. 209-249, 2021, doi: <https://doi.org/10.3322/caac.21660>.
- [2] E. Sharifi, A. Bigham, S. Yousefiasl, M. Trovato, M. Ghomi, Y. Esmaeili, P. Samadi, A. Zarrabi, M. Ashrafizadeh, S. Sharifi, R. Sartorius, F. Dabbagh Moghaddam, A. Maleki, H. Song, T. Agarwal, T. K. Maiti, N. Nikfarjam, C. Burvill, V. Mattoli, M. G. Raucci, K. Zheng, A. R. Boccaccini, L. Ambrosio, and P. Makvandi, "Mesoporous Bioactive Glasses in Cancer Diagnosis and Therapy: Stimuli-Responsive, Toxicity, Immunogenicity, and Clinical Translation," *Advanced Science*, vol. 9, no. 2, p. 2102678, 2022, doi: <https://doi.org/10.1002/advs.202102678>.
- [3] L. Zhong, Y. Li, L. Xiong, W. Wang, M. Wu, T. Yuan, W. Yang, C. Tian, Z. Miao, T. Wang, and S. Yang, "Small molecules in targeted cancer therapy: advances, challenges, and future perspectives," *Signal Transduction and Targeted Therapy*, vol. 6, no. 1, p. 201, 2021/05/31 2021, doi: 10.1038/s41392-021-00572-w.
- [4] S. Senapati, A. K. Mahanta, S. Kumar, and P. Maiti, "Controlled drug delivery vehicles for cancer treatment and their performance," *Signal Transduction and Targeted Therapy*, vol. 3, no. 1, p. 7, 2018/03/16 2018, doi: 10.1038/s41392-017-0004-3.
- [5] B. Lin, F. Gao, Y. Yang, D. Wu, Y. Zhang, G. Feng, T. Dai, and X. Du, "FLASH Radiotherapy: History and Future," (in English), *Frontiers in Oncology*, Review vol. 11, 2021-May-25 2021, doi: 10.3389/fonc.2021.644400.
- [6] E. J. Moding, M. B. Kastan, and D. G. Kirsch, "Strategies for optimizing the response of cancer and normal tissues to radiation," (in eng), *Nat Rev Drug Discov*, vol. 12, no. 7, pp. 526-542, 2013, doi: 10.1038/nrd4003.
- [7] A. Rajan and N. K. Sahu, "Review on magnetic nanoparticle-mediated hyperthermia for cancer therapy," *Journal of Nanoparticle Research*, vol. 22, no. 11, p. 319, 2020/10/21 2020, doi: 10.1007/s11051-020-05045-9.
- [8] Y. Iian, L. Wang, J. Cao, T. Liu, Z. Xu, B. Yang, T. Huang, X. Jiang, and N. Wu, "Recent advances on the magnetic nanoparticle-based nanocomposites for magnetic induction hyperthermia of tumor: a short review," *Advanced Composites and Hybrid Materials*, vol. 4, no. 4, pp. 925-937, 2021/12/01 2021, doi: 10.1007/s42114-021-00373-3.
- [9] I. Hilger, "In vivo applications of magnetic nanoparticle hyperthermia," *International Journal of Hyperthermia*, vol. 29, no. 8, pp. 828-834, 2013/12/01 2013, doi: 10.3109/02656736.2013.832815.
- [10] D. Chang, M. Lim, J. Goos, R. Qiao, Y. Y. Ng, F. M. Mansfeld, M. Jackson, T. P. Davis, and M. Kavallaris, "Biologically Targeted Magnetic Hyperthermia: Potential and Limitations," (in eng), *Front Pharmacol*, vol. 9, p. 831, 2018, doi: 10.3389/fphar.2018.00831.
- [11] X. Liu, Y. Zhang, Y. Wang, W. Zhu, G. Li, X. Ma, Y. Zhang, S. Chen, S. Tiwari, K. Shi, S. Zhang, H. M. Fan, Y. X. Zhao, and X.-J. Liang, "Comprehensive understanding of magnetic hyperthermia for improving antitumor therapeutic

- efficacy," (in eng), *Theranostics*, vol. 10, no. 8, pp. 3793-3815, 2020, doi: 10.7150/thno.40805.
- [12] V. Safronov, E. Sozontov, and M. Polikarpov, "Magnetite nanoparticles for nonradionuclide brachytherapy," (in eng), *J Appl Crystallogr*, vol. 48, no. Pt 3, pp. 690-692, 2015, doi: 10.1107/S1600576715008900.
- [13] I. Sato, M. Umemura, K. Mitsudo, H. Fukumura, J.-H. Kim, Y. Hoshino, H. Nakashima, M. Kioi, R. Nakakaji, M. Sato, T. Fujita, U. Yokoyama, S. Okumura, H. Oshiro, H. Eguchi, I. Tohnai, and Y. Ishikawa, "Simultaneous hyperthermia-chemotherapy with controlled drug delivery using single-drug nanoparticles," *Sci Rep*, vol. 6, no. 1, p. 24629, 2016/04/22 2016, doi: 10.1038/srep24629.
- [14] Y. Fang, Y. He, C. Wu, M. Zhang, Z. Gu, J. Zhang, E. Liu, Q. Xu, A. M. Asrorov, and Y. Huang, "Magnetism-mediated targeting hyperthermia-immunotherapy in "cold" tumor with CSF1R inhibitor," (in eng), *Theranostics*, vol. 11, no. 14, pp. 6860-6872, 2021, doi: 10.7150/thno.57511.
- [15] P. T. Yin, S. Shah, N. J. Pasquale, O. B. Garbuzenko, T. Minko, and K. B. Lee, "Stem cell-based gene therapy activated using magnetic hyperthermia to enhance the treatment of cancer," (in eng), *Biomaterials*, vol. 81, pp. 46-57, Mar 2016, doi: 10.1016/j.biomaterials.2015.11.023.
- [16] K. McNamara and S. A. M. Tofail, "Nanoparticles in biomedical applications," *Advances in Physics: X*, vol. 2, no. 1, pp. 54-88, 2017/01/02 2017, doi: 10.1080/23746149.2016.1254570.
- [17] B. H. Ong, N. K. Devaraj, M. Matsumoto, and M. H. Abdullah, "Thermal stability of magnetite (Fe₃O₄) nanoparticles," *MRS Proceedings*, vol. 1118, pp. 1118-K03-09, 2011, Art no. 1118-k03-09, doi: 10.1557/PROC-1118-K03-09.
- [18] C. S. S. R. Kumar and F. Mohammad, "Magnetic nanomaterials for hyperthermia-based therapy and controlled drug delivery," (in eng), *Advanced drug delivery reviews*, vol. 63, no. 9, pp. 789-808, 2011, doi: 10.1016/j.addr.2011.03.008.
- [19] V. Marghussian, "4 - Magnetic Properties of Nano-Glass Ceramics," in *Nano-Glass Ceramics*, V. Marghussian Ed. Oxford: William Andrew Publishing, 2015, pp. 181-223.
- [20] M. Johannsen, B. Thiesen, P. Wust, and A. Jordan, "Magnetic nanoparticle hyperthermia for prostate cancer," (in eng), *Int J Hyperthermia*, vol. 26, no. 8, pp. 790-5, 2010, doi: 10.3109/02656731003745740.
- [21] K. Mahmoudi, A. Bouras, D. Bozec, R. Ivkov, and C. Hadjipanayis, "Magnetic hyperthermia therapy for the treatment of glioblastoma: a review of the therapy's history, efficacy and application in humans," *International Journal of Hyperthermia*, vol. 34, no. 8, pp. 1316-1328, 2018/11/17 2018, doi: 10.1080/02656736.2018.1430867.
- [22] S. Bae, S. W. Lee, and Y. Takemura, "Applications of NiFe₂O₄ nanoparticles for a hyperthermia agent in biomedicine," *Applied Physics Letters*, vol. 89, no. 25, p. 252503, 2006, doi: 10.1063/1.2420769.
- [23] C. R. Kalaiselvan, N. D. Thorat, and N. K. Sahu, "Carboxylated PEG-Functionalized MnFe₂O₄ Nanocubes Synthesized in a Mixed Solvent: Morphology, Magnetic Properties, and Biomedical Applications," *ACS Omega*, vol. 6, no. 8, pp. 5266-5275, 2021/03/02 2021, doi: 10.1021/acsomega.0c05382.
- [24] D. Karthickraja, S. Karthi, G. A. Kumar, D. K. Sardar, G. C. Dannangoda, K. S. Martirosyan, and E. K. Girija, "Fabrication of core-shell CoFe₂O₄@HAp nanoparticles: a novel magnetic platform for biomedical applications," *New*

- Journal of Chemistry*, 10.1039/C9NJ02510C vol. 43, no. 34, pp. 13584-13593, 2019, doi: 10.1039/C9NJ02510C.
- [25] M. Srivastava, S. K. Alla, S. S. Meena, N. Gupta, R. K. Mandal, and N. K. Prasad, "Magnetic field regulated, controlled hyperthermia with $\text{Li}_x\text{Fe}_{3-x}\text{O}_4$ ($0.06 \leq x \leq 0.3$) nanoparticles," *Ceramics International*, vol. 45, no. 9, pp. 12028-12034, 2019/06/15/ 2019, doi: <https://doi.org/10.1016/j.ceramint.2019.03.097>.
- [26] A. Matsumine, K. Takegami, K. Asanuma, T. Matsubara, T. Nakamura, A. Uchida, and A. Sudo, "A novel hyperthermia treatment for bone metastases using magnetic materials," *International Journal of Clinical Oncology*, vol. 16, no. 2, pp. 101-108, 2011/04/01 2011, doi: 10.1007/s10147-011-0217-3.
- [27] E. Ruiz-Hernández, M. C. Serrano, D. Arcos, and M. Vallet-Regí, "Glass-glass ceramic thermoseeds for hyperthermic treatment of bone tumors," (in eng), *J Biomed Mater Res A*, vol. 79, no. 3, pp. 533-43, Dec 1 2006, doi: 10.1002/jbm.a.30889.
- [28] A. Farzin, S. Hassan, R. Emadi, S. A. Etesami, and J. Ai, "Comparative evaluation of magnetic hyperthermia performance and biocompatibility of magnetite and novel Fe-doped hardystonite nanoparticles for potential bone cancer therapy," (in eng), *Mater Sci Eng C Mater Biol Appl*, vol. 98, pp. 930-938, May 2019, doi: 10.1016/j.msec.2019.01.038.
- [29] R. A. Rytov, V. A. Bautin, and N. A. Usov, "Towards optimal thermal distribution in magnetic hyperthermia," *Sci Rep*, vol. 12, no. 1, p. 3023, 2022/02/22 2022, doi: 10.1038/s41598-022-07062-1.
- [30] Y. Rabin, "Is intracellular hyperthermia superior to extracellular hyperthermia in the thermal sense?," (in eng), *Int J Hyperthermia*, vol. 18, no. 3, pp. 194-202, May-Jun 2002, doi: 10.1080/02656730110116713.
- [31] D. Serantes and D. Baldomir, "Nanoparticle Size Threshold for Magnetic Agglomeration and Associated Hyperthermia Performance," *Nanomaterials*, vol. 11, no. 11, p. 2786, 2021. [Online]. Available: <https://www.mdpi.com/2079-4991/11/11/2786>.
- [32] U. M. Engelmann, E. M. Buhl, S. Draack, T. Viereck, F. Ludwig, T. Schmitz-Rode, and I. Slabu, "Magnetic Relaxation of Agglomerated and Immobilized Iron Oxide Nanoparticles for Hyperthermia and Imaging Applications," *IEEE Magnetics Letters*, vol. 9, pp. 1-5, 2018, doi: 10.1109/LMAG.2018.2879034.
- [33] R. Mejías, P. Hernández Flores, M. Talelli, J. L. Tajada-Herráiz, M. E. F. Brollo, Y. Portilla, M. P. Morales, and D. F. Barber, "Cell-Promoted Nanoparticle Aggregation Decreases Nanoparticle-Induced Hyperthermia under an Alternating Magnetic Field Independently of Nanoparticle Coating, Core Size, and Subcellular Localization," *ACS Applied Materials & Interfaces*, vol. 11, no. 1, pp. 340-355, 2019/01/09 2019, doi: 10.1021/acsami.8b18451.
- [34] D. S. M. Pereira, B. D. Cardoso, A. R. O. Rodrigues, C. O. Amorim, V. S. Amaral, B. G. Almeida, M.-J. R. P. Queiroz, O. Martinho, F. Baltazar, R. C. Calhelha, I. C. F. R. Ferreira, P. J. G. Coutinho, and E. M. S. Castanheira, "Magnetoliposomes Containing Calcium Ferrite Nanoparticles for Applications in Breast Cancer Therapy," *Pharmaceutics*, vol. 11, no. 9, p. 477, 2019. [Online]. Available: <https://www.mdpi.com/1999-4923/11/9/477>.
- [35] B. D. Cardoso, A. R. O. Rodrigues, B. G. Almeida, C. O. Amorim, V. S. Amaral, E. M. S. Castanheira, and P. J. G. Coutinho, "Stealth Magnetoliposomes Based on Calcium-Substituted Magnesium Ferrite Nanoparticles for Curcumin Transport and Release," *International Journal of Molecular Sciences*, vol. 21,

- no. 10, p. 3641, 2020. [Online]. Available: <https://www.mdpi.com/1422-0067/21/10/3641>.
- [36] L. Khanna and N. K. Verma, "Synthesis, characterization and in vitro cytotoxicity study of calcium ferrite nanoparticles," *Materials Science in Semiconductor Processing*, vol. 16, no. 6, pp. 1842-1848, 2013/12/01/ 2013, doi: <https://doi.org/10.1016/j.mssp.2013.07.016>.
- [37] A. Kheradmand, O. Vahidi, and S. M. Masoudpanah, "Magnetic, hyperthermic and structural properties of zn substituted CaFe₂O₄ powders," *Applied Physics A*, vol. 124, no. 3, p. 255, 2018/02/16 2018, doi: 10.1007/s00339-018-1672-8.
- [38] R. Bilas, K. Sriram, P. U. Maheswari, and K. M. M. Sheriffa Begum, "Highly biocompatible chitosan with super paramagnetic calcium ferrite (CaFe₂O₄) nanoparticle for the release of ampicillin," *International Journal of Biological Macromolecules*, vol. 97, pp. 513-525, 2017/04/01/ 2017, doi: <https://doi.org/10.1016/j.ijbiomac.2017.01.036>.
- [39] E. Naderi, M. Aghajanzadeh, M. Zamani, A. Sharafi, M. Naseri, and H. Danafar, "The Effect of Calcination Temperature on the Anticancer Activity of CaFe₂O₄@PVA Nanocarriers: Photodynamic Therapy and Drug Delivery Study," *Journal of Inorganic and Organometallic Polymers and Materials*, vol. 30, no. 12, pp. 5261-5269, 2020/12/01 2020, doi: 10.1007/s10904-020-01653-z.
- [40] L. Khanna and N. K. Verma, "Biocompatibility and superparamagnetism in novel silica/CaFe₂O₄ nanocomposite," *Materials Letters*, vol. 128, pp. 376-379, 2014/08/01/ 2014, doi: <https://doi.org/10.1016/j.matlet.2014.04.168>.
- [41] P. Y. Reyes-Rodríguez, D. A. Cortés-Hernández, C. A. Ávila-Orta, J. Sánchez, M. Andrade-Guel, A. Herrera-Guerrero, C. Cabello-Alvarado, and V. H. Ramos-Martínez, "Synthesis of Pluronic F127-coated magnesium/calcium (Mg_{1-x}Ca_xFe₂O₄) magnetic nanoparticles for biomedical applications," *Journal of Magnetism and Magnetic Materials*, vol. 521, p. 167518, 2021/03/01/ 2021, doi: <https://doi.org/10.1016/j.jmmm.2020.167518>.
- [42] T. Ruthradevi, J. Akbar, G. Suresh Kumar, A. Thamizhavel, G. A. Kumar, R. K. Vatsa, G. C. Dannangoda, K. S. Martirosyan, and E. K. Girija, "Investigations on nickel ferrite embedded calcium phosphate nanoparticles for biomedical applications," *Journal of Alloys and Compounds*, vol. 695, pp. 3211-3219, 2017/02/25/ 2017, doi: <https://doi.org/10.1016/j.jallcom.2016.11.300>.
- [43] R. A. Jasso-Terán, D. A. Cortés-Hernández, H. J. Sánchez-Fuentes, P. Y. Reyes-Rodríguez, L. E. de-León-Prado, J. C. Escobedo-Bocardo, and J. M. Almanza-Robles, "Synthesis, characterization and hemolysis studies of Zn(1-x)Ca_xFe₂O₄ ferrites synthesized by sol-gel for hyperthermia treatment applications," *Journal of Magnetism and Magnetic Materials*, vol. 427, pp. 241-244, 2017/04/01/ 2017, doi: <https://doi.org/10.1016/j.jmmm.2016.10.099>.
- [44] M. M. Saldívar-Ramírez, C. G. Sánchez-Torres, D. A. Cortés-Hernández, J. C. Escobedo-Bocardo, J. M. Almanza-Robles, A. Larson, P. J. Reséndiz-Hernández, and I. O. Acuña-Gutiérrez, "Study on the efficiency of nanosized magnetite and mixed ferrites in magnetic hyperthermia," (in eng), *J Mater Sci Mater Med*, vol. 25, no. 10, pp. 2229-36, Oct 2014, doi: 10.1007/s10856-014-5187-3.
- [45] A. A. Luderer, N. F. Borrelli, J. N. Panzarino, G. R. Mansfield, D. M. Hess, J. L. Brown, E. H. Barnett, and E. W. Hahn, "Glass-ceramic-mediated, magnetic-field-induced localized hyperthermia: response of a murine mammary carcinoma," (in eng), *Radiat Res*, vol. 94, no. 1, pp. 190-8, Apr 1983.

- [46] M. Miola, Y. Pakzad, S. Banijamali, S. Kargozar, C. Vitale-Brovarone, A. Yazdanpanah, O. Bretcanu, A. Ramedani, E. Vernè, and M. Mozafari, "Glass-ceramics for cancer treatment: So close, or yet so far?," (in eng), *Acta Biomater*, vol. 83, pp. 55-70, Jan 1 2019, doi: 10.1016/j.actbio.2018.11.013.
- [47] K. M. Z. Hossain, U. Patel, and I. Ahmed, "Development of microspheres for biomedical applications: a review," *Progress in Biomaterials*, vol. 4, no. 1, pp. 1-19, 2015/03/01 2015, doi: 10.1007/s40204-014-0033-8.
- [48] Y. Cai, Y. Chen, X. Hong, Z. Liu, and W. Yuan, "Porous microsphere and its applications," (in eng), *Int J Nanomedicine*, vol. 8, pp. 1111-1120, 2013, doi: 10.2147/IJN.S41271.
- [49] S. Freiberg and X. X. Zhu, "Polymer microspheres for controlled drug release," *International journal of pharmaceuticals*, vol. 282, no. 1, pp. 1-18, 2004/09/10/ 2004, doi: <https://doi.org/10.1016/j.ijpharm.2004.04.013>.
- [50] A. L. Sousa and I. Ahmed, *Manufacturing processes for polymeric micro and nanoparticles and their biomedical applications*. 2017, pp. 46-72.
- [51] A. Matamoros-Veloza, K. M. Z. Hossain, B. E. Scammell, I. Ahmed, R. Hall, and N. Kapur, "Formulating injectable pastes of porous calcium phosphate glass microspheres for bone regeneration applications," *Journal of the Mechanical Behavior of Biomedical Materials*, vol. 102, p. 103489, 2020/02/01/ 2020, doi: <https://doi.org/10.1016/j.jmbbm.2019.103489>.
- [52] D. Gupta, K. M. Z. Hossain, M. Roe, E. F. Smith, I. Ahmed, V. Sottile, and D. M. Grant, "Long-Term Culture of Stem Cells on Phosphate-Based Glass Microspheres: Synergistic Role of Chemical Formulation and 3D Architecture," *ACS Applied Bio Materials*, vol. 4, no. 8, pp. 5987-6004, 2021/08/16 2021, doi: 10.1021/acsabm.1c00120.
- [53] K. M. Z. Hossain, U. Patel, A. R. Kennedy, L. Macri-Pellizzeri, V. Sottile, D. M. Grant, B. E. Scammell, and I. Ahmed, "Porous calcium phosphate glass microspheres for orthobiologic applications," *Acta Biomaterialia*, vol. 72, pp. 396-406, 2018/05/01/ 2018, doi: <https://doi.org/10.1016/j.actbio.2018.03.040>.
- [54] E. A. Abou Neel, A. Kiani, S. P. Valappil, N. M. Mordan, S.-Y. Baek, K. M. Zakir Hossain, R. M. Felfel, I. Ahmed, K. Divakarl, W. Chrzanowski, and J. C. Knowles, "Glass microparticle- versus microsphere-filled experimental dental adhesives," *Journal of Applied Polymer Science*, vol. 136, no. 32, p. 47832, 2019, doi: <https://doi.org/10.1002/app.47832>.
- [55] B. Milborne, A. Arafat, R. Layfield, A. Thompson, and I. Ahmed, "The Use of Biomaterials in Internal Radiation Therapy," *Recent Progress in Materials*, vol. 2, pp. 1-34, 05/12 2020, doi: 10.21926/rpm.2002012.
- [56] D. Ghosh Dastidar, S. Saha, and M. Chowdhury, "Porous microspheres: Synthesis, characterisation and applications in pharmaceutical & medical fields," (in eng), *International journal of pharmaceuticals*, vol. 548, no. 1, pp. 34-48, Sep 5 2018, doi: 10.1016/j.ijpharm.2018.06.015.
- [57] M. T. Islam, N. A. Nuzulia, L. Macri-Pellizzeri, F. Nigar, Y. W. Sari, and I. Ahmed, "Evolution of silicate bioglass particles as porous microspheres with a view towards orthobiologics," *Journal of Biomaterials Applications*, vol. 36, no. 8, pp. 1427-1443, 2022/03/01 2022, doi: 10.1177/08853282211059294.
- [58] B. Arifvianto and J. Zhou, "Fabrication of Metallic Biomedical Scaffolds with the Space Holder Method: A Review," (in eng), *Materials (Basel)*, vol. 7, no. 5, pp. 3588-3622, 2014, doi: 10.3390/ma7053588.
- [59] H. Cai, W. Mu, W. Liu, X. Zhang, and Y. Deng, "Sol-gel synthesis highly porous titanium dioxide microspheres with cellulose nanofibrils-based aerogel

- templates," *Inorganic Chemistry Communications*, vol. 51, pp. 71-74, 2015/01/01/ 2015, doi: <https://doi.org/10.1016/j.inoche.2014.11.013>.
- [60] S. Hooshmand, J. Nordin, and F. Akhtar, "Porous alumina ceramics by gel casting: Effect of type of sacrificial template on the properties," *International Journal of Ceramic Engineering & Science*, vol. 1, no. 2, pp. 77-84, 2019/07/01 2019, doi: 10.1002/ces2.10013.
- [61] M. A. A. Muhamad Nor, L. C. Hong, Z. Arifin Ahmad, and H. Md Akil, "Preparation and characterization of ceramic foam produced via polymeric foam replication method," *Journal of Materials Processing Technology*, vol. 207, no. 1, pp. 235-239, 2008/10/16/ 2008, doi: <https://doi.org/10.1016/j.jmatprotec.2007.12.099>.
- [62] Y. J. Tan, X. Tan, W. Y. Yeong, and S. B. Tor, "Hybrid microsccaffold-based 3D bioprinting of multi-cellular constructs with high compressive strength: A new biofabrication strategy," *Sci Rep*, vol. 6, no. 1, p. 39140, 2016/12/14 2016, doi: 10.1038/srep39140.
- [63] J. Molinar Díaz, S. A. Samad, E. Steer, N. Neate, H. Constantin, M. T. Islam, P. D. Brown, and I. Ahmed, "Flame spheroidisation of dense and porous Ca₂Fe₂O₅ microspheres," *Materials Advances*, 10.1039/D0MA00564A vol. 1, no. 9, pp. 3539-3544, 2020, doi: 10.1039/D0MA00564A.
- [64] J. Molinar-Díaz, J. L. Woodliffe, E. Steer, N. A. Morley, P. D. Brown, and I. Ahmed, "Optimisation of the Flame Spheroidisation Process for the Rapid Manufacture of Fe₃O₄-Based Porous and Dense Microspheres," *Molecules*, vol. 28, no. 6, p. 2523, 2023. [Online]. Available: <https://www.mdpi.com/1420-3049/28/6/2523>.
- [65] J. Molinar-Díaz, J. L. Woodliffe, B. Milborne, L. Murrell, M. T. Islam, E. Steer, N. Weston, N. A. Morley, P. D. Brown, and I. Ahmed, "Ferromagnetic Cytocompatible Glass-Ceramic Porous Microspheres for Magnetic Hyperthermia Applications," *Advanced Materials Interfaces*, vol. n/a, no. n/a, p. 2202089, doi: <https://doi.org/10.1002/admi.202202089>.
- [66] Wahajuddin and S. Arora, "Superparamagnetic iron oxide nanoparticles: magnetic nanoplatforms as drug carriers," (in eng), *Int J Nanomedicine*, vol. 7, pp. 3445-71, 2012, doi: 10.2147/ijn.S30320.
- [67] Q. A. Pankhurst, J. Connolly, S. K. Jones, and J. Dobson, "Applications of magnetic nanoparticles in biomedicine," *Journal of Physics D: Applied Physics*, vol. 36, no. 13, pp. R167-R181, 2003/06/19 2003, doi: 10.1088/0022-3727/36/13/201.
- [68] V. I. Shubayev, T. R. Pisanic, 2nd, and S. Jin, "Magnetic nanoparticles for theragnostics," (in eng), *Advanced drug delivery reviews*, vol. 61, no. 6, pp. 467-77, Jun 21 2009, doi: 10.1016/j.addr.2009.03.007.
- [69] H. S. Huang and J. F. Hainfeld, "Intravenous magnetic nanoparticle cancer hyperthermia," (in eng), *Int J Nanomedicine*, vol. 8, pp. 2521-32, 2013, doi: 10.2147/ijn.S43770.
- [70] L. S. Arias, J. P. Pessan, A. P. M. Vieira, T. M. T. d. Lima, A. C. B. Delbem, and D. R. Monteiro, "Iron Oxide Nanoparticles for Biomedical Applications: A Perspective on Synthesis, Drugs, Antimicrobial Activity, and Toxicity," (in eng), *Antibiotics (Basel)*, vol. 7, no. 2, p. 46, 2018, doi: 10.3390/antibiotics7020046.
- [71] K. El-Boubbou, "Magnetic iron oxide nanoparticles as drug carriers: clinical relevance," (in eng), *Nanomedicine (London, England)*, vol. 13, no. 8, pp. 953-971, Apr 2018, doi: 10.2217/nnm-2017-0336.

- [72] M. Salimi, S. Sarkar, R. Saber, H. Delavari, A. M. Alizadeh, and H. T. Mulder, "Magnetic hyperthermia of breast cancer cells and MRI relaxometry with dendrimer-coated iron-oxide nanoparticles," *Cancer Nanotechnology*, vol. 9, no. 1, p. 7, 2018/10/08 2018, doi: 10.1186/s12645-018-0042-8.
- [73] D. D. Stueber, J. Villanova, I. Aponte, Z. Xiao, and V. L. Colvin, "Magnetic Nanoparticles in Biology and Medicine: Past, Present, and Future Trends," (in eng), *Pharmaceutics*, vol. 13, no. 7, Jun 24 2021, doi: 10.3390/pharmaceutics13070943.
- [74] X. Nan, X. Zhang, Y. Liu, M. Zhou, X. Chen, and X. Zhang, "Dual-Targeted Multifunctional Nanoparticles for Magnetic Resonance Imaging Guided Cancer Diagnosis and Therapy," *ACS Applied Materials & Interfaces*, vol. 9, no. 11, pp. 9986-9995, 2017/03/22 2017, doi: 10.1021/acsami.6b16486.
- [75] Deloitte, "Predicting the future of healthcare and life sciences in 2025," p. 10. [Online]. Available: <https://www2.deloitte.com/content/dam/Deloitte/uk/Documents/life-sciences-health-care/deloitte-uk-life-sciences-healthcare-predictions-clinicians-are-empowered-by-diagnostic-and-treatment-paradigms.pdf>
- [76] Deloitte, "Deloitte predicts health spending as a percentage of GDP will decelerate over the next 20 years." [Online]. Available: <https://www2.deloitte.com/xe/en/insights/industry/health-care/future-health-care-spending.html>
- [77] G. V. Research. Magnetic Beads Market Size, Share & Trends Analysis Report By Application (Bioresearch, In-vitro Diagnostics, Others), By Region (North America, Europe, Asia Pacific, CSA, MEA), And Segment Forecasts, 2022 - 2030 [Online] Available: <https://www.grandviewresearch.com/industry-analysis/magnetic-beads-market>
- [78] M. Geppert and M. Himly, "Iron Oxide Nanoparticles in Bioimaging - An Immune Perspective," (in eng), *Front Immunol*, vol. 12, pp. 688927-688927, 2021, doi: 10.3389/fimmu.2021.688927.
- [79] R. A. Revia and M. Zhang, "Magnetite nanoparticles for cancer diagnosis, treatment, and treatment monitoring: recent advances," (in eng), *Materials today (Kidlington, England)*, vol. 19, no. 3, pp. 157-168, Apr 2016, doi: 10.1016/j.mattod.2015.08.022.
- [80] "Magnetic sentinel lymph node biopsy. Sentimag®–Magtrace®." [Online]. Available: https://www.sysmex.cz/fileadmin/media/f100/Business_Lines/Brochure/Magtrace_brochure_EN.pdf
- [81] B. E. Crețu, G. Dodi, A. Shavandi, I. Gardikiotis, I. L. Șerban, and V. Balan, "Imaging Constructs: The Rise of Iron Oxide Nanoparticles," (in eng), *Molecules*, vol. 26, no. 11, Jun 5 2021, doi: 10.3390/molecules26113437.
- [82] H. E. Daldrup-Link, "Ten Things You Might Not Know about Iron Oxide Nanoparticles," *Radiology*, vol. 284, no. 3, pp. 616-629, 2017, doi: 10.1148/radiol.2017162759.
- [83] G. B. Toth, C. G. Varallyay, A. Horvath, M. R. Bashir, P. L. Choyke, H. E. Daldrup-Link, E. Dosa, J. P. Finn, S. Gahramanov, M. Harisinghani, I. Macdougall, A. Neuwelt, S. S. Vasanawala, P. Ambady, R. Barajas, J. S. Cetas, J. Ciporen, T. J. DeLoughery, N. D. Doolittle, R. Fu, J. Grinstead, A. R. Guimaraes, B. E. Hamilton, X. Li, H. L. McConnell, L. L. Muldoon, G. Nesbit, J. P. Netto, D. Petterson, W. D. Rooney, D. Schwartz, L. Szidonya, and E. A. Neuwelt, "Current and potential imaging applications of ferumoxytol for

- magnetic resonance imaging," *Kidney International*, vol. 92, no. 1, pp. 47-66, 2017/07/01/ 2017, doi: <https://doi.org/10.1016/j.kint.2016.12.037>.
- [84] B. Schiller, P. Bhat, and A. Sharma, "Safety and Effectiveness of Ferumoxytol in Hemodialysis Patients at 3 Dialysis Chains in the United States Over a 12-Month Period," *Clinical Therapeutics*, vol. 36, no. 1, pp. 70-83, 2014/01/01/ 2014, doi: <https://doi.org/10.1016/j.clinthera.2013.09.028>.
- [85] U. S. F. a. D. Administration, "FDA strengthens warnings and changes prescribing instructions to decrease the risk of serious allergic reactions with anemia drug Feraheme (ferumoxytol)," *Drug Safety Communications*. [Online]. Available: <https://www.fda.gov/media/91415/download>
- [86] Y. X. J. Wáng and J.-M. Idée, "A comprehensive literatures update of clinical researches of superparamagnetic resonance iron oxide nanoparticles for magnetic resonance imaging," *Quantitative Imaging in Medicine and Surgery*, vol. 7, no. 1, pp. 88-122, 2017. [Online]. Available: <https://qims.amegroups.com/article/view/13786>.
- [87] M. Jeon, M. V. Halbert, Z. R. Stephen, and M. Zhang, "Iron Oxide Nanoparticles as T(1) Contrast Agents for Magnetic Resonance Imaging: Fundamentals, Challenges, Applications, and Prospectives," (in eng), *Adv Mater*, vol. 33, no. 23, p. e1906539, Jun 2021, doi: 10.1002/adma.201906539.
- [88] F. Soetaert, P. Korangath, D. Serantes, S. Fiering, and R. Ivkov, "Cancer therapy with iron oxide nanoparticles: Agents of thermal and immune therapies," *Advanced drug delivery reviews*, vol. 163-164, pp. 65-83, 2020/01/01/ 2020, doi: <https://doi.org/10.1016/j.addr.2020.06.025>.
- [89] H. U. Ahmed. "Magnetic Nanoparticle Thermoablation-Retention and Maintenance in the Prostate:A Phase 0 Study in Men (MAGNABLATE I)." *ClinicalTrials*.
<https://clinicaltrials.gov/ct2/show/NCT02033447?term=radiotherapy+AND+magnetic+nanoparticles&draw=2&rank=1> (accessed.
- [90] "ClinicalTrials." [Online]. Available: <https://clinicaltrials.gov/ct2/results?cond=&term=iron+oxide&cntry=&state=&city=&dist=>
- [91] S. Adepu and S. Ramakrishna, "Controlled Drug Delivery Systems: Current Status and Future Directions," *Molecules*, vol. 26, no. 19, p. 5905, 2021. [Online]. Available: <https://www.mdpi.com/1420-3049/26/19/5905>.
- [92] P. T. Verma, A.; Deshmukh, K.; Jha, A.; Verma, S., "Routes of drug administration," *Int. J. Pharm. Stud. Res.*, vol. 1, pp. 54–59, 2010.
- [93] D. S. W. Benoit, C. T. Overby, K. R. Sims Jr, and M. A. Ackun-Farmmer, "2.5.12 - Drug Delivery Systems," in *Biomaterials Science (Fourth Edition)*, W. R. Wagner, S. E. Sakiyama-Elbert, G. Zhang, and M. J. Yaszemski Eds.: Academic Press, 2020, pp. 1237-1266.
- [94] J. S. McLaren, L. Macri-Pellizzeri, K. M. Z. Hossain, U. Patel, D. M. Grant, B. E. Scammell, I. Ahmed, and V. Sottile, "Porous Phosphate-Based Glass Microspheres Show Biocompatibility, Tissue Infiltration, and Osteogenic Onset in an Ovine Bone Defect Model," *ACS Applied Materials & Interfaces*, vol. 11, no. 17, pp. 15436-15446, 2019/05/01 2019, doi: 10.1021/acsami.9b04603.
- [95] N. Li, F. Michaud, Z. Nosrati, D. Loghin, C. Tremblay, R. Plantefeve, K. Saatchi, U. O. Hafeli, S. Martel, and G. Soulez, "MRI-Compatible Injection System for Magnetic Microparticle Embolization," (in eng), *IEEE Trans Biomed Eng*, vol. 66, no. 8, pp. 2331-2340, Aug 2019, doi: 10.1109/tbme.2018.2889000.

- [96] S. Y. Kim, J.-Y. Hwang, and U. S. Shin, "Preparation of nano/macroporous polycaprolactone microspheres for an injectable cell delivery system using room temperature ionic liquid and camphene," *Journal of Colloid and Interface Science*, vol. 465, pp. 18-25, 2016/03/01/ 2016, doi: <https://doi.org/10.1016/j.jcis.2015.11.055>.
- [97] B. Milborne, A. Arafat, R. Layfield, A. Thompson, and I. Ahmed, "The Use of Biomaterials in Internal Radiation Therapy," *Recent Progress in Materials*, vol. 02, no. 02, p. 012, 2020/05/12 2020, doi: 10.21926/rpm.2002012.
- [98] P. Chowdhury, A. M. Roberts, S. Khan, B. B. Hafeez, S. C. Chauhan, M. Jaggi, and M. M. Yallapu, "Magnetic nanoformulations for prostate cancer," (in eng), *Drug Discov Today*, vol. 22, no. 8, pp. 1233-1241, Aug 2017, doi: 10.1016/j.drudis.2017.04.018.
- [99] E. Kaffash, M.-A. Shahbazi, H. Hatami, and A. Nokhodchi, "An insight into gastrointestinal macromolecule delivery using physical oral devices," *Drug Discovery Today*, vol. 27, no. 8, pp. 2309-2321, 2022/08/01/ 2022, doi: <https://doi.org/10.1016/j.drudis.2022.04.014>.
- [100] B. A. Teply, R. Tong, S. Y. Jeong, G. Luther, I. Sherifi, C. H. Yim, A. Khademhosseini, O. C. Farokhzad, R. S. Langer, and J. Cheng, "The use of charge-coupled polymeric microparticles and micromagnets for modulating the bioavailability of orally delivered macromolecules," *Biomaterials*, vol. 29, no. 9, pp. 1216-1223, 2008/03/01/ 2008, doi: <https://doi.org/10.1016/j.biomaterials.2007.11.018>.
- [101] M. Beck-Broichsitter, I. E. Paulus, A. Greiner, and T. Kissel, "Modified vibrating-mesh nozzles for advanced spray-drying applications," *European Journal of Pharmaceutics and Biopharmaceutics*, vol. 92, pp. 96-101, 2015/05/01/ 2015, doi: <https://doi.org/10.1016/j.ejpb.2015.03.001>.
- [102] F. Andrade, D. Rafael, M. Videira, D. Ferreira, A. Sosnik, and B. Sarmiento, "Nanotechnology and pulmonary delivery to overcome resistance in infectious diseases," (in eng), *Advanced drug delivery reviews*, vol. 65, no. 13-14, pp. 1816-27, Nov 2013, doi: 10.1016/j.addr.2013.07.020.
- [103] N. Bertrand and J. C. Leroux, "The journey of a drug-carrier in the body: an anatomo-physiological perspective," (in eng), *Journal of controlled release : official journal of the Controlled Release Society*, vol. 161, no. 2, pp. 152-63, Jul 20 2012, doi: 10.1016/j.jconrel.2011.09.098.
- [104] X. Huang, Ma, Y., Li, Y., Han, F., & Lin, W, "Targeted Drug Delivery Systems for Kidney Diseases," *Frontiers in Bioengineering and Biotechnology*, 2021. [Online]. Available: <https://doi.org/10.3389/fbioe.2021.683247>.
- [105] S. Prijic and G. Sersa, "Magnetic nanoparticles as targeted delivery systems in oncology," (in eng), *Radiol Oncol*, vol. 45, no. 1, pp. 1-16, Mar 2011, doi: 10.2478/v10019-011-0001-z.
- [106] K. Beyatricks, "Recent trends in microsphere drug delivery system and its therapeutic applications-a review," *Crit Rev Pharm Sci*, vol. 2, 2013.
- [107] T. W. Prow, J. E. Grice, L. L. Lin, R. Faye, M. Butler, W. Becker, E. M. T. Wurm, C. Yoong, T. A. Robertson, H. P. Soyer, and M. S. Roberts, "Nanoparticles and microparticles for skin drug delivery," *Advanced drug delivery reviews*, vol. 63, no. 6, pp. 470-491, 2011/05/30/ 2011, doi: <https://doi.org/10.1016/j.addr.2011.01.012>.
- [108] D. Kohane, "Microparticles and nanoparticles for drug delivery," *Biotechnology and bioengineering*, vol. 96, pp. 203-9, 02/01 2007, doi: 10.1002/bit.21301.

- [109] M. V. Velasco, M. T. Souza, M. C. Crovace, A. J. A. d. Oliveira, and E. D. Zanotto, "Bioactive magnetic glass-ceramics for cancer treatment," *Biomedical Glasses*, vol. 5, no. 1, pp. 148-177, 2019, doi: doi:10.1515/bglass-2019-0013.
- [110] D. H. Kim, J. Chen, R. A. Omary, and A. C. Larson, "MRI visible drug eluting magnetic microspheres for transcatheter intra-arterial delivery to liver tumors," (in eng), *Theranostics*, vol. 5, no. 5, pp. 477-88, 2015, doi: 10.7150/thno.10823.
- [111] L. Liu, X. Liang, X. Xu, X. Zhang, J. Wen, K. Chen, X. Su, Z. Teng, G. Lu, and J. Xu, "Magnetic mesoporous embolic microspheres in transcatheter arterial chemoembolization for liver cancer," (in eng), *Acta Biomater*, vol. 130, pp. 374-384, Aug 2021, doi: 10.1016/j.actbio.2021.05.031.
- [112] J. Nowak-Jary and B. Machnicka, "Pharmacokinetics of magnetic iron oxide nanoparticles for medical applications," *Journal of Nanobiotechnology*, vol. 20, no. 1, p. 305, 2022/06/27 2022, doi: 10.1186/s12951-022-01510-w.
- [113] M. Magro, D. Baratella, E. Bonaiuto, A. R. J. de, and F. Vianello, "New Perspectives on Biomedical Applications of Iron Oxide Nanoparticles," (in eng), *Current medicinal chemistry*, vol. 25, no. 4, pp. 540-555, Feb 12 2018, doi: 10.2174/0929867324666170616102922.
- [114] M. Hofmann-Antenbrink, B. von Rechenberg, H. Hofmann, and M. Tan, *Superparamagnetic Nanoparticles for Biomedical Applications*. 2009.
- [115] L. Mohammed, H. G. Gomaa, D. Ragab, and J. Zhu, "Magnetic nanoparticles for environmental and biomedical applications: A review," *Particuology*, vol. 30, pp. 1-14, 2017/02/01/ 2017, doi: <https://doi.org/10.1016/j.partic.2016.06.001>.
- [116] J. Kudr, Y. Haddad, L. Richtera, Z. Heger, M. Cernak, V. Adam, and O. Zitka, "Magnetic Nanoparticles: From Design and Synthesis to Real World Applications," (in eng), *Nanomaterials (Basel)*, vol. 7, no. 9, p. 243, 2017, doi: 10.3390/nano7090243.
- [117] N. A. Stocke, S. A. Meenach, S. M. Arnold, H. M. Mansour, and J. Z. Hilt, "Formulation and characterization of inhalable magnetic nanocomposite microparticles (MnMs) for targeted pulmonary delivery via spray drying," *International journal of pharmaceuticals*, vol. 479, no. 2, pp. 320-328, 2015/02/20/ 2015, doi: <https://doi.org/10.1016/j.ijpharm.2014.12.050>.
- [118] M. Saadat, M. K. D. Manshadi, M. Mohammadi, M. J. Zare, M. Zarei, R. Kamali, and A. Sanati-Nezhad, "Magnetic particle targeting for diagnosis and therapy of lung cancers," (in eng), *Journal of controlled release : official journal of the Controlled Release Society*, vol. 328, pp. 776-791, Dec 10 2020, doi: 10.1016/j.jconrel.2020.09.017.
- [119] D. A. Edwards, A. Ben-Jebria, and R. Langer, "Recent advances in pulmonary drug delivery using large, porous inhaled particles," (in eng), *J Appl Physiol (1985)*, vol. 85, no. 2, pp. 379-85, Aug 1998, doi: 10.1152/jappl.1998.85.2.379.
- [120] T. Sadhukha, T. S. Wiedmann, and J. Panyam, "Inhalable magnetic nanoparticles for targeted hyperthermia in lung cancer therapy," (in eng), *Biomaterials*, vol. 34, no. 21, pp. 5163-71, Jul 2013, doi: 10.1016/j.biomaterials.2013.03.061.
- [121] I. M. El-Sherbiny, N. M. El-Baz, and M. H. Yacoub, "Inhaled nano- and microparticles for drug delivery," (in eng), *Glob Cardiol Sci Pract*, vol. 2015, p. 2, 2015, doi: 10.5339/gcsp.2015.2.
- [122] S. Chamorro, L. Gutiérrez, M. P. Vaquero, D. Verdoy, G. Salas, Y. Luengo, A. Brenes, and F. José Teran, "Safety assessment of chronic oral exposure to iron oxide nanoparticles," *Nanotechnology*, vol. 26, no. 20, p. 205101, 2015/04/30 2015, doi: 10.1088/0957-4484/26/20/205101.

- [123] G. R. Ferreira, T. Segura, F. G. de Souza, A. P. Umpierre, and F. Machado, "Synthesis of poly(vinyl acetate)-based magnetic polymer microparticles," *European Polymer Journal*, vol. 48, no. 12, pp. 2050-2069, 2012/12/01/ 2012, doi: <https://doi.org/10.1016/j.eurpolymj.2012.09.003>.
- [124] R. V. Ramanujan, "Magnetic Particles for Biomedical Applications," in *Biomedical Materials*, R. Narayan Ed. Boston, MA: Springer US, 2009, pp. 477-491.
- [125] J. van der Zee, "Heating the patient: a promising approach?," (in eng), *Ann Oncol*, vol. 13, no. 8, pp. 1173-84, Aug 2002, doi: 10.1093/annonc/mdf280.
- [126] S. Gao, M. Zheng, X. Ren, Y. Tang, and X. Liang, "Local hyperthermia in head and neck cancer: Mechanism, application and advance," *Oncotarget*, vol. 7, 06/30 2016, doi: 10.18632/oncotarget.10350.
- [127] Z. Behrouzki, Z. Joveini, B. Keshavarzi, N. Eyvazzadeh, and R. Z. Aghdam, "Hyperthermia: How Can It Be Used?," (in eng), *Oman Med J*, vol. 31, no. 2, pp. 89-97, Mar 2016, doi: 10.5001/omj.2016.19.
- [128] I. Rodrigo, I. Castellanos-Rubio, E. Garaio, O. K. Arriortua, M. Insausti, I. Orue, J. Á. García, and F. Plazaola, "Exploring the potential of the dynamic hysteresis loops via high field, high frequency and temperature adjustable AC magnetometer for magnetic hyperthermia characterization," *International Journal of Hyperthermia*, vol. 37, no. 1, pp. 976-991, 2020/01/01 2020, doi: 10.1080/02656736.2020.1802071.
- [129] G. F. Baronzio and E. D. Hager, *Hyperthermia In Cancer Treatment: A Primer*. Springer US, 2008.
- [130] D. Kouzoudis, G. Samourgkanidis, A. Kolokithas-Ntoukas, G. Zoppellaro, and K. Spiliotopoulos, "Magnetic Hyperthermia in the 400–1,100 kHz Frequency Range Using MIONs of Condensed Colloidal Nanocrystal Clusters," (in English), *Frontiers in Materials*, Original Research vol. 8, 2021-May-05 2021, doi: 10.3389/fmats.2021.638019.
- [131] J. Delannoy, G. Giaux, A. Dittmar, W. H. Newman, G. Delhomme, and D. Delvaley, "Measurements of effective thermal conductivity during hyperthermia: A comparison of experimental and clinical results," *International Journal of Hyperthermia*, vol. 6, no. 1, pp. 143-154, 1990/01/01 1990, doi: 10.3109/026567390009140811.
- [132] F. Reyes-Ortega, V. Delgado Á, and G. R. Iglesias, "Modulation of the Magnetic Hyperthermia Response Using Different Superparamagnetic Iron Oxide Nanoparticle Morphologies," (in eng), *Nanomaterials (Basel)*, vol. 11, no. 3, Mar 3 2021, doi: 10.3390/nano11030627.
- [133] N. N. Liu, A. P. Pyatakov, A. M. Saletsky, M. N. Zharkov, N. A. Pyataev, G. B. Sukhorukov, Y. K. Gun'ko, and A. M. Tishin, "The "field or frequency" dilemma in magnetic hyperthermia: The case of ZnMn ferrite nanoparticles," *Journal of Magnetism and Magnetic Materials*, vol. 555, p. 169379, 2022/08/01/ 2022, doi: <https://doi.org/10.1016/j.jmmm.2022.169379>.
- [134] A. Bhardwaj, K. Parekh, and N. Jain, "In vitro hyperthermic effect of magnetic fluid on cervical and breast cancer cells," (in eng), *Sci Rep*, vol. 10, no. 1, p. 15249, Sep 17 2020, doi: 10.1038/s41598-020-71552-3.
- [135] J. Plati, O. Bucur, and R. Khosravi-Far, "Apoptotic cell signaling in cancer progression and therapy," *Integrative Biology*, vol. 3, no. 4, pp. 279-296, 2011, doi: 10.1039/c0ib00144a.
- [136] W. J. Welch and J. P. Suhan, "Morphological study of the mammalian stress response: characterization of changes in cytoplasmic organelles, cytoskeleton,

- and nucleoli, and appearance of intranuclear actin filaments in rat fibroblasts after heat-shock treatment," *Journal of Cell Biology*, vol. 101, no. 4, pp. 1198-1211, 1985, doi: 10.1083/jcb.101.4.1198.
- [137] K. Ahmed, Y. Tabuchi, and T. Kondo, "Hyperthermia: an effective strategy to induce apoptosis in cancer cells," *Apoptosis*, vol. 20, no. 11, pp. 1411-1419, 2015/11/01 2015, doi: 10.1007/s10495-015-1168-3.
- [138] G. Hannon, A. Bogdanska, Y. Volkov, and A. Prina-Mello, "Comparing the Effects of Intracellular and Extracellular Magnetic Hyperthermia on the Viability of BxPC-3 Cells," (in eng), *Nanomaterials (Basel)*, vol. 10, no. 3, Mar 24 2020, doi: 10.3390/nano10030593.
- [139] V. Vilas-Boas, F. Carvalho, and B. Espiña, "Magnetic Hyperthermia for Cancer Treatment: Main Parameters Affecting the Outcome of In Vitro and In Vivo Studies," (in eng), *Molecules*, vol. 25, no. 12, p. 2874, 2020, doi: 10.3390/molecules25122874.
- [140] L. Beola, L. Asín, R. M. Fratila, V. Herrero, J. M. de la Fuente, V. Grazú, and L. Gutiérrez, "Dual Role of Magnetic Nanoparticles as Intracellular Hotspots and Extracellular Matrix Disruptors Triggered by Magnetic Hyperthermia in 3D Cell Culture Models," *ACS Applied Materials & Interfaces*, vol. 10, no. 51, pp. 44301-44313, 2018/12/26 2018, doi: 10.1021/acsami.8b18270.
- [141] P. B. Elming, B. S. Sørensen, A. L. Oei, N. A. P. Franken, J. Crezee, J. Overgaard, and M. R. Horsman, "Hyperthermia: The Optimal Treatment to Overcome Radiation Resistant Hypoxia," *Cancers*, vol. 11, no. 1, p. 60, 2019. [Online]. Available: <https://www.mdpi.com/2072-6694/11/1/60>.
- [142] C. H. Hou, F. L. Lin, S. M. Hou, and J. F. Liu, "Hyperthermia induces apoptosis through endoplasmic reticulum and reactive oxygen species in human osteosarcoma cells," (in eng), *Int J Mol Sci*, vol. 15, no. 10, pp. 17380-95, Sep 29 2014, doi: 10.3390/ijms151017380.
- [143] A. L. Oei, L. E. Vriend, J. Crezee, N. A. Franken, and P. M. Krawczyk, "Effects of hyperthermia on DNA repair pathways: one treatment to inhibit them all," (in eng), *Radiat Oncol*, vol. 10, p. 165, Aug 7 2015, doi: 10.1186/s13014-015-0462-0.
- [144] J. R. Lepock, "Cellular effects of hyperthermia: relevance to the minimum dose for thermal damage," *International Journal of Hyperthermia*, vol. 19, no. 3, pp. 252-266, 2003/01/01 2003, doi: 10.1080/0265673031000065042.
- [145] A. M. De Mendoza, S. Michlíková, J. Berger, J. Karschau, L. A. Kunz-Schughart, and D. D. McLeod, "Mathematical model for the thermal enhancement of radiation response: thermodynamic approach," *Sci Rep*, vol. 11, no. 1, p. 5503, 2021/03/09 2021, doi: 10.1038/s41598-021-84620-z.
- [146] J. C. Peeken, P. Vaupel, and S. E. Combs, "Integrating Hyperthermia into Modern Radiation Oncology: What Evidence Is Necessary?," (in eng), *Front Oncol*, vol. 7, p. 132, 2017, doi: 10.3389/fonc.2017.00132.
- [147] K. Tanderup, C. Ménard, C. Polgar, J. C. Lindegaard, C. Kirisits, and R. Pötter, "Advancements in brachytherapy," *Advanced drug delivery reviews*, vol. 109, pp. 15-25, 2017/01/15/ 2017, doi: <https://doi.org/10.1016/j.addr.2016.09.002>.
- [148] P. M. Price, W. E. Mahmoud, A. A. Al-Ghamdi, and L. M. Bronstein, "Magnetic Drug Delivery: Where the Field Is Going," (in English), *Frontiers in Chemistry*, Mini Review vol. 6, no. 619, 2018-December-11 2018, doi: 10.3389/fchem.2018.00619.

- [149] M. Torres-Lugo and C. Rinaldi, "Thermal potentiation of chemotherapy by magnetic nanoparticles," (in eng), *Nanomedicine (London, England)*, vol. 8, no. 10, pp. 1689-707, Oct 2013, doi: 10.2217/nnm.13.146.
- [150] R. D. Issels, "Hyperthermia adds to chemotherapy," *European Journal of Cancer*, vol. 44, no. 17, pp. 2546-2554, 2008/11/01/ 2008, doi: <https://doi.org/10.1016/j.ejca.2008.07.038>.
- [151] E. Pennacchioli, M. Fiore, and A. Gronchi, "Hyperthermia as an adjunctive treatment for soft-tissue sarcoma," *Expert Review of Anticancer Therapy*, vol. 9, no. 2, pp. 199-210, 2009/02/01 2009, doi: 10.1586/14737140.9.2.199.
- [152] Z. Chen, C. Wu, Z. Zhang, W. Wu, X. Wang, and Z. Yu, "Synthesis, functionalization, and nanomedical applications of functional magnetic nanoparticles," *Chinese Chemical Letters*, vol. 29, no. 11, pp. 1601-1608, 2018/11/01/ 2018, doi: <https://doi.org/10.1016/j.cclet.2018.08.007>.
- [153] A. H. Faraji and P. Wipf, "Nanoparticles in cellular drug delivery," *Bioorganic & Medicinal Chemistry*, vol. 17, no. 8, pp. 2950-2962, 2009/04/15/ 2009, doi: <https://doi.org/10.1016/j.bmc.2009.02.043>.
- [154] S. Saifullah, I. Ali, M. Kawish, R. M. El-Shabasy, L. Chen, and H. R. El-Seedi, "Chapter 12 - Surface functionalized magnetic nanoparticles for targeted cancer therapy and diagnosis," in *Metal Nanoparticles for Drug Delivery and Diagnostic Applications*, M. R. Shah, M. Imran, and S. Ullah Eds.: Elsevier, 2020, pp. 215-236.
- [155] S. Kayal, D. Bandyopadhyay, T. K. Mandal, and R. V. Ramanujan, "The flow of magnetic nanoparticles in magnetic drug targeting," *RSC Advances*, 10.1039/C1RA00023C vol. 1, no. 2, pp. 238-246, 2011, doi: 10.1039/C1RA00023C.
- [156] C. Naud, C. Thébault, M. Carrière, Y. Hou, R. Morel, F. Berger, B. Diény, and H. Joisten, "Cancer treatment by magneto-mechanical effect of particles, a review," *Nanoscale Advances*, 10.1039/D0NA00187B vol. 2, no. 9, pp. 3632-3655, 2020, doi: 10.1039/D0NA00187B.
- [157] J. B. Mathieu and S. Martel, "Aggregation of magnetic microparticles in the context of targeted therapies actuated by a magnetic resonance imaging system," (in English), *J. Appl. Phys.*, Article vol. 106, no. 4, p. 7, Aug 2009, Art no. 044904, doi: 10.1063/1.3159645.
- [158] C. M. Ellis, J. Pellico, and J. J. Davis, "Magnetic Nanoparticles Supporting Bio-responsive T(1)/T(2) Magnetic Resonance Imaging," (in eng), *Materials (Basel)*, vol. 12, no. 24, p. 4096, 2019, doi: 10.3390/ma12244096.
- [159] J. B. Mathieu and S. Martel, "Magnetic microparticle steering within the constraints of an MRI system: proof of concept of a novel targeting approach," (in eng), *Biomed Microdevices*, vol. 9, no. 6, pp. 801-8, Dec 2007, doi: 10.1007/s10544-007-9092-0.
- [160] S. Sánchez-Cabezas, R. Montes-Robles, J. Gallo, F. Sancenón, and R. Martínez-Máñez, "Combining magnetic hyperthermia and dual T1/T2 MR imaging using highly versatile iron oxide nanoparticles," *Dalton Transactions*, 10.1039/C8DT04685A vol. 48, no. 12, pp. 3883-3892, 2019, doi: 10.1039/C8DT04685A.
- [161] S. D. Shingte, A. H. Phakatkar, E. McKiernan, K. Nigoghossian, S. Ferguson, R. Shahbazian-Yassar, and D. F. Brougham, "Correlating Magnetic Hyperthermia and Magnetic Resonance Imaging Contrast Performance of Cubic Iron Oxide Nanoparticles with Crystal Structural Integrity," *Chemistry of Materials*, 2022/08/10 2022, doi: 10.1021/acs.chemmater.2c00708.

- [162] M. O. Besenhard, L. Panariello, C. Kiefer, A. P. LaGrow, L. Storozhuk, F. Perton, S. Begin, D. Mertz, N. T. K. Thanh, and A. Gavriilidis, "Small iron oxide nanoparticles as MRI T1 contrast agent: scalable inexpensive water-based synthesis using a flow reactor," *Nanoscale*, 10.1039/D1NR00877C vol. 13, no. 19, pp. 8795-8805, 2021, doi: 10.1039/D1NR00877C.
- [163] B. Cortés-Llanos, S. M. Ocampo, L. de la Cueva, G. F. Calvo, J. Belmonte-Beitia, L. Pérez, G. Salas, and Á. Ayuso-Sacido, "Influence of Coating and Size of Magnetic Nanoparticles on Cellular Uptake for In Vitro MRI," (in eng), *Nanomaterials (Basel)*, vol. 11, no. 11, Oct 28 2021, doi: 10.3390/nano11112888.
- [164] K. P. Melo, A. V. Makela, N. N. Knier, A. M. Hamilton, and P. J. Foster, "Magnetic microspheres can be used for magnetic particle imaging of cancer cells arrested in the mouse brain," (in eng), *Magn Reson Med*, vol. 87, no. 1, pp. 312-322, Jan 2022, doi: 10.1002/mrm.28987.
- [165] J. Li, J. Wang, J. Li, X. Yang, J. Wan, C. Zheng, Q. Du, G. Zhou, and X. Yang, "Fabrication of Fe(3)O(4)@PVA microspheres by one-step electrospray for magnetic resonance imaging during transcatheter arterial embolization," (in eng), *Acta Biomater*, vol. 131, pp. 532-543, Sep 1 2021, doi: 10.1016/j.actbio.2021.07.006.
- [166] D. Serantes and D. Baldomir, "Nanoparticle Size Threshold for Magnetic Agglomeration and Associated Hyperthermia Performance," (in eng), *Nanomaterials (Basel)*, vol. 11, no. 11, Oct 21 2021, doi: 10.3390/nano11112786.
- [167] Y. Gao, Y. Liu, and C. Xu, "Magnetic Nanoparticles for Biomedical Applications: From Diagnosis to Treatment to Regeneration," in *Engineering in Translational Medicine*, W. Cai Ed. London: Springer London, 2014, pp. 567-583.
- [168] L. Zhi-feng, Y. Gao, G.-M. Cao, and Z. Liu, "High-efficiency reduction behavior for the oxide scale formed on hot-rolled steel in a mixed atmosphere of hydrogen and argon," *Journal of Materials Science*, vol. 55, 02/01 2020, doi: 10.1007/s10853-019-04027-0.
- [169] Z. Sun, X. Zhou, W. Luo, Q. Yue, Y. Zhang, X. Cheng, W. Li, B. Kong, Y. Deng, and D. Zhao, "Interfacial engineering of magnetic particles with porous shells: Towards magnetic core – Porous shell microparticles," *Nano Today*, vol. 11, no. 4, pp. 464-482, 2016/08/01/ 2016, doi: <https://doi.org/10.1016/j.nantod.2016.07.003>.
- [170] B. Yong Yu and S.-Y. Kwak, *Assembly of magnetite nanocrystals into spherical mesoporous aggregates with a 3-D wormhole-like pore structure*. 2010.
- [171] L.-L. Wang and J.-S. Jiang, "Preparation of Fe₃O₄Spherical Nanoporous Particles Facilitated by Polyethylene Glycol 4000," *Nanoscale Research Letters*, journal article vol. 4, no. 12, p. 1439, September 02 2009, doi: 10.1007/s11671-009-9417-4.
- [172] G. Parkinson, *Iron Oxide Surfaces*. 2016.
- [173] Y. Hashimoto, M. Taguchi, S. Fukami, H. Momono, T. Matsushita, H. Matsuda, F. Matsui, and H. Daimon, "Site-sensitive X-ray photoelectron spectroscopy of Fe₃O₄ by photoelectron diffraction," *Surface and Interface Analysis*, vol. 51, 10/01 2018, doi: 10.1002/sia.6568.
- [174] J. Winsett, A. Moilanen, K. Paudel, S. Kamali, K. Ding, W. Cribb, D. Seifu, and S. Neupane, "Quantitative determination of magnetite and maghemite in iron oxide nanoparticles using Mössbauer spectroscopy," *SN Applied Sciences*, vol. 1, no. 12, p. 1636, 2019/11/19 2019, doi: 10.1007/s42452-019-1699-2.

- [175] R. M. Cornell and U. Schwertmann, *The Iron Oxides: Structure, Properties, Reactions, Occurrences and Uses*. Wiley, 2003.
- [176] D. Ling, N. Lee, and T. Hyeon, "Chemical Synthesis and Assembly of Uniformly Sized Iron Oxide Nanoparticles for Medical Applications," *Accounts of Chemical Research*, vol. 48, no. 5, pp. 1276-1285, 2015/05/19 2015, doi: 10.1021/acs.accounts.5b00038.
- [177] W. Kim, C.-Y. Suh, S.-W. Cho, K.-M. Roh, H. Kwon, K. Song, and I.-J. Shon, "A new method for the identification and quantification of magnetite–maghemite mixture using conventional X-ray diffraction technique," *Talanta*, vol. 94, pp. 348-352, 2012/05/30/ 2012, doi: <https://doi.org/10.1016/j.talanta.2012.03.001>.
- [178] G. Righi and R. Magri, "Reduction and Oxidation of Maghemite (001) Surfaces: The Role of Iron Vacancies," *The Journal of Physical Chemistry C*, vol. 123, no. 25, pp. 15648-15658, 2019/06/27 2019, doi: 10.1021/acs.jpcc.9b03657.
- [179] D. Cao, H. Li, L. Pan, J. Li, X. Wang, P. Jing, X. Cheng, W. Wang, J. Wang, and Q. Liu, "High saturation magnetization of γ -Fe₂O₃ nano-particles by a facile one-step synthesis approach," *Sci Rep*, vol. 6, no. 1, p. 32360, 2016/09/01 2016, doi: 10.1038/srep32360.
- [180] H. Shokrollahi, "A review of the magnetic properties, synthesis methods and applications of maghemite," *Journal of Magnetism and Magnetic Materials*, vol. 426, pp. 74-81, 2017/03/15/ 2017, doi: <https://doi.org/10.1016/j.jmmm.2016.11.033>.
- [181] "Crystal Structure," in *The Iron Oxides*, 2003, pp. 9-38.
- [182] "Electronic, Electrical and Magnetic Properties and Colour," in *The Iron Oxides*, 2003, pp. 111-137.
- [183] V. Kuldeep Chand and G. Navdeep, "Green Energy Applications of Hematite (α -Fe₂O₃), Magnetite (Fe₃O₄), and Maghemite (γ -Fe₂O₃) Nanoparticles Based Hydroelectric Cell," in *Iron Oxide Nanoparticles*, H. Xiao-Lan Ed. Rijeka: IntechOpen, 2022, p. Ch. 7.
- [184] D. Hirabayashi, T. Yoshikawa, Y. Kawamoto, K. Mochizuki, and K. Suzuki, "Characterization and Applications of Calcium Ferrites Based Materials Containing Active Oxygen Species," *Advances in Science and Technology*, vol. 45, pp. 2169-2175, 2006, doi: 10.4028/www.scientific.net/AST.45.2169.
- [185] X. M. Aretxabaleta, I. Etxebarria, and H. Manzano, "Electronic and elastic properties of brownmillerite," *Materials Research Express*, vol. 7, no. 1, p. 015516, 2020/01/01 2020, doi: 10.1088/2053-1591/ab61a1.
- [186] D. Hirabayashi, T. Yoshikawa, K. Mochizuki, K. Suzuki, and Y. Sakai, "Formation of brownmillerite type calcium ferrite (Ca₂Fe₂O₅) and catalytic properties in propylene combustion," *Catalysis Letters*, vol. 110, pp. 269-274, 09/01 2006, doi: 10.1007/s10562-006-0120-0.
- [187] C. C. Silva, I. F. Vasconcelos, A. S. B. Sombra, and M. A. Valente, "Magnetic properties study on Fe-doped calcium phosphate," *Physica Scripta*, vol. 80, no. 5, p. 055706, 2009/11 2009, doi: 10.1088/0031-8949/80/05/055706.
- [188] T. Hidayat, D. Shishin, S. Deckerov, and E. Jak, "Thermodynamic Optimization of the Ca-Fe-O System," *Metallurgical and Materials Transactions B*, vol. 47, 11/16 2015, doi: 10.1007/s11663-015-0501-0.
- [189] O. Sedighi, A. Alaghmandfard, M. Montazerian, and F. Baino, "A critical review of bioceramics for magnetic hyperthermia," *Journal of the American Ceramic Society*, vol. 105, no. 3, pp. 1723-1747, 2022, doi: <https://doi.org/10.1111/jace.17861>.

- [190] M. N. Rahaman, D. E. Day, B. S. Bal, Q. Fu, S. B. Jung, L. F. Bonewald, and A. P. Tomsia, "Bioactive glass in tissue engineering," (in eng), *Acta biomaterialia*, vol. 7, no. 6, pp. 2355-2373, 2011, doi: 10.1016/j.actbio.2011.03.016.
- [191] M. T. Islam, R. M. Felfel, E. A. Abou Neel, D. M. Grant, I. Ahmed, and K. M. Z. Hossain, "Bioactive calcium phosphate-based glasses and ceramics and their biomedical applications: A review," (in eng), *J Tissue Eng*, vol. 8, p. 2041731417719170, Jan-Dec 2017, doi: 10.1177/2041731417719170.
- [192] J. Crush, A. Hussain, K. T. M. Seah, and W. S. Khan, "Bioactive Glass: Methods for Assessing Angiogenesis and Osteogenesis," (in English), *Frontiers in Cell and Developmental Biology*, Review vol. 9, 2021-June-14 2021, doi: 10.3389/fcell.2021.643781.
- [193] A. Misaghi, A. Goldin, M. Awad, and A. A. Kulidjian, "Osteosarcoma: a comprehensive review," (in eng), *Sicot j*, vol. 4, p. 12, 2018, doi: 10.1051/sicotj/2017028.
- [194] A. Tiwari, "Current concepts in surgical treatment of osteosarcoma," (in eng), *J Clin Orthop Trauma*, vol. 3, no. 1, pp. 4-9, Jun 2012, doi: 10.1016/j.jcot.2012.04.004.
- [195] S. Tohme, R. L. Simmons, and A. Tsung, "Surgery for Cancer: A Trigger for Metastases," (in eng), *Cancer Res*, vol. 77, no. 7, pp. 1548-1552, Apr 1 2017, doi: 10.1158/0008-5472.Can-16-1536.
- [196] A. Baeza, D. Arcos, and M. Vallet-Regí, "Thermoseeds for interstitial magnetic hyperthermia: from bioceramics to nanoparticles," *Journal of Physics: Condensed Matter*, vol. 25, no. 48, p. 484003, 2013/11/07 2013, doi: 10.1088/0953-8984/25/48/484003.
- [197] G. Kaur, O. P. Pandey, K. Singh, D. Homa, B. Scott, and G. Pickrell, "A review of bioactive glasses: Their structure, properties, fabrication and apatite formation," (in eng), *J Biomed Mater Res A*, vol. 102, no. 1, pp. 254-74, Jan 2014, doi: 10.1002/jbm.a.34690.
- [198] R. K. Brow, "Review: the structure of simple phosphate glasses," *Journal of Non-Crystalline Solids*, vol. 263-264, pp. 1-28, 2000/03/01/ 2000, doi: [https://doi.org/10.1016/S0022-3093\(99\)00620-1](https://doi.org/10.1016/S0022-3093(99)00620-1).
- [199] F. Muñoz, J. Rocherullé, I. Ahmed, and L. Hu, "Phosphate Glasses," in *Springer Handbook of Glass*, J. D. Musgraves, J. Hu, and L. Calvez Eds. Cham: Springer International Publishing, 2019, pp. 553-594.
- [200] E. A. Abou Neel, I. Ahmed, J. Pratten, S. N. Nazhat, and J. C. Knowles, "Characterisation of antibacterial copper releasing degradable phosphate glass fibres," *Biomaterials*, vol. 26, no. 15, pp. 2247-2254, 2005/05/01/ 2005, doi: <https://doi.org/10.1016/j.biomaterials.2004.07.024>.
- [201] E. A. Abou Neel, L. A. O'Dell, M. E. Smith, and J. C. Knowles, "Processing, characterisation, and biocompatibility of zinc modified metaphosphate based glasses for biomedical applications," (in eng), *J Mater Sci Mater Med*, vol. 19, no. 4, pp. 1669-79, Apr 2008, doi: 10.1007/s10856-007-3313-1.
- [202] E. A. Abou Neel, W. Chrzanowski, and J. C. Knowles, "Effect of increasing titanium dioxide content on bulk and surface properties of phosphate-based glasses," (in eng), *Acta Biomater*, vol. 4, no. 3, pp. 523-34, May 2008, doi: 10.1016/j.actbio.2007.11.007.
- [203] I. Ahmed, C. A. Collins, M. P. Lewis, I. Olsen, and J. C. Knowles, "Processing, characterisation and biocompatibility of iron-phosphate glass fibres for tissue

- engineering," *Biomaterials*, vol. 25, no. 16, pp. 3223-3232, 2004/07/01/ 2004, doi: <https://doi.org/10.1016/j.biomaterials.2003.10.013>.
- [204] N. A. Spaldin, *Magnetic Materials: Fundamentals and Applications*, 2 ed. Cambridge: Cambridge University Press, 2010.
- [205] U. Jeong, X. Teng, Y. Wang, H. Yang, and Y. Xia, "Superparamagnetic Colloids: Controlled Synthesis and Niche Applications," *Advanced Materials*, vol. 19, no. 1, pp. 33-60, 2007, doi: <https://doi.org/10.1002/adma.200600674>.
- [206] S. Chikazumi and C. D. Graham, *Physics of ferromagnetism* (no. 94). Oxford university press, 1997.
- [207] A. Aharoni, *Introduction to the Theory of Ferromagnetism* (Press). 2001.
- [208] G. Florio, "Structural Features of Magnetic Materials," in *Encyclopedia of Smart Materials*, A.-G. Olabi Ed. Oxford: Elsevier, 2022, pp. 1-9.
- [209] Y. Slimani, E. Hannachi, H. Tombuloglu, S. Güner, M. A. Almessiere, A. Baykal, M. A. Aljafary, E. A. Al-Suhaimi, M. Nawaz, and I. Ercan, "Chapter 14 - Magnetic nanoparticles based nanocontainers for biomedical application," in *Smart Nanocontainers*, P. Nguyen-Tri, T.-O. Do, and T. A. Nguyen Eds.: Elsevier, 2020, pp. 229-250.
- [210] V. Sechovský, "Magnetism in Solids: General Introduction," in *Encyclopedia of Materials: Science and Technology*, K. H. J. Buschow *et al.* Eds. Oxford: Elsevier, 2001, pp. 5018-5032.
- [211] W. M. Saslow, "Chapter 9 - The Magnetism of Magnets," in *Electricity, Magnetism, and Light*, W. M. Saslow Ed. San Diego: Academic Press, 2002, pp. 384-418.
- [212] C. Binns, "Chapter 1 - Tutorial Section on Nanomagnetism," in *Frontiers of Nanoscience*, vol. 6, C. Binns Ed.: Elsevier, 2014, pp. 1-32.
- [213] P. Němec, M. Fiebig, T. Kampfrath, and A. V. Kimel, "Antiferromagnetic opto-spintronics," *Nature Physics*, vol. 14, no. 3, pp. 229-241, 2018/03/01 2018, doi: 10.1038/s41567-018-0051-x.
- [214] A. G. Kolhatkar, A. C. Jamison, D. Litvinov, R. C. Willson, and T. R. Lee, "Tuning the Magnetic Properties of Nanoparticles," *International Journal of Molecular Sciences*, vol. 14, no. 8, pp. 15977-16009, 2013. [Online]. Available: <https://www.mdpi.com/1422-0067/14/8/15977>.
- [215] P. Dobson, *Nanomedicine: Design and Applications of Magnetic Nanomaterials, Nanosensors and Nanosystems*, by Vijay K. Varadan, Linfeng Chen and Jining Xie. 2012, pp. 1-1.
- [216] D. Meier, N. Valanoor, Q. Zhang, and D. Lee, "Domains and domain walls in ferroic materials," *J. Appl. Phys.*, vol. 129, no. 23, p. 230401, 2021, doi: 10.1063/5.0057144.
- [217] L. B. Kong, L. Liu, Z. Yang, S. Li, T. Zhang, and C. Wang, "15 - Theory of ferrimagnetism and ferrimagnetic metal oxides," in *Magnetic, Ferroelectric, and Multiferroic Metal Oxides*, B. D. Stojanovic Ed.: Elsevier, 2018, pp. 287-311.
- [218] A. Adamiano, M. Iafisco, and A. Tampieri, "9 - Magnetic core-shell nanoparticles: Remote driving, hyperthermia, and controlled drug release," in *Core-Shell Nanostructures for Drug Delivery and Theranostics*, M. L. Focarete and A. Tampieri Eds.: Woodhead Publishing, 2018, pp. 259-296.
- [219] A. E. Deatsch and B. A. Evans, "Heating efficiency in magnetic nanoparticle hyperthermia," *Journal of Magnetism and Magnetic Materials*, vol. 354, pp. 163-172, 2014/03/01/ 2014, doi: <https://doi.org/10.1016/j.jmmm.2013.11.006>.
- [220] C. Blaeß, R. Müller, G. Poologasundarampillai, and D. S. Brauer, "Sintering and concomitant crystallization of bioactive glasses," *International Journal of*

- Applied Glass Science*, vol. 10, no. 4, pp. 449-462, 2019, doi: <https://doi.org/10.1111/ijag.13477>.
- [221] F. Baino, E. Fiume, J. Barberi, S. Kargozar, J. Marchi, J. Massera, and E. Verné, "Processing methods for making porous bioactive glass-based scaffolds—A state-of-the-art review," *International Journal of Applied Ceramic Technology*, vol. 16, no. 5, pp. 1762-1796, 2019, doi: <https://doi.org/10.1111/ijac.13195>.
- [222] B. Thavornnyutikarn, N. Chantarapanich, K. Sitthiseripratip, G. Thouas, and Q. Chen, "Bone Tissue Engineering Scaffolding: Computer-Aided Scaffolding Techniques," *Progress in Biomaterials*, vol. 3, pp. 61-102, 12/01 2014, doi: 10.1007/s40204-014-0026-7.
- [223] X. W. Zhu, "Preparation of reticulated porous ceramics with a controlled pore structure," *Journal of Inorganic Materials*, Article vol. 17, no. 1, pp. 79-85, 2002. [Online]. Available: <https://www.scopus.com/inward/record.uri?eid=2-s2.0-31044440051&partnerID=40&md5=e4d05912f35e93d35f130ecab0e70da4>.
- [224] P. S. Liu and G. F. Chen, "Chapter Five - Fabricating Porous Ceramics," in *Porous Materials*, P. S. Liu and G. F. Chen Eds. Boston: Butterworth-Heinemann, 2014, pp. 221-302.
- [225] X. Q. Meng and P. Li, "Porous ceramic materials," *Chin Bldg Mat*, Article vol. 10, pp. 92-94, 2008. [Online]. Available: <https://www.scopus.com/inward/record.uri?eid=2-s2.0-85013918971&partnerID=40&md5=07c6a20c165ad3f1c5db97f8a2e7265e>.
- [226] L. Roseti, V. Parisi, M. Petretta, C. Cavallo, G. Desando, I. Bartolotti, and B. Grigolo, "Scaffolds for Bone Tissue Engineering: State of the art and new perspectives," *Materials Science and Engineering: C*, vol. 78, pp. 1246-1262, 2017/09/01/ 2017, doi: <https://doi.org/10.1016/j.msec.2017.05.017>.
- [227] T. Fukasawa, Z. Y. Deng, M. Ando, T. Ohji, and Y. Goto, "Pore structure of porous ceramics synthesized from water-based slurry by freeze-dry process," *Journal of Materials Science*, vol. 36, no. 10, pp. 2523-2527, 2001/05/01 2001, doi: 10.1023/A:1017946518955.
- [228] C. Minas, D. Carnelli, E. Tervoort, and A. R. Studart, "3D Printing of Emulsions and Foams into Hierarchical Porous Ceramics," *Advanced Materials*, vol. 28, no. 45, pp. 9993-9999, 2016, doi: 10.1002/adma.201603390.
- [229] L. Alison, S. Menasce, F. Bouville, E. Tervoort, I. Mattich, A. Ofner, and A. R. Studart, "3D printing of sacrificial templates into hierarchical porous materials," *Scientific Reports*, vol. 9, no. 1, p. 409, 2019/01/23 2019, doi: 10.1038/s41598-018-36789-z.
- [230] A. Dasan, J. Kraxner, L. Grigolato, G. Savio, H. Elsayed, D. Galusek, and E. Bernardo, "3D Printing of Hierarchically Porous Lattice Structures Based on Auring;kermanite Glass Microspheres and Reactive Silicone Binder," *Journal of Functional Biomaterials*, vol. 13, no. 1, p. 8, 2022. [Online]. Available: <https://www.mdpi.com/2079-4983/13/1/8>.
- [231] T. I. N A Nuzulia, A Saputra, T Sudiro, G E Timuda, T Mart, Y W Sari and I Ahmed, "Developing Highly Porous Glass Microspheres via a Single-Stage Flame Spheroidisation Process," *Journal of Physics: Conference Series*, vol. 2243, no. 1, 2022, doi: 10.1088/1742-6596/2243/1/012005.
- [232] E. Ruiz-Hernández, A. López-Noriega, D. Arcos, and M. Vallet-Regí, "Mesoporous magnetic microspheres for drug targeting," *Solid State Sciences*, vol. 10, no. 4, pp. 421-426, 2008/04/01/ 2008, doi: <https://doi.org/10.1016/j.solidstatesciences.2007.11.026>.

- [233] Y. Gao, Y. Wang, Y. Yan, K. Tang, and C.-F. Ding, "Self-assembly of poly(ionic liquid) functionalized mesoporous magnetic microspheres for the solid-phase extraction of preservatives from milk samples," *Journal of Separation Science*, vol. 43, no. 4, pp. 766-773, 2020, doi: <https://doi.org/10.1002/jssc.201900851>.
- [234] K. Li, Z. Zeng, J. Xiong, L. Yan, H. Guo, S. Liu, Y. Dai, and T. Chen, "Fabrication of mesoporous Fe₃O₄@SiO₂@CTAB-SiO₂ magnetic microspheres with a core/shell structure and their efficient adsorption performance for the removal of trace PFOS from water," *Colloids and Surfaces A: Physicochemical and Engineering Aspects*, vol. 465, pp. 113-123, 2015/01/20/ 2015, doi: <https://doi.org/10.1016/j.colsurfa.2014.10.044>.
- [235] H. Liu, S. Ji, Y. Zheng, M. Li, and H. Yang, "Modified solvothermal synthesis of magnetic microspheres with multifunctional surfactant cetyltrimethyl ammonium bromide and directly coated mesoporous shell," *Powder Technology*, vol. 246, pp. 520-529, 2013/09/01/ 2013, doi: <https://doi.org/10.1016/j.powtec.2013.06.007>.
- [236] Y. Gao, M.-W. Chang, Z. Ahmad, and J.-S. Li, *Magnetic-Responsive Microparticles with Customized Porosity for Drug Delivery*. 2016.
- [237] M. T. Islam, L. Macri-Pellizzeri, K. M. Z. Hossain, V. Sottile, and I. Ahmed, "Effect of varying the Mg with Ca content in highly porous phosphate-based glass microspheres," *Materials Science and Engineering: C*, vol. 120, p. 111668, 2021/01/01/ 2021, doi: <https://doi.org/10.1016/j.msec.2020.111668>.
- [238] M. T. Islam, L. Macri-Pellizzeri, V. Sottile, and I. Ahmed, "Rapid conversion of highly porous borate glass microspheres into hydroxyapatite," *Biomaterials Science*, 10.1039/D0BM01776K vol. 9, no. 5, pp. 1826-1844, 2021, doi: 10.1039/D0BM01776K.
- [239] P. Sinitsyna, O. Karlström, C. Sevonius, and L. Hupa, "In vitro dissolution and characterisation of flame-sprayed bioactive glass microspheres S53P4 and 13-93," *Journal of Non-Crystalline Solids*, vol. 591, p. 121736, 2022/09/01/ 2022, doi: <https://doi.org/10.1016/j.jnoncrysol.2022.121736>.
- [240] M. T. Islam, N. A. Nuzulia, L. Macri-Pellizzeri, F. Nigar, Y. W. Sari, and I. Ahmed, "Evolution of silicate bioglass particles as porous microspheres with a view towards orthobiologics," (in eng), *J Biomater Appl*, vol. 36, no. 8, pp. 1427-1443, Mar 2022, doi: 10.1177/08853282211059294.
- [241] D. Gupta, K. M. Z. Hossain, I. Ahmed, V. Sottile, and D. M. Grant, "Flame-Spheroidized Phosphate-Based Glass Particles with Improved Characteristics for Applications in Mesenchymal Stem Cell Culture Therapy and Tissue Engineering," (in eng), *ACS applied materials & interfaces*, vol. 10, no. 31, pp. 25972-25982, Aug 8 2018, doi: 10.1021/acsami.8b05267.
- [242] M. T. Islam, "Manufacture and Characterisation of Porous Phosphate, Borate and Silicate Glass Microspheres for Biomedical Applications," Doctor of Philosophy, Faculty of Engineering, The University of Nottingham, United Kingdom, 2019.
- [243] J. C. R. Sverre Mayhra, "Characterization of nanostructures," *CRC Press*, p. 314, 2013.
- [244] L. Reimer, "Scanning Electron Microscopy - Physics of Image Formation and Microanalysis," *Springer-Verlag Berlin Heidelberg*, pp. XIV, 529, 1998.
- [245] B. J. Inkson, "2 - Scanning electron microscopy (SEM) and transmission electron microscopy (TEM) for materials characterization," in *Materials Characterization Using Nondestructive Evaluation (NDE) Methods*, G.

- Hübschen, I. Altpeter, R. Tschuncky, and H.-G. Herrmann Eds.: Woodhead Publishing, 2016, pp. 17-43.
- [246] M. Ezzahmouly, A. Elmoutaouakkil, M. Ed-Dhahraouy, H. Khallok, A. Elouahli, A. Mazurier, A. ElAlbani, and Z. Hatim, "Micro-computed tomographic and SEM study of porous bioceramics using an adaptive method based on the mathematical morphological operations," *Heliyon*, vol. 5, no. 12, p. e02557, 2019/12/01/ 2019, doi: <https://doi.org/10.1016/j.heliyon.2019.e02557>.
- [247] J. I. Goldstein, D. E. Newbury, J. R. Michael, N. W. M. Ritchie, J. H. J. Scott, and D. C. Joy, *Scanning Electron Microscopy and X-Ray Microanalysis*. Springer New York, 2017.
- [248] W. Zhou, R. Apkarian, Z. L. Wang, and D. Joy, "Fundamentals of Scanning Electron Microscopy (SEM)," in *Scanning Microscopy for Nanotechnology: Techniques and Applications*, W. Zhou and Z. L. Wang Eds. New York, NY: Springer New York, 2007, pp. 1-40.
- [249] C. R. Brundle, J. Charles A. Evans, and S. Wilson, "Encyclopedia of Materials Characterization: Surfaces, Interfaces, Thin Films," *Butterworth-Heinemann*, 1992.
- [250] I. Materials Evaluation and Engineering. "ENERGY DISPERSIVE X-RAY SPECTROSCOPY (EDS)." <https://www.mee-inc.com/hamm/energy-dispersive-x-ray-spectroscopyeds/> (accessed).
- [251] P. Sylvester, *Use of the Mineral Liberation Analyzer (MLA) for mineralogical studies of sediments and sedimentary rocks*. 2012, pp. 1-16.
- [252] R. Fandrich, Y. Gu, D. Burrows, and K. Moeller, "Modern SEM-based mineral liberation analysis," *International Journal of Mineral Processing*, vol. 84, no. 1, pp. 310-320, 2007/10/19/ 2007, doi: <https://doi.org/10.1016/j.minpro.2006.07.018>.
- [253] F. Sima, C. Ristoscu, L. Duta, O. Gallet, K. Anselme, and I. N. Mihailescu, "3 - Laser thin films deposition and characterization for biomedical applications," in *Laser Surface Modification of Biomaterials*, R. Vilar Ed.: Woodhead Publishing, 2016, pp. 77-125.
- [254] A. K. Chatterjee, "8 - X-Ray Diffraction," in *Handbook of Analytical Techniques in Concrete Science and Technology*, V. S. Ramachandran and J. J. Beaudoin Eds. Norwich, NY: William Andrew Publishing, 2001, pp. 275-332.
- [255] E. P. Bertin, "Qualitative and Semiquantitative Analysis," in *Introduction to X-Ray Spectrometric Analysis*. Boston, MA: Springer US, 1978, pp. 255-278.
- [256] R. L. Fagaly, "Superconducting quantum interference device instruments and applications," *Review of Scientific Instruments*, vol. 77, no. 10, p. 101101, 2006, doi: 10.1063/1.2354545.
- [257] *Handbook of Induction Heating* (Handbook of Induction Heating). CRC Press, 2017.
- [258] V. Schünemann and H. Paulsen, "Mössbauer Spectroscopy," in *Encyclopedia of Inorganic and Bioinorganic Chemistry*.
- [259] N. Saadatkhah, A. Carillo Garcia, S. Ackermann, P. Leclerc, M. Latifi, S. Samih, G. S. Patience, and J. Chaouki, "Experimental methods in chemical engineering: Thermogravimetric analysis—TGA," *The Canadian Journal of Chemical Engineering*, vol. 98, no. 1, pp. 34-43, 2020, doi: <https://doi.org/10.1002/cjce.23673>.
- [260] K. E. Sickafus, "2.4 - TEM: Transmission Electron Microscopy," in *Encyclopedia of Materials Characterization*, C. R. Brundle, C. A. Evans, and S. Wilson Eds. Boston: Butterworth-Heinemann, 1992, pp. 99-115.

- [261] R. J. Yeo, *Ultrathin Carbon-Based Overcoats for Extremely High Density Magnetic Recording*. Springer Singapore, 2017.
- [262] C. A. Gorski and M. M. Scherer, "Determination of nanoparticulate magnetite stoichiometry by Mössbauer spectroscopy, acidic dissolution, and powder X-ray diffraction: A critical review," *American Mineralogist*, vol. 95, no. 7, pp. 1017-1026, 2010, doi: 10.2138/am.2010.3435.
- [263] G. M. da Costa, E. de Grave, P. M. A. De Barker, and R. E. Vandenberghe, "Influence of Nonstoichiometry and the Presence of Maghemite on the Mössbauer Spectrum of Magnetite," *Clays and Clay Minerals*, vol. 43, no. 6, pp. 656-668, 1995/12/01 1995, doi: 10.1346/CCMN.1995.0430602.
- [264] S. J. Oh, D. C. Cook, and H. E. Townsend, "Characterization of Iron Oxides Commonly Formed as Corrosion Products on Steel," *Hyperfine Interactions*, vol. 112, no. 1, pp. 59-66, 1998/12/01 1998, doi: 10.1023/A:1011076308501.
- [265] R. E. Vandenberghe, C. A. Barrero, G. M. da Costa, E. Van San, and E. De Grave, "Mössbauer characterization of iron oxides and (oxy)hydroxides: the present state of the art," *Hyperfine Interactions*, vol. 126, pp. 247-259, 2000.
- [266] E. J. Lavernia and T. S. Srivatsan, "The rapid solidification processing of materials: science, principles, technology, advances, and applications," *Journal of Materials Science*, vol. 45, no. 2, pp. 287-325, 2010/01/01 2010, doi: 10.1007/s10853-009-3995-5.
- [267] !!! INVALID CITATION !!! [13-16].
- [268] H. Hou, Z. Ji, Z. Xie, and H. Jin, "Spheroidizing mechanisms and simulation of spherical silica in Oxygen-Acetylene flame," *Advanced Powder Technology*, vol. 29, no. 3, pp. 789-795, 2018/03/01/ 2018, doi: <https://doi.org/10.1016/j.appt.2017.12.018>.
- [269] H. Jin, L. Xu, and S. Hou, "Preparation of spherical silica powder by oxygen-acetylene flame spheroidization process," *Journal of Materials Processing Technology*, vol. 210, no. 1, pp. 81-84, 2010/01/01/ 2010, doi: <https://doi.org/10.1016/j.jmatprotec.2009.08.009>.
- [270] D. Levy, R. Giustetto, and A. Hoser, "Structure of magnetite (Fe₃O₄) above the Curie temperature: a cation ordering study," *Physics and Chemistry of Minerals*, vol. 39, no. 2, pp. 169-176, 2012/02/01 2012, doi: 10.1007/s00269-011-0472-x.
- [271] A. Milanti, V. Matikainen, G. Bolelli, H. Koivuluoto, L. Lusvarghi, and P. Vuoristo, "Microstructure and Sliding Wear Behavior of Fe-Based Coatings Manufactured with HVOF and HVOF Thermal Spray Processes," *Journal of Thermal Spray Technology*, vol. 25, no. 5, pp. 1040-1055, 2016/06/01 2016, doi: 10.1007/s11666-016-0410-z.
- [272] M. Jadidi, S. Moghtadernejad, and A. Dolatabadi, "A Comprehensive Review on Fluid Dynamics and Transport of Suspension/Liquid Droplets and Particles in High-Velocity Oxygen-Fuel (HVOF) Thermal Spray," *Coatings*, vol. 5, no. 4, pp. 576-645, 2015. [Online]. Available: <https://www.mdpi.com/2079-6412/5/4/576>.
- [273] J. Yu, X. Liu, Y. Yu, H. Li, P. Liu, K. Huang, and R. Sun, "Research and Application of High-Velocity Oxygen Fuel Coatings," *Coatings*, vol. 12, no. 6, p. 828, 2022. [Online]. Available: <https://www.mdpi.com/2079-6412/12/6/828>.
- [274] R. E. Vandenberghe, C. A. Barrero, G. M. da Costa, E. Van San, and E. De Grave, "Mössbauer characterization of iron oxides and (oxy)hydroxides: the present state of the art," *Hyperfine Interactions*, vol. 126, no. 1, pp. 247-259, 2000/07/01 2000, doi: 10.1023/A:1012603603203.

- [275] J. Tucek, R. Zboril, and D. Petridis, "Maghemite nanoparticles by view of Mössbauer spectroscopy," (in eng), *J Nanosci Nanotechnol*, vol. 6, no. 4, pp. 926-47, Apr 2006, doi: 10.1166/jnn.2006.183.
- [276] M. Ceretti, S. Corallini, and W. Paulus, "Influence of Phase Transformations on Crystal Growth of Stoichiometric Brownmillerite Oxides: Sr₂ScGaO₅ and Ca₂Fe₂O₅," *Crystals*, vol. 6, 11/01 2016, doi: 10.3390/cryst6110146.
- [277] M. Li and P. D. Christofides, "Computational study of particle in-flight behavior in the HVOF thermal spray process," *Chemical Engineering Science*, vol. 61, no. 19, pp. 6540-6552, 2006/10/01/ 2006, doi: <https://doi.org/10.1016/j.ces.2006.05.050>.
- [278] F. R. X. Kahlenberg V, "Crystal growth and cation distribution in doped dicalcium ferrite Ca₂(Fe_{1-x}Me_x)₂O₅ (Me=Al,Ga)," *European Journal of Mineralogy*, vol. 12, pp. 129-135, 2000. [Online]. Available: https://rruff.info/repository/sample_child_record_powder/by_minerals/Srebrodolskite_R130096-9_Powder_DIF_File_11700.txt.
- [279] S. Dhankhar, D. S. Vavilapalli, G. Bhalerao, S. Ganesamoorthy, S. Hussain, K. Baskar, and S. Singh, "Growth of brownmillerite Ca₂Fe₂O₅ single crystals under air, oxygen and argon atmospheres using optical floating zone technique: a comparative study," *Bulletin of Materials Science*, vol. 45, no. 1, p. 31, 2022/02/08 2022, doi: 10.1007/s12034-021-02609-w.
- [280] D. S. Vavilapalli, S. Banik, R. G. Peri, M. B, M. Miryala, M. Murakami, K. Alicja, A. K, R. R. M. S, and S. Singh, "Nitrogen Incorporated Photoactive Brownmillerite Ca₂Fe₂O₅ for Energy and Environmental Applications," *Sci Rep*, vol. 10, no. 1, p. 2713, 2020/02/17 2020, doi: 10.1038/s41598-020-59454-w.
- [281] J. He, M. Ice, and E. Lavernia, "Particle melting behavior during high-velocity oxygen fuel thermal spraying," *Journal of Thermal Spray Technology*, vol. 10, no. 1, pp. 83-93, 2001/03/01 2001, doi: 10.1361/105996301770349547.
- [282] P. D. Christofides, "Control of an HVOF Thermal Spray Process," in *Model-Based Control of Particulate Processes*. Dordrecht: Springer Netherlands, 2002, pp. 163-189.
- [283] M. Li and P. D. Christofides, "Modeling and Control of High-Velocity Oxygen-Fuel (HVOF) Thermal Spray: A Tutorial Review," *Journal of Thermal Spray Technology*, vol. 18, no. 5, p. 753, 2009/03/27 2009, doi: 10.1007/s11666-009-9309-2.
- [284] J. Tikkanen, K. A. Gross, C. C. Berndt, V. Pitkänen, J. Keskinen, S. Raghu, M. Rajala, and J. Karthikeyan, "Characteristics of the liquid flame spray process," *Surface and Coatings Technology*, vol. 90, no. 3, pp. 210-216, 1997/04/01/ 1997, doi: [https://doi.org/10.1016/S0257-8972\(96\)03153-2](https://doi.org/10.1016/S0257-8972(96)03153-2).
- [285] B. F. Amorim, M. A. Morales, F. Bohn, A. S. Carriço, S. N. de Medeiros, and A. L. Dantas, "Synthesis of stoichiometric Ca₂Fe₂O₅ nanoparticles by high-energy ball milling and thermal annealing," *Physica B: Condensed Matter*, vol. 488, pp. 43-48, 2016/05/01/ 2016, doi: <https://doi.org/10.1016/j.physb.2016.01.029>.
- [286] E. Asenath-Smith, I. N. Lokuhewa, S. T. Mixture, and D. D. Edwards, "p-Type thermoelectric properties of the oxygen-deficient perovskite Ca₂Fe₂O₅ in the brownmillerite structure," *Journal of Solid State Chemistry*, vol. 183, no. 7, pp. 1670-1677, 2010/07/01/ 2010, doi: <https://doi.org/10.1016/j.jssc.2010.05.016>.

- [287] T. C. Hanson, C. M. Hackett, and G. S. Settles, "Independent control of HVOF particle velocity and temperature," *Journal of Thermal Spray Technology*, vol. 11, no. 1, pp. 75-85, 2002/03/01 2002, doi: 10.1361/105996302770349005.
- [288] S. Kamnis and S. Gu, "Study of In-Flight and Impact Dynamics of Nonspherical Particles from HVOF Guns," *Journal of Thermal Spray Technology*, vol. 19, no. 1, pp. 31-41, 2010/01/01 2010, doi: 10.1007/s11666-009-9382-6.
- [289] M. T. Islam, L. Macri-Pellizzeri, V. Sottile, and I. Ahmed, "Rapid conversion of highly porous borate glass microspheres into hydroxyapatite," (in eng), *Biomater Sci*, vol. 9, no. 5, pp. 1826-1844, Mar 10 2021, doi: 10.1039/d0bm01776k.
- [290] R. P. Singh, S. Kumar, S. Dubey, and A. Singh, "A review on working and applications of oxy-acetylene gas welding," *Materials Today: Proceedings*, vol. 38, pp. 34-39, 2021/01/01/ 2021, doi: <https://doi.org/10.1016/j.matpr.2020.05.521>.
- [291] E. R. Monazam, R. W. Breault, and R. Siriwardane, "Kinetics of Magnetite (Fe₃O₄) Oxidation to Hematite (Fe₂O₃) in Air for Chemical Looping Combustion," *Industrial & Engineering Chemistry Research*, vol. 53, no. 34, pp. 13320-13328, 2014/08/27 2014, doi: 10.1021/ie501536s.
- [292] T. K. Sandeep Kumar, N. N. Viswanathan, H. Ahmed, A. Dahlin, C. Andersson, and B. Bjorkman, "Investigation of Magnetite Oxidation Kinetics at the Particle Scale," *Metallurgical and Materials Transactions B*, vol. 50, no. 1, pp. 150-161, 2019/02/01 2019, doi: 10.1007/s11663-018-1459-5.
- [293] S. Nasrazadani and A. Raman, "The application of infrared spectroscopy to the study of rust systems—II. Study of cation deficiency in magnetite (Fe₃O₄) produced during its transformation to maghemite (γ-Fe₂O₃) and hematite (α-Fe₂O₃)," *Corrosion Science*, vol. 34, no. 8, pp. 1355-1365, 1993/08/01/ 1993, doi: [https://doi.org/10.1016/0010-938X\(93\)90092-U](https://doi.org/10.1016/0010-938X(93)90092-U).
- [294] Z. Li, C. Chanéac, G. Berger, S. Delaunay, A. Graff, and G. Lefèvre, "Mechanism and kinetics of magnetite oxidation under hydrothermal conditions," *RSC Advances*, 10.1039/C9RA03234G vol. 9, no. 58, pp. 33633-33642, 2019, doi: 10.1039/C9RA03234G.
- [295] T. Beuvier, J. F. Bardeau, B. Calvignac, G. Corbel, F. Hindré, J.-M. Greneche, F. Boury, and A. Gibaud, "Phase transformations in CaCO₃/iron oxide composite induced by thermal treatment and laser irradiation," *Journal of Raman Spectroscopy*, vol. 44, pp. 489-495, 03/01 2013, doi: 10.1002/jrs.4200.
- [296] B. Boyanov, "Solid state interactions in the systems CaO(CaCO₃)-Fe₂O₃ and CuFe₂O₄-CaO," *Journal of Mining and Metallurgy, Section B : Metallurgy*, vol. 41 B, 01/01 2005, doi: 10.2298/JMMB0501067B.
- [297] T. L. Phan, P. T. Tho, N. Tran, D. H. Kim, B. W. Lee, D. S. Yang, D. V. Thiet, and S. L. Cho, "Crystalline and Electronic Structures and Magnetic and Electrical Properties of La-Doped Ca₂Fe₂O₅ Compounds," *Journal of Electronic Materials*, vol. 47, no. 1, pp. 188-195, 2018/01/01 2018, doi: 10.1007/s11664-017-5841-x.
- [298] X. Bo, D. Wang, and X. G. Wan, "Calculated magnetic exchange interactions in brownmillerite Ca₂Fe₂O₅," *Physics Letters A*, vol. 394, p. 127202, 2021/04/02/ 2021, doi: <https://doi.org/10.1016/j.physleta.2021.127202>.
- [299] I. Kagomiya, Y. Hirota, K. I. Kakimoto, K. Fujii, M. Shiraiwa, M. Yashima, A. Fuwa, and S. Nakamura, "Weak ferromagnetic ordering in brownmillerite Ca₂Fe₂O₅ and its effect on electric field gradients," (in eng), *Phys Chem Chem*

- Phys*, vol. 19, no. 46, pp. 31194-31201, Nov 29 2017, doi: 10.1039/c7cp04520d.
- [300] Z. Shaterabadi, G. Nabiyouni, and M. Soleymani, "Physics responsible for heating efficiency and self-controlled temperature rise of magnetic nanoparticles in magnetic hyperthermia therapy," *Progress in Biophysics and Molecular Biology*, vol. 133, pp. 9-19, 2018/03/01/ 2018, doi: <https://doi.org/10.1016/j.pbiomolbio.2017.10.001>.
- [301] M. V. Velasco, M. T. Souza, M. C. Crovace, A. J. A. d. Oliveira, and E. D. Zanotto, "Bioactive magnetic glass-ceramics for cancer treatment," (in English), vol. 5, no. 1, p. 148, 2019, doi: <https://doi.org/10.1515/bglass-2019-0013>.
- [302] R. Hergt and S. Dutz, "Magnetic Particle Hyperthermia – Biophysical Limitations of a Visionary Tumour Therapy," *Journal of Magnetism and Magnetic Materials*, vol. 311[^], pp. 187–192, 04/01 2007, doi: 10.1016/j.jmmm.2006.10.1156.
- [303] A. S. Khan, M. F. Nasir, M. T. Khan, A. Murtaza, and M. A. Hamayun, "Study of structural, magnetic and radio frequency heating aptitudes of pure and (Fe-III) doped manganite (La_{1-x} Sr_xMnO₃) and their incorporation with Sodium Poly-Styrene Sulfonate (PSS) for magnetic hyperthermia applications," *Physica B: Condensed Matter*, vol. 600, p. 412627, 2021/01/01/ 2021, doi: <https://doi.org/10.1016/j.physb.2020.412627>.
- [304] J.-H. Park, A. M. Derfus, E. Segal, K. S. Vecchio, S. N. Bhatia, and M. J. Sailor, "Local Heating of Discrete Droplets Using Magnetic Porous Silicon-Based Photonic Crystals," *Journal of the American Chemical Society*, vol. 128, no. 24, pp. 7938-7946, 2006/06/01 2006, doi: 10.1021/ja0612854.
- [305] A. K. Fahlvik, E. Holtz, and J. Klaveness, "Relaxation efficacy of paramagnetic and superparamagnetic microspheres in liver and spleen," *Magnetic Resonance Imaging*, vol. 8, no. 4, pp. 363-369, 1990/01/01/ 1990, doi: [https://doi.org/10.1016/0730-725X\(90\)90043-2](https://doi.org/10.1016/0730-725X(90)90043-2).
- [306] D. Xiao, T. Lu, R. Zeng, and Y. Bi, "Preparation and highlighted applications of magnetic microparticles and nanoparticles: a review on recent advances," *Microchimica Acta*, vol. 183, no. 10, pp. 2655-2675, 2016/10/01 2016, doi: 10.1007/s00604-016-1928-y.
- [307] K. El-Boubbou, R. Ali, H. Al-Zahrani, T. Trivilegio, A. H. Alanazi, A. L. Khan, M. Boudjelal, and A. AlKushi, "Preparation of iron oxide mesoporous magnetic microparticles as novel multidrug carriers for synergistic anticancer therapy and deep tumor penetration," (in eng), *Sci Rep*, vol. 9, no. 1, pp. 9481-9481, 2019, doi: 10.1038/s41598-019-46007-z.
- [308] M. Aldén, "Spatially and temporally resolved laser/optical diagnostics of combustion processes: From fundamentals to practical applications," *Proceedings of the Combustion Institute*, 2022/07/31/ 2022, doi: <https://doi.org/10.1016/j.proci.2022.06.020>.
- [309] O. E. Jegede, R. F. Cochrane, and A. M. Mullis, "Metastable monotectic phase separation in Co–Cu alloys," *Journal of Materials Science*, vol. 53, no. 16, pp. 11749-11764, 2018/08/01 2018, doi: 10.1007/s10853-018-2417-y.
- [310] R. P. Shi, C. P. Wang, D. Wheeler, X. J. Liu, and Y. Wang, "Formation mechanisms of self-organized core/shell and core/shell/corona microstructures in liquid droplets of immiscible alloys," *Acta Materialia*, vol. 61, no. 4, pp. 1229-1243, 2013/02/01/ 2013, doi: <https://doi.org/10.1016/j.actamat.2012.10.033>.
- [311] N. Wang, L. Zhang, Y. L. Peng, and W. J. Yao, "Composition-dependence of core-shell microstructure formation in monotectic alloys under reduced gravity

- conditions," *Journal of Alloys and Compounds*, vol. 663, pp. 379-386, 2016/04/05/ 2016, doi: <https://doi.org/10.1016/j.jallcom.2015.12.015>.
- [312] F. M. Galogahi, Y. Zhu, H. An, and N.-T. Nguyen, "Core-shell microparticles: Generation approaches and applications," *Journal of Science: Advanced Materials and Devices*, vol. 5, no. 4, pp. 417-435, 2020/12/01/ 2020, doi: <https://doi.org/10.1016/j.jsamd.2020.09.001>.
- [313] S. M. Kim, M. Patel, and R. Patel, "PLGA Core-Shell Nano/Microparticle Delivery System for Biomedical Application," *Polymers*, vol. 13, no. 20, p. 3471, 2021. [Online]. Available: <https://www.mdpi.com/2073-4360/13/20/3471>.
- [314] R. S. van der Kooij, R. Steendam, H. W. Frijlink, and W. L. J. Hinrichs, "An overview of the production methods for core-shell microspheres for parenteral controlled drug delivery," *European Journal of Pharmaceutics and Biopharmaceutics*, vol. 170, pp. 24-42, 2022/01/01/ 2022, doi: <https://doi.org/10.1016/j.ejpb.2021.11.007>.
- [315] M. Khanmohammadi, V. Zolfagharzadeh, Z. Bagher, H. Soltani, and J. Ai, "Cell encapsulation in core-shell microcapsules through coaxial electrospinning system and horseradish peroxidase-catalyzed crosslinking," *Biomedical Physics & Engineering Express*, vol. 6, no. 1, p. 015022, 2020/01/13 2020, doi: 10.1088/2057-1976/ab6035.
- [316] Z. Wang, J. Qi, N. Yang, R. Yu, and D. Wang, "Core-shell nano/microstructures for heterogeneous tandem catalysis," *Materials Chemistry Frontiers*, 10.1039/DOQM00538J vol. 5, no. 3, pp. 1126-1139, 2021, doi: 10.1039/DOQM00538J.
- [317] G. Yu, X. Chen, A. Wang, and Y. Wang, "Carbon@SnS₂ core-shell microspheres for lithium-ion battery anode materials," *Ionics*, vol. 24, no. 10, pp. 2915-2923, 2018/10/01 2018, doi: 10.1007/s11581-018-2596-1.
- [318] D. Guo, X. Song, F. Li, L. Tan, H. Ma, L. Zhang, and Y. Zhao, "Oriented synthesis of Co₃O₄ core-shell microspheres for high-performance asymmetric supercapacitor," *Colloids and Surfaces A: Physicochemical and Engineering Aspects*, vol. 546, pp. 1-8, 2018/06/05/ 2018, doi: <https://doi.org/10.1016/j.colsurfa.2018.02.072>.
- [319] G. Wang, Q. Liu, M. Chang, J. Jang, W. Sui, C. Si, and Y. Ni, "Novel Fe₃O₄@lignosulfonate/phenolic core-shell microspheres for highly efficient removal of cationic dyes from aqueous solution," *Industrial Crops and Products*, vol. 127, pp. 110-118, 2019/01/01/ 2019, doi: <https://doi.org/10.1016/j.indcrop.2018.10.056>.
- [320] M. Zhao, Z. Cui, D. Pan, F. Fan, J. Tang, Y. Hu, Y. Xu, P. Zhang, P. Li, X.-Y. Kong, and W. Wu, "An Efficient Uranium Adsorption Magnetic Platform Based on Amidoxime-Functionalized Flower-like Fe₃O₄@TiO₂ Core-Shell Microspheres," *ACS Applied Materials & Interfaces*, vol. 13, no. 15, pp. 17931-17939, 2021/04/21 2021, doi: 10.1021/acsami.1c00556.
- [321] A. Ahmed, K. Skinley, S. Herodotou, and H. Zhang, "Core-shell microspheres with porous nanostructured shells for liquid chromatography," *Journal of Separation Science*, vol. 41, no. 1, pp. 99-124, 2018/01/01 2018, doi: 10.1002/jssc.201700850.
- [322] J. Tom, K. Ohno, and S. Perrier, "Surface-initiated SET living radical polymerisation for the synthesis of silica-polymer core-shell nanoparticles," *Polymer Chemistry*, 10.1039/C6PY01290F vol. 7, no. 39, pp. 6075-6083, 2016, doi: 10.1039/C6PY01290F.

- [323] W. Liu, W. D. Wu, C. Selomulya, and X. D. Chen, "Facile Spray-Drying Assembly of Uniform Microencapsulates with Tunable Core–Shell Structures and Controlled Release Properties," *Langmuir*, vol. 27, no. 21, pp. 12910-12915, 2011/11/01 2011, doi: 10.1021/la203249v.
- [324] J. Ji, L. Liang, H. Xu, G. Xiang, H. Li, P. Li, X. Zhou, and X. Guo, "Facile solvent evaporation synthesis of core-shell structured Al@PVDF nanoparticles with excellent corrosion resistance and combustion properties," *Combustion and Flame*, vol. 238, p. 111925, 2022/04/01/ 2022, doi: <https://doi.org/10.1016/j.combustflame.2021.111925>.
- [325] Y. Lu, Y. Yin, Z.-Y. Li, and Y. Xia, "Synthesis and Self-Assembly of Au@SiO₂ Core–Shell Colloids," *Nano Letters*, vol. 2, no. 7, pp. 785-788, 2002/07/01 2002, doi: 10.1021/nl025598i.
- [326] H. T. T. Ta, A. K. Tieu, H. Zhu, H. Yu, T. D. Ta, S. Wan, N. V. Tran, and H. M. Le, "Chemical Origin of Sodium Phosphate Interactions on Iron and Iron Oxide Surfaces by First Principle Calculations," *The Journal of Physical Chemistry C*, vol. 122, no. 1, pp. 635-647, 2018/01/11 2018, doi: 10.1021/acs.jpcc.7b10731.
- [327] F. d'Yvoire, M. Pintard-Scrépel, E. Bretey, and M. de la Rochère, "Phase transitions and ionic conduction in 3D skeleton phosphates A₃M₂(PO₄)₃ : A = Li, Na, Ag, K ; M = Cr, Fe," *Solid State Ionics*, vol. 9-10, pp. 851-857, 1983/12/01/ 1983, doi: [https://doi.org/10.1016/0167-2738\(83\)90101-7](https://doi.org/10.1016/0167-2738(83)90101-7).
- [328] S. S. Danewalia and K. Singh, "Bioactive glasses and glass-ceramics for hyperthermia treatment of cancer: state-of-art, challenges, and future perspectives," (in eng), *Mater Today Bio*, vol. 10, pp. 100100-100100, 2021, doi: 10.1016/j.mtbio.2021.100100.
- [329] L. Tonthat, Y. Yamamoto, F. Aki, H. Saito, and K. Mitobe, "Thermosensitive Implant for Magnetic Hyperthermia by Mixing Micro-Magnetic and Nano-Magnetic Particles," *IEEE Transactions on Magnetics*, vol. 54, no. 6, pp. 1-4, 2018, doi: 10.1109/TMAG.2018.2821271.
- [330] P.-E. L. Renard, F. Buchegger, A. Petri-Fink, F. Bosman, D. Rüfenacht, H. Hofmann, E. Doelker, and O. Jordan, "Local moderate magnetically induced hyperthermia using an implant formed in situ in a mouse tumor model," *International Journal of Hyperthermia*, vol. 25, no. 3, pp. 229-239, 2009/01/01 2009, doi: 10.1080/02656730802713557.
- [331] J. V. Wandiyanto, V. K. Truong, M. Al Kobaisi, S. Juodkazis, H. Thissen, O. Bazaka, K. Bazaka, R. J. Crawford, and E. P. Ivanova, "The Fate of Osteoblast-Like MG-63 Cells on Pre-Infected Bactericidal Nanostructured Titanium Surfaces," *Materials*, vol. 12, no. 10, p. 1575, 2019. [Online]. Available: <https://www.mdpi.com/1996-1944/12/10/1575>.
- [332] N. J. Lakhkar, I.-H. Lee, H.-W. Kim, V. Salih, I. B. Wall, and J. C. Knowles, "Bone formation controlled by biologically relevant inorganic ions: Role and controlled delivery from phosphate-based glasses," *Advanced drug delivery reviews*, vol. 65, no. 4, pp. 405-420, 2013/04/01/ 2013, doi: <https://doi.org/10.1016/j.addr.2012.05.015>.
- [333] E. A. Abou Neel, I. Ahmed, J. J. Blaker, A. Bismarck, A. R. Boccaccini, M. P. Lewis, S. N. Nazhat, and J. C. Knowles, "Effect of iron on the surface, degradation and ion release properties of phosphate-based glass fibres," *Acta Biomaterialia*, vol. 1, no. 5, pp. 553-563, 2005/09/01/ 2005, doi: <https://doi.org/10.1016/j.actbio.2005.05.001>.
- [334] X. Yu, D. E. Day, G. J. Long, and R. K. Brow, "Properties and structure of sodium-iron phosphate glasses," *Journal of Non-Crystalline Solids*, vol. 215,

- no. 1, pp. 21-31, 1997/07/01/ 1997, doi: [https://doi.org/10.1016/S0022-3093\(97\)00022-7](https://doi.org/10.1016/S0022-3093(97)00022-7).
- [335] N. Kuganathan and A. Chronos, "Defect Chemistry and Na-Ion Diffusion in Na(3)Fe(2)(PO(4))(3) Cathode Material," (in eng), *Materials (Basel)*, vol. 12, no. 8, Apr 25 2019, doi: 10.3390/ma12081348.
- [336] S. Tan, Y. Wang, Y. Du, Y. Xiao, and S. Zhang, "Injectable bone cement with magnesium-containing microspheres enhances osteogenesis via anti-inflammatory immunoregulation," (in eng), *Bioact Mater*, vol. 6, no. 10, pp. 3411-3423, 2021, doi: 10.1016/j.bioactmat.2021.03.006.
- [337] J. García-García, G. Azuara, O. Fraile-Martinez, C. García-Montero, M. A. Álvarez-Mon, S. Ruíz-Díez, M. Álvarez-Mon, J. Buján, N. García-Honduvilla, M. A. Ortega, and B. De la Torre, "Modification of the Polymer of a Bone Cement with Biodegradable Microspheres of PLGA and Loading with Daptomycin and Vancomycin Improve the Response to Bone Tissue Infection," (in eng), *Polymers (Basel)*, vol. 14, no. 5, Feb 23 2022, doi: 10.3390/polym14050888.
- [338] W. Luo, Z. Geng, Z. Li, S. Wu, Z. Cui, S. Zhu, Y. Liang, and X. Yang, "Controlled and sustained drug release performance of calcium sulfate cement porous TiO(2) microsphere composites," (in eng), *Int J Nanomedicine*, vol. 13, pp. 7491-7501, 2018, doi: 10.2147/ij.n.S177784.
- [339] Y. Zhao, S. Yu, X. Wu, H. Dai, W. Liu, R. Tu, and T. Goto, "Construction of macroporous magnesium phosphate-based bone cement with sustained drug release," *Materials & Design*, vol. 200, p. 109466, 2021/02/15/ 2021, doi: <https://doi.org/10.1016/j.matdes.2021.109466>.
- [340] E. Zeimaran, S. Pourshahrestani, A. Fathi, N. A. b. A. Razak, N. A. Kadri, A. Sheikhi, and F. Baino, "Advances in bioactive glass-containing injectable hydrogel biomaterials for tissue regeneration," *Acta Biomaterialia*, vol. 136, pp. 1-36, 2021/12/01/ 2021, doi: <https://doi.org/10.1016/j.actbio.2021.09.034>.
- [341] L. Sun, S. Zhou, W. Wang, X. Li, J. Wang, and J. Weng, "Preparation and characterization of porous biodegradable microspheres used for controlled protein delivery," *Colloids and Surfaces A: Physicochemical and Engineering Aspects*, vol. 345, no. 1, pp. 173-181, 2009/08/05/ 2009, doi: <https://doi.org/10.1016/j.colsurfa.2009.04.053>.
- [342] Z. Zhao, Z. Wang, G. Li, Z. Cai, J. Wu, L. Wang, L. Deng, M. Cai, and W. Cui, "Injectable Microfluidic Hydrogel Microspheres for Cell and Drug Delivery," *Advanced Functional Materials*, vol. 31, no. 31, p. 2103339, 2021, doi: <https://doi.org/10.1002/adfm.202103339>.
- [343] X. Liu, K. A. Fundora, Z. Zhou, A. L. Miller, 2nd, and L. Lu, "Composite Hydrogel Embedded with Porous Microspheres for Long-Term pH-Sensitive Drug Delivery," (in eng), *Tissue Eng Part A*, vol. 25, no. 3-4, pp. 172-182, 2019, doi: 10.1089/ten.TEA.2018.0071.
- [344] H. Shan, K. Li, D. Zhao, C. Chi, Q. Tan, X. Wang, J. Yu, and M. Piao, "Locally Controlled Release of Methotrexate and Alendronate by Thermo-Sensitive Hydrogels for Synergistic Inhibition of Osteosarcoma Progression," (in eng), *Front Pharmacol*, vol. 11, p. 573, 2020, doi: 10.3389/fphar.2020.00573.
- [345] S. Dong, Y. Chen, L. Yu, K. Lin, and X. Wang, "Magnetic Hyperthermia-Synergistic H₂O₂ Self-Sufficient Catalytic Suppression of Osteosarcoma with Enhanced Bone-Regeneration Bioactivity by 3D-Printing Composite Scaffolds," *Advanced Functional Materials*, vol. 30, no. 4, p. 1907071, 2020, doi: <https://doi.org/10.1002/adfm.201907071>.

- [346] K. Takegami, T. Sano, H. Wakabayashi, J. Sonoda, T. Yamazaki, S. Morita, T. Shibuya, and A. Uchida, "New ferromagnetic bone cement for local hyperthermia," *Journal of Biomedical Materials Research*, vol. 43, no. 2, pp. 210-214, 1998, doi: [https://doi.org/10.1002/\(SICI\)1097-4636\(199822\)43:2<210::AID-JBM16>3.0.CO;2-L](https://doi.org/10.1002/(SICI)1097-4636(199822)43:2<210::AID-JBM16>3.0.CO;2-L).
- [347] M. Miola, F. Laviano, R. Gerbaldo, M. Bruno, A. Lombardi, A. Cochis, L. Rimondini, and E. Verné, "Composite bone cements for hyperthermia: modeling and characterization of magnetic, calorimetric and in vitro heating properties," *Ceramics International*, vol. 43, no. 6, pp. 4831-4840, 2017/04/15/2017, doi: <https://doi.org/10.1016/j.ceramint.2016.12.049>.
- [348] M. Bruno, M. Miola, O. Bretcanu, C. Vitale-Brovarone, R. Gerbaldo, F. Laviano, and E. Verné, "Composite bone cements loaded with a bioactive and ferrimagnetic glass-ceramic. Part I: Morphological, mechanical and calorimetric characterization," (in eng), *J Biomater Appl*, vol. 29, no. 2, pp. 254-267, Aug 2014, doi: 10.1177/0885328214521847.
- [349] J. B. Mamani, T. K. F. Souza, M. P. Nucci, F. A. Oliveira, L. P. Nucci, A. H. Alves, G. N. A. Rego, L. Marti, and L. F. Gamarra, "In Vitro Evaluation of Hyperthermia Magnetic Technique Indicating the Best Strategy for Internalization of Magnetic Nanoparticles Applied in Glioblastoma Tumor Cells," (in eng), *Pharmaceutics*, vol. 13, no. 8, Aug 7 2021, doi: 10.3390/pharmaceutics13081219.